Multiscale fracture modelling of concrete using a variational micromechanics-enriched embedded strong discontinuity Finite Element Method

by

Carlos Xavier Azúa-González

born in Guayaquil, Ecuador

A dissertation submitted in partial fulfillment for the degree of

Doctor of Philosophy in Engineering

at the Division of Architectural and Civil Engineering (ACE) - School of Engineering

Cardiff University

Cardiff, Wales, United Kingdom, 2022

Copyright Notice

This work was sponsored by UKRI through the EPSRC grant RM4L, which imposes public release of all funded research material.

This thesis is dedicated to my family. Their unconditional love made
this small step in my career possible.

Acknowledgements

The author highly appreciates the constant efforts of his supervisors, Prof. Tony Jefferson and Dr. Iulia Mihai, to provide valuable guidance and encouraging discussions throughout this research period, within the Materials for life (M4L) group, directed initially by Prof. Em. Bob Lark at Cardiff University's School of Engineering. Despite constant setbacks on the thought-to-be straight-forward research path, they never ceased motivating me in my research on computational modelling of quasi-brittle fracture in concrete. I am indebted to them for sharing with me their expertise, and for coordinating internal and external funding sources that enabled me to undertake my PhD in the UK.

I am grateful for the good times with my PhD-path colleagues of the group: Amrit, Tharmesh, James, Gwylem, Sina, Evan, Louis; and with Research Associates of the group: Brubeck, Cristina, Brunella, Magda, Pedro, Riccardo, Kumaran, Muaaz; and the list goes on, if I mention my interaction with other researchers in Cardiff, across the UK and Europe; to all of you my whole-hearted thanks for the great time.

On the other more personal side, I value the huge support of my family, and that of close friends who watched the enjoyable, as well as the hard times during this PhD. My gratitude is for Seri, who patiently showed me, through love, her support even in the difficult and 'moody' times.

Financial support from the EPSRC-funded grant RM4L, and support by Cardiff University, which helped me to be fully funded as an international student in the UK, are well received. The financial aid received from LUSAS FEA Ltd. at the final stages of my PhD is very appreciated.

Abstract

The focus of this research is the development of a novel physics-based variational multiscale formulation and its computer implementation for modelling diffuse directional microcrack growth and localised macrocrack propagation in a general class of quasi-brittle solids, the so-called cementitious composites. For this task, Micromechanics-based formulations at the material scale, previously developed at Cardiff University, have been improved to cope with deformation localisation objectively, by using Finite Elements with embedded strong discontinuities at the macroscale.

The newly coupled numerical scheme seeks to enable a robust and efficient multiscale fracture propagation framework, which avoids remeshing. The framework predicts deformation and stress response at the homogenised bulk and predicts the propagation of macrocracks until failure is attained. In this context, failure is modelled as a consequence of progressive macroscopic softening with feedback from microscale material deterioration. This Micromechanics-enhanced nonlinear Finite Element framework with embedded strong discontinuities has been implemented into the in-house Fortran code Cardinal. In combination with an existing Matlab post-processor, interfaces have been coded between Cardinal and the open-source visualisation toolkit Paraview. In this way, meshes for representative problems were generated and display effectively.

Finally, validation of the computational framework has been carried out by comparisons of numerical predictions against experimental data of benchmark-type Boundary Value Problems (BVPs) in unreinforced concrete specimens, under various mechanical actions including combined shear and normal deformation upon macrocrack nucleation.

Research Highlights

Key features of the new specialised finite elements are summarised below:

- The method for failure analysis of cement-based materials and structures has been derived using a **multiscale variational principle** and aims to preserve a *minimum energy solution* in the homogenised system with macro-discontinuities in every global incremental iterative step, while remeshing is avoided;
- A *Smooth-Unloading-Reloading* (SUR) method has been used at the macrocrack level, while traction continuity is enabled weakly along macrocracks, to allow *good convergence* characteristics of the new multiscale finite element method. This SUR method employs element-wise tangents from the unloading-reloading branch which remain positive definite;
- Strategies to provide *good computational efficiency* have been tailored. These are twofold:
  - Reduction of computational consumption at the homogenised constitutive level is attained by using directional integration rules for micromechanical solids, and
  - Reduction of global degrees of freedom to a minimum is achieved by using an element-wise quasi-static condensation scheme, which ensures that only the nodal macroscopic displacement field is solved in every global incremental iterative step.

Contents

List of Figures

List of Tables

Chapter 1

Introduction

> *"Truth ... is much too complicated to allow anything but approximations."*
> **John von Neumann** 1903 – 57
> Hungarian-born American mathematician and computer pioneer

1.1 Motivation

The behaviour of cementitious materials, and more generally quasi-brittle materials, has been investigated extensively over the last four decades, in efforts to understand and capture numerically the mechanisms underlying fracture and failure. The first attempt to understand *abrupt* failure from rigorous first principles is attributed to Griffith (1921). In his pioneering work, an expression to predict critical stresses, for catastrophic crack growth, was estimated based on a minimisation of the potential energy in a cracked solid. The main contribution of Griffith lies in the realization that fracture at macroscopic level may be affected by processes at smaller length scales, especially for cracks of length equivalent to a few times the representative molecular length scale. In his representation of the total potential energy, Griffith considered the surface tension arising from unbalanced molecular attraction, which is exerted on particles adjacent to the crack edge upon fracture. Nowadays, the failure of quasi-brittle materials is widely acknowledged to be a consequence of microfractures coalescing into macroscopic cracks (Mazars, 1986; Ortiz, 1988). From a phenomenological point of view, micro and macro fracture manifest as a descending load carrying capacity during ongoing deformation, which is typically referred as the strain-softening response. An example of the so-called strain-softening response is depicted in Figure 1.1, where a one-dimensional bar is subjected to uniaxial extension.

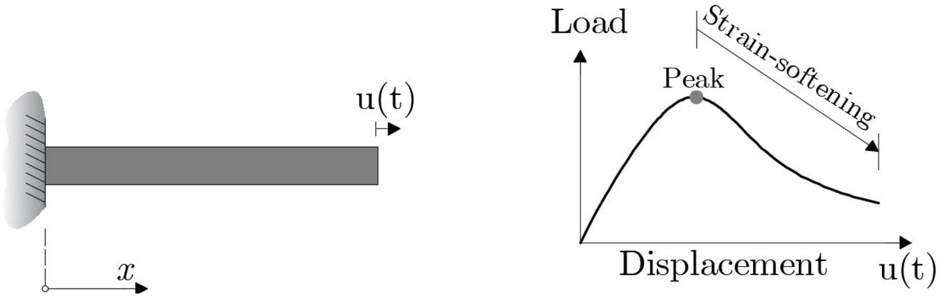

Figure 1.1: One-dimensional bar, corresponding to a quasi-brittle material, subjected to uniaxial extension: geometry and boundary conditions (left), (typical) load carrying capacity vs. displacement (right).

This descending branch of the structural response (in load vs. displacement space) poses numerical challenges when implemented in a Finite Element program (Bažant, 1976; Crisfield, 1982; De Borst, 1987), such as strong mesh dependency of the response and numerical breakdown of iterative solvers, in addition to the complexities involved in the development of appropriate (constitutive-level) material laws for quasi-brittle solids. Furthermore, the widely acknowledged multiscale nature of the response of cementitious composites (Van Mier, 1984) presents additional theoretical challenges at the constitutive-level, since macroscopic constitutive schemes do not have sufficient accuracy, and adding multiscale mechanics components brings often prohibitive computational demand. These challenges mean that this research branch has remained active amongst the Computational Mechanics community for several decades.

The ideal computational technique for modelling the non-linear behaviour of concrete would incorporate components to model fracture across multiple scales, to allow an adequate prediction of the structural-level response till failure, and would be *modest in computational demand* to allow engineering predictions on standard computers.

The aim of this PhD research is to develop a specialised Finite Element framework for modelling the fracture response of cementitious materials, which couples a multiscale constitutive formulation with computational techniques for fracture propagation.

A short discussion on the scope of such formulation and outline of this thesis is provided in the next sections.

1.2 Scope of the thesis

The current thesis was developed within the *Resilient Materials for life* project, with acronym RM4L, funded by the Engineering and Physical Sciences Research Council (EPSRC) from the United Kingdom. The main purpose of the EPSRC-funded project lies in the development of the next generation of smart-responsive-sustainable concrete materials to be incorporated into the UK civil infrastructure. The achievement of this goal requires further understanding of multiscale fracture processes in concrete.

This thesis describes research on computational tools for the numerical prediction of Micromechanics-based material degradation and macrocrack propagation within cementitious materials. Therefore, the challenge of capturing strain-softening objectively, as described previously, is the focus of this study. The chosen *remedy*, to cope with fracture across scales in concrete, brings together Finite Elements with embedded strong discontinuities (EFEM) (Freeman et al., 2020; Oliver et al., 2003; Simo et al., 1993) and Micromechanical constitutive formulations (Jefferson and Bennett, 2010, 2007; Mihai and Jefferson, 2011). Particularly, variational principles of minimum energy consumption have been used for coupling these model components seamlessly.

The work described in this thesis was conducted simultaneously with other numerical and experimental studies within the RM4L project. Therefore, the numerical formulations of this study were implemented in the in-house Fortran code Cardinal. Formulations at the element-level were first implemented in Mathcad, and tested using meshes of up to three elements. This first Mathcad implementation eased verification of the Fortran code, which was designed for use in large-scale Boundary Value Problems (BVPs). The Fortran implementation in Cardinal enabled the simulations presented in the chapter of numerical examples, which presents a series of experimental validations of the numerical model.

In addition to an existing Matlab pre and post processor, the author developed interfaces between Cardinal and the open-source visualisation toolkit Paraview (`https://www.paraview.org/`), as well as an additional pre-processor in C++ to allow re-ordering of elements in generated meshes. This allowed meshes for more complex geometries to be generated efficiently and the results displayed effectively.

1.3 Outline of the thesis

Ch. 1. Introduction.

A brief introduction highlights the challenges on modelling cementitious composites and quasi-brittle materials, using the Finite Element Method with a focus to capture deformation localisation. In addition, the scope and outline of the thesis is presented.

Ch. 2. Literature Review: Micromechanics & quasi-brittle fracture.

The literature review describes the essential concepts and techniques for modelling failure and micromechanical behaviour in quasi-brittle solids. A research gap, which is discussed in this chapter, is identified on methods to couple Micromechanics and Finite Elements with embedded strong discontinuities.

Ch. 3. Micromechanics & variational mechanics of quasi-brittle fracture.

This chapter describes mechanical concepts at micro and macro-scale which compose the new fracture model, namely, (i) a Micromechanics material model, and (ii) an EFEM approach. The EFEM model is based on a variational principle of minimum energy. The author's implementation of these micro and macro models are tested for simple BVPs, and briefly discussed for compatibility.

Ch. 4. Variationally-consistent coupling of Micromechanics & EFEM.

This chapter describes the multiscale coupling of the new micromechanical EFEM model and shows the computational strategies for the linearisation of the multiscale non-linear system. Also potential challenges in obtaining tangents for the coupled system are addressed. Also, numerical strategies for macrocrack tracking, robust implementation and other numerical details are presented.

Ch. 5. Numerical examples of multiscale quasi-brittle fracture.

At first, a theoretical calibration of the mulsticale model at the element level is presented. Secondly, the model as presented in previous chapters is calibrated and validated against experimental data. Emphasis is given to features acquired by the new multiscale EFEM to reproduce fracture in realistic BVPs, where no notch is present, under combined normal and shear mechanical actions.

Ch. 6. Conclusions & future directions.

Finally, some conclusions and recommendations for future work are given. In addition, the limitations of the numerical framework proposed in this study are discussed.

1.4 Research dissemination

This research has been used to draft a journal paper. In addition, several conference and workshop presentations have been prepared throughout this PhD as shown here.

Drafted Journal paper:

1. **Azua-Gonzalez, C.X.**, Mihai, I., Jefferson, A.D., Variational Micro-to-Macro Embedded Strong Discontinuity FEM (VM^{2}EFEM) for seamless micro-diffuse and macro-localised quasi-brittle fracture: A new efficient and robust multiscale method is proposed for fracture propagation in quasi-brittle materials, which avoids remeshing and provides a minimum energy solution. The method uses embedded strong discontinuities (EFEM) at the macroscale and a directional homogenisation scheme at the bulk domain, which allows a seamless modelling of diffuse directional microcracking and macrocracking. Traction continuity along propagating macrocrack surfaces is preserved, while macrocrack degrees of freedom are quasi-statically condensed. A smooth unloading reloading method is used at the macrocrack level to ensure global tangents in a Newton-Raphson scheme remain positive definite. Directional homogenisation rules coupled with EFEM provide a modest computational cost, while accuracy is found adequate to capture the fracture process zone. The new numerical model is validated against a series of experimental tests in concrete structures.

Conference Proceedings:

2. **Azua-Gonzalez, C.X.**, Mihai, I., Jefferson, A.D. (2021), *Coupled Micromechanics - embedded strong discontinuity model for quasi-brittle fracture: a variational appraisal.* UKACM conference 2021, Loughborough. doi.org/10.17028/rd.lboro.14587497.v1.

3. **Azua-Gonzalez, C.X.**, Mihai, I., Jefferson, A.D. (2020), *Micromechanics-driven variational method for diffuse-to-localised fracture in quasi-brittle solids.* 14th World Congress on Computational Mechanics - ECCOMAS conference. doi: 10.23967/wccm-eccomas.2020.200

4. **Azua-Gonzalez, C.X.**, Mihai, I., Jefferson, A.D. (2019), *A combined Micromechanics Strong Discontinuity approach for modelling distributed and localised fracture in cementitious materials.* UKACM conference 2019, London. Open access to Proceedings at: http://ukacm.org/wp-content/uploads/proceedings/.

Posters, talks and other presentations:

5. **Azua-Gonzalez, C.X.**, Mihai, I., Jefferson, A.D. (2021), Variational Micro/Macro-mechanics Method for fracture and damage prediction, presented in pitch competition at Winter Materials simulation Workshop H2020 DRIVEN, virtual event launched by Luxembourg University on Jan 26-29th 2021.

6. **Azua-Gonzalez, C.X.**, Mihai, I., Jefferson, A.D. (2019), A combined Micromechanics Strong-Discontinuity approach for modelling failure of cementitious materials, presented at Materials Modelling Workshop, Cardiff University on June 11th 2019.

7. **Azua-Gonzalez, C.X.**, Mihai, I., Jefferson, A.D. (2018), *Numerical modelling of diffuse and localised cracking in cementitious composite materials* , 2nd SARCOS COST - RILEM Doctoral course, Skopje - Ohrid, Macedonia 2 - 7 Sept 2018.

1.5 Starting point of research and original contribution

Two-scale mechanical components, namely (i) the micromechanical formulations at the constitutive level, and (ii) the EFEM formulation at the element level, which are presented consistently in Chapter 3 from their original form in the literature (Freeman et al., 2020; Jefferson and Bennett, 2010; Jefferson and Freeman, 2022; Jefferson and Bennett, 2007), were suggested as a starting point of research by the supervisory team to the author. The author coded these separately to study their compatibility, at first in Mathcad, and then into the in-house code Cardinal using Fortran programming. Therefore, the implementations that were used to present simulation results from Chapter 3 onwards correspond to those of the author.

Before the start of this research, such numerical components mentioned in the previous paragraph had never been coupled together. The author proposed a form of seamless coupling of the two-scale components in Chapters 4 to 5, which enables a multiscale fracture response of cementitious composites that preserves a minimum energy solution at the element level.

Other relevant attempts in the literature (Zhao et al., 2018) do not introduce element-based macrocrack dofs, and therefore use EFEM concepts that degenerate into a simple smeared micromechanics model, as opposed to the newly proposed rigorous variational treatment and simultaneous coupling of quasi-statically condensed macrocrack dofs and micromechanically-driven bulk behaviour (Azua-Gonzalez et al., 2019, 2020, 2021).

Chapter 2

Literature review: Micromechanics & quasi-brittle fracture

"A hypothetical theory is necessary, as a preliminary step, to reduce the expression of the phenomena to simplicity and order before it is possible to make any progress in framing an abstractive theory."
William Rankine 1820 – 72
Scottish engineer and pioneer of Thermodynamics theory and Mechanics

2.1 Focus of literature study

This chapter describes an overview of Mechanical theories in terms of material modelling and fracture propagation in quasi-brittle solids, at first separately, and then as a multiscale coupling problem. The focus of the study is threefold:

- Section 2.2: Micromechanical constitutive models and scale-bridging material modelling frameworks are described. Attention is provided to approaches which have been or could be coupled with numerical techniques for fracture propagation in quasi-brittle solids, with emphasis on cementitious composites,
- Section 2.3: A brief description is presented for numerical techniques used for solving the mechanical response of solids with evolving discontinuities such as cracks. Focus is given to fracture modelling techniques with strong discontinuities (Freeman et al., 2020; Jefferson and Freeman, 2022; Oliver et al., 2006),
- Section 2.4: Advanced micro-macro fracture models from the literature are described with focus on Finite Elements with strong discontinuities, such as those based on the addition of new dofs (Belytschko et al., 1988; Xu and Needleman, 1994), and on element-based condensation of fracture dofs such as EFEM (Oliver et al., 2006) among others.

A research gap has been identified on multiscale methods that couple Continuum Micromechanics and an EFEM approach, and this is discussed in concluding remarks in Section 2.5.

2.2 Micromechanical constitutive homogenisation

Macroscopic material modelling approaches often result incapable of reproducing key micro-mechanisms in composites (Jefferson and Bennett, 2007). Examples of such popular theories are the well-known Flow theory of Plasticity (Koiter, 1953; Prager, 1949) and Damage Mechanics (Fonseka and Krajcinovic, 1981; Krajcinovic and Fonseka, 1981). These theories are primarily based on phenomenological assumptions, and these are not sufficient for modelling appropriately the behaviour of cementitious composites (Jefferson and Bennett, 2010, 2007).

Micromechanical models are multiscale and mechanistic in nature, and use fewer phenomenological assumptions than comparable macro-models. These models aim to estimate the macroscopic response of a fundamental material volume or RVE using length-scale bridging strategies, a.k.a. *homogenisation* procedures.

The following paragraphs present a brief description of various groups of micromechanical models which are used for modelling cementitious composites.

2.2.1 Constitutive frameworks based on mixture theory

The theory of mixtures is a micromechanical approach that is used to devise the homogenised response of a continuum comprised of various phases. A major period of growth in the field lies in the decades between 1950s to 1990s, with prominent contributions such as Eshelby (1957, 1959); Hashin and Shtrikman (1961); Mori and Tanaka (1973); Nemat-Nasser et al. (1996), among others. In this regard, Hill established the principles of Continuum Micromechanics by obtaining the homogenised response of a continuum composite.

The micro to macro scale transition for a mixture of continuum-based micro-constituents is typically governed by the Hill-Mandel condition (see e.g. Geers et al. (2017)). This postulate establishes that the energetics from each of the micro-constituents must be transferred to the corresponding homogenised material point in the macroscale:

$$\frac{1}{||\Omega||} \cdot \int_{\Omega} \boldsymbol{\sigma}^{\mathrm{m}} : \delta \boldsymbol{\varepsilon}^{\mathrm{m}} d\Omega = \bar{\boldsymbol{\sigma}} : \delta \bar{\boldsymbol{\varepsilon}} \tag{2.1}$$

where $||\Omega||$ stands for the elementary volume being homogenised, $\bar{\boldsymbol{\sigma}}$ and $\bar{\boldsymbol{\varepsilon}}$ are the stress and strain at the macroscale, and $\boldsymbol{\sigma}^{\mathrm{m}}$ and $\boldsymbol{\varepsilon}^{\mathrm{m}}$ stand for micro stress and strain.

Various studies have been presented in the literature regarding the use of the theory of mixtures with application to concrete modelling, by coupling homogenisation principles and other material modelling theories which are illustrated further in the following sections.

2.2.1.1 Micro-plane constitutive models for quasi-brittle solids

The microplane models (Bažant, 1984; Bažant and Prat, 1988a,b; Ožbolt and Bažant, 1992) may be considered as the models that popularised the use of micromechanical principles for modelling the effective response of concrete and more generally cohesive-frictional geo-materials. Bažant (1984) recalled directional mechanics principles acknowledging its previous use in crystallographic materials (Taylor, 1938). Microplane models assume the change in macroscopic strain-energy per unit volume of a material point is the average of the change of strain-energy per unit volume occurring in microscopic zones where microcracks are distinctively aligned with preferential planes, the so-called microplanes defined by the (unit) normal vector $\mathbf{r}$ ($\|\mathbf{r}\| = 1$). The macroscopic strain-energy density is then obtained by numerical integration over the surface of a unit hemisphere $\sum_{1/2}$, i.e. in a discrete number of microplane directions $\mathbf{r}_i$ as illustrated in Figure 2.1 and expressed in Equation 2.2.

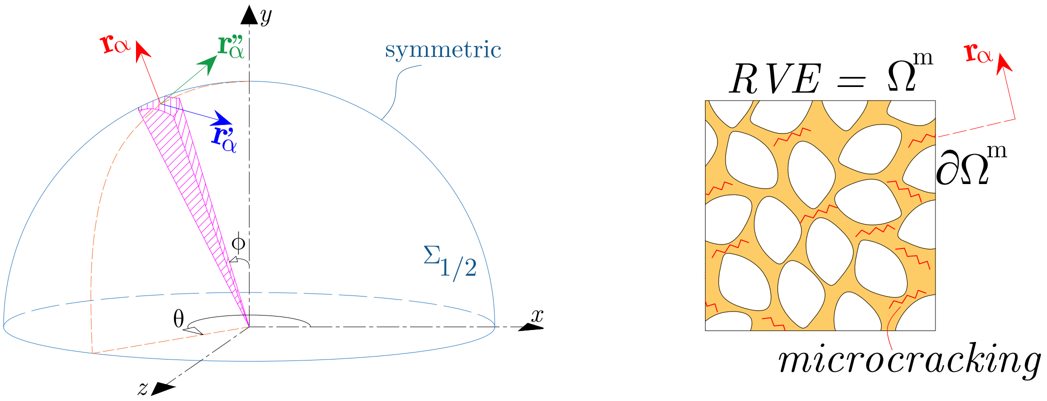

(a) Integration on a unit hemisphere (b) RVE: Cementitious composite

Figure 2.1: Micromechanical principles used for homogenisation in microplane models (Bažant, 1984)

$$\boldsymbol{\sigma} : \delta\boldsymbol{\varepsilon} \approx \frac{1}{4\pi}\left(2\iint_{\Sigma_{1/2}}\left(\boldsymbol{s} : \delta\boldsymbol{e}\right)\underbrace{sin(\phi)\delta\phi\delta\theta}_{\delta S}\right) \tag{2.2}$$

where the micro-planes, each one perpendicular to the corresponding unit normal **r**, are expected to behave through independent stress-strain laws, though assumptions are common, that the microplane stress $\boldsymbol{s}$ or strains $\boldsymbol{e}$ are used in the form of the resolved components of their macroscopic fields ($\boldsymbol{\sigma}$,$\boldsymbol{\varepsilon}$) for computational purposes.

Microplane models, e.g models by Bažant and Prat (1988b); Di Luzio and Cusatis (2013); Lale and Cusatis (2021), have been shown to capture the response of concrete materials. Some examples of the performance of calibrated micro-planes models are presented in Figure 2.2.

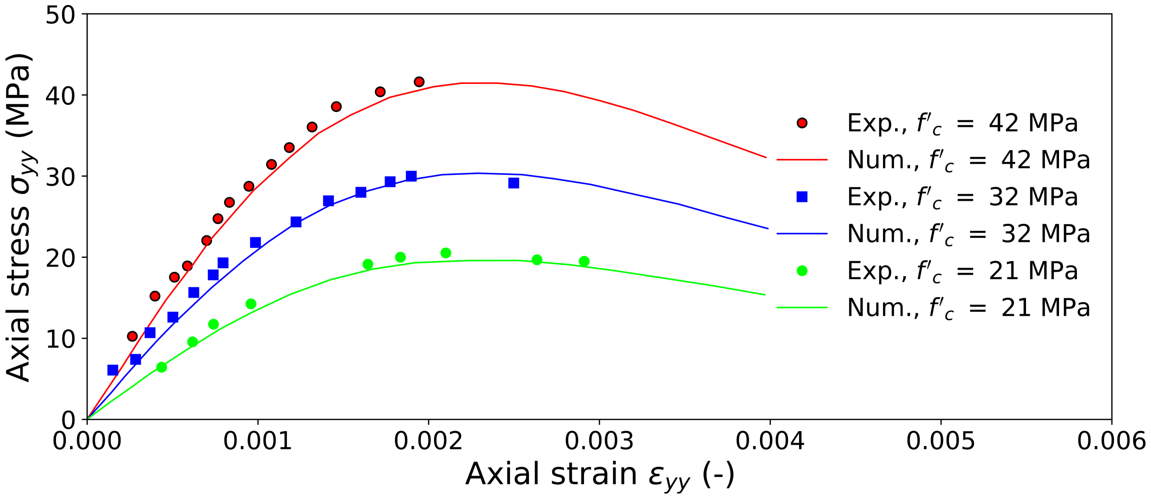

Figure 2.2: Validation of micro-plane models as published in Bažant and Prat (1988b), using monotonic uniaxial compression tests by Hognestad et al. (1955).

The latest version of micro-plane models is the so-called M7 (Bazant et al., 2022), which has been recently compared with other modern models that use standard Finite Elements through a crack band approach, as well as against the predictions of advanced numerical discretisation techniques such as phase-field (PF)(Miehe et al., 2010c) and peridynamic models (PD)(Hashim et al., 2020; Silling and Askari, 2005). The M7 model performed very well against some poor behaviour of PF and PD model responses. A point has been made in Bazant et al. (2022), that the predictive capability of a numerical framework can be limited by the accuracy of the coupled constitutive law no matter how advanced and robust the underlying numerical technique for fracture propagation is.

2.2.1.2 Mixture theory and plasticity-damage for quasi-brittle solids

In the literature, the mixture theory has been coupled to plasticity-damage constitutive modelling strategies. This class of micromechanical models use various degradation techniques to represent the response of microcracking and its interaction with that of the aggregate phase in a cementitious composite.

Ortiz (1985) proposed to use the theory of mixture to model micro and macro interactions in concrete and more generally quasi-brittle materials during fracture and subsequent failure. In particular, the proposed constitutive framework was able to capture some inelastic features of the behaviour of concrete materials. This framework employed averaging principles, with the aim of capturing the overall mechanical response of the mixture of a cementitious matrix enclosing an aggregate phase. Some of the degradation mechanisms included in the model are illustrated in Figure 2.3.

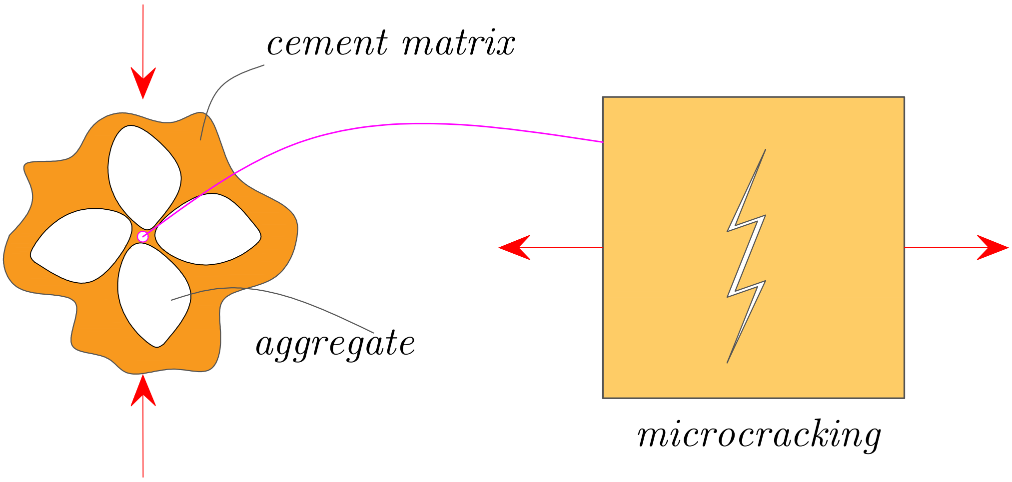

Figure 2.3: Solid phases in concrete leading to a splitting mechanism under compression, with matrix-based microcracking development parallel to the load direction over the mixture of cement matrix and aggregate, reproducible by the theory of mixtures Ortiz (1985).

Ortiz (1985) proposed to consider the role of microcracks as a mechanism of material damage in the matrix, by adding a mechanics-based measure of additional material flexibility, and by considering the duality mortar-aggregate in concrete using the theory of mixtures:

$$\left.\begin{array}{ll}\text{Mixture-theory:} & \dot{\boldsymbol{\sigma}} = \frac{\Omega_a}{\Omega}\cdot\dot{\boldsymbol{\sigma}}_a + \frac{\Omega_m}{\Omega}\cdot\dot{\boldsymbol{\sigma}}_m \\ \text{Homogeneous strain transfer:} & \dot{\boldsymbol{\varepsilon}} = \dot{\boldsymbol{\varepsilon}}_a = \dot{\boldsymbol{\varepsilon}}_m \\ \text{Homogenised rate constitutive equation:} & \dot{\boldsymbol{\sigma}} = \left[\frac{\Omega_a}{\Omega}\cdot\boldsymbol{D}_a^{(\mathrm{T})} + \frac{\Omega_m}{\Omega}\cdot\boldsymbol{D}_m^{(\mathrm{T})}\right] : \dot{\boldsymbol{\varepsilon}}\end{array}\right\} \qquad (2.3)$$

where $\mathbf{\Omega} \equiv \mathbf{\Omega}_a \cup \mathbf{\Omega}_m$ stands for a Representative Volume Element (RVE) of aggregate $(\cdot)_a$ and cement-based matrix $(\cdot)_m$ mixture, $\boldsymbol{\sigma}$ is the Cauchy stress, $\boldsymbol{\varepsilon}$ is the overall strain of the mixture (which is considered as uniform over the mixture).

The constitutive relation upon homogenisation (Ortiz, 1985; Tenchev and Purnell, 2005) has been found to reproduce the behaviour of concrete in compression and to estimate its decreased strength in tension under monotonic conditions as illustrated in Figure 2.4.

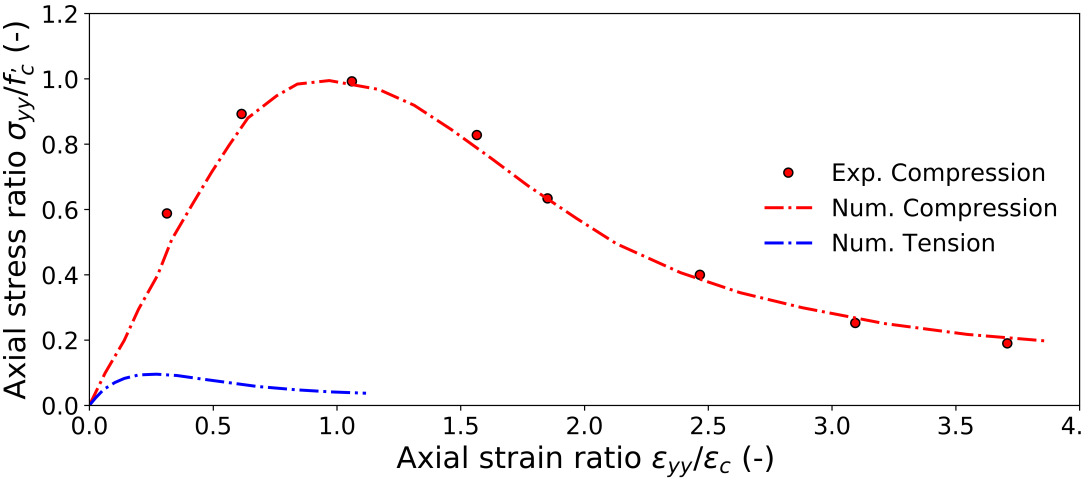

Figure 2.4: Prediction of concrete behaviour employing mixture theory as published by Ortiz (1985). The model is calibrated for monotonic uniaxial tests by Bresler and Bertero (1979).

2.2.1.3 Mixture theory and Micromechanics of defects in solids

The use of micromechanical analytical solutions for micro-defects embedded within a classical continuum constitutive approach, were first presented by Andrieux et al. (1986), and in a more general sense by Pensée et al. (2002). The latter, presented a three-dimensional framework of the preceding method by Andrieux et al. (1986) for modelling a cracked solid with sets of aligned dilute penny-shaped microcracks. In this framework, the crack density parameter (Budiansky and O'Connell, 1976) controls local damage in each sets of families of microcracks, and the macroscopic free energy of the material borrows the homogenisation concept of the microplane models (Bažant, 1984). In addition, Micromechanics-informed continuum damage theories have been developed at Cardiff University (Jefferson and Bennett, 2010, 2007), similar to those of Andrieux et al. (1986); Pensée et al. (2002), though with a focus to replicate damage-induced inelastic response in concrete materials subjected to both tensile and combined shear-compressive loading paths. A simple sketch of micromechanical constituents are elucidated in Figure 2.5.

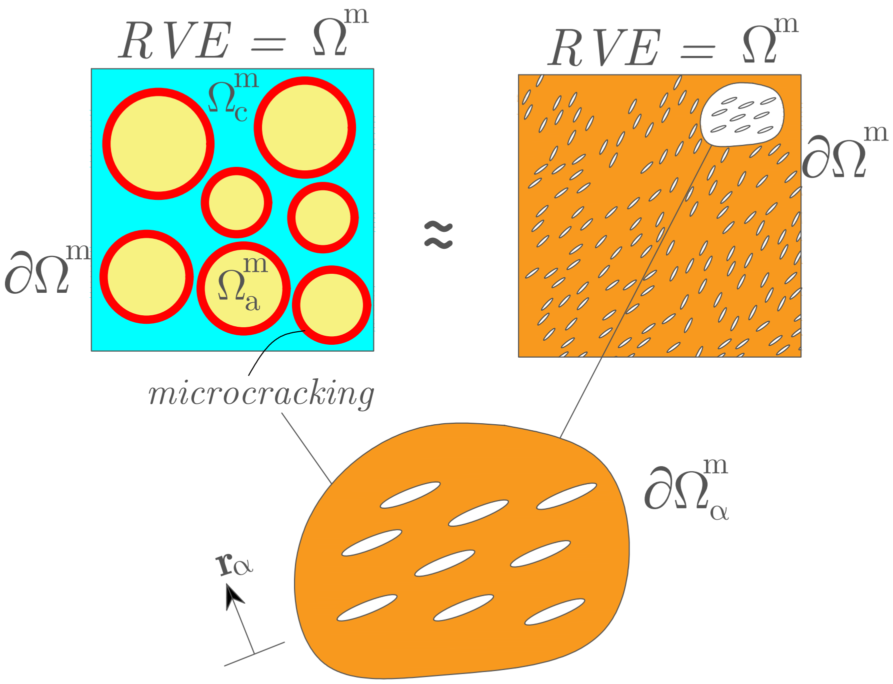

Figure 2.5: Micro-constituents in an RVE within the framework of Micromechanical consitutive models aided by micro-defect theory: two-phase composite model by Jefferson and Bennett (2010, 2007)(left), single-phase composite model Andrieux et al. (1986); Pensée et al. (2002)(right).

The problem of homogenisation of a cracking solid with a single set of meso-cracks (or microcracks depending on what is the length-scale of reference), has been shown to be solvable by splitting the overall (resolved) strain $\boldsymbol{\varepsilon}$ into an elastic part and a contribution from the micro-defects (Nemat-Nasser et al., 1996; Pensée et al., 2002). Without the loss of generality and for the sake of illustration, it is assumed in the following expression that the microcracking set is aligned with one of the Cartesian axes (Pensée et al., 2002):

$$\left.\begin{array}{ll} \text{Elastic:} & \boldsymbol{\varepsilon}^{e} = \boldsymbol{D}_{e}^{-1} : \boldsymbol{\sigma} \\ \text{Micromechanical:} & \boldsymbol{\varepsilon}^{m_1} = \beta_{m}^{ck} \cdot \left(\mathbf{n}^{m_1} \otimes \mathbf{n}^{m_1}\right) + \left(\gamma_{m}^{ck} \otimes \mathbf{n}^{m_1}\right)^{s} \end{array}\right\} \tag{2.4}$$

where $(\cdot)^{e}$ stands for the elastic part, $(\cdot)^{m_1}$ is the inelastic part induced due to the presence of a penny-shaped microcrack set m_1 with microcrack-plane normal $\mathbf{n}^{m_1}$, $\boldsymbol{D}_{e}$ is the isotropic elasticity tensor of the uncracked solid, β_{m}^{ck} is a scalar variable representing the microcrack normal opening, and γ_m^{ck} stands for a sliding component which read as follow in Equation 2.5.

$$\left.\begin{array}{ll}\text{Normal opening component:} & \beta_m^{ck} = \mathcal{N}_{m_1} \int_{\partial\Gamma_m^+} [u_n]^{\partial\Gamma_m} dS \\ \text{Sliding component:} & \gamma_m^{ck} = \mathcal{N}_{m_1} \int_{\partial\Gamma_m^+} \left([\mathbf{u}]^{\partial\Gamma_m} - [u_n]^{\partial\Gamma_m} \cdot \mathbf{n}^{m_1}\right) dS\end{array}\right\} \quad (2.5)$$

where the operation $\left(\mathbf{n}^{m_1} \otimes \mathbf{n}^{m_1}\right)^s = \mathbf{n}^{m_1} \otimes \mathbf{n}^{m_1}$ has been used as an identity in Equation 2.4 for simplification, the operator $(\cdot)^s$ stands for the computation of the symmetric part and $(\cdot) \otimes (\cdot)$ denotes the outer product, $[\mathbf{u}]^{\partial\Gamma_m}$ is the microcrack opening displacement, $\mathcal{N}_{m_1} = \mathscr{F}_{m_1}/a^3$ represents the number of microcracks per unit volume, and equals the ratio of the microcrack density parameter $\mathscr{F}_{m_1}$ to the cube of the microcrack radius a. The model by Pensée et al. (2002) has been successfully validated for the response of rocks as illustrated in Figure 2.6.

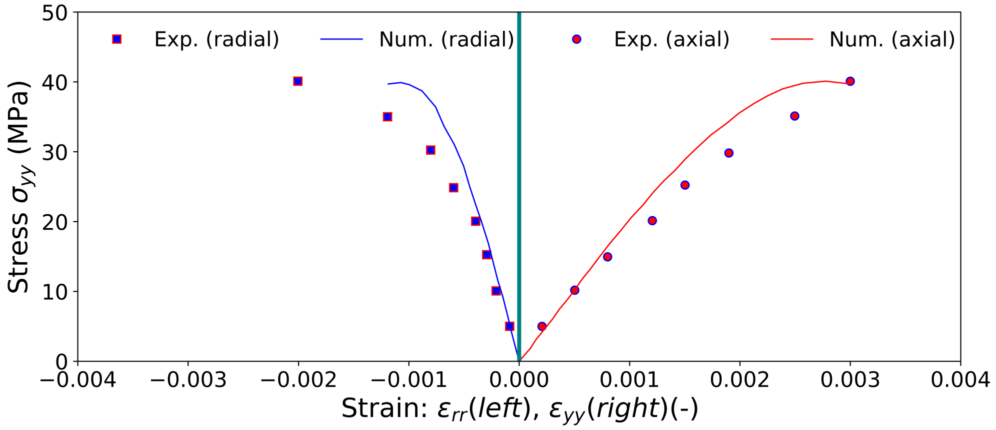

Figure 2.6: Validation of micromechanics-aided constitutive model by Andrieux et al. (1986); Pensée et al. (2002) for Sandstone from Vosges (France), experimental data by Charlez (1993).

Regarding Micromechanical models developed at Cardiff, some of these have been upgraded to consider rough contact in microcracking sets. This type of mechanical component has been (and is still) ignored in almost all other Micromechanical models available in the literature. These enhanced micromechanical models are good in capturing the biaxial failure envelope of cementitious solids, and this is illustrated in Figure 2.7 (Jefferson and Bennett, 2010). In this figure the biaxial response of concrete is validated against experimental data by Kupfer et al. (1969). Without venturing into computational aspects, a derivation of a simpler version of this Micromechanical model is presented in the next chapter in Section 3.2.

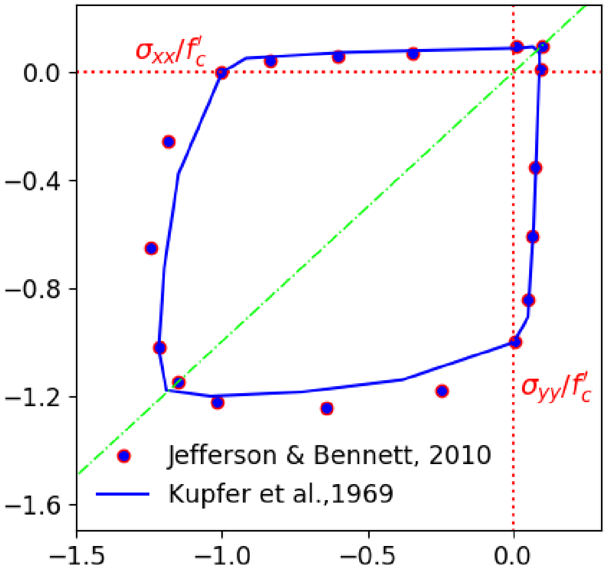

Figure 2.7: Validation of concrete biaxial response predicted by Micromechanics model (Jefferson and Bennett, 2010) against experimental data (Kupfer et al., 1969).

This range of micromechanical models has proved to predict successfully the multiaxial strain-softening response in cementitious materials, as a consequence of dilute microcracking (Van Mier, 1984), without the necessity to run through time-consuming *computational material homogenisation* techniques such as FE^2 methods Desrues et al. (2019); Feyel and Chaboche (2000). Although direct representation of microdefects and microconstituents is avoided in Micromechanical constitutive models for computational efficiency, these micromechanical models (Jefferson and Bennett, 2010, 2007) can capture phenomena occurring at smaller length scales. The addition of mechanisms such as post-peak volumetric dilation in microcracking sets (Jefferson and Bennett, 2007) or extension into two-phase homogenisation schemes (Jefferson and Bennett, 2010), improves the accuracy of the model although without much overhead cost since this model avoids multi-grid homogenisation. This type of response is achieved with a unique parameter set, and with a reduced number of phenomenological assumptions in contrast to traditional macroscopic models.

N.B.: This PhD research has made use of this type of micromechanical formulations in Section 2.2.1.3 for modelling cementitious materials, e.g. (Jefferson and Bennett, 2010, 2007; Mihai and Jefferson, 2011), due to their computational efficiency and good *mechanistic* reproduction of phenomena at lower length-scales.

2.2.2 Discrete modelling frameworks for quasi-brittle media

Discrete modelling approaches aim to use connected elements and contact-particle mechanics frameworks at the RVE level, to simulate the response of quasi-brittle materials such as concrete, rocks and strain-softening soils. In order to categorise some of these numerical schemes through similarities, the following branches can be mentioned:

- **Lattice methods employing inter-connected spring-beam networks:** These models aim to reduce the complexity of a continuum by representing it with rigid-body-interconnected lattices, e.g. generating equivalent mechanical systems comprised of beams. Common assumption is to remove failed elements to reproduce fracture (Bolander and Saito, 1998; Bolander and Sukumar, 2005; Garboczi and Day, 1995; Schlangen and Garboczi, 1996, 1997). Key constituents of such models are illustrated with an example of a typical RVE domain in Figure 2.8.
- **Contact/Particle mechanics-based Lattice methods:** These models can enclose i) Distinct Element Methods (DEM), originally developed for geomaterials (such as rocks and soils) (Borja and Wren, 1995; Cundall, 1988; Cundall and Strack, 1979; Hentz et al., 2004; Wren and Borja, 1997), ii) Lattice - Discrete Particle FEM methods (LDPFEM) for modelling cement-based materials, based on the use of spherical/ellipsoidal/polyhedral particles that can interact through contact as a lattice framework (e.g. Cusatis et al. (2011)). Some authors have proposed combined numerical schemes within standard multi-scale Finite Element frameworks (Nitka et al., 2011; Rousseau et al., 2008), or regularized multiscale frameworks (Desrues et al., 2019; Miehe et al., 2010a).
- **Bond-based and State-based Peridynamics:** Peridynamics was proposed as an alternative to classical Continuum Mechanics (Silling and Askari, 2005). This methodology avoids the use of continuous spatial gradients opposed to standard FEM analysis, by postulating that a particle interacts with other particles even beyond the closest neighbourhood, which is defined as the 'horizon'. This eases the modelling of evolving discontinuities without additional numerical treatment. Bond-based Peridynamics, which was the original form of Peridynamics, presented constraints on the way constitutive formulations were linked to the underlying numerical framework, and therefore, other variants were created, i.e. State-based Peridynamics, which can be ordinary or non-ordinary (Hashim et al., 2020).

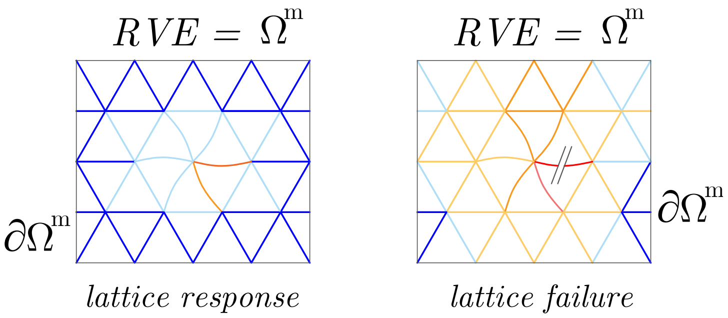

Figure 2.8: Illustration of a lattice-type RVE consisting of connected spring-beams: elastic response to external action (left), local lattice failure (right).

Although the simplicity of the computational schemes in lattice methods would seem attractive to model cement-based materials across scales in a coupled Lattice-FEM scheme, issues like the need to generate *adequate* random interconnected spring-beam networks, to render an unbiased response to fracture with respect to mesh distribution (Bolander and Sukumar, 2005; Schlangen and Garboczi, 1996), would still need to be solved at the lower lenght-scale. In addition, the nested system of equations for such coupled system, i.e. a Lattice FEM x FEM nested system, would resemble an FE^2 method, which could then demand a very high computational power (Mosby and Matouš, 2016).

2.2.3 Computational material homogenisation of heterogeneous media

Computational homogenisation schemes are used to model heterogeneous media employing nested computations in combination with volume averaging schemes across scales (Feyel and Chaboche, 2000; Kouznetsova et al., 2002; Terada et al., 2000). A sketch of the typical multi-grid nature of micro-to-macro nested BVPs to enable the analysis of composites, as employed in computational material homogenisation schemes, is illustrated within a particular example of a composite-based solid beam in Figure 2.9.

Although the initial developments on computational homogenisation schemes were commonly acknowledged to be unable to predict deformation localisation across scales (Geers et al., 2017), some recent literature shows efforts to extend the method to fracture problems, see e.g. Coenen et al. (2012); Karamnejad et al. (2017); Karamnejad and Sluys (2014); Nguyen et al. (2011); Xu et al. (2021).

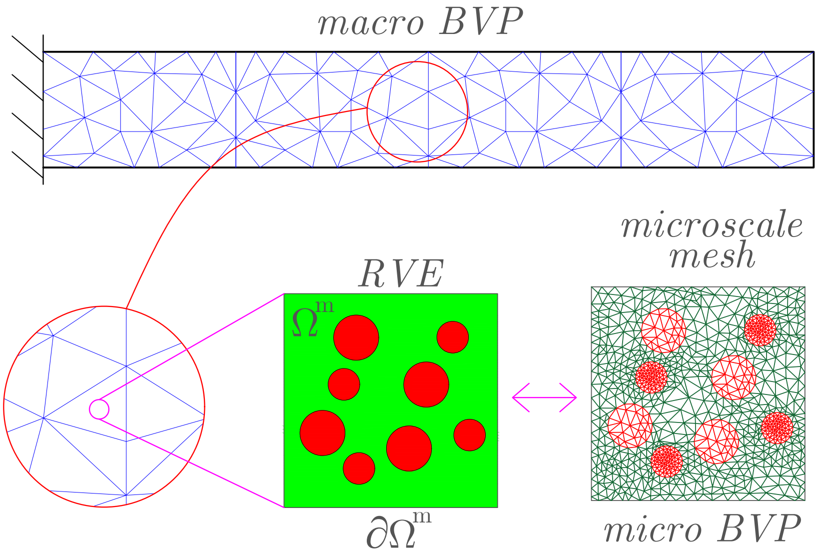

Figure 2.9: Boundary Value Problem (BVP) considering a solid beam composed of heterogeneous material. The sketch elucidates the flexibility of multi-grid computational multiscale homogenisation procedures towards the macroscale analysis of a range of composites.

2.3 Numerical techniques for fracture propagation

In the past, macroscopic-based constitutive models for quasi-brittle materials implemented in a Finite Element framework led to numerical issues such as excessive mesh dependency of the structural response in BVPs (Bažant and Oh, 1983), and numerical instabilities related to the negative tangent as a result of strain softening (Bažant, 1976; Crisfield, 1982). Many authors have proposed strategies to alleviate these numerical issues in FEM-based implementations. These strategies have increased in number after the leading contributions of Bažant and Oh (1983); Cedolin and Bažant (1980), who developed the so-called crack band approach, and non-local theories (Bažant and Pijaudier-Cabot, 1988; Pijaudier-Cabot and Bažant, 1987). Some of these other theories are now considered below.

i **Embedded localisation band FEM** (Belytschko et al., 1988; Haghighat and Pietruszczak, 2016; Pietruszczak and Mróz, 1981), **and embedded weak/strong discontinuity approaches** (Armero and Linder, 2009; Freeman et al., 2020; Jirásek, 2000; Oliver et al., 2003; Raina and Linder, 2015; Simo et al., 1993)**:** Models that use the notion of a deformation band of finite thickness to model displacement jumps or cracking-induced strains;

ii **Gradient-enhanced plasticity and damage models** (De Borst and Mühlhaus, 1992; De Borst and Verhoosel, 2016; Peerlings et al., 1996; Sluys et al., 1993)**:** Models that use the notion of diffuse Continuum damage and often introduce an additional damage-related variable and associated governing equation;

iii **Micropolar continuum theory** (De Borst, 1991; Mühlhaus and Vardoulakis, 1987; Neuner et al., 2020)**:** These models use the notion of couple stresses due to additional rotational degrees of freedom to represent a generalised continua, which extends the original work of Cosserat and Cosserat (1909) by introducing a length scale parameter;

iv **Meshless methods applied to static and dynamic fracture** (Belytschko et al., 1995, 1994; Hashim et al., 2020; Silling and Askari, 2005)**:** Methods such as the Element-free Galerkin Finite Elements (EFG-FE) make use of general interpolations such as least square based methods, which do not use the traditional notion of element-wise discretisation;

v **The Extended Finite Element Method (XFEM)** (Agathos et al., 2016; Belytschko and Black, 1999; Bordas et al., 2007; Moës et al., 1999)**:** These methods introduce displacement discontinuities and nodal enrichments to enhance the strain field in (i) elements cut by the discontinuities, as well as in (ii) elements containing the crack front;

vi **Phase field approaches for smeared crack propagation** (Giambanco and La Malfa Ribolla, 2019; Miehe et al., 2010c; Nguyen et al., 2020; Verhoosel and de Borst, 2013)**:** These models use an additional set of governing equations to represent the diffuse nature of crack propagation by using an associated phase-field variable. Although there are similarities with gradient-based models, they require very fine meshes;

vii **Configurational force based fracture models** (Bird et al., 2022; Gurtin and Podio-Guidugli, 1996; Kaczmarczyk et al., 2017; Miehe et al., 2007)**:** Models that use configurational forces to drive crack propagation that is associated with a Griffith's criterion to enforce maximum local dissipation at the evolving crack tip.

2.3.1 Brief comparison of fracture models

Some relevant computational aspects of various categories of fracture methods are considered in the Table 2.1. Here the type of 'efficiency' reported partly disregards important aspects of error analysis such as the order of convergence to a true solution due to higher order interpolation (Oden and Reddy, 2010), and only focuses on the iterative convergence rate of the algorithm. It seems that most publications concentrate in proving a method works for a few types of numerical examples, while efficiency and error analysis is often left to stages where the method is very developed and has become popular. In this regard, the degree of interpolations is not included in Table 2.1.

Table 2.1: Overview of fracture modelling methods: computational aspects

Method	extra dofs / int. variables	efficiency	mesh-based	length parameter
Embedded discontinuity FEM (Linder and Armero, 2007; Oliver et al., 2003)	✓ element-wise crack dofs enrichment (Oliver et al., 2006)	✓ order $\in (1.0, 2.0)$	✓ element-level differential operators (Simo et al., 1993)	✓ (constant) fracture band width (Armero and Linder, 2009)
Non-local (Pijaudier-Cabot and Bažant, 1987), gradient-based continuum	✓ scalar variable 2nd gradient (De Borst and Mühlhaus, 1992)	✓ order ≈ 2.0	✓ element imbrication can occur (Bažant et al., 1984)	✓ (constant) scalar, which controls localisation spatially
Micro-polar continua (Mühlhaus and Vardoulakis, 1987)	✓ rotation dofs are added De Borst (1991)	✓ order ≈ 2.0	✓ element nodes can rotate, aside to translation	✓ Shear band thickness De Borst (1991)
Mesh-free FEM for fracture (Belytschko et al., 1994)	X though large number of points often required	✓ order ≈ 2.0	X domains of influence depend on weighting	✓ space-grading constants (Belytschko et al., 1995)
Node-enriched FEM (XFEM) (Belytschko and Black, 1999)	✓ near-crack enriched dofs (Belytschko and Black, 1999)	✓ order $\in (1.0, 2.0)$	✓ minimal remeshing (Moës et al., 1999)	✓ crack-tip characteristic length (Moës et al., 1999)
Phase field methods for fracture (Miehe et al., 2010c)	✓ phase field (Verhoosel and de Borst, 2013)	✓ order ≈ 2.0	✓ no element imbrication	✓ smeared crack length-scale (Miehe et al., 2010c)

The methods present in Table 2.1 have different merits, disadvantages, complexities and areas of applicability. These are considered below:

- **On additional dofs and internal variables in fracture methods:**
  Only the Mesh-free Galerkin type of methods (EFG-FEM) may be considered naturally able to represent cracks without the inclusion of enrichment degrees of freedom. Due to the meshless nature of the method, growing cracks are modelled simply by extending the existing free surfaces as an artifice to represent the loss of interaction between points at either side of a propagating crack (Belytschko et al., 1995, 1994). On the other hand, it has been reported that a large number of integration points (nodal locations which float without depicting connectivity of elements) is needed to represent cracks accurately (Belytschko et al., 1994). An alternative to this is adaptive Discontinuous Galerkin discretisations (Bird et al., 2022), which are able to adapt the mesh at the inter-element boundaries to enable a new crack path. Other methods require additional degrees of freedom to cope with discontinuities, either in i) a (semi) direct form (Linder and Armero, 2007; Oliver et al., 2003; Simo et al., 1993) by adding dofs to the standard displacement field (e.g. nodal enrichment to account for displacement jumps and crack-tip enrichment with asymptotic fields (Belytschko and Black, 1999), or by adding Cosserrat's rotational degrees of freedom (Mühlhaus and Vardoulakis, 1987)), or in ii) an indirect form by accounting for the spatial localisation of deformation through weighting functions (Pijaudier-Cabot and Bažant, 1987) or a diffusive type representation of macroscopic damage employing the second gradient of a damage/plasticity/crack-phase scalar variable (De Borst, 1991; Miehe et al., 2010c; Sluys et al., 1993).

- **On algorithmic efficiency of fracture methods:**
  Hereby, it is acknowledged that overall computational costs shall be also taken into account when analysing computational efficiency; nonetheless, it is recognised from the literature of development of fracture methods, that computational cost is rarely reported. Some exceptions can occur, e.g. for problems with high computational demand such as $\boldsymbol{FE}^2$-based multiscale fracture methods (Desrues et al., 2019). On the other side, equilibrium convergence rates are regularly reported to cope with computational efficiency. Although equilibrium convergence rates tend to be reported, common practice is that the authors do not discuss to the detail required the convergence of failure patterns with

respect to refinement of the mesh, or at least one or the other measure of convergence is not considered. Exceptions can be found when there are enough particular assumptions so that error estimates can be computed, e.g. fracture propagation analyses through an elastic body (Bird et al., 2022, 2019). It can be highlighted that most fracture methods present a global algorithmic efficiency (e.g. convergence rate of a global Newton's iteration over an increment) better than linear convergence rate, even if methods are derived using consistently linearised tangents (Simo and Taylor, 1985) due to the complex changes of state caused by multiple cracks propagating.

- **On the Mesh and/or Meshless nature of fracture methods:**
  Although meshing can be a modest overhead time-cost in BVPs of simple geometries, this is not true for structures with complex geometries. Hughes et al. (2005) highlighted the inefficiency of using a CAD model for the geometry that is different from the geometric model that is used for the analysis. He and coworkers proposed using the same NURBS-based functions for both the geometry and the analysis, and the idea is being investigated worldwide. Although the idea is of general use in Finite Elements, this idea has also started to resonate among developers of methods for fracture propagation (De Borst, 2018). In this regard, a methodology with least computational overhead due to mesh refinement sounds appealing. Such methodologies that include the least effort for crack propagation problems include X-FEM (Agathos et al., 2016; Belytschko and Black, 1999; Moës et al., 1999) and EFEM (Jefferson and Freeman, 2022; Oliver et al., 2006; Simo et al., 1993) among variants of these approaches.

- **On the use of an internal length in fracture methods:**
  Methods for fracture propagation often introduce a numerical or physical length scale, in order to preserve objectivity with respect to mesh refinement upon deformation localisation (Belytschko and Black, 1999; Belytschko et al., 1988, 1994; De Borst, 1991; Linder and Armero, 2007; Miehe et al., 2010c; Moës et al., 1999; Mühlhaus and Vardoulakis, 1987; Oliver et al., 2003; Pijaudier-Cabot and Bažant, 1987; Simo et al., 1993). However, the links of this internal length to a physical mechanism is rather vague and most numerical techniques tend to use it a numerical regularisation artifice. In a multiscale setting, it is yet an answer to be found whether multiple internal length parameters are needed for each of the length-scales being coupled (Coenen et al., 2012; Geers et al., 2017).

2.3.2 Finite Elements and embedded strong discontinuities

Various forms of deriving Finite Elements with embedded strong discontinuities exist in the literature, and each one with different assumptions on the transfer of rigid body kinematics due to fracture at the element-level (Jirásek, 2000). A common assumption is the split of the deformation field to allow a jump within the element domain as illustrated in Figure 2.10 for various types of dof-based enrichment.

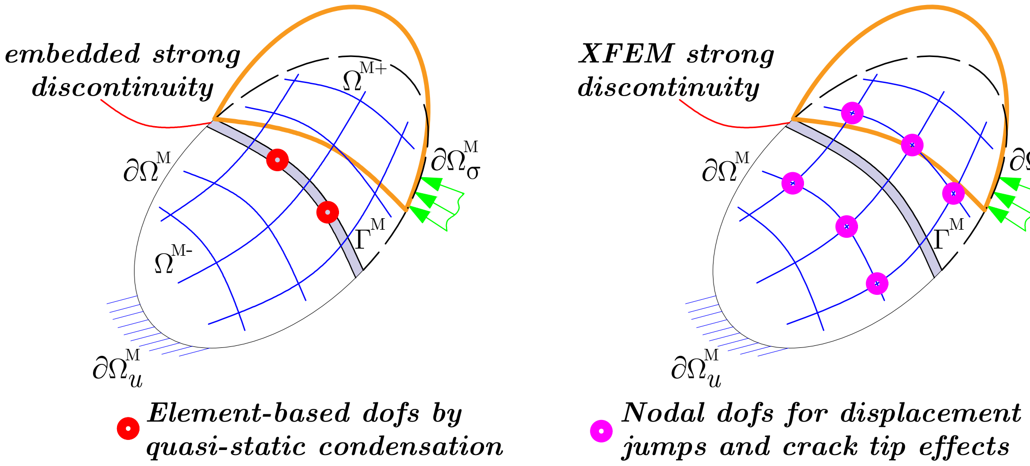

Figure 2.10: Enrichment of a continuum for fracture modelling with strong discontinuities by Oliver et al. (2006): EFEM (left), XFEM (right).

In this regard, the split of the deformation and its associated strain field reads as follows:

$$\left.\begin{array}{ll}\text{Decomposition of deformation field:} & \mathbf{u} = \mathbf{u}_c + M_{\Omega}(\mathbf{x}) \otimes [|\mathbf{u}|] \\ \text{Fracture-enriched strain field:} & \boldsymbol{\varepsilon} = \nabla^s\left(\mathbf{u}_c + M_{\Omega}(\mathbf{x}) \otimes [|\mathbf{u}|]\right)\end{array}\right\} \tag{2.6}$$

where the scalar-valued $M_{\Omega}(\mathbf{x})$ function takes various forms, e.g. of the form of a Heaviside function summed with other trial smooth functions (Oliver, 1995) or simply a Heavisde function (Oliver et al., 2003), the sum of a Heaviside function and a linear combination of shape functions (Regueiro and Borja, 1999). There is debate on whether there is a better type of definition of the scalar-valued function $M_{\Omega}(\mathbf{x})$, although it is clearly manipulated towards the type of final solution of the BVP, which is solved either as a condensation scheme by eliminating cracking dofs internally at the element-level, or by solving coupled equations to obtain additional dofs due to fracture in a monolithic algebraic form. A few critical observations are made towards various solutions, i.e. through nodal and elemental enrichment in terms of the merits and disadvantages of one or the other. Such analysis is important towards extending a fracture-enriched FEM into a multiscale framework.

2.3.2.1 Nodal enrichment FEM with embedded discontinuities

The variational BVP that is solved for the rate of the displacement field $\dot{\mathbf{u}} \in V_\eta$, takes the following form (Oliver and Huespe, 2004):

$$V_n := \left\{ \boldsymbol{\eta} = \bar{\boldsymbol{\eta}} + H_\Omega \tilde{\boldsymbol{\eta}}; \quad \bar{\boldsymbol{\eta}}, \tilde{\boldsymbol{\eta}} \in [H^1(\Omega)]^{n_{\mathrm{dim}}} \right\} \tag{2.7}$$

$$\int_\Omega \nabla^s \boldsymbol{\eta}^0 : \dot{\boldsymbol{\sigma}} d\Omega - \left[\int_\Omega \boldsymbol{\eta}^0 \cdot \dot{\boldsymbol{b}} d\Omega + \int_{\partial\Omega_\sigma} \boldsymbol{\eta}^0 \cdot \dot{\boldsymbol{t}} d\Gamma \right] = \mathbf{0} \quad \forall \boldsymbol{\eta}^0 \in V_\eta^0 \tag{2.8}$$

where the customised FE expression for the displacement rate and the strain rate field read as follows:

$$\left. \begin{array}{ll} \text{Total nodal displacement rate:} & \dot{\mathbf{u}}^{\mathrm{el}} = \mathbf{N}\dot{\mathbf{d}} + \mathbf{N}^* \dot{\boldsymbol{\beta}} \\ \text{FEM-based fracture-enhanced strain rate:} & \dot{\boldsymbol{\varepsilon}} = \mathbf{B}\dot{\mathbf{d}} + \mathbf{G}\dot{\boldsymbol{\beta}} \end{array} \right\} \tag{2.9}$$

where linearisation of the variational problem in Equation 2.8 using the FE discretisation in Equation 2.9 leads to the coupled matrix system in Equation 2.10.

$$\begin{bmatrix} \mathbf{K}^{dd} & \mathbf{K}^{d\beta} \\ \mathbf{K}^{\beta d} & \mathbf{K}^{\beta\beta} \end{bmatrix} \begin{Bmatrix} \dot{\mathbf{d}} \\ \dot{\boldsymbol{\beta}} \end{Bmatrix} = \begin{Bmatrix} \dot{\mathbf{f}}_{\mathrm{d}} \\ \dot{\mathbf{f}}_\beta \end{Bmatrix} \tag{2.10}$$

Note that the loading vectors in array form $\dot{\mathbf{f}}_d$ and $\dot{\mathbf{f}}_\beta$ are computed in standard form by using the standard $\mathbf{N}$ and modified shape functions $\mathbf{N}^*$, respectively. Note that an additional requirement to integrate the stiffness terms is to obtain specific integration rules over each of the positive $\boldsymbol{\Omega}^+$ and negative domain $\boldsymbol{\Omega}^-$ of the element, and therefore the initiation and the propagation direction of the discontinuity must be known (Belytschko and Black, 1999; Moës et al., 1999). In recent, work the tracking of the evolving discontinuities has been proposed to be refined by level-sets (Agathos et al., 2016).

Note that depending on the assumptions made by manipulating the variational statement in Equation 2.8, the Finite Element solution of the equilibrium equation in Equation 2.10 may differ slightly. Nonetheless, recent work shows that the final matrix system for and enhanced FEM with nodal enrichment and embedded discontinuities is coupled in a similar structure as presented in (Borja, 2008; Liu, 2015). Since the right hand side vector in Equation 2.10 has each of the entries filled with general real values, and the unknowns are strictly unique at shared nodes, there is no opportunities for element-based condensation of fracture dofs, as opposed to EFEM solution techniques (Oliver et al., 2006). In this regard, as fracture propagates new dofs are solved for in the global incremental iterative solution.

2.3.2.2 FEM quasi-static condensation of embedded discontinuities

The variational BVP that is solved for the rate of the displacement field $\dot{\mathbf{u}} \in V_\eta$, takes the following form (Borja, 2008; Oliver and Huespe, 2004), including an expression for the continuity of tractions along nucleated discontinuity surfaces:

$$V_n := \left\{ \boldsymbol{\eta} = \hat{\boldsymbol{\eta}} + M_\Omega \tilde{\boldsymbol{\eta}}; \quad \bar{\boldsymbol{\eta}}, \tilde{\boldsymbol{\eta}} \in [H^1(\Omega)]^{n_{\dim}} \right\} \tag{2.11}$$

$$\int_{\Omega\backslash\Gamma} \nabla^s \hat{\boldsymbol{\eta}}^0 : \dot{\boldsymbol{\sigma}} d\Omega - \left[\int_{\Omega\backslash\Gamma} \hat{\boldsymbol{\eta}}^0 \cdot \dot{\boldsymbol{b}} d\Omega + \int_{\partial\Omega_\sigma} \hat{\boldsymbol{\eta}}^0 \cdot \dot{\boldsymbol{t}} d\Gamma \right] = \mathbf{0} \quad \forall \hat{\boldsymbol{\eta}}^0 \in V_\eta^0 \tag{2.12}$$

$$\int_{\partial\Gamma} \tilde{\boldsymbol{\eta}} \cdot (\dot{\boldsymbol{\sigma}}_\Gamma - \dot{\boldsymbol{\sigma}}_{\Omega\backslash\Gamma}) \cdot \mathbf{n} d\Gamma \quad \forall \tilde{\boldsymbol{\eta}} \in L_2(\partial\Gamma) \tag{2.13}$$

where the tailored FE expression for the displacement rate and the strain rate field read as follows:

$$\left. \begin{array}{ll} \text{Total nodal displacement rate:} & \dot{\mathbf{u}}^{\mathrm{el}} = \mathbf{N}\dot{\mathbf{d}} + \mathbf{M}_\beta \dot{\boldsymbol{\beta}} \\ \text{FEM-based fracture-enhanced strain rate:} & \dot{\boldsymbol{\varepsilon}} = \mathbf{B}\dot{\mathbf{d}} + \mathbf{G}\dot{\boldsymbol{\beta}} \end{array} \right\} \tag{2.14}$$

The Finite Element solution in rate form takes the expression in Equation 2.15.

$$\begin{bmatrix} \mathbf{K}^{dd} & \mathbf{K}^{d\beta} \\ \mathbf{K}^{\beta d} & \mathbf{K}^{\beta\beta} \end{bmatrix} \begin{Bmatrix} \dot{\mathbf{d}} \\ \dot{\boldsymbol{\beta}} \end{Bmatrix} = \begin{Bmatrix} \dot{\mathbf{f}}_{\mathrm{d}} \\ \mathbf{0} \end{Bmatrix} \tag{2.15}$$

where the zero vector component in the right-hand side of Equation 2.15 allows for element-based quasi-static condensation of fracture dofs. The algorithmic advantage of EFEM vs XFEM methods lies therefore in the opportunities for quasi-static condensation of fracture dofs (Armero, 2012; Freeman et al., 2020; Jefferson and Freeman, 2022; Oliver et al., 2006).

This brief review of mesh-based methods with strong discontinuities (nodal and element-based enrichment), which do not require remeshing when cracks form, suggests that the methods are well-suited to be extended to cope with general inelastic consitutive formulations, e.g. including constitutive homogenisation type of formulations as defined in Section 2.2.

The next Section describes a short overview on numerical enhancement in Finite Element methods with embedded strong discontinuities which enable regularisation at the constitutive level, opposed to element-based treatment through additional dofs.

2.3.3 Embedded discontinuities within material points

The first attempt to address quasi-brittle response enclosed in a computational framework with embedded deformation bands was by Pietruszczak and Mróz (1981). In this computational framework, (elastic) material behaviour (constitutive response at the Gauss Point level) was considered in a combined fashion with a (plastic) localised response in a narrow band of finite thickness, with a formulation derived at the element level, and applied to Boundary Value Problems under plain strain settings. The proposed formulations, where derived and implemented in Constant-Strain Triangular (CST) elements.

In Pietruszczak and Mróz (1981), the occurrence of plasticity entails plastic strain increments $\dot{\varepsilon}^p_\Gamma$ within the localised band only, complemented with a rigid body motion and elastic straining of the bulk material. In this approach the overall constitutive relationship is obtained by considering the homogenised plastic strain increment as the average on an RVE (Reference Volume Element) of the same dimensions of a Finite Element, i.e. $\dot{\varepsilon}^p =< \dot{\varepsilon}^p >_{RVE}$ [1]. A sketch of the splitting criteria of failure modes for applying homogenisation of strain fields at the integration point with volume $\boldsymbol{\Omega}^m \times t_g$ (with t_g being the out-of-page thickness) is shown in Figure 2.11.

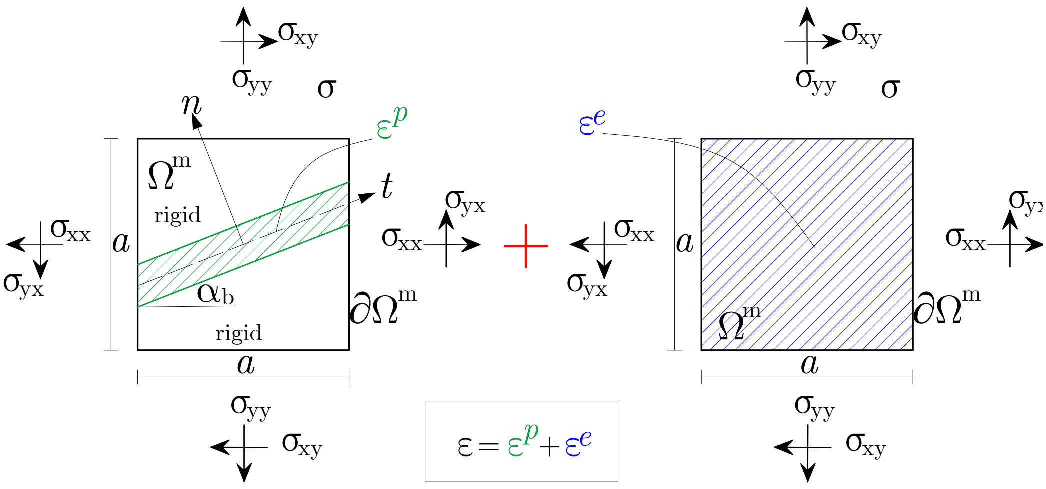

Figure 2.11: Sketch of failure mode splitting at the integration point level, as employed for the homogenisation-based failure analysis method with embedded discontinuities by Pietruszczak and Mróz (1981), where volume fractions are considered for averaging.

In this contribution only constant strain elements were used, then an equivalent

---

[1] $< \cdot >_{RVE}$ denotes the average on the volume of the Reference Volume Element

length is defined as $a = \sqrt{\Omega^m}$. The ratio of the volume undergoing plastic straining Ω^m_Γ (i.e. the localised band of finite thickness) to the volume of the element Ω^m defines the homogenised plastic strain increment $\dot{\boldsymbol{\varepsilon}}^p = \frac{\Omega^m_\Gamma}{\Omega^m}\dot{\boldsymbol{\varepsilon}}^p_\Gamma$, where $\frac{\Omega^m_\Gamma}{\Omega^m} = \frac{t_b}{a} \cdot \frac{1}{\cos(\alpha_b)}$ and $\frac{t_b}{a} = \eta_b$ is a geometric parameter that denotes the ratio of the deformation band thickness t_b to equivalent element length $\sqrt{\Omega^m}$. Upon some derivations including the consistency condition of the plastic straining band, the homogenised constitutive relationship takes an incremental form after the application of rotation operations into a Cartesian reference:

$$\dot{\boldsymbol{\sigma}} = \mathbf{T}^T \cdot \left\{ \frac{\Omega^m_\Gamma}{\Omega^m} \frac{1}{H} \left(\frac{\partial f_\Gamma}{\partial \boldsymbol{\sigma}_\Gamma} \right) \otimes \left(\frac{\partial f_\Gamma}{\partial \boldsymbol{\sigma}_\Gamma} \right) + \boldsymbol{D}_e^{-1} \right\}^{-1} \cdot \mathbf{T} \cdot \dot{\boldsymbol{\varepsilon}} \tag{2.16}$$

where $\dot{\boldsymbol{\sigma}}$ denotes the Cauchy stress rate in vector form, $\dot{\boldsymbol{\varepsilon}}$ is the strain rate vector, $\mathbf{T}$ stands for a rotation operator in matrix form, H is the hardening modulus, $\boldsymbol{D}_e$ stands for the (isotropic) Elasticity matrix, $\boldsymbol{\sigma}_\Gamma$ is the stress vector that characterizes the localised band response in local coordinates, $f_\Gamma = f_\Gamma(\boldsymbol{\sigma}_\Gamma, \beta)$ stands for the yield surface of the localised band in local coordinates, with β being the softening parameter, and $(\cdot) \otimes (\cdot)$ denotes outer vector product. In this formulation, the plain strain matrix representation of the inverse of the isotropic elasticity stiffness follows:

$$\boldsymbol{D}_e^{-1} = \frac{1}{E} \begin{bmatrix} (1-\nu^2) & -\nu(1+\nu) & 0 \\ -\nu(1+\nu) & (1-\nu^2) & 0 \\ 0 & 0 & 2(1+\nu) \end{bmatrix} \tag{2.17}$$

where $\boldsymbol{D}_e^{-1} = \boldsymbol{C}_e$ with $\boldsymbol{C}_e$ being the elastic compliance matrix in plain strain setting, and E and ν stand for Young's Modulus and Poisson's ratio, respectively.

Note that the aforementioned approach does not take into account the position of the shear band with respect to the element, and only a volume-based averaging procedure is used upon localisation. Therefore the averaging procedure only takes into account the inclination of the localisation band α_b, since the inclination affects the volume ratio Ω^m_Γ/Ω^m.

Further development of FEMs with *embedded* localisation bands at the constitutive level has been undertaken in Belytschko et al. (1988); Haghighat and Pietruszczak (2016); Klisinski et al. (1991); Simo et al. (1993); Zhao et al. (2018).

2.4 Advanced micro-macro fracture models

A review of latest computational developments for multiscale quasi-brittle fracture propagation is presented. In particular, attention is paid to models that consider coupling between two length-scales, i.e. micro to macroscopic length-scales. Methods which employ Finite Elements with strong-discontinuities are directly reported.

The Finite Element method with strong discontinuities (either through XFEM nodal enrichment or element-wise treatment of embedded strong discontinuities) has been used recently in various *multi-level* forms, which are often implemented numerically as multi-grid schemes, with the aim of representing physical phenomena occurring across scales, see e.g. Coenen et al. (2012); Holl et al. (2014); Karamnejad and Sluys (2014); Linder and Raina (2013); Loehnert and Belytschko (2007); Lu et al. (2016, 2017); Nguyen et al. (2011); Oskay et al. (2020); Raina and Linder (2015); Toro et al. (2014). Indeed, an unresolved dilemma in multiscale modelling, lies in the interaction of various length-scales during and after the onset of mechanical instabilities, such as fracture and progressive failure of structures (Geers et al., 2017). A brief description of what has been achieved in the last two decades is presented below.

Loehnert and Belytschko (2007) proposed a multiscale projection method for micro and macrocracks occurrence, where cracks at different lenght-scales where resolved using the Extended Finite Element approach (XFEM) (Belytschko and Black, 1999; Moës et al., 1999). Nguyen et al. (2011) constructed RVEs to represent the upscaled response of localised zones for a class of quasi-brittle materials, and tested the method for modelling embedded cohesive and adhesive macrocrack response against direct numerical simulations. Coenen et al. (2012) proposed new boundary conditions for RVEs to account for directional localisation of microstructures. Toro et al. (2014) presented a two-scale based formulation for microstructured effective continua, using strong discontinuity kinematics enhancement for representing the effective macroscopic localised response and standard RVEs for the non-localised continua. Holl et al. (2014) proposed a three-dimensional multiscale fracture propagation method based on XFEM strategies. Raina and Linder (2015) described a numerical scheme for up-scaling the response of non-wovens during failure in the finite deformation range, using a micromechanical model at the effective continua and strong discontinuity kinematics enhancement at the macro-scale. Lu et al. (2016) presented a multiscale methodology using embedded discontinuities at multiple scales, and upgraded the method to cope with deformation localisation under coupled fluid-flow and solid deformation in porous solids (Lu et al., 2017). Oskay et al. (2020) proposed a model reduction technique to multiscale fracture propagation in composites, where micro-scale deformation upon fracture is tracked efficiently using the philosophy of eigen-deformation.

In addition, a number of authors simulated *diffuse* fracture phenomena at the microstructural level during macroscopic fracture in a more classical form, i.e. making use of single-scale damage/plasticity frameworks, which are most of the times phenomenologically-driven. In these contributions, authors often pay more attention to the enhancement of numerical schemes for fracture modelling and so-called regularisation strategies, given that macro-Continuum level theories for a diverse range of materials are advanced enough in the literature, e.g. Beese et al. (2018); Duda et al. (2015); Neuner et al. (2020); Saksala et al. (2015, 2016); Wang and Waisman (2016), among others. Clearly, these simplified approaches possess advantages in terms of computational cost, relative to those of multi-grid fracture approaches (Coenen et al., 2012; Feyel and Chaboche, 2000; Kouznetsova et al., 2002).

Among other attempts to account for microcracking in quasi-brittle media, authors have explored the explicit use of penny-shaped embedded fractures within unstructured 3D FE meshes, where appropriate frictional contact rules are taken into account (Nejati et al., 2016).

2.4.1 Multi-level Embedded Strong Discontinuity FEM

Linder and Raina (2013) used the Embedded strong discontinuity method (EFEM) across adaptive zones of refinement, which then provide the flexibility to cope with the propagation of macroscopic fracture surfaces, as well as, multiple crack-branching surfaces typically describing phenomena in more detailed as it would occur in the microscale (e.g. microcracking and fragmentation) as illustrated in Figure 2.12.

In the multi-level approach by Linder and Raina (2013), there are sub-sets of BVPs following a domain decomposition, which incorporates the standard EFEM methodology at the sub-domain providing a greater resolution to capture even multiple cracks typical of dynamically-triggered crack branching, while condensation of crack dofs is kept for efficiency. In this regard an additive decomposition of the deformation field is used as shown in Equation 2.18.

$$\left.\begin{array}{lll}\text{Local displacement field:} & \mathbf{u}_{\mathrm{SBVP}}(\mathbf{x}) = \mathbf{u}(\mathbf{x}) + \tilde{\mathbf{u}}([|\mathbf{u}|]_{\mathrm{SBVP}}) & \text{in sub-domain } \boldsymbol{\Omega} \\ \text{Local strain field:} & \boldsymbol{\varepsilon}_{\mathrm{SBVP}} = \boldsymbol{\varepsilon}(\mathbf{x}) + \tilde{\boldsymbol{\varepsilon}}([|\mathbf{u}|]_{\mathrm{SBVP}}) & \text{in sub-domain } \boldsymbol{\Omega}\end{array}\right\} \tag{2.18}$$

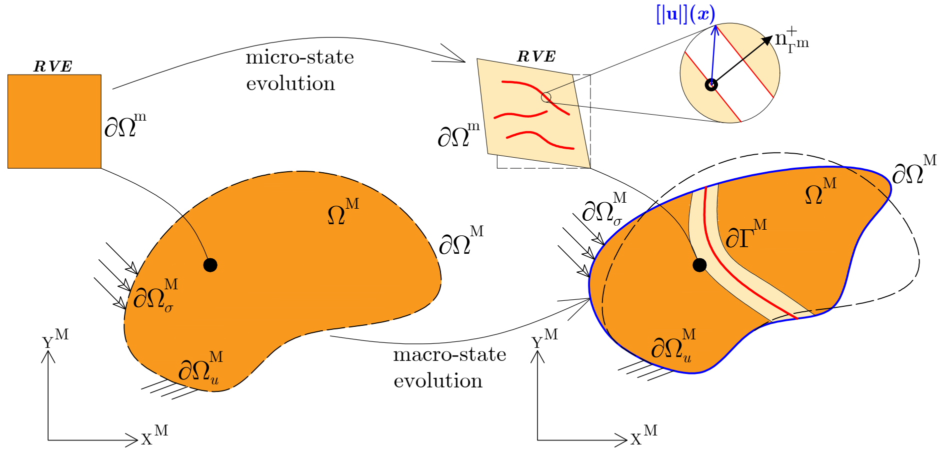

(a) Multiscale Boundary Value Problem with EFEM

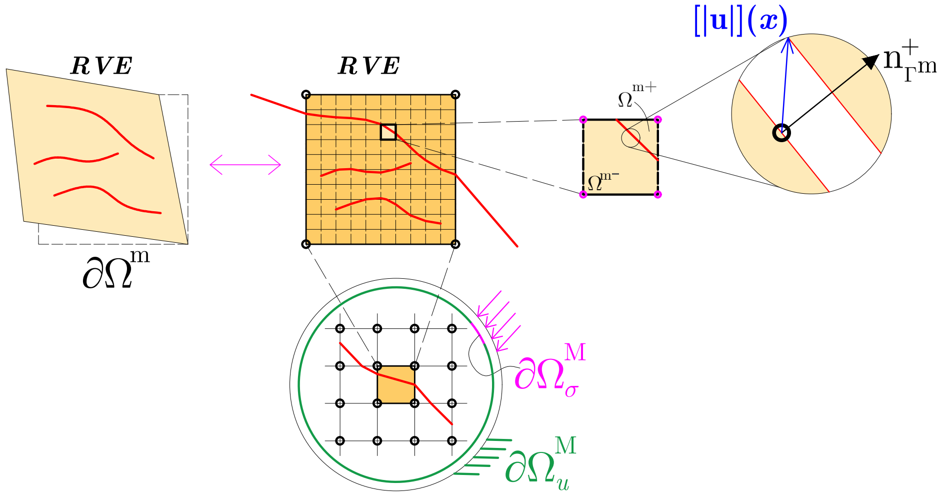

(b) Multi-level discretisation with EFEM

Figure 2.12: Sketch of typical mechanical components of a BVP for modelling quasi-brittle solids by multi-level EFEM (Linder and Raina, 2013): multiscale Boundary Value Problem (top), multi-level discretisation with EFEM (bottom).

where $\mathbf{u}(\mathbf{x})$ and $\boldsymbol{\varepsilon}(\mathbf{x})$ pertain to the interpolated displacement and strain field from the global solution, and the additional components $\tilde{\mathbf{u}}([|\mathbf{u}|]_{\mathrm{SBVP}})$ and $\tilde{\boldsymbol{\varepsilon}}([|\mathbf{u}|]_{\mathrm{SBVP}})$ are computed to account for the presence of strong discontinuities across elements in this sub-domain $\boldsymbol{\Omega}$. Where the recovered stresses within any element the sub-domain $\boldsymbol{\Omega}$ follow from the enhanced local strain that accounts for the potential presence of strong discontinuities, and interpolated displacements in pseudo-nodes follows a kinematic constraint as shown in Equation 2.19.

$$\left.\begin{array}{lll} \text{Local stress recovery:} & \boldsymbol{\sigma} = \boldsymbol{D}_e : \boldsymbol{\varepsilon}_{\mathrm{SBVP}} & \text{in } \boldsymbol{\Omega} \\ \text{Kinematic constraint:} & \mathbf{u}_{\mathrm{SBVP}}(\mathbf{x}_{inode}) = \phi^{\mathrm{el}}_{kc}(\mathbf{x}_{inode}, \mathbf{u}^{\mathrm{el}}, [|\mathbf{u}|](\mathbf{x}_{\mathbf{ck}})) & \text{along } \partial\boldsymbol{\Omega} \end{array}\right\} \tag{2.19}$$

Note that the solution of the SBVP is then complete as the whole boundary for the sub-domain has known displacements and internal nodes are in equilibrium with body and inertial forces. In the case of dynamic analysis, the procedure of condensation and solution can then follow the method by Armero and Linder (2009). The solution of the sub problem is then nested within the global solution of the main BVP, which can create theoretical and numerical challenges during the up-scaling stage.

In other important attempts to cope with multiscale response, the embedded strong discontinuity has served as the basis for crack computations while other mechanistic components have been incorporated to account for response across scales. Tjioe and Borja (2015) used a crystal plasticity framework combined with embedded discontinuities (which accounted for microcracks) to capture the response of failing quasi-brittle geo-materials, where the main components followed a natural sequence from the previous work on geo-material bifurcation presented in Borja (2002); Borja and Aydin (2004); Foster et al. (2007). Similarly, the Distinct Element method (Cundall and Strack, 1979) has been coupled hierarchically (see e.g. Phillips et al. (1999)) with the embedded strong discontinuity method to cope for the multiscale response of granular geo-materials (Andrade and Tu, 2009; Chen et al., 2011).

2.4.2 Micromechanical failure modelling with cohesive-cracks

The framework presented by Kaczmarczyk and Pearce (2009), is considered first in this section. Such a Finite Element scheme was proposed for modelling quasi-brittle solids with heterogeneities, although by direct numerical simulation of inclusions, which arguably makes the method computationally inefficient for simulating highly heterogeneous solids, opposed to periodic homogenisation solutions for highly heterogenous solids (see e.g. Terada et al. (2000)). In addition, matrix as well as inclusion materials were considered as hyper-elastic with non-linearities coming from displacement discontinuities at the inter-element boundaries only (Tijssens, 2001; Xu and Needleman, 1994). Consequently, cohesive-crack zone elements are placed *a priori* only at element boundaries, i.e. are placed when mesh is generated originally. Hence, fracture propagation paths are mesh-dependent, which was proposed to be alleviated to some extent by generating random triangular meshes. In this mixed FE formulation, two primary fields are considered, namely, the stress field $\boldsymbol{\sigma}$ which is interpolated within an element domain $\boldsymbol{\Omega}^{el}$, and the displacement field $\boldsymbol{u}$ which is approximated only at the element boundaries as illustrated in Figure 2.13.

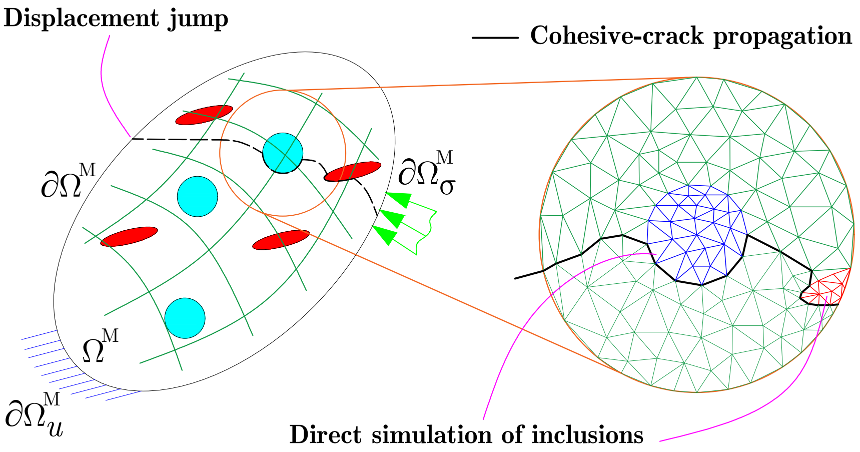

(a) Domain discretisation in a mixed FE formulation with inter-element cohesive-cracks

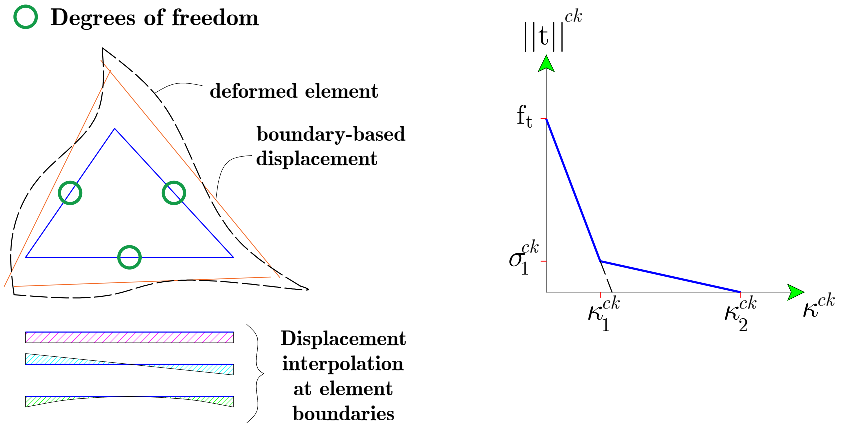

(b) Hybrid element with deformed modes (left), cohesive-crack softening law (right)

Figure 2.13: Sketch of typical mechanical components of a BVP for modelling heterogenous solids by mixed Finite elements (Kaczmarczyk and Pearce, 2009): a) mesh to account for heterogeneities and inter-element cohesive cracks generated *a priori*, b) element to illustrate different deformed modes based on separate interpolation of stress and displacement fields, and inter-element cohesive crack softening law.

The governing equations for a BVP employing a mixed FE formulation reads as in Equation 2.20.

$$\left.\begin{array}{lcl}\text{Mechanical balance:} & \mathbf{L}^{\mathrm{T}}\cdot\boldsymbol{\sigma}=\mathbf{0} & \text{in } \boldsymbol{\Omega}^{el}\\ \text{Constitutive relation:} & \boldsymbol{\sigma}=\mathbf{D}_{e}\cdot\boldsymbol{\varepsilon} & \text{in } \boldsymbol{\Omega}^{el}\\ \text{Kinematics relation:} & \boldsymbol{\varepsilon}=\mathbf{L}\cdot\mathbf{u} & \text{in } \boldsymbol{\Omega}^{el}\\ \text{Natural boundary conditions:} & \mathbf{G}_{\mathrm{n}}\cdot\boldsymbol{\sigma}=\check{\mathbf{t}} & \text{on } \partial\boldsymbol{\Omega}^{\mathrm{el}}_{\sigma}\\ \text{Essential boundary conditions:} & \mathbf{u}=\check{\mathbf{u}} & \text{on } \partial\boldsymbol{\Omega}^{\mathrm{el}}_{u}\end{array}\right\} \tag{2.20}$$

where $\boldsymbol{\sigma}$ stands for the vectorised form of Cauchy stress which is interpolated within the element domain, $\boldsymbol{\varepsilon} = \boldsymbol{\varepsilon}^e$ is the vector form of strain components which is equivalent to its elastic part at all times (De Freitas, 1998; Jirousek and Zielinski, 1993), $\mathbf{u}$ stands for the boundary-approximated displacement field which can be interpolated through various forms as illustrated in Figure 2.13b, $\check{\mathbf{t}}$ represents the imposed tractions on $\partial\Omega^{el}_{\sigma}$ given, while $\check{\mathbf{u}}$ defines the imposed boundary displacements on $\boldsymbol{\Omega}^{el}_{u}$ noticing that $\partial\Omega^{el}_{\sigma} \cap \partial\Omega^{el}_{u} = \varnothing$, $\mathbf{L}$ is a matrix filled-in with differential operations and the $\mathbf{G}_{\mathrm{n}}$ matrix contains cartesian projections of the unit vector $\mathrm{n}_{\partial\Omega^{el}_{\sigma}} = [\mathrm{n}_x, \mathrm{n}_y]^{\mathrm{T}}$. In particular, the matrices $\mathbf{L} = \begin{pmatrix} \partial_x & 0 & \partial_y \\ 0 & \partial_y & \partial_x \end{pmatrix}^{\mathrm{T}}$ and $\mathbf{G}_{\mathrm{n}} = \begin{pmatrix} \mathrm{n}_x & 0 & \mathrm{n}_y \\ 0 & \mathrm{n}_y & \mathrm{n}_x \end{pmatrix}$ are used under 2-D geometrical settings.

Note that displacement jumps $[\![\mathbf{u}]\!]_L = \left[[\![\mathrm{u}]\!]_n, [\![\mathrm{u}]\!]_s\right]^{\mathrm{T}}$, which are defined in terms of local normal and shear components, are activated upon fracture detection as illustrated with a softening curve in Figure 2.13b. In particular, strong discontinuities are only allowed through inter-element boundaries by the activation of cohesive-crack line models, in the case of 2D implementations as found in Kaczmarczyk and Pearce (2009). Note that in this mixed formulation with dofs at the face instead of element corners, a crack zone initiation can occur across one-element width, while in standard FEM formulations at least two elements play a role as illustrated in Figure 2.14.

It is the local displacement jumps $[\![\mathbf{u}]\!]_L$ that define local tractions through a bi-linear softening law, which reads mathematically as follows:

$$\left.\begin{array}{ll} \text{Softening rule:} & \|\mathrm{t}\|^{ck} = \begin{cases} \frac{\sigma_1^{ck} - f_t}{\kappa_1^{ck}}\kappa^{ck} + f_t & \text{if } \kappa^{ck} \leq \kappa_1^{ck} \\ \frac{\sigma_1^{ck}}{\kappa_1^{ck} - \kappa_2^{ck}}\left(\kappa^{ck} - \kappa_2^{ck}\right) & \text{if } \kappa_1^{ck} < \kappa^{ck} \leq \kappa_2^{ck} \\ 0 & \text{if } \kappa^{ck} > \kappa_2^{ck} \end{cases} \\ \text{Loading function:} & \Phi_{ck}\left([\![\mathbf{u}]\!]_L, \kappa^{ck}\right) = \sqrt{[\![\mathrm{u}]\!]_n{}^2 + \alpha^{ck}[\![\mathrm{u}]\!]_s{}^2} - \kappa^{ck} \end{array}\right\} \quad (2.21)$$

where $\kappa_1^{ck} = G_f/f_t$, $\kappa_2^{ck} = 10\kappa_1$, $\sigma_1^{ck} = 0.1 f_t$ and $\|\mathrm{t}\|^{ck} = \sqrt{\mathrm{t}_n^2 + \alpha^{ck}\mathrm{t}_s^2}$. Note that the aforementioned bi-linear softening model becomes complete with three material properties, namely, tensile strength f_t, fracture energy G_f and the weighting factor α^{ck}, which factors the shear displacement jumps to be taken into account for computing the decreased inter-element cohesive-crack strength $\|\mathrm{t}\|^{ck}$.

Seeking further developments of the formulation presented by Kaczmarczyk and Pearce (2009), a Finite Element framework that approximates the effects of *ellipsoidal* inclusions in Finite Element subdomains has been proposed by Novák et al. (2012), with the aim to present an efficient Micomechanics-enhanced Finite Element method

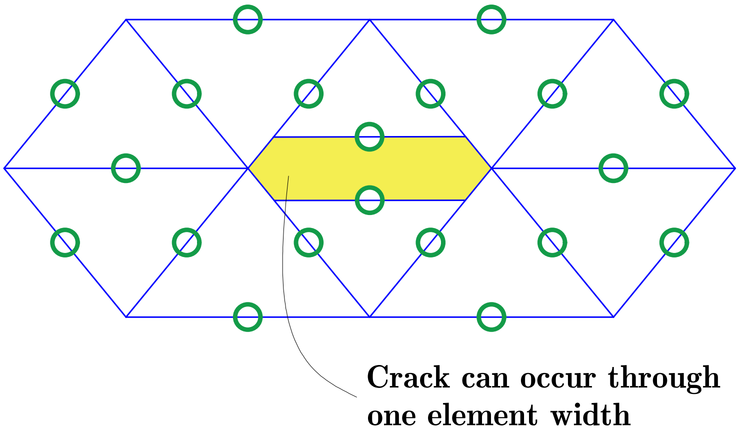

(a) Crack initiation in a mixed FE formulation with inter-element cohesive-cracks

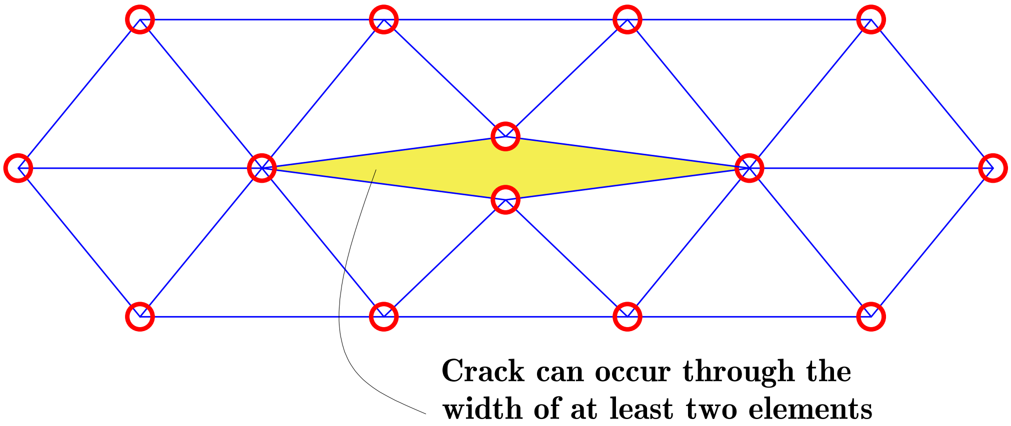

(b) Crack initiation in a standard FE formulation with inter-element cohesive-cracks

Figure 2.14: Sketch of crack propagation analysis by employing inter-element cohesive-cracks zones, where minimum number of elements playing a role varies for a mixed FEM (Kaczmarczyk and Pearce, 2009; Tijssens, 2001; Xu and Needleman, 1994), when compared to standard FEM.

for modelling heterogeneous materials. The highlights of this formulation is that the mechanical inclusions are not solved explicitly within the subdomains, the so-called RVE, but approximations on the perturbations of the macroscopic Finite Element fields are done using closed-form Eshelby's solutions (Eshelby, 1957, 1959). These perturbations on macroscopic fields were enclosed within the equivalent-inclusion method (Mura, 1987). Interaction between inclusions was approximated using an iterative self-compatibility algorithm, were the eigen-fields within inclusions were considered as constant but forced-to-be compatible with the average macrostrain. In Novák et al. (2012), the finite element formulations were first discussed on how they may be adapted from a Partition of Unity method (Belytschko and Black, 1999;

Moës et al., 1999). Nevertheless, the authors pointed out the necessity to increase the local degrees of freedom by 18 additional degrees in each node per inclusion within the domain. Such method would have been computational expensive and instead the hybrid-Trefftz stress element formulation (Kaczmarczyk and Pearce, 2009) was adopted as an alternative.

2.4.3 Strong-discontinuity zones in micromechanical constitutive laws

Following the idea that an embedded deformation band can be cast in a classical quasi-brittle macro-Continuum directly into the constitutive-level under certain simplifying assumptions as revised previously from the work of Pietruszczak and Mróz (1981) in Section 2.3.3, others have attempted to cast an embedded localisation zone into a homogenised quasi-brittle macro-continuum. key feature is the coupling of the embedded localisation zone with evolving penny-shaped microcracking zones in the bulk before macrocracking (Zhao et al., 2018).

In the study by Zhao et al. (2018), a slightly modified version of strain averaging procedure (Haghighat and Pietruszczak, 2016; Moallemi and Pietruszczak, 2017; Nguyen et al., 2012, 2014) has been used, opposed to simple averaging procedures as presented in Pietruszczak and Mróz (1981), now including a more rigorous analysis of the effect of a sharp embedded localisation zone at the regularised constitutive-level, which is referred here as a FEM/CLED strategy (Finite Element methodology employing a constitutive law enriched locally with an embedded strong discontinuity). The strong discontinuity $\partial\boldsymbol{\Gamma}^{\mathrm{m}}$ applies a jump $[\![\mathbf{u}]\!]$ in the displacement field $\mathbf{u}$ within the volume $\boldsymbol{\Omega}^{\mathrm{m}}$ considered for averaging as illustrated in Figure 2.15. Accordingly, this method seeks a regularisation at the quadrature-points, by embedding a sharp macrocrack $\partial\boldsymbol{\Gamma}^{\mathrm{m}}$ within $\boldsymbol{\Omega}^{\mathrm{m}}$, opposed to an element-level enrichment in advanced fracture modelling techniques such as EFEM (Armero and Linder, 2009; Oliver et al., 2006, 2003; Simo et al., 1993).

Therefore, the following mathematical expression applies for the displacement and strain field $\{\mathbf{u}, \boldsymbol{\varepsilon}\}$ within the RVE-level (volume used for averaging at quadrature-point), which is illustrated as well in Figure 2.16.

$$\left.\begin{array}{lll} \text{Strong form of displacement field:} & \mathbf{u} = \mathbf{u}_c + H_{\Omega}(\mathbf{x}) \otimes [\![\mathbf{u}]\!] & \forall \mathbf{x} \in \boldsymbol{\Omega}^{\mathrm{m}} \\ \text{Strong form of strain field:} & \boldsymbol{\varepsilon} = \nabla^s\big(\mathbf{u}_c + H_{\Omega}(\mathbf{x}) \otimes [\![\mathbf{u}]\!]\big) & \forall \mathbf{x} \in \boldsymbol{\Omega}^{\mathrm{m}} \end{array}\right\} \quad (2.22)$$

where $\nabla^s(\cdot) = \frac{1}{2}\big(\nabla(\cdot) + (\nabla(\cdot))^{\mathrm{T}}\big)$ stands for the symmetric part of the gradient of a field, and $H_{\Omega}(\mathbf{x}) = \left\{\begin{array}{ll} 1 & ,\forall \mathbf{x} \in \boldsymbol{\Omega}^{\mathrm{m}+} \\ 0 & ,\forall \mathbf{x} \in \boldsymbol{\Omega}^{\mathrm{m}-} \end{array}\right.$ is a Heaviside function within the RVE.

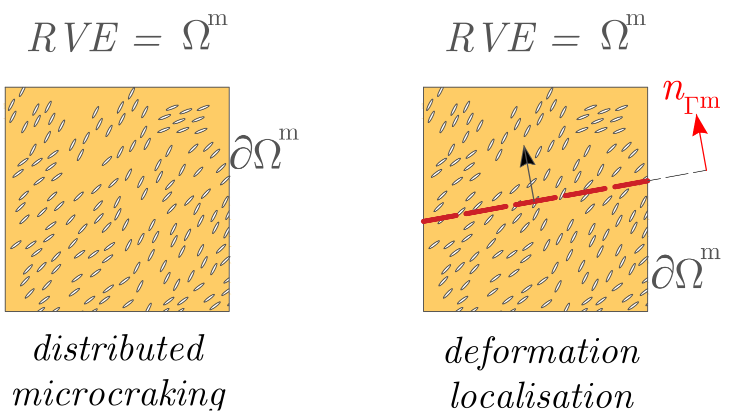

Figure 2.15: Sketch of a quasi-brittle RVE with embedded strong discontinuities at the constitutive-level: distributed microcracking before deformation localisation (left), onset of deformation localisation by strong discontinuity assumption (right).

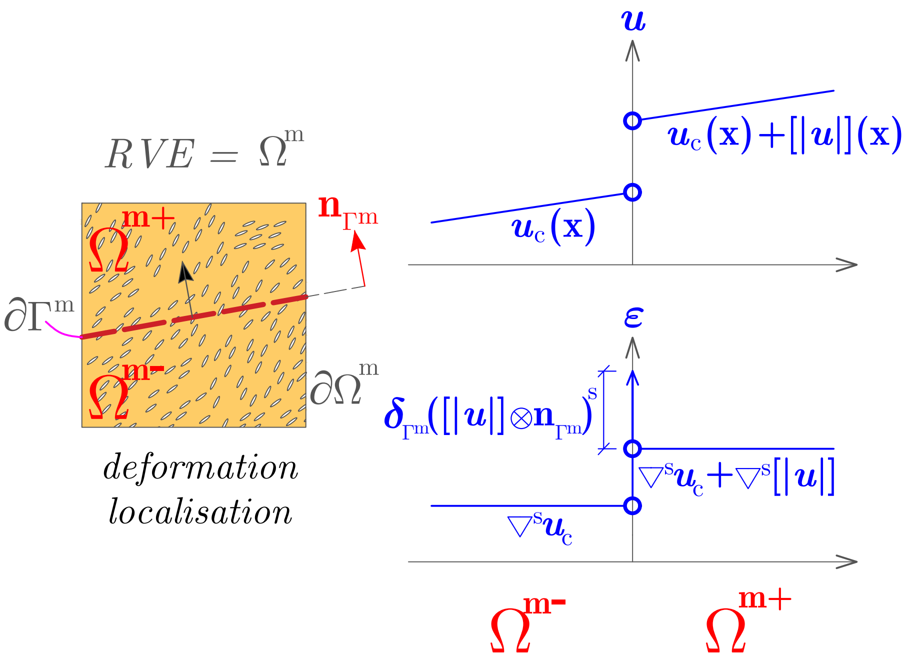

Figure 2.16: Sketch of a quasi-brittle RVE with embedded strong discontinuities at the constitutive-level: displacement and strain field $\{\mathbf{u}, \boldsymbol{\varepsilon}\}$ distribution over the RVE.

Further elaboration leads to the volume-averaged strain field $\bar{\boldsymbol{\varepsilon}}$ over the RVE-level, used for computations at the quadrature points in Equation 2.23.

$$\text{Overall strain:} \quad \bar{\boldsymbol{\varepsilon}} = \frac{1}{||\Omega^{\mathrm{m}}||}\int_{\Omega^{\mathrm{m}}}\Big(\underbrace{\nabla^s \mathbf{u}_c + H_\Omega(\mathbf{x}) \otimes \nabla^s[|\mathbf{u}|]}_{\text{regular part}} + \underbrace{([|\mathbf{u}|] \otimes (\delta_{\Gamma^{\mathrm{m}}} \otimes \mathbf{n}_{\Gamma^{\mathrm{m}}}))^s}_{\text{unbounded part}}\Big) d\Omega^{\mathrm{m}} \tag{2.23}$$

where $\delta_{\Gamma^{\mathrm{m}}}$ is the scalar-valued surface-type Dirac delta function (with units of the reciprocal of length), which explodes ($\delta_{\Gamma^{\mathrm{m}}} \rightarrow \infty$) for every position right over the discontinuity surface $\partial\Gamma^{\mathrm{m}}$ and vanishes everywhere else ($\delta_{\Gamma^{\mathrm{m}}} \rightarrow 0$), and $\mathbf{n}_{\Gamma^{\mathrm{m}}}$ is the unit normal to the crack surface $\partial\Gamma^{\mathrm{m}}$. It is emphasised, that considering the RVE-domain is small enough, then changes of the displacement gradient fields $\boldsymbol{\nabla}^s\mathbf{u}_c$ and $\boldsymbol{\nabla}^s[|\mathbf{u}|]$ within $\boldsymbol{\Omega}^{\mathrm{m}}$ are negligible, which yields to further simplification. Additional elaboration, using the identity $\delta_{\Gamma^{\mathrm{m}}}(\mathbf{x} \in \partial\Gamma^{\mathrm{m}}) \cdot dV_{\Gamma^{\mathrm{m}}} = dS_{\Gamma^{\mathrm{m}}}$ over the incipient volume $dV_{\Gamma^{\mathrm{m}}}$ that surrounds the sharp discontinuity surface $\partial\Gamma^{\mathrm{m}}$, leads to a regularisation of the integral term that involves $\delta_{\Gamma^{\mathrm{m}}}(\mathbf{x})$ as shown in Equation 2.24.

$$\begin{aligned}
\bar{\boldsymbol{\varepsilon}} \quad &\equiv \quad \boldsymbol{\nabla}^s\mathbf{u}_c + \tfrac{\boldsymbol{\nabla}^s[|\mathbf{u}|]}{||\boldsymbol{\Omega}^{\mathrm{m}}||}\int_{\boldsymbol{\Omega}^{\mathrm{m+}}\cup\boldsymbol{\Omega}^{\mathrm{m-}}} H_{\boldsymbol{\Omega}}(\mathbf{x})d\boldsymbol{\Omega}^{\mathrm{m}} + \tfrac{([|\mathbf{u}|]\otimes\mathbf{n}_{\Gamma^{\mathrm{m}}})^s}{||\boldsymbol{\Omega}^{\mathrm{m}}||}\int_{\Gamma^{\mathrm{m}}} \delta_{\Gamma^{\mathrm{m}}}(\mathbf{x} \in \partial\Gamma^{\mathrm{m}}) \cdot dV_{\Gamma^{\mathrm{m}}} \\
&\approx \quad \boldsymbol{\nabla}^s\mathbf{u}_c + \tfrac{||\boldsymbol{\Omega}^{\mathrm{m+}}||}{||\boldsymbol{\Omega}^{\mathrm{m}}||}\boldsymbol{\nabla}^s[|\mathbf{u}|] + \tfrac{\int_{\partial\Gamma^{\mathrm{m+}}} dS_{\Gamma^{\mathrm{m}}}}{||\boldsymbol{\Omega}^{\mathrm{m}}||}([|\mathbf{u}|] \otimes \mathbf{n}_{\Gamma^{\mathrm{m}}})^s \\
&\approx \quad \boldsymbol{\nabla}^s\left(\mathbf{u}_c + \tfrac{||\boldsymbol{\Omega}^{\mathrm{m+}}||}{||\boldsymbol{\Omega}^{\mathrm{m}}||}[|\mathbf{u}|]\right) + \left(\tfrac{A_{\Gamma^{\mathrm{m+}}}}{||\boldsymbol{\Omega}^{\mathrm{m}}||}[|\mathbf{u}|] \otimes \mathbf{n}_{\Gamma^{\mathrm{m}}}\right)^s \\
&\approx \quad \boldsymbol{\nabla}^s\left(\mathbf{u}_c + \xi_{\Gamma^{\mathrm{m}}} \cdot [|\mathbf{u}|]\right) + \left(\tfrac{1}{l_{\Gamma^{\mathrm{m}}}}[|\mathbf{u}|] \otimes \mathbf{n}_{\Gamma^{\mathrm{m}}}\right)^s \\
&\approx \quad \boldsymbol{\nabla}^s(\mathbf{u}_c + \xi_{\Gamma^{\mathrm{m}}} \cdot [|\mathbf{u}|]) + (\mathbf{g}_{\Gamma^{\mathrm{m}}} \otimes \mathbf{n}_{\Gamma^{\mathrm{m}}})^s
\end{aligned} \tag{2.24}$$

where $l_{\Gamma^{\mathrm{m}}} = ||\boldsymbol{\Omega}^{\mathrm{m}}||/A_{\Gamma^{\mathrm{m+}}}$ represents the characteristic length that regularises deformation localisation within the RVE-level, $\xi_{\Gamma^{\mathrm{m}}} = ||\boldsymbol{\Omega}^{\mathrm{m+}}||/||\boldsymbol{\Omega}^{\mathrm{m}}||$ is the volume fraction for the positive part of the domain, and $\mathbf{g}_{\Gamma^{\mathrm{m}}} = (1/l_{\Gamma^{\mathrm{m}}}) \cdot [|\mathbf{u}|]$ considers a normalised measure of the displacement jump $[|\mathbf{u}|]$.

Note that the first term $\boldsymbol{\nabla}^s(\mathbf{u}_c + \xi_{\Gamma^{\mathrm{m}}} \cdot [|\mathbf{u}|]) \approx \boldsymbol{\nabla}^s\mathbf{u}_c$ occurring in the bulk material(o bulk domain) can be approximated by the behaviour of a homogenised quasi-brittle macro-continuum. In Zhao et al. (2018), the response of this continuous strain component $\boldsymbol{\nabla}^s\mathbf{u}_c = \bar{\boldsymbol{\varepsilon}}^e + \bar{\boldsymbol{\varepsilon}}^{\Gamma^{\mathrm{m}},d}$ is then split into two components, with $\bar{\boldsymbol{\varepsilon}}^e = \boldsymbol{D}_e^{-1} : \bar{\boldsymbol{\sigma}}$ and $\bar{\boldsymbol{\varepsilon}}^{\Gamma^{\mathrm{m}},d}$ being micromechanics based, by employing numerical homogenisation (Andrieux et al., 1986; Pensée et al., 2002; Zhao et al., 2016; Zhu et al., 2008a,b, 2011; Zhu, 2017) and the Eshelby's equivalent inclusion method (Mura, 1987) accounting for penny-shaped microcracks growing in number, according to the microcracking density parameter $\mathscr{F}_\alpha^m$ (Budiansky and O'Connell, 1976), in various direction sets $\alpha_m = \{\alpha_{m,1}, \alpha_{m,2}, \alpha_{m,3}...\alpha_{m,n}\}$.

On the other hand, the regularised-strain term $(\mathbf{g}_{\Gamma^{\mathrm{m}}} \otimes \mathbf{n}_{\Gamma^{\mathrm{m}}})^s \equiv \bar{\boldsymbol{\varepsilon}}^{\Gamma^{\mathrm{m}},l}$ represents the localised strain contribution due to the presence of a sharp failure surface embedded at the RVE-level. Therefore, the homogenised strain $\bar{\boldsymbol{\varepsilon}}$ could be re-formulated as follows for a micromechanical quasi-brittle solid venturing deformation localisation at the RVE-level as shown in Equation 2.25.

$$\bar{\boldsymbol{\varepsilon}} = \underbrace{\boldsymbol{D}_e^{-1} : \bar{\boldsymbol{\sigma}} + \bar{\boldsymbol{\varepsilon}}^{\Gamma^{\mathrm{m}},d}}_{\text{distributed microcracking}} + \underbrace{\bar{\boldsymbol{\varepsilon}}^{\Gamma^{\mathrm{m}},l}}_{\text{Localised fracture}} \quad \text{(computation at quadrature points)} \tag{2.25}$$

Discussion on limitations of the model by Zhao et al. (2018): Note that the implementation by Zhao et al. (2018) allows for evaluation at the quadrature-level, ensuring regularisation of the load-displacement response for simple paths, although the interaction between the phenomena at the homogenised quadrature points and that occurring at the element-level has not yet being reported to be successful.

2.4.4 Micro-to-macro fracture transition in multiscale FEM

Some of the criteria used to **detect macrocracks** and to establish adequate **fracture transition**, from microcracking to fully developed localised fracture, are discussed.

One of the criterion for macro-scale cracking detection as used in various publications is based on a measure of macroscopic stress fields (e.g. Rankine's postulate of cracking propagating perpendicular to the major principal stress direction) (Haghighat and Pietruszczak, 2016; Kaczmarczyk and Pearce, 2009; Moallemi and Pietruszczak, 2017). In this context, the stress criterion $t_{\sigma,ck}(\sigma_1) > \sigma_{crit}$ shall be met for crack detection, with evaluation typically at the element-level (Haghighat and Pietruszczak, 2016; Moallemi and Pietruszczak, 2017). Such a criterion can be used in the *activation* of fracture interfaces, e.g. in inter-element cohesive-crack surfaces (Tijssens, 2001; Xu and Needleman, 1994), or to propagate embedded macrocracks in micromechanics-enriched methodologies with focus on strong-discontinuities having an effect at the constitutive-level (Moallemi and Pietruszczak, 2017). Note that such a criterion can be inaccurate in cases of severe cracking, and statistical algorithms for smoothening crack patterns have been proposed as remedy, with algorithm evaluation within a specified cracking-related radius $R_{s,ck}$. In addition, geometric corrections can be imposed to macrocack direction when incident macrocracks meet in one element (Alfaiate et al., 2003, 2002; Freeman et al., 2020; Moallemi and Pietruszczak, 2017) as illustrated in Figure 2.17.

The usefulness of coupling semi-analytical micromechanical homogenisation schemes with strong discontinuities has been further exploited at the constitutive-level in Zhao et al. (2018), by using the directional nature of microcracking as a drive for macrocrack activation within the quadrature points. The microcrack density parameter $\mathscr{F}_{\alpha}^{m}$

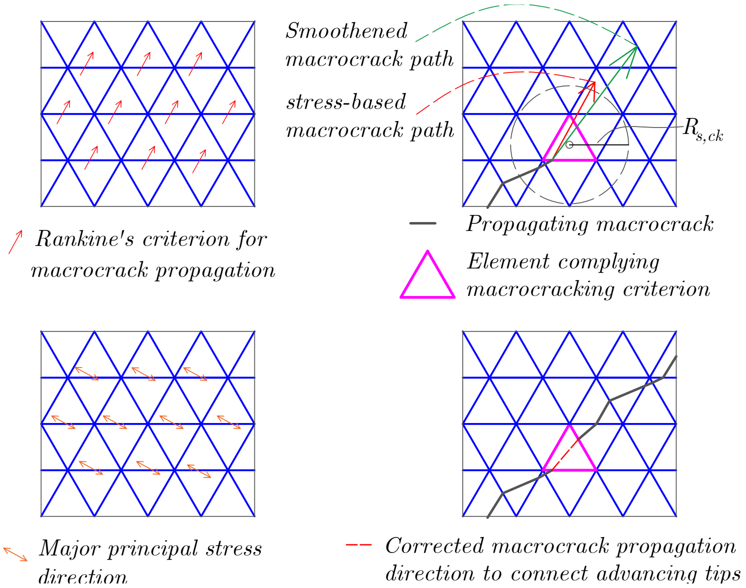

Figure 2.17: Sketch of stress criterion to set macrocracking direction, and correction based on (i) smoothening algorithm in $r_{s,ck} \leq R_{s,ck}$ or (ii) by connecting macrocracks.

(Budiansky and O'Connell, 1976) has been used in this regard, which is evaluated for various microcracking directions $\alpha_m = [\alpha_{m,1}, \alpha_{m,2}, ...\alpha_{m,n}]^{\mathrm{T}}$. The idea follows the assumption that as soon as the microcracking density exceeds a critical value, deformation localisation would occur. In a mathematical sense, this activation criteria can be expressed as shown in Equation 2.26.

$$\left.\begin{array}{ll}\text{Macrocrack detection:} & \Theta_{\alpha}^{\mathrm{mM}}\left(\mathscr{F}_{\alpha}^{\mathrm{m}}, \mathscr{F}_{crit}^{\mathrm{m}}\right) = \mathscr{F}_{\alpha}^{m} - \mathscr{F}_{crit}^{m} \leq 0 \\ \\ \text{Microcracking directions:} & \alpha_m = [\alpha_{m,1}, \alpha_{m,2}, ...\alpha_{m,n}]^{\mathrm{T}} \end{array}\right\} \tag{2.26}$$

where the macrocrack detection criterion $\Theta_{\alpha}^{\mathrm{mM}}\left(\mathscr{F}_{\alpha}^{m}, \mathscr{F}_{crit}^{m}\right) = 0$ is effectively complied when one of the microcracking directions pushes forward the critical microcracking density $\mathscr{F}_{crit}^{m}$ expected for the onset of localisation. An illustration of deformation-induced multiscale phenomena and the micro-to-macro facture transition occurring at the RVE-level are shown in Figure 2.18.

Note that in Zhao et al. (2018) the evolution of microcracks is frozen at the moment of macrocrack activation at the constitutive-level. Therefore, upon deformation localisation the inelastic response is dominated by the embedded strong discontinuity, which was particularly tailored as an isotropic damage cohesive-crack model.
The model by Zhao et al. (2018) was shown to be able to capture the response exhibited in the triaxial compression tests on rock samples by Martin (1997) as shown in Figure 2.19.

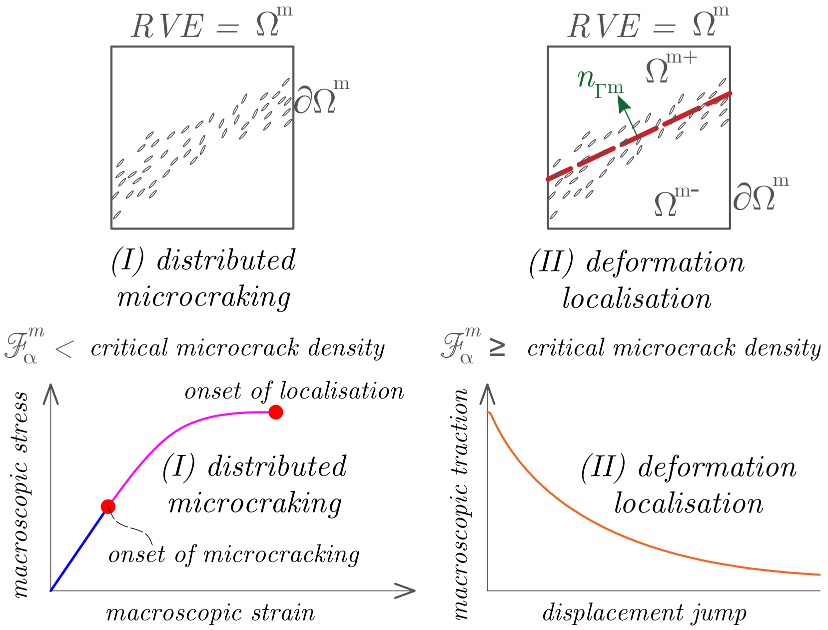

Figure 2.18: Sketch of micro-to-macro fracture transition in a homogenised quasi-brittle macro-constitutive model by Zhao et al. (2018).

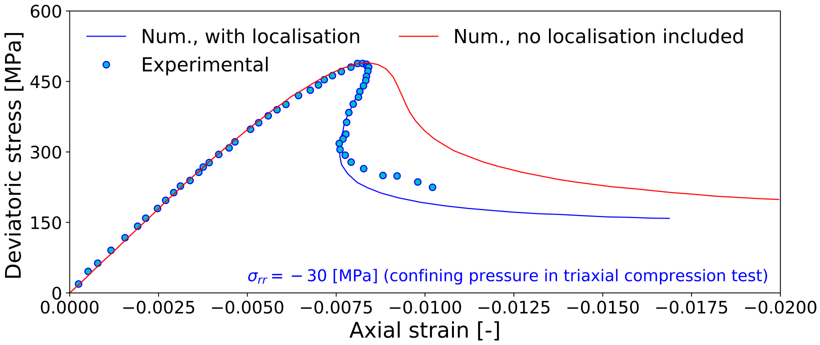

(a) Confining pressure: $\sigma_{rr} = -30$ [MPa]

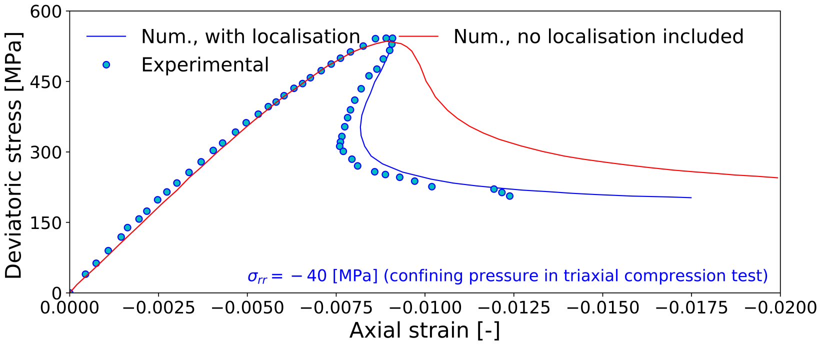

(b) Confining pressure: $\sigma_{rr} = -40$ [MPa]

Figure 2.19: Simulations of rock triaxial compression tests (experiments by Martin (1997)) showing smooth micro-to-macro fracture transition, using homogenised quasi-brittle macro-constitutive model by Zhao et al. (2018).

Limitations of the micromechanics-to-localisation transition in Zhao et al. (2018): The premise of microcracking ceasing at the onset of macrocracking may hinder the general use of the model, since such a response may only be appropriate for loading conditions which do not induce rotations of principal directions. Under general loading, it is expected that densely populated microcracking sets may keep growing in directions unaligned with nucleating macrocracks, before and after macrocracking has started (Nooru-Mohamed et al., 1993; Van Mier, 1984).

2.5 Concluding remarks

The review presented in this Chapter has focused on numerical schemes which can be used to tailor micromechanical models for quasi-brittle fracture, including some material-specific non-linear features for modelling cementitious composites. In addition, numerical techniques have been reviewed for non-linear quasi-brittle fracture propagation with focus on strong discontinuities.

It is concluded that methods employing embedded strong discontinuity kinematics such as EFEM (Jefferson and Freeman, 2022; Linder and Armero, 2007; Oliver et al., 2003; Simo et al., 1993) can be used to tailor micromechanics-informed modelling techniques for quasi-brittle fracture propagation. While such ideas have been presented previously in the literature (see e.g. Linder and Raina (2013); Toro et al. (2014); Zhao et al. (2018)), a rigorous variational element-wise treatment of macro-fracture dofs coupled with *efficient* multiscale homogenisation schemes is still to be resolved. Challenges in such multiscale fracture methods are associated with computational efficiency and interaction across scales upon the occurrence of material instabilities (e.g. fracture onset and propagation) (Geers et al., 2017).

Quasi-static condensation procedures of macrocrack dofs in EFEM become attractive for coupling with multiscale fracture schemes, due to the immediate invariability of the number of global-level dofs to be solved in every incremental iterative procedure. In addition, variational principles could be used as one of the additional criteria needed to resolve the interaction across scales upon the nucleation of macroscopic fractures, rendering the numerical schemes to always follow a *minimum-energy failure mechanism* while multiscale features are active.

Finally, the micromechanical information transferred to the upper length-scale offers opportunities to improve macrocrack detection and tracking algorithms, since more accurate homogenised invariants as well as micromechanical state variables become available on the fly.

Chapter 3

Micromechanics & variational mechanics of quasi-brittle fracture

"Nothing takes place in the world whose meaning is not that of some maximum or minimum."
Leonhard Euler 1707 - 1783
Swiss Mathematical Physicist and pioneer of the Mechanics of elastic solids

3.1 Two-scale modelling in quasi-brittle solids

This chapter describes the theory used for computer implementation in this PhD. The theory is presented in a comprehensive and consistent form for (i) a micromechanical constitutive model in Section 3.2, and (ii) an element with embedded strong discontinuities to simulate macro-cracking in Section 3.3. Various versions of such mechanical components are in the literature, although a physically-sound and mathematically-rigorous unification of micro and macro concepts did not exist before the research undertaken in this PhD. These models in original form are described below:

- Section 3.2: A homogenised constitutive relationship which uses evolving directional diffuse microcracking as a means to simulate inelasticity in quasi-brittle cementitious solids (Jefferson and Bennett, 2010, 2007), and
- Section 3.3: A variationally-consistent element with embedded strong discontinuities able to simulate fracture propagation at the macro-scale (Freeman et al., 2020; Jefferson and Freeman, 2022).

The author implemented these micro- and macro-mechanical formulations in the in-house Fortran code Cardinal, and tested these components separately in Section 3.4. A consistent summary is presented in Section 3.5. The author proposed an original strategy of coupling these two-scale concepts exploiting a variational principle, which is detailed in Chapter 4 and validated in coupled form in Chapter 5.

3.2 Micromechanical constitutive homogenisation

3.2.1 Micromechanical view of Damage Mechanics

The concept of *damage* is explained after a one-dimensional *Hookean* model (De Borst et al., 2012). Consider a macroscopic bar, composed by horizontally aligned microscopic material fibres within a Representative Volume Element (RVE), i.e. at the material point **P**. The RVE volume is $\delta V = \delta A \times \delta x$ with cross sectional area δA populated with n_b aligned micro-bars as illustrated in Figure 3.1.

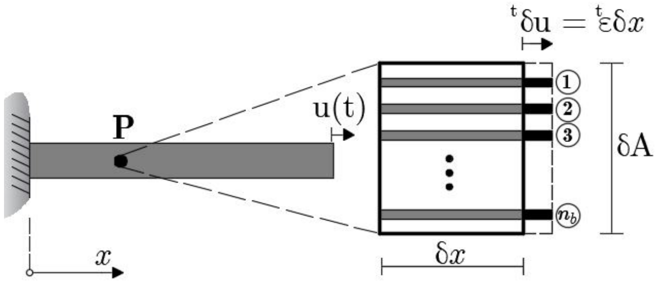

(a) Macro and micro scale geometry and boundary conditions

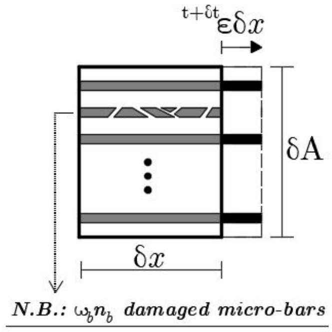

(b) Evolving material damage and boundary conditions at the micro-scale

Figure 3.1: One-dimensional bar with microstructure under uniaxial extension.

The macrostress is computed using the remaining active forces at the lower scale:

$$\text{Macrostress:} \quad \sigma_x = \frac{1}{\delta A}\Big(n_b - \omega_b n_b\Big)\delta F_{xi} = (1-\omega_b)\frac{n_b E_b A_b}{\delta A}\varepsilon_x = (1-\omega_b)\bar{E}\varepsilon_x \tag{3.1}$$

where $\omega_b = \frac{n_{bf}}{n_b} \geq 0$ is the number of *failed* micro-bars n_{bf}, normalised by the initial population of micro-bars n_b within an RVE, A_b is the area of each micro-bar, E_b and $\bar{E}$ stand for Young's modulus of each bar and for the homogenised crossed section in intact state. This theory is generalised for an isotropic media (Krajcinovic and Fonseka, 1981; Lemaitre and Chaboche, 1990), and reads as follows:

$$\text{Cauchy macrostress:} \quad \boldsymbol{\sigma} = (1-\omega)\boldsymbol{D}_e : \boldsymbol{\varepsilon} = \boldsymbol{D}_{sec} : \boldsymbol{\varepsilon} = \boldsymbol{D}_e : (\boldsymbol{\varepsilon} - \omega\boldsymbol{\varepsilon}) \tag{3.2}$$

where the scalar $\omega \in [0,1]$ represents the overall internal state variable, $\boldsymbol{\sigma}$ is the

Cauchy stress tensor, $\boldsymbol{D}_e$ is the elastic material stiffness tensor, $\boldsymbol{D}_{sec}(\omega)$ is the secant material stiffness tensor and $\boldsymbol{\varepsilon}$ is the strain tensor.

The damage mechanics concept can be expanded into a multi-plane framework, for which independent unloading-reloading conditions read as follows:

$$\left.\begin{array}{lr} \text{Scalar damage variable irreversibility:} & \dot{\omega}_i(\zeta_i) \geq 0 \\ \text{Damage surface:} & f_{d,i}(\boldsymbol{\varepsilon}, \zeta_i) \leq 0 \\ \text{Damage increase:} & f_{d,i}(\boldsymbol{\varepsilon}, \zeta_i) \cdot \dot{\omega}(\zeta_i) = 0 \end{array}\right\} \tag{3.3}$$

where the subscript $(\cdot)_i$ denotes the number of degradation plane, and ζ_i stands for an internal variable that memorises the deformation history.

3.2.2 Plasticity-enhancement in Damage Mechanics

The inelastic strains $\boldsymbol{\varepsilon}^p$ remain upon unloading in Computational Plasticity, opposed to what happens in damage-induced inelastic strains. Indeed, in standard Damage Mechanics the inelastic strains $\boldsymbol{\varepsilon}^p = \omega\boldsymbol{\varepsilon}$ vanish upon full unloading $(\boldsymbol{\varepsilon} \rightarrow 0)$(see Equation 3.2). This difference is apparent in the unloading reloading branch in the stress-strain space, and is illustrated in Figure 3.2. Such a plasticity component can improve the predictions in cyclic fracture problems in future research. The treatment of cyclic fracture problems escapes from the current PhD, since monotonic fracture is the focus.

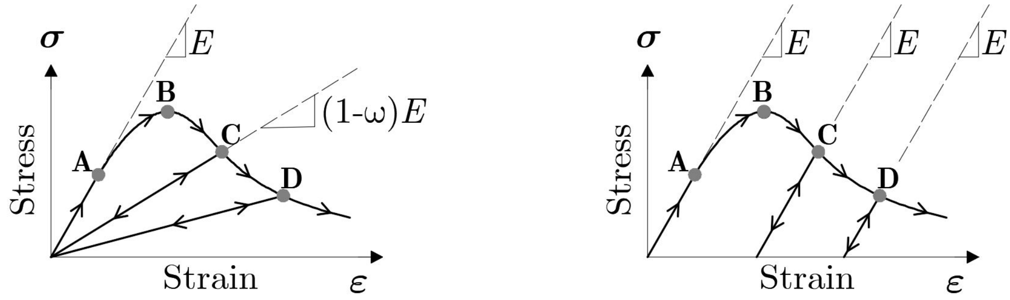

(a) Damage Mechanics

(b) Damage-Plasticity

Figure 3.2: Conceptual unloading-reloading stress-strain response under uniaxial conditions, with $\bar{E} = E$ being Young's modulus. Stages: A) elasticity limit, B) peak state, C) first unloading-reloading branch, D) second unloading-reloading branch.

The following section describes how microcracking sets are embedded in a Continuum, and a damage-informed version of this theory is presented for implementation in a Finite Element Framework.

3.2.3 Eshelby's equivalent inclusion method for embedded ellipsoidal microcracks

Consider an *infinite* solid body, under a far-field uniform stress $\boldsymbol{\sigma}^{\infty}$, with volume $\boldsymbol{\Omega} \equiv \mathrm{M}_{\Omega} \cup \Gamma_m$ and outward normal $\mathbf{n}_{\Omega}$, where M_{Ω} represents the volume of the *elastic* matrix and Γ_m stands for the volume of an embedded *stress-free* ellipsoidal microcrack within the domain $\left(x'_r/a_r\right)^2 + \left(x'_s/a_s\right)^2 + \left(x'_t/a_t\right)^2 \leq 1$, where the space $\{x'_r, x'_s, x'_t\}$ corresponds to the local coordinate system $\{\mathbf{r}, \mathbf{s}, \mathbf{t}\}$ of the microcrack with $\mathbf{t}$ being orthogonal to the plane containing $\mathbf{r}$ and $\mathbf{s}$ as shown in Figure 3.3.

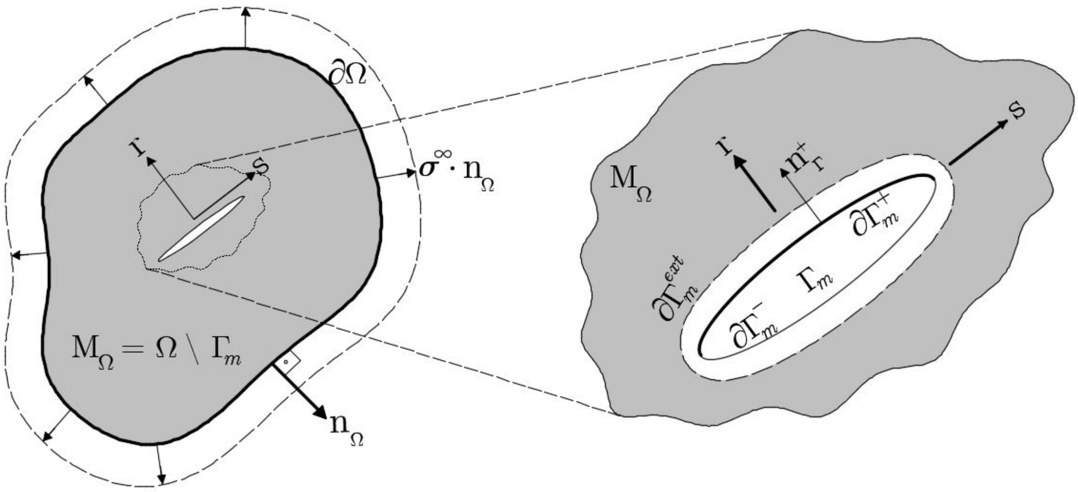

(a) Embedded ellipsoidal microcrack: macroscopic boundary conditions

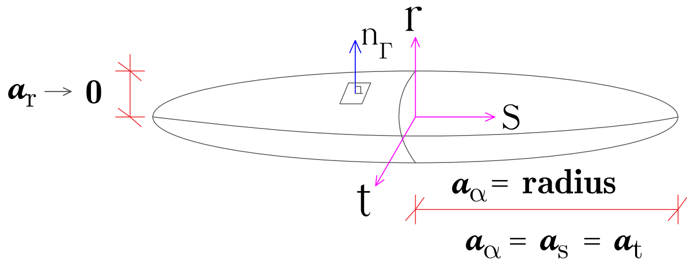

(b) Microcrack's local axes: constant radius a_α placed orthogonal to $\mathbf{r}$ gives a penny shape.

Figure 3.3: Infinite solid body, subjected to uniform stress field at the external boundary, with an embedded stress-free ellipsoidal microcrack.

The problem described in the previous paragraph and illustrated in Figure 3.3 is solved for the strain perturbations $\boldsymbol{\varepsilon}^{\Gamma_m}(x)$, i.e. the additional strains in the far-field due to microcracking as compared to the elastic solution with intact material, using the Equivalent Inclusion Method by Mura (1987). This method splits the problem into (i) a loaded fictitious domain $\boldsymbol{\Omega}$, and (ii) this same domain under the action of eigen-strains within the embedded ellipsoidal microcrack. Such a BVP (Eshelby, 1957, 1959) is defined as shown in Equation 3.4.

$$\begin{aligned}
&\mathrm{Div}[\boldsymbol{\sigma}^{\Gamma_m}(x)] = 0, && \forall x \in \Omega \\
&\boldsymbol{\sigma}^{\Gamma_m}(x) = \bar{\boldsymbol{D}}_e : (\boldsymbol{\varepsilon}^{\Gamma_m}(x) - \boldsymbol{\varepsilon}^*(x)), && \forall x \in \Omega \\
&\boldsymbol{\sigma}^{\Gamma_m}(x) \cdot \mathbf{n}_\Omega = 0, && \forall x \in \partial\Omega \\
&\boldsymbol{\varepsilon}^*(x) = \boldsymbol{\varepsilon}^*, && \forall x \in \Gamma_m \\
&\boldsymbol{\varepsilon}^*(x) = \mathbf{0}, && \forall x \in \Omega \setminus \Gamma_m
\end{aligned} \tag{3.4}$$

where the additional constraint $\boldsymbol{\sigma}^\infty + \boldsymbol{\sigma}^{\Gamma_m}(x) = 0$ applies in the microcrack domain Γ_m since it is stress-free, $\boldsymbol{\sigma}^{\Gamma_m}(x)$ stands for the stress field in the self-equilibrating domain, and $\boldsymbol{\varepsilon}^*$ is the eigen-strain which is constant within the ellipsoidal microcrack.

Elaboration on the Eshelby's interior point solution to that problem, aided by energy-based first principles (Mura, 1987), the microcrack opening displacement field $\left[\boldsymbol{u}_\alpha^{\Gamma_m}\right](x')$ and the perturbation of the macrostrain field $\boldsymbol{\varepsilon}_\alpha^{\Gamma_m}$ are derived in local coordinates:

$$\left.\begin{aligned}
\boldsymbol{\varepsilon}_\alpha^{\Gamma_m} \equiv \text{uniform} \quad &= \tfrac{1}{\|\Omega\|} \int_{\partial\Gamma_m} \left(\boldsymbol{u}_\alpha^{\Gamma_m}(x') \otimes \mathbf{n}_\Gamma(x')\right)^s d\boldsymbol{S} \\
&= \tfrac{1}{\|\Omega\|} \int_{\partial\Gamma_m^+} \left(\left[\boldsymbol{u}_\alpha^{\Gamma_m}\right](x') \otimes \mathbf{r}_\alpha\right)^s d\boldsymbol{S}
\end{aligned}\right\} \quad \forall x' \in \partial\Omega \tag{3.5}$$

$$\left[\boldsymbol{u}_\alpha^{\Gamma_m}\right](x') = \begin{pmatrix} {}^+u_r^{\Gamma_m}(x') -^- u_r^{\Gamma_m}(x') \\ {}^+u_s^{\Gamma_m}(x') -^- u_s^{\Gamma_m}(x') \\ {}^+u_t^{\Gamma_m}(x') -^- u_t^{\Gamma_m}(x') \end{pmatrix} = \frac{8(1-\bar{\upsilon}^2)}{\pi \bar{E}} \sqrt{a_\alpha^2 - (x'_s)^2 - (x'_t)^2} \begin{pmatrix} \sigma_{rr}^\infty \\ \frac{2}{2-\bar{\upsilon}} \sigma_{rs}^\infty \\ \frac{2}{2-\bar{\upsilon}} \sigma_{rt}^\infty \end{pmatrix}, \quad \forall x' \in \partial\Gamma_m \tag{3.6}$$

where $\bar{E}$ and $\bar{\upsilon}$ are the elastic constants of the undamaged Continuum.

Integration of the right-hand side term in Equation 3.5, using the microcrack opening displacement field in Equation 3.6 (Nemat-Nasser et al., 1996) gives:

$$\boldsymbol{\varepsilon}_\alpha^{\Gamma_m} = \mathscr{F}_\alpha \frac{16(1-\bar{\upsilon}^2)}{3\bar{E}} \begin{pmatrix} \bar{\sigma}_{rr} & \frac{1}{2-\bar{\upsilon}} \bar{\sigma}_{rs} & \frac{1}{2-\bar{\upsilon}} \bar{\sigma}_{rt} \\ & 0 & 0 \\ \text{symm} & & 0 \end{pmatrix} \quad \forall x' \in \partial\Omega \tag{3.7}$$

where $\mathscr{F}_\alpha = \mathscr{N}_\alpha a_\alpha^3$ is the crack density parameter by Budiansky and O'Connell (1976), $\mathscr{N}_\alpha$ is the number of microcracks per unit volume in the microcrazking zone α, and a_α is the radius of one microcrack, and here due to simplicity all the microcracks are regarded to have the same radius in the plane orthogonal to the collapsed axis, since the microcracks are considered as penny-shaped; note that given that the microcracking zones are *sufficiently* large, the volume-average Cauchy stress tensor $\bar{\boldsymbol{\sigma}}_L$ tends to approximate the far-field stress $\boldsymbol{\sigma}^{\infty}$.

3.2.4 Damage-informed microcracking-induced inelastic strain

A damage informed version of the local microcracking-induced inelastic strains in Equation 3.7 was presented in Jefferson and Bennett (2010, 2007):

$$\boldsymbol{\varepsilon}_{\alpha}^{\Gamma_m} = \frac{\omega_{\alpha}^{\mathrm{m}}}{1-\omega_{\alpha}^{\mathrm{m}}} \cdot \frac{1}{\bar{E}} \begin{pmatrix} \bar{\sigma}_{rr} & \frac{1}{2-\bar{\upsilon}}\bar{\sigma}_{rs} & \frac{1}{2-\bar{\upsilon}}\bar{\sigma}_{rt} \\ & 0 & 0 \\ \mathrm{symm} & & 0 \end{pmatrix} \quad \forall x' \in \partial\Omega \tag{3.8}$$

where $\omega_{\alpha}^{\mathrm{m}} = \omega_{\alpha}^{\mathrm{m}}(\zeta_{\alpha}^{\mathrm{m}})$ is a (local) scalar microcracking variable ($\omega_{\alpha}^{\mathrm{m}} \in [0,1]$), $\mathscr{F}_{\alpha} \approx \frac{3}{16(1-\bar{\upsilon}^2)}\frac{\omega_{\alpha}^{\mathrm{m}}}{1-\omega_{\alpha}}$ is computed phenomenologically using an equivalent strain $\zeta_{\alpha}^{\mathrm{m}}$, which depends on the deformation history.

N.B.: The Equation 3.8 replaces that of Equation 3.7 to allow a general deformation history to enable microcracking occurrence, including shear and normal deformation. Such form eases further derivations of a general micromechanical constitutive law and its material tangent.

For convenience in Finite Element formulations, the microcracking-induced inelastic strain $\boldsymbol{\varepsilon}_{\alpha}^{\Gamma_m}$ is defined in vector form $\boldsymbol{\varepsilon}_{\alpha}^{add}$ in local coordinates as follows:

$$\boldsymbol{\varepsilon}_{\alpha}^{add} = \frac{\omega_{\alpha}^{\mathrm{m}}}{1-\omega_{\alpha}^{\mathrm{m}}} \cdot \mathbf{C}_L^{3D} \cdot \mathbf{N}_{\sigma} \cdot \bar{\boldsymbol{\sigma}}, \quad \forall x' \in \partial\Omega \tag{3.9}$$

where $\boldsymbol{\varepsilon}_{\alpha}^{\Gamma_m} = [\varepsilon_{rr}^{\Gamma_m}, \gamma_{rs}^{\Gamma_m}, \gamma_{rt}^{\Gamma_m}]^{\mathrm{T}}$ is defined by the non-zero microcracking-induced inelastic components only, $\bar{\boldsymbol{\sigma}}_L = [\bar{\sigma}_{rr}, \bar{\sigma}_{rs}, \bar{\sigma}_{rt}]^{\mathrm{T}} = \mathbf{N}_{\sigma} \cdot \bar{\boldsymbol{\sigma}}$ is the resolved components of the Cauchy stress, $\mathbf{N}_{\sigma}$ is a rotation matrix (see Equation 3.16), and the local compliance is defined as follows:

$$\mathbf{C}_L^{3D} = \frac{1}{\bar{E}} \begin{pmatrix} 1 & 0 & 0 \\ 0 & \frac{2}{2-\bar{\upsilon}} & 0 \\ 0 & 0 & \frac{2}{2-\bar{\upsilon}} \end{pmatrix} \text{ in 3D}, \quad \text{or} \quad \mathbf{C}_L = \frac{1}{\bar{E}} \begin{bmatrix} 1 & 0 \\ 0 & \frac{2}{2-\bar{\upsilon}} \end{bmatrix} \text{ in 2D} \tag{3.10}$$

The next section treats the mechanical components used for homogenisation of the bulk domain in a cementitious composite, which can experience microcracking in multiple directions.

3.2.5 On computational homogenisation of Micromechanical solids with directional microcracks

Let the subdomain $\boldsymbol{\Omega}^{\mathrm{m}}$ be representative domain of the Micromechanical solid $\boldsymbol{\Omega}^{\mathrm{M}}$. In general, the Micromechanical solid may possess various micro-constituents, e.g. a solid matrix, aggregates and microcracks. For mathematical convenience the microcracks can be be idealised as penny-shaped in this framework. Originally, the matrix-aggregate mixture departs from an intact state with no microcracks. Directional microcrack nucleation is then considered along with the macroscopic deformation history as illustrated in Figure 3.4.

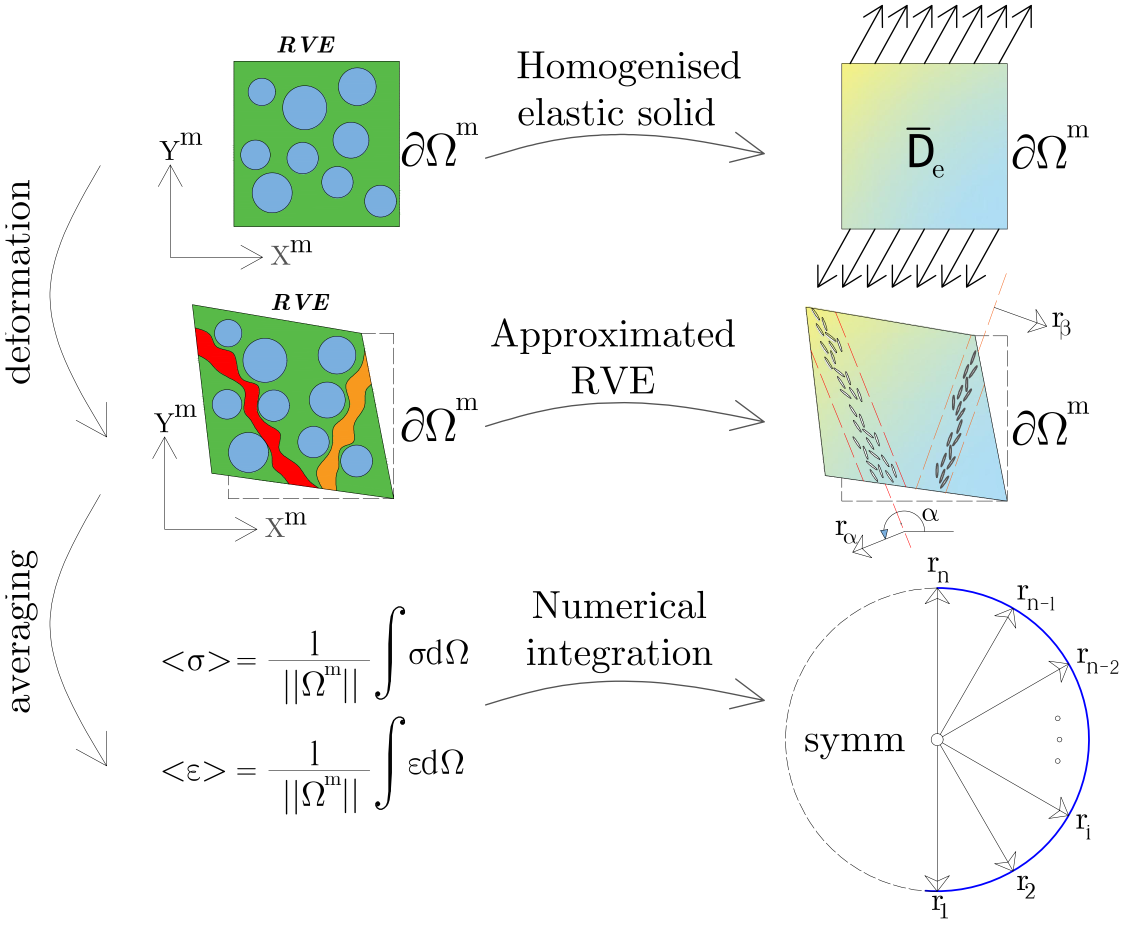

Figure 3.4: Sketch of homogenisation procedures for Micromechanical solids with directional diffuse microcracking within an RVE. Particularly, sets of degradation direction $\boldsymbol{\pi}_{\alpha}$ are used for numerical integration over the perimeter on a semi-circle.

An overall elasticity tensor $\bar{\boldsymbol{D}}_e$ is first defined for the matrix-aggregate mixture. This may be defined by either, (i) from the knowledge of elastic properties, volume fraction and orientation of the inclusion phase embedded in the solid matrix, see e.g. solutions for spherical aggregates in a cementitious matrix in Jefferson and Bennett (2010); Mihai and Jefferson (2011), or (ii) via calibration upon experimental data on incipient (elastic) macroscopic response. A summary of homogenisation strategies for two-phase composites (elastic matrix with spherical inclusions) was presented by Zimmerman (1991), with discussions including the Mori-Tanaka method (Mori and Tanaka, 1973), self-consistent method (Hill, 1963; Nemat-Nasser et al., 1996) and the differential scheme (McLaughlin, 1977), which are shown to follow theoretical limits as defined by Hashin-Shtrikman bounds (Hashin and Shtrikman, 1961). Strategy (ii) is adopted for the numerical examples in this PhD, without invalidation of key research findings.

In a subsequent homogenisation step, directional microcracking is then accounted for (Jefferson and Bennett, 2010, 2007; Mihai and Jefferson, 2011). Hence, the overall constitutive response of the Micromechanical solid in Cartesian reference is derived as follows, including the effect of various sets of aligned microcracks:

$$\bar{\boldsymbol{\sigma}} = \bar{\boldsymbol{D}}_e : \big(\underbrace{\bar{\boldsymbol{\varepsilon}} - \bar{\boldsymbol{\varepsilon}}^{\Gamma_m}}_{\bar{\boldsymbol{\varepsilon}}^e}\big) \tag{3.11}$$

$$\bar{\boldsymbol{\varepsilon}}^{\Gamma_m} = \frac{1}{2\pi} \int_{\theta=0}^{\theta=2\pi} \int_{\psi=0}^{\psi=\frac{\pi}{2}} \Big[\boldsymbol{N}_{\varepsilon}^{-1}(\boldsymbol{r}_{\alpha}) : \boldsymbol{\varepsilon}_{\alpha}^{\Gamma_m}(\bar{\boldsymbol{\varepsilon}}) sin(\psi) \Big] d\psi d\theta \tag{3.12}$$

where the homogenised inelastic strain $\bar{\boldsymbol{\varepsilon}}^{\Gamma_m}$, due to directional microcracking, is taken as the volume average for all the sets of aligned microcraking zones. Conveniently, Equation 3.12 can be degraded into an integral over the perimeter of a semi-circle in the case of two-dimensional analysis, and a simplified expression for the microcracking-induced strains reads as $\bar{\boldsymbol{\varepsilon}}^{\Gamma_m} = \frac{1}{\pi} \int_{\text{semi-circle}} \Big[\boldsymbol{N}_{\varepsilon}^{-1}(\boldsymbol{r}_{\alpha}) : \boldsymbol{\varepsilon}_{\alpha}^{\Gamma_m}(\bar{\boldsymbol{\varepsilon}}) \Big] dl$.

Note that a discrete number of degradation directions $\mathrm{n}_{int}^{\mathrm{m}}$ is used in the two-dimensional integration scheme (Equation 3.12). A convergence check was performed by the author on the integration rule adopted for practical problems in a standard FE framework at the beginning of the PhD, and it has been found that for most cases, an adequate number of degradation directions is $\mathrm{n}_{int}^{\mathrm{m}} = 21$. The array of resolved components of the inelastic strain $\boldsymbol{\varepsilon}_{\alpha}^{\Gamma_m}(\bar{\boldsymbol{\varepsilon}})$ comes after an analysis of distributed microcracking using stress-free penny-shaped ellipsoids as shown in Equation 3.8.

Following re-arrangement of the transformation operators into matrix form, the additional strains in Cartesian space $\boldsymbol{N}_{\varepsilon}^{-1}(\boldsymbol{r}_{\alpha}) : \boldsymbol{\varepsilon}_{\alpha}^{\Gamma_m}(\bar{\boldsymbol{\varepsilon}})$, due to a single set of aligned penny-shaped microcracks, are computed in a vector form as $\mathbf{N}_{\sigma}^{\mathrm{T}}\boldsymbol{\varepsilon}_{\alpha}^{\Gamma_m} = \mathbf{N}_{\sigma}^{\mathrm{T}}\frac{\omega_{\alpha}^{\mathrm{m}}}{1-\omega_{\alpha}^{\mathrm{m}}}\mathbf{C}_L\mathbf{N}_{\sigma}\bar{\boldsymbol{\sigma}}$.

Furthermore, using Equation 3.8 into Equations 3.11 and 3.12, an expression for the overall secant stiffness operator $\bar{\boldsymbol{D}}_{sec}$ is defined as follows:

$$\bar{\boldsymbol{\sigma}} = \bar{\boldsymbol{D}}_{sec} : \bar{\boldsymbol{\varepsilon}} = \left(\bar{\boldsymbol{D}}_e^{-1} + \bar{\boldsymbol{C}}^{\Gamma_m}(\bar{\boldsymbol{\varepsilon}})\right)^{-1} : \bar{\boldsymbol{\varepsilon}} \tag{3.13}$$

$$\bar{\boldsymbol{C}}^{\Gamma_m}(\bar{\boldsymbol{\varepsilon}}) = \frac{1}{2\pi}\left\{\int_{\theta=0}^{\theta=2\pi}\int_{\psi=0}^{\psi=\frac{\pi}{2}}\left[\boldsymbol{N}_{\varepsilon}^{-1}(\boldsymbol{r}_{\alpha}) : \frac{\omega_{\alpha}^{\mathrm{m}}(\bar{\boldsymbol{\varepsilon}})}{1-\omega_{\alpha}^{\mathrm{m}}(\bar{\boldsymbol{\varepsilon}})}\boldsymbol{C}_L : \boldsymbol{N}_{\sigma}(\boldsymbol{r}_{\alpha}) sin(\psi)\right]d\psi d\theta\right\} \tag{3.14}$$

where $\bar{\boldsymbol{C}}^{\Gamma_m}(\bar{\boldsymbol{\varepsilon}})$ is the constitutive additional compliance tensor. Note that the local compliance tensor $\boldsymbol{C}_L$ remains constant for every degradation direction assuming isotropic elastic behaviour of the matrix-aggregate mixture in an intact state.

For convenience in Finite Element formulations, the local compliance $\boldsymbol{C}_L$ is used in the form presented in Equation 3.10; and the isotropic elasticity material stiffness operator for the homogenised matrix-aggregate mixture $\bar{\boldsymbol{D}}_e$ gets the following matrix form under plane-stress settings:

$$\bar{\mathbf{D}}_e = \frac{\bar{E}_{am}}{1-\bar{\upsilon}_{am}^2}\begin{bmatrix} 1 & \bar{\upsilon}_{am} & 0 \\ \bar{\upsilon}_{am} & 1 & 0 \\ 0 & 0 & (1-\bar{\upsilon}_{am})/2 \end{bmatrix} \tag{3.15}$$

where $\bar{E}_{am}$ and $\bar{\upsilon}_{am}$ are the homogenised elastic constants of the aggregate-matrix mixture in intact state.

Note that the transformation operators to convert stress and strain Cartesian components into local reference in a 2D setting (see 3D version of rotation matrices in Jefferson (2003a,b)) take a matrix form for finite element computations as follows:

$$\left.\begin{aligned} \bar{\boldsymbol{\varepsilon}}_L = \mathbf{N}_{\varepsilon}\bar{\boldsymbol{\varepsilon}} &= \begin{bmatrix} r_{\alpha,x}^2 & r_{\alpha,y}^2 & r_{\alpha,x}r_{\alpha,y} \\ 2r_{\alpha,x}s_{\alpha,x} & 2r_{\alpha,y}s_{\alpha,y} & r_{\alpha,y}s_{\alpha,x}+r_{\alpha,x}s_{\alpha,y} \end{bmatrix}\bar{\boldsymbol{\varepsilon}} \\ \bar{\boldsymbol{\sigma}}_L = \mathbf{N}_{\sigma}\bar{\boldsymbol{\sigma}} &= \begin{bmatrix} r_{\alpha,x}^2 & r_{\alpha,y}^2 & 2r_{\alpha,x}r_{\alpha,y} \\ r_{\alpha,x}s_{\alpha,x} & r_{\alpha,y}s_{\alpha,y} & r_{\alpha,y}s_{\alpha,x}+r_{\alpha,x}s_{\alpha,y} \end{bmatrix}\bar{\boldsymbol{\sigma}} \end{aligned}\right\} \tag{3.16}$$

where $\boldsymbol{r}_{\alpha} = [r_{\alpha,x}, r_{\alpha,y}, 0]^{\mathrm{T}}$, and $\boldsymbol{s}_{\alpha} = [s_{\alpha,x}, s_{\alpha,y}, 0]^{\mathrm{T}}$ are in-plane unit vectors, perpendicular to each other, used to rotate strain/ stress vectors into a local space.

3.2.6 Standard microcracking growth law of $\omega_\alpha^{\mathrm{m}}$

The directional degradation of the scalar variables $\omega_\alpha^{\mathrm{m}}(\bar{\boldsymbol{\varepsilon}})$ is computed in standard form using an exponential law (Jefferson and Bennett, 2007) as follows:

$$\omega_\alpha^{\mathrm{m}}(\zeta_\alpha^{\mathrm{m}}(\bar{\boldsymbol{\varepsilon}})) = 1 - \frac{\varepsilon_t^{\mathrm{m}}}{\zeta_\alpha^{\mathrm{m}}} \exp\left[-c_s \frac{\zeta_\alpha^{\mathrm{m}} - \varepsilon_t^{\mathrm{m}}}{\zeta_{max}^{\mathrm{m}} - \varepsilon_t^{\mathrm{m}}}\right], \quad \zeta_\alpha^{\mathrm{m}} \geq \varepsilon_t^{\mathrm{m}} \tag{3.17}$$

where $\omega_\alpha^{\mathrm{m}} \in (0,1)$ is a direction-dependent microcracking scalar variable ($\omega_\alpha^{\mathrm{m}} = 0$ for no microcracking, and $\omega_\alpha^{\mathrm{m}} = 1$ for substantial microcracking), which is a function of an equivalent microcracking state variable $\zeta_\alpha^{\mathrm{m}}(\bar{\boldsymbol{\varepsilon}})$ defined as a strain measure; c_s is a dimensionless softening constant typically in the range ≈ 5 to 8; $\varepsilon_t^{\mathrm{m}} = f_t^{\mathrm{m}}/\bar{E}_{am}$ is the uniaxial tensile strain for first micromechanical damage under plane stress conditions, and ζ_{max}^{m} defines the ultimate strain at which the microcracking zone is fully populated with aligned microcracks.

The standard microcracking growth law is made dependent on the element characteristic length h_{el} by setting $\zeta_{max}^{\mathrm{m}} = u_{max}/h_{el}$ when the relationship is used in a standard Finite Element program, i.e. by using a crack band approach (Bažant and Oh, 1983); with u_{max} being the maximum displacement discontinuity that can be observed due to fracture at the macroscopic level before collapse, when a specimen is subjected to such uniaxial action.

Note that this is a standard growth law since the scalar $\omega_\alpha^{\mathrm{m}}$ depends only on the maximum experienced $\zeta_\alpha^{\mathrm{m}}$, opposed to a nonlinear and smooth unloading-reloading branch using a Smooth-Unloading-Reloading response (Alnaas and Jefferson, 2016).

3.2.7 Relationship between macroscopic strain $\bar{\boldsymbol{\varepsilon}}$ and the equivalent microcracking strain $\zeta_\alpha^{\mathrm{m}}(\bar{\boldsymbol{\varepsilon}})$

The equivalent microcracking state variable $\zeta_\alpha^{\mathrm{m}}$ in each microcracking direction is computed as a function of the resolved strain components $\bar{\boldsymbol{\varepsilon}}_L(\bar{\boldsymbol{\varepsilon}})$. This equivalent microcracking strain $\zeta_\alpha^{\mathrm{m}}$ is interpreted as the magnitude of an equivalent uniaxial tensile strain needed to make the local microcracking surface to grow up to its current 'size', in the (local) shear - normal strain space.

The microcracking surface is defined in Equation 3.18, and loading / unloading conditions are expressed in Equation 3.19 as follows:

$$\Phi_\alpha(\bar{\boldsymbol{\varepsilon}}_L, \zeta_\alpha^{\mathrm{m}}) = \frac{\bar{\varepsilon}_{rr}}{2}\left[1 + \left(\frac{\mu_\varepsilon}{r_\varepsilon}\right)^2\right] + \frac{1}{2r_\varepsilon^2}\sqrt{\left(r_\varepsilon^2 - \mu_\varepsilon^2\right)^2 \bar{\varepsilon}_{rr}^2 + 4r_\varepsilon^2\left(\bar{\gamma}_{rs}^2 + \bar{\gamma}_{rt}^2\right)} - \zeta_\alpha^{\mathrm{m}} = \zeta_{\alpha,eff}^{\mathrm{m}} - \zeta_\alpha^{\mathrm{m}} \tag{3.18}$$

$$\dot{\zeta}_\alpha^{\mathrm{m}} \geq 0, \quad \Phi_\alpha \cdot \dot{\zeta}_\alpha^{\mathrm{m}} = 0, \quad \Phi_\alpha \leq 0 \tag{3.19}$$

where $\boldsymbol{\Phi}_\alpha = 0$ and $\dot{\boldsymbol{\Phi}}_\alpha = 0$ is satisfied when an updated homogenised strain $\bar{\boldsymbol{\varepsilon}}$ enforces the equivalent microcracking state variable $\zeta_\alpha^{\mathrm{m}}$ to grow in the current microcraking direction, the resolved strain tensor $\bar{\boldsymbol{\varepsilon}}_L = \boldsymbol{N}_\varepsilon(\boldsymbol{r}_\alpha) : \bar{\boldsymbol{\varepsilon}}$ is computed using the transformation tensor $\boldsymbol{N}_\varepsilon$, $\bar{\gamma}_L^2 = \bar{\gamma}_{rs}^2 + \bar{\gamma}_{rt}^2$ is the in-plane resultant engineering shear strain occurring in a plane defined by the microcraking plane normal $\boldsymbol{r}_\alpha$, $\mu_\varepsilon = \mu_\sigma \frac{\bar{E}_{am}}{\bar{G}_{s,am}}$ and $r_\varepsilon = r_\sigma \frac{\bar{E}_{am}}{\bar{G}_{s,am}}$ with r_σ being the cohesion-to-tensile strength ratio and μ_σ being the (residual) shear-to-normal stress ratio, and $\bar{G}_{s,am} = \bar{E}_{am}/(2(1+\bar{\upsilon}_{am}))$ being the secant shear modulus.

The local microcracking surface resembles a hyperbolic variation of a smoothed Mohr-Coulomb type surface, although presented in the local shear - normal strain space (Jefferson, 2003a,b). The local microcracking surface is illustrated in Figure 3.5.

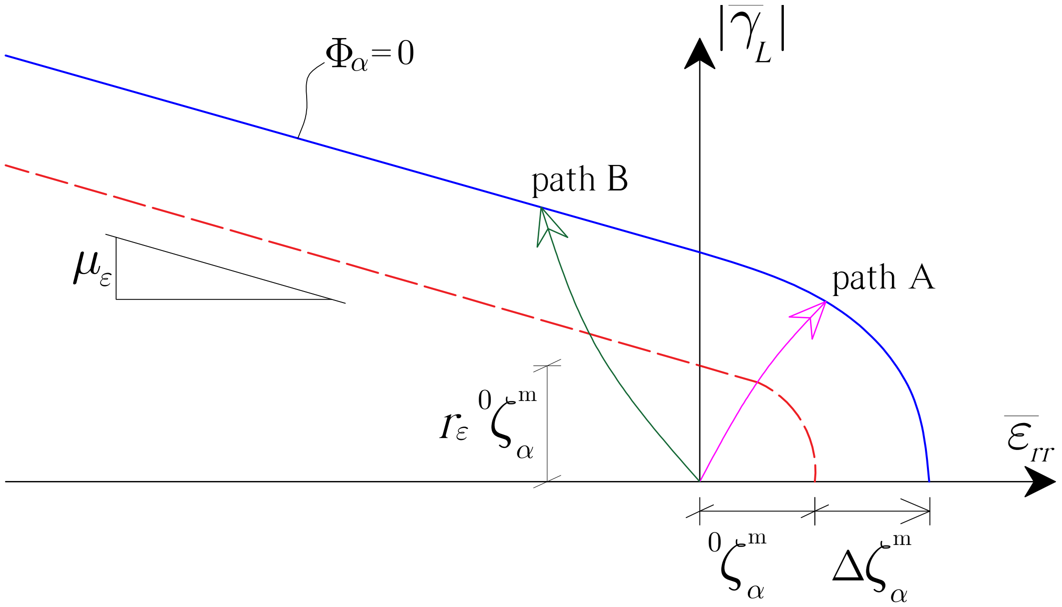

Figure 3.5: Microcracking surface in local strain space. Microcracking growth is illustrated as induced by different path-types: path A is dominated by combined shear-tensile strain state, and path B by combined shear-compressive strain state.

This sketch shows the capabilities of such microcracking surface to capture material directional degradation ($\Delta\zeta_\alpha^{\mathrm{m}} > 0$, $\omega_\alpha^{\mathrm{m}} > 0$, and in turn $\Delta\mathscr{F}_\alpha > 0$) under various (local) strain paths. Degradation-inducing deformation paths include those such as path A for combined shear-tension deformation, and path B for shear-compression deformation. Nevertheless, proportional paths would not induce degradation if these were parallel or with a gradient less than the asymptotic residual ratio μ_ε.

3.2.8 Material tangent stiffness for Micromechanical continua

By differentiating the homogenised constitutive law for a Micromechanical solid (Equation 3.13), the tangent operator $\bar{\mathbf{D}}_{tan}$ is derived as follows:

$$\bar{\mathbf{D}}_{tan} = (\mathbf{I} + \bar{\mathbf{D}}_e \bar{\mathbf{C}}^{\Gamma_m})^{-1} \bar{\mathbf{D}}_e \left[\mathbf{I} - \sum^{\mathrm{n}^{\mathrm{m}}_{int}} \frac{w^{\mathrm{num}}_{\alpha}}{(1-\omega^{\mathrm{m}}_{\alpha})^2} \frac{\partial \omega^{\mathrm{m}}_{\alpha}}{\partial \zeta^{\mathrm{m}}_{\alpha}} \frac{\partial \zeta^{\mathrm{m}}_{\alpha}}{\partial \zeta^{\mathrm{m}}_{\alpha,\mathrm{eff}}} \mathbf{N}^{\mathrm{T}}_{\sigma} \mathbf{C}_L \mathbf{N}_{\sigma} \bar{\boldsymbol{\sigma}} \left\{ \frac{\partial \zeta^{\mathrm{m}}_{\alpha,\mathrm{eff}}}{\partial \bar{\boldsymbol{\varepsilon}}_L} \right\}^{\mathrm{T}} \mathbf{N}_{\varepsilon} \right] \tag{3.20}$$

where $w^{\mathrm{num}}_{\alpha}$ is the set of coefficients for numerical integration, based on $\mathrm{n}^{\mathrm{m}}_{int}$ integration directions over the perimeter of a semi-circle for two-dimensional analysis whereas full 3D implementation requires integration over a hemisphere (Stroud, 1971); regarding plane-stress setting the three partial derivatives are defined, at first $\frac{\partial \omega^{\mathrm{m}}_{\alpha}}{\partial \zeta^{\mathrm{m}}_{\alpha}} = \left(1 - \omega^{\mathrm{m}}_{\alpha}\right) \left[\frac{1}{\zeta^{\mathrm{m}}_{\alpha}} + \frac{c_s}{u_{max}/h_{el} - \varepsilon^{\mathrm{m}}_t} \right]$, secondly, the gradient $\frac{\partial \zeta^{\mathrm{m}}_{\alpha,\mathrm{eff}}}{\partial \bar{\boldsymbol{\varepsilon}}_L}$ is evaluated in closed form (see Equation 3.21), and thirdly, it is noted that the gradient $\partial \zeta^{\mathrm{m}}_{\alpha} / \partial \zeta^{\mathrm{m}}_{\alpha,\mathrm{eff}}$ is discontinuous, which implies a tangent operator is used once state-variables are sufficiently settled within the non-linear iterative procedure (see comment box below and description of existing cases for the derivative).

N.B.: A secant stiffness $\bar{\mathbf{D}}_{sec}$ (see Equation 3.13) is used instead of the micromechanics-derived consistent tangent $\bar{\mathbf{D}}_{tan}$, for the first few global iterations to detect which degradation sets show further microcrack growth.

The two existing cases for computing the gradient $\partial \zeta^{\mathrm{m}}_{\alpha} / \partial \zeta^{\mathrm{m}}_{\alpha,\mathrm{eff}}$ are shown below:

i. $\partial \zeta^{\mathrm{m}}_{\alpha} / \partial \zeta^{\mathrm{m}}_{\alpha,\mathrm{eff}} = 0$ in case the effective equivalent strain $\zeta^{\mathrm{m}}_{\alpha,eff}$ is under the microcracking surface, i.e. $\boldsymbol{\Phi}_{\alpha} < 0$ (see Equations 3.18 and 3.19).

ii. $\partial \zeta^{\mathrm{m}}_{\alpha} / \partial \zeta^{\mathrm{m}}_{\alpha,\mathrm{eff}} = 1$ in case the effective equivalent strain $\zeta^{\mathrm{m}}_{\alpha,eff}$ is on the microcracking surface, i.e. $\boldsymbol{\Phi}_{\alpha} = 0$ (see Equations 3.18 and 3.19).

Further development of chain rules in the Equation 3.18 provides the partial derivatives of the effective micro-state $\zeta^{\mathrm{m}}_{\alpha,\mathrm{eff}}$ with respect to the resolved strain components $\bar{\boldsymbol{\varepsilon}}_L = [\bar{\varepsilon}_{rr}, \bar{\gamma}_{rs}]^{\mathrm{T}} = \mathbf{N}_{\varepsilon} \bar{\boldsymbol{\varepsilon}}$, and these are presented below:

$$\left.\begin{aligned} \partial \zeta^{\mathrm{m}}_{\alpha,\mathrm{eff}} / \partial \bar{\boldsymbol{\varepsilon}}_L &= [\partial \zeta^{\mathrm{m}}_{\alpha,\mathrm{eff}} / \partial \bar{\varepsilon}_{rr} \ , \ \partial \zeta^{\mathrm{m}}_{\alpha,\mathrm{eff}} / \partial \bar{\gamma}_{rs}]^{\mathrm{T}} \\ \partial \zeta^{\mathrm{m}}_{\alpha,\mathrm{eff}} / \partial \bar{\varepsilon}_{rr} &= \tfrac{1}{2} \left[1 + \left(\mu_{\varepsilon} / r_{\varepsilon} \right)^2 \right] + \left[(r^2_{\varepsilon} - \mu^2_{\varepsilon})^2 \bar{\varepsilon}_{rr} \right] / \left[2 r^2_{\varepsilon} \sqrt{(r^2_{\varepsilon} - \mu^2_{\varepsilon})^2 \bar{\varepsilon}^2_{rr} + 4 r^2_{\varepsilon} \bar{\gamma}^2_{rs}} \right] \\ \partial \zeta^{\mathrm{m}}_{\alpha,\mathrm{eff}} / \partial \bar{\gamma}_{rs} &= \left[2 \bar{\gamma}_{rs} \right] / \left[\sqrt{(r^2_{\varepsilon} - \mu^2_{\varepsilon})^2 \bar{\varepsilon}^2_{rr} + 4 r^2_{\varepsilon} \bar{\gamma}^2_{rs}} \right] \end{aligned}\right\} \tag{3.21}$$

3.3 Formulation of an element with embedded strong discontinuities (EFEM)

The next subsections describe the basic components of an element with embedded strong discontinuities alone, presented with consistent notation from Freeman et al. (2020); Jefferson and Freeman (2022). The coupling of this embedded strong discontinuity approach with a Micromechanics framework, able to induce microcracking at the bulk domain as presented in Section 3.2, is described in Section 4.1.

3.3.1 Governing equation of BVP for elastic solid with embedded discontinuities

Let the body $\boldsymbol{\Omega}^e$ in Figure 3.6 be constituted by an elastic solid with an embedded strong discontinuity. The BVP is solved for the displacement field $\mathbf{u} : \boldsymbol{\Omega}^e \times (0, T] \rightarrow \mathbb{R}^2$, where $t \in (0, T]$. Considering the mechanical response to be quasi-static, equilibrium gives:

$$\left.\begin{array}{lcr}
\text{1 Momentum balance:} & \mathbf{Div}[\boldsymbol{\sigma}] + \boldsymbol{b} = \mathbf{0} & \text{in } \boldsymbol{\Omega}^e \\
\text{2 Constitutive relation:} & \boldsymbol{\sigma} = \boldsymbol{D}_e : \boldsymbol{\varepsilon} & \text{in } \boldsymbol{\Omega}^e \backslash \Gamma \\
\text{3 Kinematic relation:} & \boldsymbol{\varepsilon} = \nabla^s \mathbf{u} = \nabla^s (\mathbf{u}_c + H_\Omega(\mathbf{x}) \otimes [|\mathbf{u}|]) & \text{in } \boldsymbol{\Omega}^e \backslash \Gamma \\
\text{4 Traction continuity:} & \boldsymbol{\sigma}_{\Omega^+} \cdot \mathbf{n}_\Gamma^+ + \boldsymbol{\sigma}_{\Omega^-} \cdot \mathbf{n}_\Gamma^- = \mathbf{0} & \text{on } \partial\Gamma \\
\text{5 Traction equilibrium:} & \boldsymbol{\sigma}_{\Omega^+} \cdot \mathbf{n}_\Gamma^+ + \mathbf{t}_{\Gamma^+} = \mathbf{0} & \text{on } \partial\Gamma \\
\text{6 Natural boundary condition:} & \boldsymbol{\sigma} \cdot \mathbf{n}_{\partial\Omega_\sigma^e} - \check{\mathbf{t}} = \mathbf{0} & \text{on } \partial\boldsymbol{\Omega}_\sigma^e \\
\text{7 Essential boundary condition:} & \mathbf{u} = \check{\mathbf{u}} & \text{on } \partial\boldsymbol{\Omega}_u^e
\end{array}\right\} \tag{3.22}$$

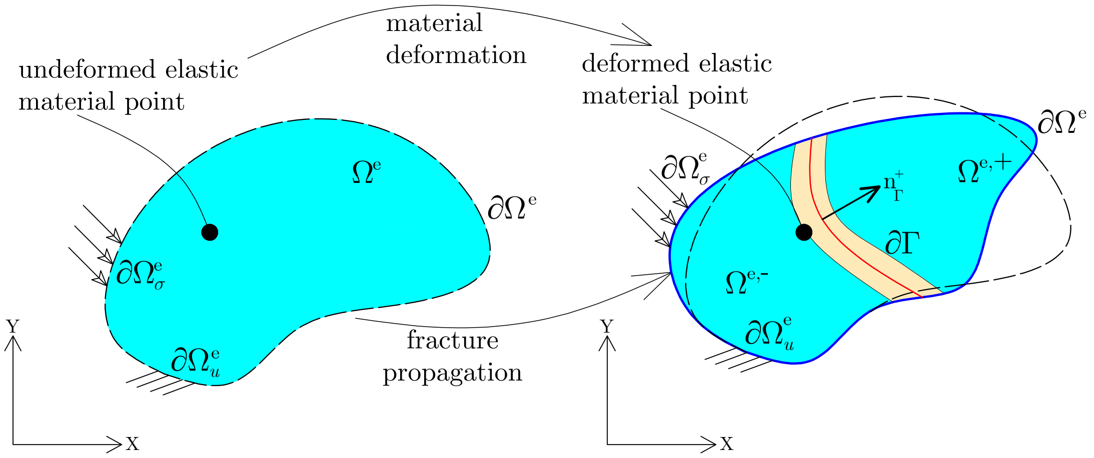

Figure 3.6: BVP of fracturing quasi-brittle solids that possess elastic bulk.

where Equation 3.22-1 stands for momentum balance, $\mathbf{Div}[\cdot]$ being the divergence operation and $\boldsymbol{b}$ corresponds to body forces per unit volume. Equation 3.22-2 provides the constitutive equation, where the material constants $\boldsymbol{E}$ and $\boldsymbol{\upsilon}$ define the elasticity tensor $\boldsymbol{D_e}$ for the isotropic Continuum. Equation 3.22-3 yields the kinematic relations considering embedded strong discontinuities, $H_{\Omega}(\mathbf{x} \in \boldsymbol{\Omega}^e)$ being a Heaviside-type function in $\boldsymbol{\Omega}^e$, $\mathbf{u}_c$ and $[|\mathbf{u}|]$ being the continuous and discontinuous displacement components. Notice that though $H_{\Omega}(\mathbf{x} \in \boldsymbol{\Omega}^e) \otimes [|\mathbf{u}|](\mathbf{x})$ imposes a discontinuity in the displacement field $\mathbf{u}$, the field $[|\mathbf{u}|](\mathbf{x})$ itself is continuous over the domain $\boldsymbol{\Omega}^e$. It is clarified that the Heaviside-type function $H_{\Omega}(\mathbf{x} \in \boldsymbol{\Omega}^e)$ is scalar valued, while $[|\mathbf{u}|] : \boldsymbol{\Omega}^e \times (0, T] \rightarrow \mathbb{R}^2$, where $t \in (0, T]$, hence, the product $H_{\Omega}(\mathbf{x} \in \boldsymbol{\Omega}^e) \otimes [|\mathbf{u}|](\mathbf{x})$ is admissible and renders a first-order array. More details on embedded strong discontinuity kinematics as adopted here (Freeman et al., 2020), is described in the Section 3.3.3. Equation 3.22-4 enforces traction continuity in the bulk across a propagating crack surface. Equation 3.22-5 ensures there is traction equilibrium between an embedded crack band and the adjacent bulk. Equation 3.22-6 provides the natural (stress/traction) boundary condition and Equation 3.22-7 gives the essential (displacement) boundary condition.

3.3.2 Degrees of Freedom (dofs) associated with an embedded localisation band

Three dofs are introduced in an embedded localisation band $\partial\Gamma$, and they are cast in the vector $\mathbf{W} = [u_{rc}, u_{sc}, \alpha_c]^{\mathrm{T}}$ as illustrated in Figure 3.7.

where the vector $\mathbf{W}$ defines the total displacement discontinuity occurring at the centre of the embedded localisation band, with u_{rc} being the normal aperture, u_{sc} stands for the tangential relative displacement and α_c represents the relative rotation between positive and negative macrocrack surfaces, all three components given in local coordinates.

Note that the embedded localisation band shows zero thickness in the Finite Element representation, although it possesses a virtual thickness for computations of local tractions $\mathbf{t}'_{\Gamma^+}(\mathbf{x}' \text{ on } \partial\Gamma)$ and further details are in Section 3.3.6.

Additive decomposition is employed over the crack relative displacement vector $\mathbf{W} = \mathbf{W}^e + \widehat{\mathbf{W}}$, with $\mathbf{W}^e$ and $\widehat{\mathbf{W}}$ being the elastic and inelastic components, respectively. The displacement associated with the rigid body motion $[|\mathbf{u}|]$ over $\boldsymbol{\Omega}^+$, used for kinematic enhancement at the element-level upon fracture, is solely a function of the inelastic component $\widehat{\mathbf{W}}$. The inelastic component of $\mathbf{W}$ is derived from the

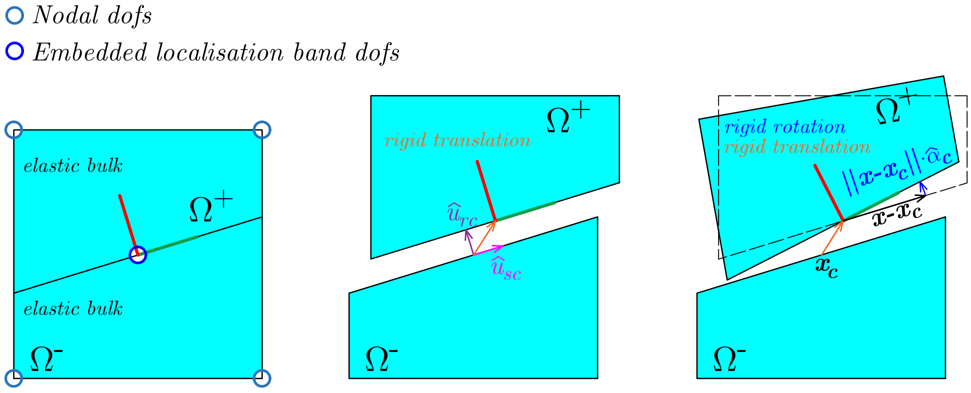

Original configuration

Rigid translation due to small deformation

Rigid rotation due to small deformation

Figure 3.7: Four-noded element for failure analysis assuming embedded strong-discontinuity kinematics: local axis convention and dofs (left); crack opening and sliding (centre), and combined rotational-translational relative displacement (right).

definition of the equivalent force of the localisation band $\mathbf{F}_{\text{ck}}$ (see Equation 3.40), and reads as follows:

$$\widehat{\mathbf{W}} = (\mathbf{I} - (\mathbf{K}_\Gamma^e)^{-1}\mathbf{K}_\Gamma) \cdot \mathbf{W} = \hat{\mathbf{I}} \cdot \mathbf{W} \tag{3.23}$$

where $\mathbf{K}_\Gamma$ and $\mathbf{K}_\Gamma^e$ are the equivalent stiffness matrices for the embedded localisation band, and these matrices are defined in Equations 3.41 and 3.42 (see Section 3.3.6); and the matrix $\hat{\mathbf{I}}$ that transforms the total vector $\mathbf{W}$ into its inelastic component $\widehat{\mathbf{W}}$ is defined as $\hat{\mathbf{I}} = (\mathbf{I} - (\mathbf{K}_\Gamma^e)^{-1}\mathbf{K}_\Gamma)$ with $\mathbf{I}$ being the identity matrix.

Hence, upon updates of the crack relative displacement vector $\mathbf{W}$, the displacement component $[|\mathbf{u}|](\mathbf{x} \in \boldsymbol{\Omega})$, which is associated with the rigid body motion due to fracture, is computed as follows:

$$[|\mathbf{u}|](\mathbf{x}) = \mathbf{T}_w(\mathbf{x}) \cdot \hat{\mathbf{I}} \cdot \mathbf{W} = \mathbf{T}_w(\mathbf{x}) \cdot \widehat{\mathbf{W}}, \quad \text{in } \boldsymbol{\Omega} \tag{3.24}$$

where $\mathbf{T}_w(\mathbf{x} \in \boldsymbol{\Omega})$ stands for the transformation matrix that computes small-strain rigid body motion due to fracture, and it is given by:

$$\mathbf{T}_w(\mathbf{x}) = \left[\begin{array}{c:c:c} \{\mathbf{r}_\Gamma\}_{(1)} & \{\mathbf{r}_\Gamma^\perp\}_{(1)} & \{\boldsymbol{t}_{op} \times (\mathbf{x} - \mathbf{x}_{\text{ck}})\}_{(1)} \\ \hdashline \{\mathbf{r}_\Gamma\}_{(2)} & \{\mathbf{r}_\Gamma^\perp\}_{(2)} & \{\boldsymbol{t}_{op} \times (\mathbf{x} - \mathbf{x}_{\text{ck}})\}_{(2)} \end{array}\right] \tag{3.25}$$

with $\mathbf{r}_\Gamma = -\mathbf{n}_\Gamma^+$, $\mathbf{r}_\Gamma \cdot \mathbf{r}_\Gamma^\perp = 0$, $\mathbf{r}_\Gamma^\perp$ is a unit vector in-plane to the $x - y$ space, $\boldsymbol{t}_{op} \times \mathbf{r}_\Gamma^\perp = \mathbf{r}_\Gamma$, $\boldsymbol{t}_{op}$ is the unit vector pointing towards out of the page, and $\mathbf{x}_{\text{ck}}$ stands for the Cartesian coordinates of the centre of the embedded localisation band. Note that only the first two components from the assembling vectors $\{\cdot\}_{(1)}$ and $\{\cdot\}_{(2)}$ are embedded into $\mathbf{T}_w(\mathbf{x})$, i.e. those within the x-y space, although these vectors are more generally defined in $\mathbb{R}^3$.

3.3.3 On embedded strong discontinuity kinematics in solids

Let the elastic body $\boldsymbol{\Omega}^e$ being fully cut by an embedded discontinuity $\boldsymbol{\Gamma}$. In a Finite Element setting, a subdomain $\boldsymbol{\Omega} \subset \boldsymbol{\Omega}^e$ is defined such that $\boldsymbol{\Omega} = \boldsymbol{\Omega}^+ \cup \boldsymbol{\Omega}^-$. The embedded crack band possesses zero thickness in the Finite Element domain, although it presents a virtual thickness h_{ca} for traction-separation computations, which is often taken as band that is a few times thicker the size of the coarse aggregate, and it is mostly used as a numerical parameter that is equivalent to a fraction of the element length h_{el}. When cracking is detected, the strain tensor is enhanced to account for the rigid body translation and rotation of the positive part of the body $\boldsymbol{\Omega}^+$. In this regard, the displacement field $\mathbf{u}$ is separated into continuous and discontinuous parts, i.e. $\mathbf{u} = \mathbf{u}_c + H_\Omega \otimes [|\mathbf{u}|]$ in $\boldsymbol{\Omega}$. The jump function is defined as $H_\Omega(\mathbf{x}) = 1$ in $\boldsymbol{\Omega}^+$, and $H_\Omega(\mathbf{x}) = 0$ in $\boldsymbol{\Omega}^-$, and its effects as kinematic enhancement is illustrated in Figure 3.8.

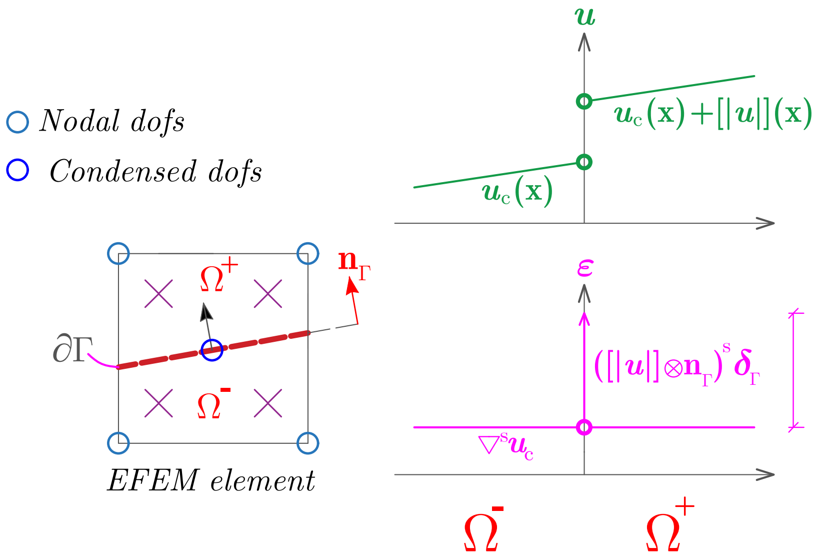

Figure 3.8: Illustration of kinematic enhancement effects on displacement and strain fields at the element level in elastic solids as it is used in EFEM.

Following elaborations on the enhanced kinematics, the strain tensor is defined by a regular part in the whole domain $\mathbf{\Omega}$, and by an unbounded part at the discontinuity (Freeman et al., 2020; Simo et al., 1993):

$$\boldsymbol{\varepsilon} = \nabla^s \mathbf{u} = \underbrace{\nabla^s \mathbf{u}_c}_{\text{regular}} + \underbrace{\left([|\mathbf{u}|] \otimes (\delta_\Gamma \otimes \mathbf{n}_\Gamma)\right)^s}_{= \mathbf{0}\text{ , only unbounded in }\Gamma} + H_\Omega \otimes \underbrace{\nabla^s [|\mathbf{u}|]}_{\approx \mathbf{0}}, \quad \text{in } (\mathbf{\Omega}^+ \cup \mathbf{\Omega}^-)\backslash\Gamma \tag{3.26}$$

where $\delta_\Gamma(\mathbf{x}) \otimes \mathbf{n}_\Gamma = \nabla H_\Omega(\mathbf{x})$, $\delta_\Gamma(\mathbf{x})$ stands for the Dirac delta function. Hence, the strain in the elastic bulk domain is taken as the symmetric part of the continuous displacement gradient $\boldsymbol{\varepsilon} = \nabla^s \mathbf{u}_c$.

The current implementation assumes a small strain setting, and the gradient of the displacement component due to fracture $\nabla[|\mathbf{u}|] \to \mathbf{0}$ vanishes. Particularly, the current method links $[|\mathbf{u}|]$ (in Cartesian reference) to an inelastic deformation component of the embedded localisation band $\widehat{\mathbf{W}}$ (see Equation 3.23).

In addition, element shape functions and a way to compute deformation gradients (Equation 3.26), at Gauss Points in the bulk domain, are described in Sections 3.3.4 and 3.3.5.

3.3.4 Standard interpolation of continuous fields and associated gradients

The interpolation of smooth fields is carried out using iso-parametric elements. In this context, it is highlighted that the displacement field $\mathbf{u}$ is discontinuous upon fracture, and therefore, special treatment needs to be taken for the interpolation of displacements at the element-level. This deviates from standard FEM implementations, in which the primary field (e.g. nodal displacement $\mathbf{u}$) is interpolated directly using shape functions.

The challenge of deriving the displacement field for the continuous part of an element arrives, since the overall displacement field $\mathbf{u}^{\text{el}}$ for the fracturing solid is discontinuous. Therefore, for every global update of the displacement field $\mathbf{u}^{\text{el}}$ various possible continuous displacement fields can occur due to iterating values of $\mathbf{W}$ (see definition of crack relative displacement in Section 3.3.2), which converge to a minimum energy solution at the element-level.

The purpose of this subsection is to give the essential FE interpolation and mapping theory required for the description of the strong discontinuity element. The remainder of the theory considered standard can be found in traditional textbooks

(De Borst et al., 2012; Hinton and Owen, 1979). In this research, shape functions assume bi-linear interpolation over the domain of 4-noded quadrilateral elements, while integrations over the element domain $\mathbf{\Omega}\backslash\mathbf{\Gamma}$ are done using 2 by 2 Gauss Point rules.

Note that given the nodal coordinates $\mathbf{x}^{\text{el}} = [x_{n1}, y_{n1}, x_{n2}, y_{n2}, x_{n3}, y_{n3}, x_{n4}, y_{n4}]^{\text{T}}$ and the continuous displacement $\mathbf{u}_c^{\text{el}} = [u_{c,x1}, u_{c,y1}, u_{c,x2}, u_{c,y2}, u_{c,x3}, u_{c,y3}, u_{c,x4}, u_{c,y4}]^{\text{T}}$, the interpolation of the position and that of the continuous displacement field are:

$$\left.\begin{aligned} \mathbf{x}(\xi,\eta) &= \begin{bmatrix} N_1 & 0 & N_2 & 0 & N_3 & 0 & N_4 & 0 \\ 0 & N_1 & 0 & N_2 & 0 & N_3 & 0 & N_4 \end{bmatrix} \mathbf{x}^{\text{el}} \\ \mathbf{u}_c(\xi,\eta) &= \begin{bmatrix} N_1 & 0 & N_2 & 0 & N_3 & 0 & N_4 & 0 \\ 0 & N_1 & 0 & N_2 & 0 & N_3 & 0 & N_4 \end{bmatrix} \mathbf{u}_c^{\text{el}} \end{aligned}\right\} \tag{3.27}$$

$$\left.\begin{aligned} N_1 &= \tfrac{1}{4}(1-\xi)\cdot(1-\eta) \\ N_2 &= \tfrac{1}{4}(1+\xi)\cdot(1-\eta) \\ N_3 &= \tfrac{1}{4}(1+\xi)\cdot(1+\eta) \\ N_4 &= \tfrac{1}{4}(1-\xi)\cdot(1+\eta) \end{aligned}\right\} \tag{3.28}$$

where ξ and η are the Gaussian coordinates; N_i stand for the shape functions; $\mathbf{x}(\xi,\eta)$ and $\mathbf{u}_c(\xi,\eta)$ are the interpolated vectorial position and the interpolated continuous field. This iso-parametric interpolation is illustrated in Figure 3.9.

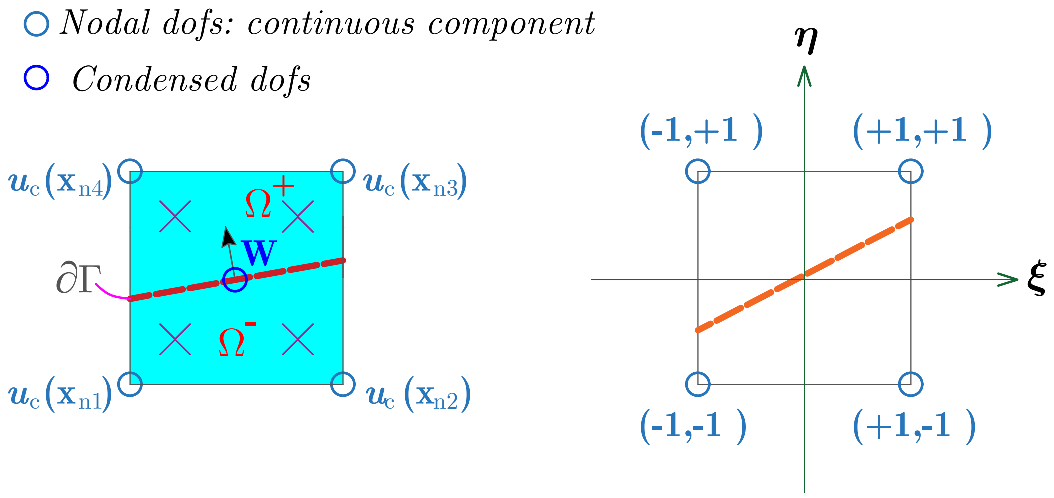

EFEM element in Euclidean domain

EFEM element in Gaussian domain

Figure 3.9: Illustration of interpolation for 'continuous' displacement field in an iso-parametric 4-noded quadrilateral element with an embedded strong discontinuity.

Note that the computation of Cartesian gradients of shape functions, i.e. $\partial N_i/\partial x$ and $\partial N_i/\partial y$, involves the use of the Jacobian of the space transformation $\mathbf{J}$. The Jacobian is derived using chain rules over the shape functions with respect to Euclidean and Gaussian spaces (De Borst et al., 2012; Hinton and Owen, 1979), and they read as follows:

$$\left.\begin{array}{ll}\text{Jacobian of the space transformation:} & \mathbf{J} = \begin{bmatrix} \frac{\partial x}{\partial \xi} & \frac{\partial y}{\partial \xi} \\ \\ \frac{\partial x}{\partial \eta} & \frac{\partial y}{\partial \eta} \end{bmatrix} \\ \\ \text{Cartesian derivatives of shape functions:} & \begin{Bmatrix} \frac{\partial N_i}{\partial x} \\ \\ \frac{\partial N_i}{\partial y} \end{Bmatrix} = \mathbf{J}^{-1} \cdot \begin{Bmatrix} \frac{\partial N_i}{\partial \xi} \\ \\ \frac{\partial N_i}{\partial \eta} \end{Bmatrix} \end{array}\right\} \tag{3.29}$$

where the mapping between Euclidean and Gaussian spaces is admissible for any convex shapes for the 4-noded elements.

3.3.5 Deformation gradients in elements with embedded strong discontinuity

The strain tensor $\boldsymbol{\varepsilon} = \nabla^s \mathbf{u}_c$ (Equation 3.26) in the Micromechanical bulk is defined as the symmetric part of the continuous displacement gradient, which is expressed in vector form $\boldsymbol{\varepsilon} = \{\nabla^s \mathbf{u}_c\}_{\text{vec}} = [\varepsilon_{xx}, \varepsilon_{yy}, 2 \cdot \varepsilon_{xy}]^{\mathrm{T}} = [\varepsilon_{xx}, \varepsilon_{yy}, \gamma_{xy}]^{\mathrm{T}}$ as follows:

$$\boldsymbol{\varepsilon} = \mathbf{B}\mathbf{u}_c^{\text{el}} = \begin{bmatrix} \partial_x N_1 & 0 & \partial_x N_2 & 0 & \partial_x N_3 & 0 & \partial_x N_4 & 0 \\ 0 & \partial_y N_1 & 0 & \partial_y N_2 & 0 & \partial_y N_3 & 0 & \partial_y N_4 \\ \partial_y N_1 & \partial_x N_1 & \partial_y N_2 & \partial_x N_2 & \partial_y N_3 & \partial_x N_3 & \partial_y N_4 & \partial_x N_4 \end{bmatrix} \mathbf{u}_c^{\text{el}}, \quad \text{in } \Omega\backslash\Gamma \tag{3.30}$$

where $\boldsymbol{\varepsilon} = [\varepsilon_{xx}, \varepsilon_{yy}, \gamma_{xy}]^{\mathrm{T}}$ in $\Omega\backslash\Gamma = (\Omega^- \cup \Omega^+)\backslash\Gamma$, with $\gamma_{xy} = 2\varepsilon_{xy}$ being the engineering shear strain, and $\mathbf{B}$ being the strain-displacement matrix. Note that the 'continuous' component of the displacement field at each node is expressed as follows (see Section 3.3.3):

$$\mathbf{u}_{c,\text{inode}} = \mathbf{u}_{\text{inode}} - H_\Omega(\mathbf{x}_{\text{inode}}) \otimes [|\mathbf{u}|]_{inode}(\mathbf{x}_{\text{inode}}) \tag{3.31}$$

where the term $H_{\Omega}(\mathbf{x}_{\text{inode}}) \otimes [|\mathbf{u}|]_{inode}(\mathbf{x}_{\text{inode}})$ is non-zero for the positive part of the domain $\mathbf{\Omega}^{+}$ only, and it is equivalent to $H_{\Omega}(\mathbf{x}_{\text{inode}}) \otimes \mathbf{T}_{w}(\mathbf{x}_{\text{inode}}) \cdot \hat{\mathbf{I}} \cdot \mathbf{W}$ (see Equation 3.24).

Therefore, the array of nodal continuous displacement can be evaluated as follows:

$$
\begin{aligned}
\mathbf{u}_{c}^{\text{el}} &= \left\{ \begin{array}{c} \mathbf{u}_{c,\text{node1}} \\ \hdashline \mathbf{u}_{c,\text{node2}} \\ \hdashline \vdots \\ \hdashline \mathbf{u}_{c,\text{nnode}} \end{array} \right\} = \left\{ \begin{array}{c} \mathbf{u}_{\text{node1}} \\ \hdashline \mathbf{u}_{\text{node2}} \\ \hdashline \vdots \\ \hdashline \mathbf{u}_{\text{nnode}} \end{array} \right\} - \left\{ \begin{array}{c} H_{\Omega}(\mathbf{x}_{\text{node1}}) \otimes [|\mathbf{u}|]_{node1}(\mathbf{x}_{\text{node1}}) \\ \hdashline H_{\Omega}(\mathbf{x}_{\text{node2}}) \otimes [|\mathbf{u}|]_{node2}(\mathbf{x}_{\text{node2}}) \\ \hdashline \vdots \\ \hdashline H_{\Omega}(\mathbf{x}_{\text{nnode}}) \otimes [|\mathbf{u}|]_{nnode}(\mathbf{x}_{\text{nnode}}) \end{array} \right\} \\
&= \left\{ \begin{array}{c} \mathbf{u}_{\text{node1}} \\ \hdashline \mathbf{u}_{\text{node2}} \\ \hdashline \vdots \\ \hdashline \mathbf{u}_{\text{nnode}} \end{array} \right\} - \left\{ \begin{array}{c} H_{\Omega}(\mathbf{x}_{\text{node1}}) \otimes \mathbf{T}_{w}(\mathbf{x}_{\text{node1}}) \cdot \hat{\mathbf{I}} \cdot \mathbf{W} \\ \hdashline H_{\Omega}(\mathbf{x}_{\text{node2}}) \otimes \mathbf{T}_{w}(\mathbf{x}_{\text{node2}}) \cdot \hat{\mathbf{I}} \cdot \mathbf{W} \\ \hdashline \vdots \\ \hdashline H_{\Omega}(\mathbf{x}_{\text{nnode}}) \otimes \mathbf{T}_{w}(\mathbf{x}_{\text{nnode}}) \cdot \hat{\mathbf{I}} \cdot \mathbf{W} \end{array} \right\}
\end{aligned} \tag{3.32}
$$

Using Equation 3.32 in Equation 3.30, and following re-arrangement of matrix-vector multiplication into blocks, the computation of strains at the Gauss Points in the bulk domain is conveniently re-formulated:

$$
\begin{aligned}
\boldsymbol{\varepsilon} &= \textstyle\sum^{nnode} \mathbf{B}_{inode} \cdot \mathbf{u}_{c,\text{inode}} & , \quad \text{in } \mathbf{\Omega} \backslash \mathbf{\Gamma} \\
&= \textstyle\sum^{nnode} \mathbf{B}_{inode}\left(\mathbf{u}_{\text{inode}} - H_{\Omega} \otimes [|\mathbf{u}|]_{inode}\right) & , \quad \text{in } \mathbf{\Omega} \backslash \mathbf{\Gamma} \\
&= \mathbf{B} \cdot \mathbf{u}^{\text{el}} - \left(\textstyle\sum^{nnode} \mathbf{B}_{inode} H_{\Omega} \otimes \mathbf{T}_{w}(\mathbf{x}_{\text{inode}}) \right) \hat{\mathbf{I}} \mathbf{W} & , \quad \text{in } \mathbf{\Omega} \backslash \mathbf{\Gamma}
\end{aligned} \tag{3.33}
$$

further simplification is obtained by defining the matrices $\widehat{\mathbf{M}}$ and $\mathbf{M}$:

$$
\left.\begin{aligned}
\widehat{\mathbf{M}} &= \mathbf{M} \hat{\mathbf{I}} \\
\mathbf{M} &= \textstyle\sum^{nnode} \mathbf{B}_{inode} H_{\Omega} \otimes \mathbf{T}_{w}(\mathbf{x}_{\text{inode}})
\end{aligned}\right\} \tag{3.34}
$$

where $\hat{\mathbf{I}}$ and $\mathbf{T}_{w}$ are defined in the Equations 3.23 and 3.25, and the node-based strain-displacement matrix $\mathbf{B}_{inode}$ gets defined as follows:

$$
\mathbf{B}_{inode} = \begin{bmatrix} \partial_{x} N_{inode} & 0 \\ 0 & \partial_{y} N_{inode} \\ \partial_{y} N_{inode} & \partial_{x} N_{inode} \end{bmatrix} \tag{3.35}
$$

Finally, Equation 3.33 becomes into an expression for the strains in the bulk domain, upon the nodal displacement field $\mathbf{u}^{\text{el}}$ and the vector $\mathbf{W}$ being known at the element level:

$$\boldsymbol{\varepsilon} = \mathbf{B} \cdot \mathbf{u}^{\text{el}} - \widehat{\mathbf{M}} \cdot \mathbf{W} \tag{3.36}$$

Note that strain computations are done in Gauss Points for integration over the element domain $\boldsymbol{\Omega} \backslash \Gamma$, as well as at a Dummy central Gauss Point to ease the detection of fracture occurrence as illustrated in Figure 3.10.

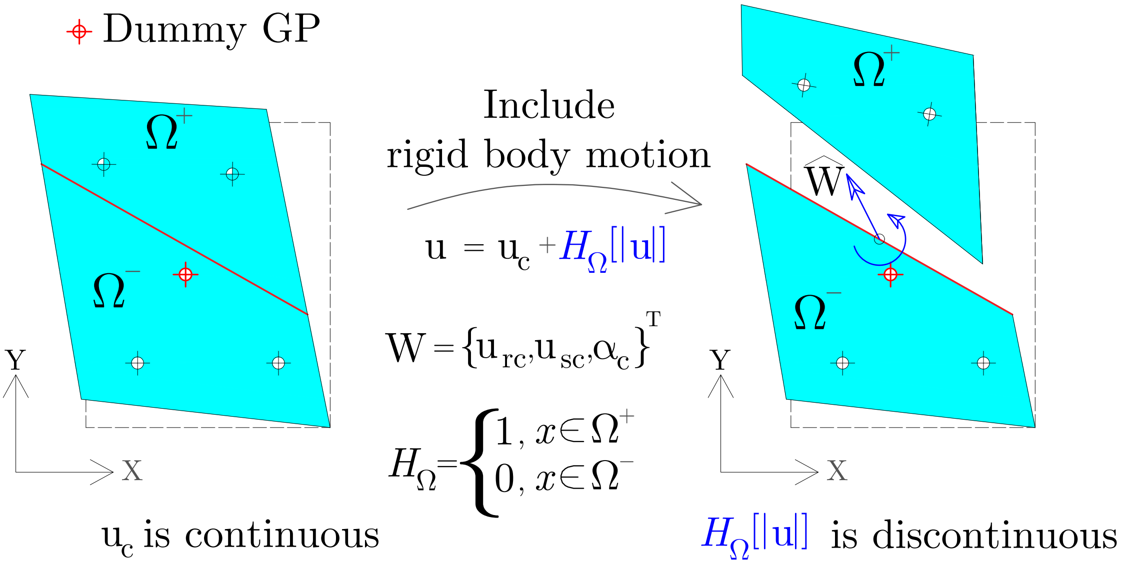

Figure 3.10: Kinematic enhancement activation in a fractured solid due to inelastic deformation of the embedded localisation band. The continuum deformation is often tracked in a dummy Gauss Point at the centre of the element for fracture detection.

3.3.6 Local tractions in embedded strong discontinuities and the equivalent crack force

The tractions $\mathbf{t}'_{\Gamma}(x' \text{ on } \partial\Gamma)$ occurring along the embedded localisation band are related to the damage evolution of $\omega(\zeta, \zeta_{eff})$ at the crack surface and the local displacement jump $\Delta\mathbf{u}_{\Gamma}$ (Freeman et al., 2020):

$$\mathbf{t}'_{\Gamma^+}(x') = \frac{1 - \omega(x')}{h_{ca}} \begin{bmatrix} E & 0 \\ 0 & E/(2(1+\upsilon)) \end{bmatrix} \Delta\mathbf{u}_{\Gamma}(x'), \quad \forall x' \in \partial\Gamma \tag{3.37}$$

where $\mathbf{t}'_{\Gamma \mathrm{M}+}(x')$ is the local traction on the macrocrack surface in contact with the positive bulk domain $\boldsymbol{\Omega}^{+}$; the damage evolution of $\omega(\zeta, \zeta_{eff})$ follows a Smooth-Unloading-Reloading method (see Section 3.3.7) with the equivalent cracking relative displacement in effective and maximum experienced version being $\zeta_{eff}(\Delta \mathbf{u}_{\Gamma}(\mathbf{W}))$ and ζ (see Section 3.3.8); h_{ca} is the virtual thickness of the localisation band; and the local discontinuity jump $\Delta \mathbf{u}_{\Gamma}(\mathbf{W})$ being defined in Equation 3.38.

$$\left.\begin{array}{rcl} \Delta \mathbf{u}_{\Gamma}(x') & = & \boldsymbol{\Lambda} \cdot \mathbf{W}, \quad \forall x' \in \partial\Gamma \\ \\ \boldsymbol{\Lambda} & = & \begin{bmatrix} 1 & 0 & l(x' \text{ on } \partial\Gamma) \\ \\ 0 & 1 & 0 \end{bmatrix} \end{array}\right\} \tag{3.38}$$

where l is the relative position along the embedded localisation from its centre.

Note that the actual local displacement jump occurring at the Finite Element is equivalent to the inelastic part of $\Delta \mathbf{u}_{\Gamma}(x')$, and this inelastic jump is associated with the rigid body motion on the positive part of the domain $\boldsymbol{\Omega}^{+}$. The local inelastic displacement jump $\Delta \widehat{\mathbf{u}}_{\Gamma}(x')$ is shown in Equation 3.39.

$$\Delta \widehat{\mathbf{u}}_{\Gamma}(x') = \boldsymbol{\Lambda} \cdot \widehat{\mathbf{W}}, \quad \forall x' \in \partial\Gamma \tag{3.39}$$

where the inelastic vector $\widehat{\mathbf{W}}$ is taken as in Equation 3.23. An illustration of the response of the embedded localisation band is presented in Figure 3.11, which emphasises the effects of the deformation of the embedded localisation band on local tractions and on the rigid body motion transferred to the positive part $\boldsymbol{\Omega}^{+}$.

Furthermore, upon numerical integration of the work done by local tractions along the embedded localisation band, following some re-arrangement of terms, the work-conjugated equivalent force vector $\mathbf{F}_{\mathrm{ck}}$, is derived to be:

$$\mathbf{F}_{\mathrm{ck}} = \left[F_{rc}, F_{sc}, M_c\right]^{\mathrm{T}} = \mathbf{K}_{\Gamma}\mathbf{W} = \mathbf{K}^{e}_{\Gamma}\{\mathbf{W} - \widehat{\mathbf{W}}\}, \quad \text{at centre of } \partial\Gamma \tag{3.40}$$

$$\mathbf{K}_{\Gamma} = \frac{E \cdot t_g}{h_{ca}} \left[\begin{array}{c:c:c} \int_{\partial\Gamma}(1-\omega)dl & 0 & \int_{\partial\Gamma}(1-\omega)l dl \\ \hdashline & \int_{\partial\Gamma} \frac{1-\omega}{2(1+\upsilon)} dl & 0 \\ \hdashline \text{symm} & & \int_{\partial\Gamma}(1-\omega)l^2 dl \end{array}\right] \tag{3.41}$$

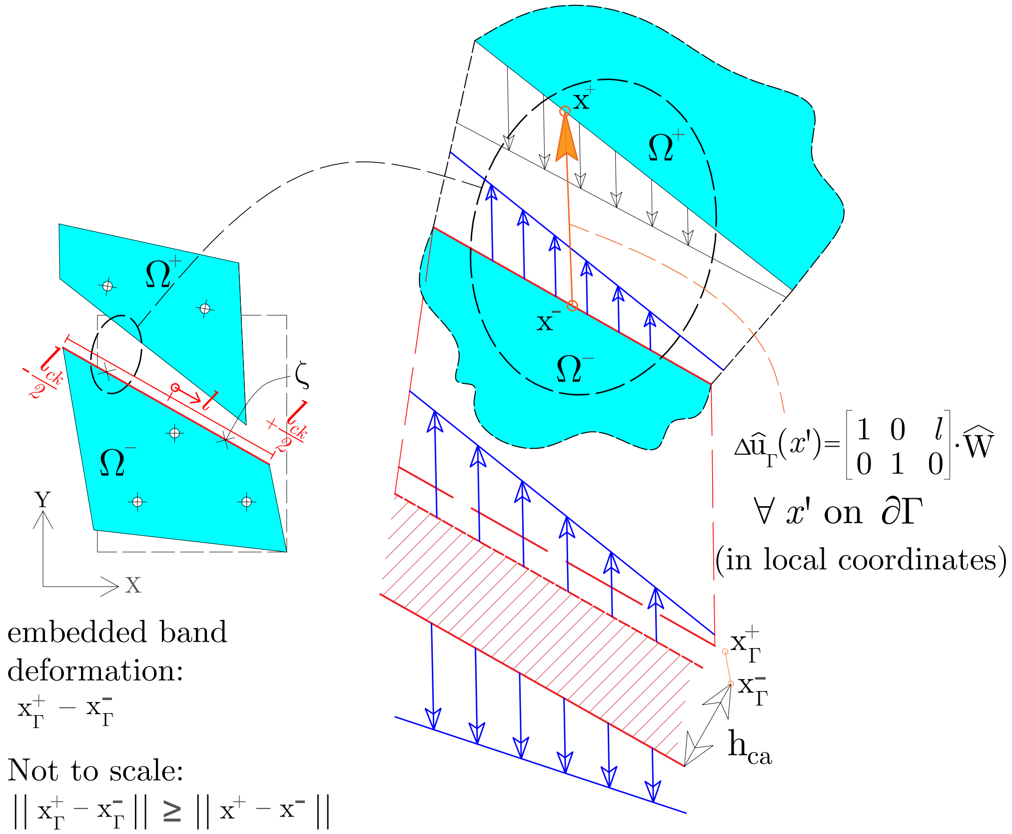

Figure 3.11: Illustration of embedded localisation band concept in elastic continua, and the effect of its inelastic deformation $\widehat{\mathbf{W}}$ on the local displacement discontinuity $\boldsymbol{\Delta}\widehat{\mathbf{u}}_\Gamma(x')$ at the fracture surface $\partial\Gamma$.

$$\mathbf{K}_\Gamma^e = \frac{E \cdot t_g}{h_{ca}} \left[\begin{array}{c:c:c} \int_{\partial\Gamma} dl & 0 & \int_{\partial\Gamma} l dl \\ \hdashline & \int_{\partial\Gamma} \frac{1}{2(1+\upsilon)} dl & 0 \\ \hdashline \text{symm} & & \int_{\partial\Gamma} l^2 dl \end{array} \right] \tag{3.42}$$

where t_g is the out-of-page thickness, $l \in [-l_{\rm ck}/2, l_{\rm ck}/2]$ is the local axis for numerical integration, conveniently located at the crack centre and aligned with the crack propagation direction.

Note that $\mathbf{F}_{\rm ck} = \mathbf{K}_\Gamma \mathbf{W}$ (Equation 3.40) is the work-conjugate to the increment of inelastic crack relative displacement $\delta\widehat{\mathbf{W}}$.

It is noted that the transformation of the local linear space into a "Gaussian" linear space $\xi_{ck} = l \cdot \frac{2}{l_{ck}}$, within $l \in (-l_{ck}/2, l_{ck}/2)$, gives a scalar Jacobian determinate, i.e. $\det(J)_{\rm ck} = \frac{l_{ck}}{2}$. Therefore, the integral operations over the crack length are obtained using Equation 3.43.

$$\begin{aligned}\int_{\partial\Gamma}(\cdot)dl &= \int_{\xi_{ck}\in(-1.0,1.0)}(\cdot)\det(J)_{ck}d\xi_{ck}\\ &= \tfrac{l_{ck}}{2}\cdot\int_{\xi_{ck}\in(-1.0,1.0)}(\cdot)d\xi_{ck}\end{aligned}\qquad(3.43)$$

where a Gaussian 2-point rule integration is used along an embedded macrocrack.

3.3.7 Damage evolution along cracks using Smooth-Unloading-Reloading functions

The SUR degradation law $\omega(\zeta,\zeta_{eff})$ employs an equivalent traction-separation response curve under uniaxial conditions, similar to the degradation law for directional microcracking previously described in Section 3.2.6. The smooth nature of the function was selected to aid convergence of the overall nonlinear solution process (Jefferson and Mihai, 2015). The unloading-reloading branch is updated for the first few iterations of a numerical step but is then frozen after a selected iteration number (**itfix**). In practice, **itfix** = 3 seems to be adequate for most problems. In the nonlinear solution scheme, a secant stiffness matrix is used in the first few iterations and then a tangent stiffness is used once the iteration number exceeds **itfix**. The tangent is based on the tangent of the unloading-reloading function. This means that the stiffness matrix is always positive definite. The SUR degradation evolution law for embedded localisation bands is illustated in Figure 3.12 and reads as follows:

$$\omega(\zeta,\zeta_{eff}) = 1-\frac{\mathrm{t}^n_{\Gamma,ur}(\zeta,\zeta_{eff,\mathrm{aux}})}{E\left[\zeta_{eff,\mathrm{aux}}/h_{ca}\right]}\quad,\ \zeta_{eff,\mathrm{aux}}=\begin{cases}a_{p,ur}\zeta & ,\ \zeta_{eff}\leq a_{p,ur}\zeta\\ \zeta_{eff} & ,\ \zeta_{eff}>a_{p,ur}\zeta\end{cases}\qquad(3.44)$$

where the SUR branch $\mathrm{t}^n_{\Gamma,ur}(\zeta,\zeta_{eff})$ from Equation 3.45 is dependent on the effective ζ_{eff} and the maximum experienced equivalent cracking relative displacementstates ζ, where ζ establishes the intersection of this SUR function and the target softening function $\mathrm{t}^n_{\Gamma,t}(\zeta)$ from Equation 3.46. The nonlinear SUR branch gets defined by an exponential expression which grows asymptotically towards the traction $\mathrm{t}^n_{\Gamma,k}(\zeta)$ from Equation 3.47.

The key functions for the SUR method are presented below:

$$\mathrm{t}^n_{\Gamma,ur}(\zeta,\zeta_{eff}) = \mathrm{t}^n_{\Gamma,k}(\zeta)\left[1-\left(1-\frac{a_{p,ur}}{\nu_{ur}}\right)\exp\left\{-\frac{\zeta_{eff}-a_{p,ur}\zeta}{(\nu_{ur}-a_{p,ur})\zeta}\right\}\right],\zeta_{eff}\geq a_{p,ur}\zeta\qquad(3.45)$$

$$\mathrm{t}^n_{\Gamma,t}(\zeta) = f_t^{\mathrm{M}}\left[r_s^{\mathrm{M}}+(1-r_s^{\mathrm{M}})\exp\left\{-c_s\frac{\zeta-a_{k,ur}h_{ca}f_t^{\mathrm{M}}/E}{u_{max}-a_{k,ur}h_{ca}f_t^{\mathrm{M}}/E}\right\}\right],\zeta\geq a_{k,ur}h_{ca}\frac{f_t^{\mathrm{M}}}{E}\qquad(3.46)$$

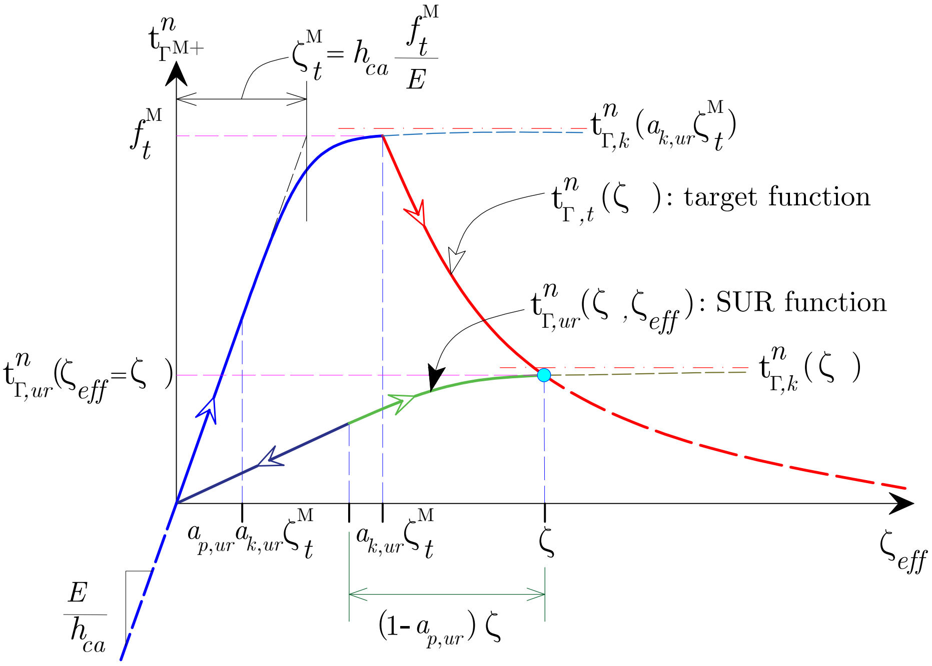

Figure 3.12: Equivalent traction-separation law describing SUR concept, as adopted at the embedded localisation band.

where the maximum experienced macro-state $\zeta \geq a_{k,ur} \cdot \zeta_t^{\mathrm{M}}$ gets initialised at the displacement projection of the first peak of the uniaxial curve, to attain an expected macroscopic uniaxial tensile strength f_t^{M}; the elastically-derived projected relative displacement $\zeta_t^{\mathrm{M}} = h_{ca}\frac{f_t^{\mathrm{M}}}{E}$ is defined by extending the first linear response until the peak strength f_t^{M}, with E being the elastic stiffness of the undamaged cementitious material; h_{ca} stands for the virtual thickness of the embedded localisation band; c_s is a softening constant; the effective end of the post-peak response is defined at $\zeta \approx u_{max}$; and r_s^{M} is a residual ratio that defines the tail of the softening branch (see comment box below).

N.B.: In the SUR method the smallest traction upon a very large value of equivalent crack relative displacement approximates to that of $\mathbf{lim}_{\zeta_{eff}\to\infty}\left(\mathrm{t}^n_{\Gamma,t}(\zeta)\right) = r_s^{\mathrm{M}} \cdot f_t^{\mathrm{M}}$, where the residual strength ratio $r_s^{\mathrm{M}} > 0$ is always positive to avoid ill-posed tangents. Typical values of the residual tensile strength ratio are shown in Table 3.2.

By intersecting the SUR nonlinear branch and the target function at $\zeta_{eff} = \zeta$, the asymptotic re-gained strength function $\mathrm{t}^n_{\Gamma,k}(\zeta)$ is derived in Equation 3.47.

$$\mathrm{t}^n_{\Gamma,k}(\zeta) = \mathrm{t}^n_{\Gamma,t}(\zeta) \cdot \nu_{ur} \cdot a_{k,ur}, \text{in } \zeta \geq a_{k,ur} h_{ca}\frac{f_t^{\mathrm{M}}}{E} \tag{3.47}$$

The parameter $a_{k,ur}$ is used to define the target function and asymptotic unloading reloading response, which is derived to comply with features of continuity in path and tangents (Alnaas and Jefferson, 2016; Jefferson and Mihai, 2015), and reads as shown below:

$$a_{k,ur} = \frac{1}{\nu_{ur} \cdot \left[1 - \left(1 - \frac{a_{p,ur}}{\nu_{ur}}\right) \exp\left\{ - \frac{1 - a_{p,ur}}{\nu_{ur} - a_{p,ur}} \right\} \right]} \tag{3.48}$$

where the SUR parameter $a_{k,ur}$ gets defined solely as a function of the SUR constants $a_{p,ur}$ and ν_{ur}.

Combining Equations 3.45 and 3.46, with $\mathrm{t}^{n}_{\Gamma,t}(\zeta)$ having an initial value of f_t^{M} the full expression for the U-R branch is derived:

$$\begin{aligned} \mathrm{t}^{n}_{\Gamma,ur}(\zeta, \zeta_{eff}) \quad = \quad & \mathrm{t}^{n}_{\Gamma,t}(\zeta) \cdot \nu_{ur} \cdot a_{k,ur} \cdot \left[1 - \left(1 - \frac{a_{p,ur}}{\nu_{ur}}\right) \exp\left\{ - \frac{\zeta_{eff} - a_{p,ur}\zeta}{(\nu_{ur} - a_{p,ur})\zeta} \right\} \right] \\ & , \forall \zeta_{eff} \geq a_{p,ur}\zeta, \forall \zeta \geq a_{k,ur} h_{ca} \frac{f_t^{\mathrm{M}}}{E} \end{aligned} \tag{3.49}$$

Note that the SUR nonlinear branch returns to a state of linear unloading, which connects through the origin, for an effective equivalent macrocrack relative displacement $\zeta_{eff} \leq a_{p,ur} \cdot \zeta$. Therefore, Gauss Points evaluated along the embedded localisation band that experience opening, sliding and rotation within this linear unloading branch, respond by freezing macrocrack stiffness and effective macroscopic damage variation. Hence, the cracking scalar variables, which are associated with linear unloading SUR response, are computed as the cracking scalar variables at the transition between nonlinear and linear SUR response.

Details on the damage surface defined for computing increments of effective equivalent cracking relative displacement $\zeta_{eff}(\Delta \mathbf{u}_{\Gamma})$ and its maximum experienced version ζ are described in Section 3.3.8

3.3.8 Relationship between crack displacement jump $\Delta \mathbf{u}_{\Gamma}$ and the equivalent cracking relative displacement $\zeta(\Delta \mathbf{u}_{\Gamma})$

The effective equivalent cracking relative displacement ζ_{eff} gets updated using a damage-informed hyperbolic function which is illustrated in Figure 3.13 and is defined in Equation 3.50. This damage function is consistent with that of micromechanical models by Jefferson and Bennett (2010, 2007); Mihai and Jefferson (2011). The unloading-reloading conditions of the damage surface are shown in Equation 3.51. Note that only states of loading would change the maximum experienced ζ.

$$\left.\begin{aligned} \zeta_{eff}(\Delta\mathbf{u}_\Gamma) = \tfrac{1}{2}\Delta\mathrm{u}_\Gamma^\mathrm{n}\left[1+\left(\tfrac{\mu_\varepsilon}{r_\varepsilon}\right)^2\right] + \tfrac{1}{2r_\varepsilon^2}\sqrt{\left(r_\varepsilon^2-\mu_\varepsilon^2\right)^2\Delta\mathrm{u}_\Gamma^\mathrm{n} + 4r_\varepsilon^2\left(\Delta\mathrm{u}_\Gamma^\mathrm{t}\right)} \\ \mathbf{\Phi}(\zeta,\zeta_{eff}) = \zeta_{eff}-\zeta \end{aligned}\right\} \tag{3.50}$$

$$\dot{\zeta} \geq 0, \quad \mathbf{\Phi}\cdot\dot{\zeta} = 0, \quad \mathbf{\Phi} \leq 0 \tag{3.51}$$

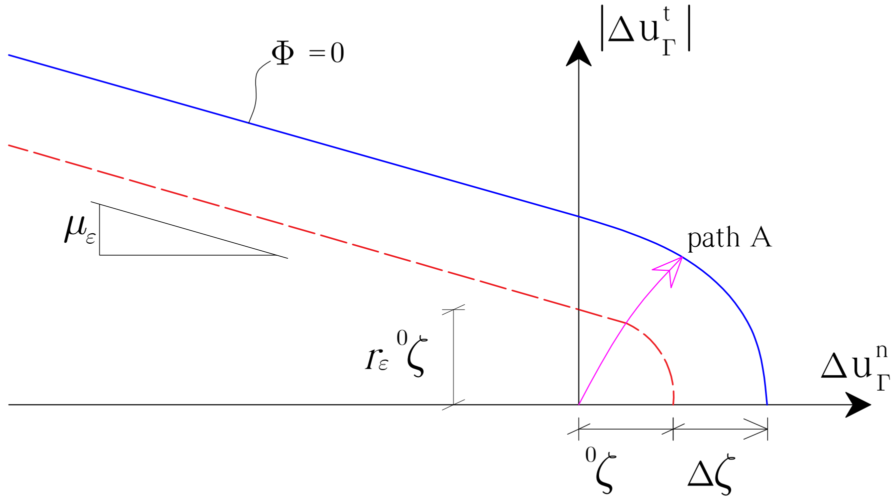

Figure 3.13: Damage surface is illustrated for Gauss Points along the embedded localisation band. As an example of the relative deformation path required to update the damage surface, path A is presented which consideres both opening and sliding in the embedded band.

3.3.9 Weak form of BVP for fracturing solid: a variational approach

A variational principle of least-energy consumption is exploited, as a means for finding the optimal solution to the BVP as posed in Section 3.3.1. In this regard, momentum balance $\mathbf{Div}[\boldsymbol{\sigma}]+\boldsymbol{b}=\mathbf{0}$ (inertial effects are neglected) is re-worked for small energetic variations weakly enforced in $\mathbf{\Omega}^+$ and $\mathbf{\Omega}^-$, which comprise the subdomain $\mathbf{\Omega}\subset\mathbf{\Omega}^e$

($\boldsymbol{\Omega} = \boldsymbol{\Omega}^+ \cup \boldsymbol{\Omega}^-$) crossed entirely by an embedded strong discontinuity $\boldsymbol{\Gamma}$ with surface $\partial\Gamma = \partial\Gamma^+ \cup \partial\Gamma^-$:

$$\overset{\boldsymbol{\Omega}^+}{\delta\Pi} = \int_{\Omega^+} \nabla^s(\delta\mathbf{u}_c) : \boldsymbol{\sigma} d\Omega + \underbrace{\int_{\partial\Gamma^+} \left(\delta\mathbf{u}_c + \delta[|\mathbf{u}|]\right) \cdot \mathbf{t}_{\Gamma^+} d\Gamma}_{-\int_{\partial\Gamma^+} \delta\mathbf{u}\cdot\left(\sigma\cdot\mathbf{n}\right)d\Gamma} - \int_{\Omega^+} \delta\mathbf{u}\cdot\boldsymbol{b} d\Omega - \int_{\partial\Omega^+_\sigma} \delta\mathbf{u}\cdot\mathbf{t}_{\partial\Omega^+} dS = 0 \tag{3.52}$$

$$\overset{\boldsymbol{\Omega}^-}{\delta\Pi} = \int_{\Omega^-} \nabla^s(\delta\mathbf{u}_c) : \boldsymbol{\sigma} d\Omega \underbrace{- \int_{\partial\Gamma^-} \delta\mathbf{u}_c \cdot \mathbf{t}_{\Gamma^+} d\Gamma}_{-\int_{\partial\Gamma^-} \delta\mathbf{u}\cdot\left(\boldsymbol{\sigma}\cdot\mathbf{n}\right)d\Gamma} - \int_{\Omega^-} \delta\mathbf{u} \cdot \boldsymbol{b} d\Omega - \int_{\partial\Omega^-_\sigma} \delta\mathbf{u} \cdot \mathbf{t}_{\partial\Omega^-} dS = 0 \tag{3.53}$$

where $\delta(\cdot)$ denotes a small variation, $\mathbf{t}_{\Gamma^+} = -\mathbf{t}_{\Gamma^-}$, $\mathbf{t}_{\Gamma^+} = \mathbf{t}_\Gamma(\boldsymbol{x} \in \partial\Gamma)$ and $\mathbf{t}_{\Gamma^-} = \mathbf{t}_\Gamma(\boldsymbol{x} \in \partial\Gamma^-)$ are the tractions at each side of an embedded localisation band.

Note that weak enforcement of (i) traction continuity along the embedded localisation band, and of (ii) traction equilibrium between the embedded localisation band and the continua, are both exploited in Equations 3.52 and 3.53. Formally, this weak enforcement of traction equilibrium and traction continuity are expressed as follows:

$$\left.\begin{array}{r} \int_{\partial\Gamma^+} \delta[|\mathbf{u}|] \cdot \left(\boldsymbol{\sigma} \cdot \mathbf{n}^+_\Gamma + \mathbf{t}_{\Gamma^+}\right) d\Gamma = 0 \\[2ex] \int_{\partial\Gamma^+} \delta|[\mathbf{u}|] \cdot \left(\boldsymbol{\sigma} \cdot \mathbf{n}^+_\Gamma + \boldsymbol{\sigma} \cdot \mathbf{n}^-_\Gamma\right) d\Gamma = 0 \end{array}\right\} \tag{3.54}$$

The following expression $\delta\Psi_{\Omega\backslash\Gamma} := \overset{\boldsymbol{\Omega}^+}{\delta\Pi} + \overset{\boldsymbol{\Omega}^-}{\delta\Pi}$ is derived by adding up energetic variations for each of the subdomain components $\boldsymbol{\Omega}^+$ and $\boldsymbol{\Omega}^-$ (Equations 3.52 and 3.53):

$$\delta\Psi_{\Omega\backslash\Gamma} = \underbrace{\int_{\Omega\backslash\Gamma} \nabla^s(\delta\mathbf{u}_c) : \boldsymbol{\sigma} d\Omega + \int_{\partial\Gamma^+} \delta[|\mathbf{u}|] \cdot \mathbf{t}_{\Gamma^+} d\Gamma}_{\overset{*}{\delta\Pi}_{int}} \underbrace{- \int_{\Omega} \delta\mathbf{u} \cdot \boldsymbol{b} d\Omega - \int_{\partial\Omega_\sigma} \delta\mathbf{u} \cdot \mathbf{t}_{\partial\Omega} dS}_{-\delta\Pi_{ext}} = 0 \tag{3.55}$$

where the minimisation of the functional $\delta\Psi_{\Omega\backslash\Gamma} := \delta\Pi_{int} - \delta\Pi_{ext}$ serves as a means to express the variational principle shown in Equation 3.56.

$$\underset{in\ \boldsymbol{\Omega}\backslash\boldsymbol{\Gamma}}{\textbf{minimise}}\left\{\int_{\Omega\backslash\Gamma}\nabla^{s}(\delta\mathbf{u}_{c}):\boldsymbol{\sigma}d\Omega+\int_{\partial\Gamma^{+}}\delta[|\mathbf{u}|]\cdot\mathbf{t}_{\Gamma^{+}}d\Gamma-\int_{\Omega}\delta\mathbf{u}\cdot\boldsymbol{b}d\Omega-\int_{\partial\Omega_{\sigma}}\delta\mathbf{u}\cdot\mathbf{t}_{\partial\Omega}dS\right\} \tag{3.56}$$

Note that the external forces are independent of the variations of the fracture-associated displacement, upon fixing the displacement field. Therefore, the Equation 3.56 is reduced to the minimisation expression in Equation 3.57.

$$\delta\Pi_{int} := \underset{in\ \boldsymbol{\Omega}\backslash\boldsymbol{\Gamma}}{\textbf{inf}}\left\{\delta\overset{\boldsymbol{\Omega}^{+}}{\Pi}+\delta\overset{\boldsymbol{\Omega}^{-}}{\Pi}+\delta\Pi_{ext}\right\} = \underset{in\ \boldsymbol{\Omega}\backslash\boldsymbol{\Gamma}}{\textbf{inf}}\left\{\overset{*}{\delta\Pi}_{int}\right\} \tag{3.57}$$

where the functional $\overset{*}{\delta\Pi}_{int}$ possesses a strain energy component, exerted by the continua, and a fracture energy component, induced by the embedded localisation band as shown in Equation 3.58.

$$\boxed{\overset{*}{\delta\Pi}_{int} := \underbrace{\int_{(\Omega^{+}\cup\Omega^{-})\backslash\Gamma}\nabla^{s}(\delta\mathbf{u}_{c}):\boldsymbol{\sigma}d\Omega}_{\text{strain energy}}+\underbrace{\int_{\partial\Gamma^{+}}\delta[|\mathbf{u}|]\cdot\mathbf{t}_{\Gamma^{+}}d\Gamma}_{\text{fracture energy}}} \tag{3.58}$$

3.3.10 Variational Finite Element setting of solids with embedded strong discontinuities

The following elaborations consider an element region as the subdomain $\boldsymbol{\Omega} \subset \boldsymbol{\Omega}^{e}$. Using the Equation 3.58 and an approximation of the gradient of the continuous displacement field $\boldsymbol{\varepsilon} = \{\nabla^{s}\mathbf{u}_{c}\}_{\text{vec}}$ (Sections 3.3.4 and 3.3.5), along with an approximation of work done by the embedded localisation band $\boldsymbol{\delta}\widehat{\mathbf{W}}^{\text{T}} \cdot \mathbf{F}_{\text{ck}}$ (Section 3.3.6) gives:

$$\boldsymbol{\delta}\overset{*}{\Pi}_{int}(\mathbf{u}^{\text{el}},\mathbf{W}) = \int_{\Omega\backslash\Gamma}\left(\boldsymbol{\delta\varepsilon}^{\text{T}}\mathbf{D}_{e}\boldsymbol{\varepsilon}\right)d\Omega+\boldsymbol{\delta}\widehat{\mathbf{W}}^{\text{T}}\mathbf{F}_{\text{ck}} \tag{3.59}$$

Now re-arranging Equations 3.56 and 3.57 gives Equation 3.60.

$$\left.\begin{aligned} \boldsymbol{\delta}\Psi_{\Omega\backslash\Gamma} &= \boldsymbol{\delta}\Pi_{ext} - \boldsymbol{\delta}\Pi_{int} = 0 \\ \boldsymbol{\delta}\Pi_{ext} &= \{\delta\mathbf{u}^{\mathrm{el}}\}^{\mathrm{T}}\mathbf{F}^{\mathrm{el}}_{\mathrm{ext}} \\ \boldsymbol{\delta}\Pi_{int} &= \inf_{in\ \Omega\backslash\Gamma}\left\{\overset{*}{\boldsymbol{\delta}\Pi}_{int}\right\} \end{aligned}\right\} \tag{3.60}$$

where $\mathbf{F}^{\mathrm{el}}_{\mathrm{ext}}$ is defined as the nodal forces applied externally. External distributed forces and body forces are included in standard form, while the method enables the embeddment of macrocrack-inducing tractions inside the element domain.

Expansion of the strain vector considering strong-discontinuity kinematic enhancement $\boldsymbol{\varepsilon} = \mathbf{B}\mathbf{u}^{\mathrm{el}} - \mathbf{M}\widehat{\mathbf{W}}$ (Equation 3.36) into Equation 3.59 yields:

$$\overset{*}{\boldsymbol{\delta}\Pi}_{int}(\mathbf{u}^{\mathrm{el}},\mathbf{W}) = \int_{\Omega\backslash\Gamma}\left(\left\{\mathbf{B}\delta\mathbf{u}^{\mathrm{el}} - \mathbf{M}\delta\widehat{\mathbf{W}}\right\}^{\mathrm{T}}\mathbf{D}_e\boldsymbol{\varepsilon}\right)d\Omega + \delta\widehat{\mathbf{W}}^{\mathrm{T}}\mathbf{F}_{\mathrm{ck}} \tag{3.61}$$

Re-arrrangement of common terms with respect to variations of the displacement $\delta\mathbf{u}^{\mathrm{el}}$ and that of the crack relative displacement $\delta\widehat{\mathbf{W}}$ in Equation 3.61 gives:

$$\overset{*}{\boldsymbol{\delta}\Pi}_{int}(\mathbf{u}^{\mathrm{el}},\mathbf{W}) = \{\delta\mathbf{u}^{\mathrm{el}}\}^{\mathrm{T}}\left\{\int_{\Omega\backslash\Gamma}\mathbf{B}^{\mathrm{T}}\mathbf{D}_e\boldsymbol{\varepsilon}d\Omega\right\} + \{\delta\widehat{\mathbf{W}}\}^{\mathrm{T}}\left\{\mathbf{F}_{\mathrm{ck}} - \int_{\Omega\backslash\Gamma}\mathbf{M}^{\mathrm{T}}\mathbf{D}_e\boldsymbol{\varepsilon}d\Omega\right\} \tag{3.62}$$

By replacing the inelastic component of variation of crack relative displacement $\delta\widehat{\mathbf{W}} = \hat{\mathbf{I}}\cdot\delta\mathbf{W}$ (Equation 3.23) in Equation 3.62, further simplification is attained:

$$\left.\begin{aligned} \overset{*}{\boldsymbol{\delta}\Pi}_{int}(\mathbf{u}^{\mathrm{el}},\mathbf{W}) &= \{\delta\mathbf{u}^{\mathrm{el}}\}^{\mathrm{T}}\left\{\partial\overset{*}{\Pi}_{int}/\partial\mathbf{u}^{\mathrm{el}}\right\} + \{\delta\mathbf{W}\}^{\mathrm{T}}\left\{\partial\overset{*}{\Pi}_{int}/\partial\mathbf{W}\right\} \\ \left\{\partial\overset{*}{\Pi}_{int}/\partial\mathbf{u}^{\mathrm{el}}\right\}(\mathbf{u}^{\mathrm{el}},\mathbf{W}) &= \textstyle\int_{\Omega\backslash\Gamma}\mathbf{B}^{\mathrm{T}}\mathbf{D}_e\boldsymbol{\varepsilon}d\Omega \\ \left\{\partial\overset{*}{\Pi}_{int}/\partial\mathbf{W}\right\}(\mathbf{u}^{\mathrm{el}},\mathbf{W}) &= \hat{\mathbf{I}}\left\{\mathbf{F}_{\mathrm{ck}} - \textstyle\int_{\Omega\backslash\Gamma}\mathbf{M}^{\mathrm{T}}\mathbf{D}_e\boldsymbol{\varepsilon}d\Omega\right\} \end{aligned}\right\} \tag{3.63}$$

where element-wise quasi-static condensation of crack dofs $\mathbf{W}$ becomes possible, by ensuring that the internal energy variation is minimum, and this gives:

$$\boxed{\mathbf{W} := \mathbf{Arg}\left\{\inf_{in\ \Omega\backslash\Gamma}\left\{\overset{*}{\boldsymbol{\delta}\Pi}_{int}\right\}\right\}} \tag{3.64}$$

Minimisation of the variation of internal energy $\eth\overset{*}{\Pi}_{int}$ is physically meaningful, and implies that the additional external work needed to propagate fractures is the least for any fixed displacement $\boldsymbol{\delta}\mathbf{u}^{\mathrm{el}} = \mathbf{0}$ and any variation of crack relative displacement vector $\boldsymbol{\delta}\mathbf{W} \neq \mathbf{0}$, at the element level as illustrated in Figure 3.14.

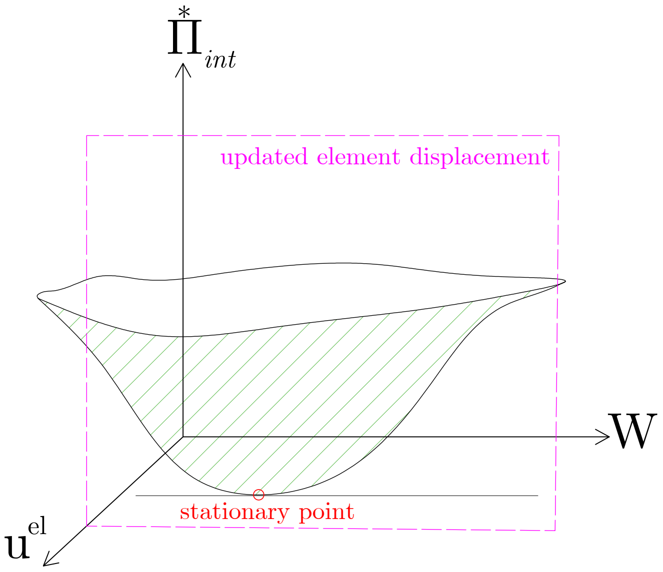

(a) Sketch of energy-based Functional for any arbitrary deformation states

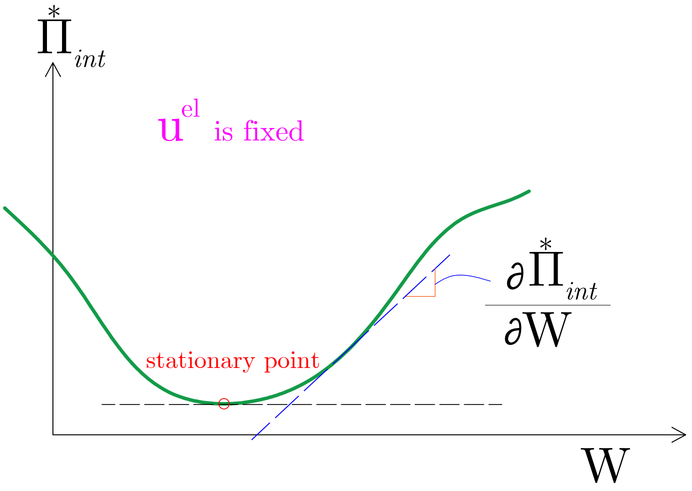

(b) Sketch of energy-based Functional for arbitrary crack relative displacement, given an updated element displacement

Figure 3.14: Schematic interpretation of a local minima within an energy-based Functional of a fracturing solid. Top sketch stands for a general surface of the energy-based functional, and bottom sketch for a slice of the surface given a specific element displacement.

The local minimum of $\eth\overset{*}{\Pi}_{int}$ is obtained from fixing displacement field $\mathbf{u}^{\mathrm{el}}$ in Equation 3.63 while enforcing the constraint $\eth\overset{*}{\Pi}_{int} = 0$:

$$\left.\begin{array}{c}\left\{\partial\overset{*}{\Pi}_{int}/\partial\mathbf{W}\right\}(\mathbf{u}^{\mathrm{el}},\mathbf{W})=\mathbf{0}\\[2ex]\Rightarrow\mathbf{K}_\Gamma\mathbf{W}-\int_{\Omega\backslash\Gamma}\mathrm{M}^{\mathrm{T}}\mathbf{D}_e\left\{\mathbf{B}\mathbf{u}^{\mathrm{el}}-\widehat{\mathrm{M}}\mathbf{W}\right\}d\Omega=\mathbf{0}\end{array}\right\}\tag{3.65}$$

where further re-arrangement of Equation 3.65, which depicts a stationary point for the internal energy variation $\overset{*}{\mathfrak{d}\Pi}_{int}$ gives :

$$\left\{\mathbf{K}_\Gamma+\left\{\int_\Omega\mathrm{M}^{\mathrm{T}}\mathbf{D}_e\mathrm{M}d\Omega\right\}\hat{\mathbf{I}}\right\}\mathbf{W}=\left\{\int_\Omega\mathrm{M}^{\mathrm{T}}\mathbf{D}_e\mathbf{B}d\Omega\right\}\mathbf{u}^{\mathrm{el}}\tag{3.66}$$

In addition, by isolating the crack centre relative displacement vector $\mathbf{W}$, the additional set of PDEs, used for element-wise quasi-static condensation, are conveniently derived, and are presented in Equation 3.67.

$$\left.\begin{array}{c}\boldsymbol{\phi}_w^{\mathrm{el}}(\mathbf{W}):=\mathbf{W}-\mathbf{C}_\Gamma(\mathbf{W},\mathbf{u}^{\mathrm{el}})\cdot\mathbf{u}^{\mathrm{el}}=\mathbf{0}\\\mathbf{C}_\Gamma(\mathbf{W},\mathbf{u}^{\mathrm{el}})=\mathbf{B}_\Gamma^{-1}\cdot\mathbf{A}_\Gamma\\\mathbf{B}_\Gamma=\mathbf{K}_\Gamma+\mathbf{B}_\Gamma^{*}\cdot\hat{\mathbf{I}}\\\mathbf{B}_\Gamma^{*}=\int_{\Omega\backslash\Gamma}\mathbf{M}^{\mathrm{T}}\mathbf{D}_e\mathbf{M}d\Omega\\\mathbf{A}_\Gamma=\int_{\Omega\backslash\Gamma}\mathbf{M}^{\mathrm{T}}\mathbf{D}_e\mathbf{B}d\Omega\end{array}\right\}\tag{3.67}$$

where Equation 3.67 corresponds to three unknowns stacked in $\mathbf{W}$, with three available differential equations for any given displacement update $\mathbf{u}^{\mathrm{el}}$.

Now combining Equations 3.63 and 3.65, for the desired stationary condition $\partial\overset{*}{\Pi}_{int}/\partial\mathbf{W}=\mathbf{0}$, and the finite element form of the variational principle in Equation 3.60, an energetically-optimal equilibrium equation for fracture propagation with embedded strong discontinuities is derived, and it is presented in Equation 3.68.

$$\left.\begin{array}{c}\boldsymbol{\phi}_F^{\mathrm{el}}(\mathbf{u}^{\mathrm{el}}):=\mathbf{F}_{\mathrm{ext}}^{\mathrm{el}}-\mathbf{F}_{\mathrm{int}}^{\mathrm{el}}(\mathbf{u}^{\mathrm{el}})=\mathbf{0}\\[2ex]\mathbf{F}_{\mathrm{int}}^{\mathrm{el}}(\mathbf{u}^{\mathrm{el}}):=\int_{\Omega\backslash\Gamma}\mathbf{B}^{\mathrm{T}}\mathbf{D}_e\left\{\mathbf{B}\mathbf{u}^{\mathrm{el}}-\widehat{\mathrm{M}}\mathbf{W}\right\}d\Omega\ ,\quad\mathbf{W}=\mathbf{C}_\Gamma(\mathbf{W},\mathbf{u}^{\mathrm{el}})\cdot\mathbf{u}^{\mathrm{el}}\end{array}\right\}\tag{3.68}$$

where the crack dofs $\mathbf{W}$, upon weakly enforced energetic minimisation of the embedded strong discontinuity element, drive the update of maximum experienced and effective equivalent crack relative displacement ζ and ζ_{eff} at the integration points along the crack length; whereas the newly updated enhanced strain $\boldsymbol{\varepsilon}$ drives the update of stresses within the bulk domain.

Conveniently, when no cracks have formed, Equation 3.68 degrades into a standard FEM approach, since $\widehat{\mathbf{M}} = \mathbf{0}$ for cracks undergoing elastic deformation with floating propagation direction.

3.3.11 Numerical tangent stiffness for cracked elements

At first, an intermediate step is taken for devising a consistently linearized element tangent operator (Simo and Taylor, 1985) for an element with embedded strong discontinuities, which lies in deriving an element-wise secant stiffness operator. By combining Equations 3.60 and 3.61, upon quasi-static condensation of crack degrees of freedom $\mathbf{W} = \mathbf{C}_{\Gamma}\mathbf{u}^{\mathrm{el}}$ (Equation 3.67):

$$\begin{aligned}\delta\Pi_{int}(\mathbf{u}^{\mathrm{el}}) \quad = \quad & \int_{\Omega\setminus\Gamma}\left\{\mathbf{B}\delta\mathbf{u}^{\mathrm{el}} - \mathbf{M}\hat{\mathbf{I}}\{\mathbf{C}_{\Gamma}\delta\mathbf{u}^{\mathrm{el}}\}\right\}^{\mathrm{T}}\mathbf{D}_{e}\left\{\mathbf{B}\mathbf{u}^{\mathrm{el}} - \mathbf{M}\hat{\mathbf{I}}\{\mathbf{C}_{\Gamma}\mathbf{u}^{\mathrm{el}}\}\right\}d\Omega \\ & +\left\{\hat{\mathbf{I}}\{\mathbf{C}_{\Gamma}\delta\mathbf{u}^{\mathrm{el}}\}\right\}^{\mathrm{T}}\mathbf{K}_{\Gamma}\left\{\mathbf{C}_{\Gamma}\mathbf{u}^{\mathrm{el}}\right\}\end{aligned} \tag{3.69}$$

Note that the approximation $\delta\widehat{\mathbf{W}} \approx \hat{\mathbf{I}}\{\mathbf{C}_{\Gamma}\delta\mathbf{u}^{\mathrm{el}}\}$ has been used, under the assumption of a small variation of $\delta\mathbf{u}^{\mathrm{el}}$. Then, re-arranging terms from Equation 3.69 gives:

$$\begin{aligned}\delta\Pi_{int}(\mathbf{u}^{\mathrm{el}}) \quad = \quad & \int_{\Omega\setminus\Gamma}\left\{\delta\mathbf{u}^{\mathrm{el}}\right\}^{\mathrm{T}}\left\{\mathbf{B} - \mathbf{M}\hat{\mathbf{I}}\mathbf{C}_{\Gamma}\right\}^{\mathrm{T}}\mathbf{D}_{e}\left\{\mathbf{B} - \mathbf{M}\hat{\mathbf{I}}\mathbf{C}_{\Gamma}\right\}\left\{\mathbf{u}^{\mathrm{el}}\right\}d\Omega \\ & +\left\{\delta\mathbf{u}^{\mathrm{el}}\right\}^{\mathrm{T}}\left\{\hat{\mathbf{I}}\mathbf{C}_{\Gamma}\right\}^{\mathrm{T}}\mathbf{K}_{\Gamma}\left\{\mathbf{C}_{\Gamma}\right\}\left\{\mathbf{u}^{\mathrm{el}}\right\}\end{aligned} \tag{3.70}$$

Further, by taking terms that do not change within the domain of integration out of the integral expression on the right-hand side from Equation 3.70, and by replacing the equivalent terms $\widehat{\mathbf{M}} = \mathbf{M}\hat{\mathbf{I}}$ (Equation 3.34) and $\widehat{\mathbf{K}}_{\Gamma} = \hat{\mathbf{I}}\mathbf{K}_{\Gamma} = \hat{\mathbf{I}}^{\mathrm{T}}\mathbf{K}_{\Gamma}$ gives:

$$\begin{aligned}\delta\Pi_{int}(\mathbf{u}^{\mathrm{el}}) \quad = \quad & \left\{\delta\mathbf{u}^{\mathrm{el}}\right\}^{\mathrm{T}}\left\{\int_{\Omega\setminus\Gamma}\left\{\mathbf{B} - \widehat{\mathbf{M}}\mathbf{C}_{\Gamma}\right\}^{\mathrm{T}}\mathbf{D}_{e}\left\{\mathbf{B} - \widehat{\mathbf{M}}\mathbf{C}_{\Gamma}\right\}d\Omega\right\}\left\{\mathbf{u}^{\mathrm{el}}\right\} \\ & +\left\{\delta\mathbf{u}^{\mathrm{el}}\right\}^{\mathrm{T}}\left\{\mathbf{C}_{\Gamma}^{\mathrm{T}}\widehat{\mathbf{K}}_{\Gamma}\mathbf{C}_{\Gamma}\right\}\left\{\mathbf{u}^{\mathrm{el}}\right\}\end{aligned} \tag{3.71}$$

By re-arranging common terms from the right-hand side of Equation 3.71 and by combining with Equation 3.60, to conveniently use the FE setting of the variational principle:

$$\left\{\delta\mathbf{u}^{\mathrm{el}}\right\}^{\mathrm{T}}\left\{\int_{\Omega\setminus\Gamma}\left\{\mathbf{B} - \widehat{\mathbf{M}}\mathbf{C}_{\Gamma}\right\}^{\mathrm{T}}\mathbf{D}_{e}\left\{\mathbf{B} - \widehat{\mathbf{M}}\mathbf{C}_{\Gamma}\right\}d\Omega + \mathbf{C}_{\Gamma}^{\mathrm{T}}\widehat{\mathbf{K}}_{\Gamma}\mathbf{C}_{\Gamma}\right\}\left\{\mathbf{u}^{\mathrm{el}}\right\} = \{\delta\mathbf{u}^{\mathrm{el}}\}^{\mathrm{T}}\mathbf{F}_{\mathrm{ext}}^{\mathrm{el}} \tag{3.72}$$

Therefore, the secant stiffness at the element level can be devised after cancelling $\delta\mathbf{u}^{\mathrm{el}} \neq \mathbf{0}$ from both sides of Equation 3.72:

$$\left\{\int_{\Omega\backslash\Gamma}\{\mathbf{B}-\widehat{\mathbf{M}}\mathbf{C}_\Gamma\}^{\mathrm{T}}\mathbf{D}_e\{\mathbf{B}-\widehat{\mathbf{M}}\mathbf{C}_\Gamma\}d\Omega+\mathbf{C}_\Gamma^{\mathrm{T}}\widehat{\mathbf{K}}_\Gamma\mathbf{C}_\Gamma\right\}\{\mathbf{u}^{\mathrm{el}}\}=\mathbf{F}^{\mathrm{el}}_{\mathrm{int}} \tag{3.73}$$

$$\mathbf{K}^{\mathrm{el}}_{\mathrm{EFEM,sec}}=\int_{\Omega\backslash\Gamma}\{\mathbf{B}-\widehat{\mathbf{M}}\mathbf{C}_\Gamma\}^{\mathrm{T}}\mathbf{D}_e\{\mathbf{B}-\widehat{\mathbf{M}}\mathbf{C}_\Gamma\}d\Omega+\mathbf{C}_\Gamma^{\mathrm{T}}\widehat{\mathbf{K}}_\Gamma\mathbf{C}_\Gamma \tag{3.74}$$

By differentiating each side of Equation 3.73, derivation of a consistent tangent for a cracked element is enabled considering an elastic bulk domain under deformation and embedded cracks being simultaneously active:

$$\underbrace{\left\{\partial(\mathbf{K}^{\mathrm{el}}_{\mathrm{EFEM,sec}}\mathbf{u}^{\mathrm{el}})/\{\partial\mathbf{u}^{\mathrm{el}}\}\right\}}_{\mathbf{K}^{\mathrm{el}}_{\mathrm{EFEM}}}\{\dot{\mathbf{u}}^{\mathrm{el}}\}=\dot{\mathbf{F}}^{\mathrm{el}}_{\mathrm{int}} \tag{3.75}$$

Further development of chain rules yields the following numerically derived expression for the consistent tangent $\mathbf{K}^{\mathrm{el}}_{\mathrm{EFEM}}$, in index notation:

$$\left\{K^{\mathrm{el}}_{\mathrm{EFEM}}\right\}_{ij}=\left\{K^{\mathrm{el}}_{\mathrm{EFEM,sec}}\right\}_{ij}+\underbrace{\left(\frac{\partial\{K^{\mathrm{el}}_{\mathrm{EFEM,sec}}\}_{ir}}{\partial u^{\mathrm{el}}_j}\right)}_{\text{by central differences}}u^{\mathrm{el}}_r,\quad i,j,r=1\ldots\underbrace{\mathrm{ndofn}\cdot\mathrm{nnode}}_{\mathrm{ndofe}} \tag{3.76}$$

where central difference approximations are used for sufficiently small nodal perturbations $\delta\mathrm{u}^{\mathrm{el}}_j$, and $\mathbf{K}^{\mathrm{el}}_{\mathrm{EFEM,sec}}$ is updated forwardly and backwardly for each of these steps, consistently with the quasi-static condensation procedure described previously in order to compute the difference expression:

$$\frac{\partial\{K^{\mathrm{el}}_{\mathrm{EFEM,sec}}\}_{ir}}{\partial u^{\mathrm{el}}_j}\approx\frac{\{K^{\mathrm{el}}_{\mathrm{EFEM,sec}}(u^{\mathrm{el}+})\}_{ir}-\{K^{\mathrm{el}}_{\mathrm{EFEM,sec}}(u^{\mathrm{el}-})\}_{ir}}{2|\Delta_{\mathrm{FD}}u^{\mathrm{el}}_j|},\quad i,j,r=1\ldots\mathrm{ndofe} \tag{3.77}$$

where $\Delta_{\mathrm{FD}}(\cdot)$ stands for a Finite-Difference based forward or backward step size. Note that a numerical tangent is preferred over one in closed form, since the latter becomes sophisticated to compute due to the highly-nonlinear system of equations. Note that a central difference scheme is preferred since the error induced is expected to be second order $O(|\Delta_{\mathrm{FD}}u^{\mathrm{el}}_j|^2)$.

N.B.: Secant operators are used until the macrocracking direction is settled, and this is generally known 'a posteriori' of updating cracking dofs using quasi-static element-based condensation. Therefore, consistent tangent operators for cracked elements are only used for global iterations after macrocrack activation.

3.4 Numerical examples of nonlinear diffuse-micro and localised-macro quasi-brittle response

The models described in Sections 3.2 and 3.3 have been implemented separately to model failure of quasi-brittle solids in practical numerical examples. The following sub-section presents a number of examples in which the uniqueness of the solution is analysed for various meshes upon fracture occurrence.

3.4.1 Uniaxial extension test: uniqueness for various grids

Models were tested under simple uniaxial conditions for checking mesh insensitivty of the mechanical response. Bilinear quadrilateral elements in plane-stress settings have been used. Chosen grids comprise: 1 square element, 25 square elements and 225 square elements. Central elements were assumed slightly weaker to drive deformation localisation. Macrocrack nucleation in EFEM approach was allowed when major principal stress exceeds peak tensile strength. Boundary conditions are shown in Figure 3.15, and parameters[1] in Table 3.1.

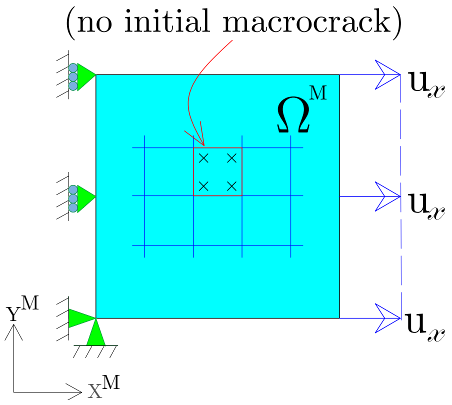

Figure 3.15: Boundary conditions for failure analyses of quasi-brittle cementitious solid of domain $\Omega^{\mathrm{M}}(50mm\times50mm\times50mm)$ in uniaxial extension.

Table 3.1: Summary of model parameters for uniaxial extension test.

EFEM model with elastic bulk adjusted from Alnaas (2016)							
E $[N/mm^2]$	υ [-]	$f_t^{\mathrm{M}}[N/mm^2]$	h_{ca} [mm]	r_σ [-]	μ_σ [-]	u_{max} [mm]	r_s^{M} [-]
30000	0.20	3.00	1.00	1.50	1.00	0.20	0.04

Smeared-crack micromechanical model adjusted from Jefferson and Bennett (2007)					
E $[N/mm^2]$	υ [-]	$f_t^{\mathrm{m}}[N/mm^2]$	r_σ [-]	μ_σ [-]	u_{max} [mm]
30000	0.20	1.85	1.50	1.00	0.30

---

[1] Softening: $c_s \approx 6.0$; SUR macrocracking: $\nu_{ur} = 0.85$, $a_{p,ur} = 0.65$; homogenisation: $\mathrm{n}_{int}^{\mathrm{m}} = 21$

3.4.2 Guidance on calibration of models for micro-diffuse and macro-localised quasi-brittle response

Note that most parameters are common for both the micromechanics and strong discontinuity models, except for tensile strength parameters as shown in Table 3.2.

Table 3.2: Guidance on model calibration for modelling quasi-brittle response.

Parameter	Comments on calibration
E	The Young's modulus should allow to capture the correct stiffness of the cementitious composite under initial deformation in uniaxial setting. A good first estimate is 30000 [N/mm^2] for standard concrete.
υ	The Poisson's ratio can be set to a typical value between 0.2 to 0.3 for cementitious composites. Calibration should reflect transversal stiffness correctly under incipient deformation in uniaxial setting.
f_t^{M}	The macroscopic strength should match that observed from experimental data in uniaxial deformation setting. Note that f_t^{M} is larger than f_t^{m}.
f_t^{m}	The microscale strength should match that observed from incipient nonlinear response in experimental data in uniaxial deformation setting, since microcracking is acknowledged to be responsible for these nonlinearities.
h_{ca}	The macrocrack band virtual width can be taken as a few times the coarse aggregate size, e.g $h_{ca} \approx 5$ to 20 mm if it is a concrete with both fine and coarse aggregate, or up to 2 mm if it is mortar.
r_σ	This ratio is computed as $r_\sigma = \frac{c'}{f_t^{\mathrm{M}}}$. A typical value for this ratio can be in the range of 1.0 to 1.5.
μ_σ	This ratio is equivalent to the asymptotic shear to compressive stregnth ratio in σ_{rs} - σ_{rr} space when a micro or macrocrack is loaded. A typical value for this ratio can be in the order 0.50 to 1.30.
u_{max}	This is the ultimate crack opening at which most residual fracture resistance vanishes, with typical value for concrete between 0.2 to 0.3 mm.
r_s^{M}	This macrocrack's residual tensile strength ratio can be set typically in the range 0.01 to 0.05, with the purpose to avoid vanishing strength.

3.4.3 Discussion of simulation results: uniaxial tensile test

3.4.3.1 EFEM analysis: mesh convergence test

The uniaxial extension response simulated via the EFEM approach employs a constant macrocrack-band width $h_{ca} = 1.0\ mm$ to render an objective response in the load-displacement curves, as shown in Figure 3.16e, even if various element sizes are used for different mesh configurations. It is highlighted that both an objective peak response and an objective post peak response are obtained. In addition, deformation fields for various grids remain objective at the ultimate stage as observed in Figures 3.16a and 3.16b. Note that only the macrocrack relative displacement exerts macroscopic inelastic response upon deformation. The macrocrack gets nucleated when major principal stress exceeds the tensile strength ($\sigma_1 > f_t^{\mathrm{M}}$), and macro-fracture advancing direction is perpendicular to the major principal strain direction. In addition, as a consequence of the relaxation of the domain at the end stage shown in Figures 3.16c and 3.16d. This behaviour implies the strain of the elastic bulk returns to almost original nil strain, then the macrocrack opening takes over the deformation imposed along the right edge of the domain, i.e. $\Delta \mathrm{u}^{\mathrm{n}}_{\Gamma^{\mathrm{M}}}(\mathbf{x} \text{ on } \partial\Gamma^{\mathrm{M}}) \approx \Delta u_x$ with $\mathrm{n}^{+}_{\Gamma^{\mathrm{M}}} = [1, 0, 0]^{\mathrm{T}}$.

3.4.3.2 Smeared-crack micromechanical analysis: mesh convergence test

The micromechanical material model employed a smeared-crack approach (Bažant and Oh, 1983). In this regard, the ultimate strain for failure to occur at the quadrature-level $\zeta^{\mathrm{m}}_{\max} = \varepsilon^{\mathrm{m}}_{\max} = u_{\max}/h_{el}$ is set to be inversely proportional the element size h_{el}. It is observed from results of load-displacement curves in Figure 3.17e, that although this simple approach helps to promote an objective end of the strain-softening branch, peak response is still sensitive to mesh size and therefore fracture energy is not preserved adequately. Deformation fields for various mesh configurations are also presented for reference in Figures 3.17a to 3.17b. Note that upon failure, there is a concentration of strain in a band of defined thickness, which is not completely objective with respect to mesh refinement, as observed in Figures 3.17c and 3.17d.

3.4.3.3 Hypothesis on improvement due to coupling of methodologies

Coupling of a Micromechanical model and an EFEM approach would allow an objective peak and post peak structural response for quasi-brittle cementitious composites, while additional accuracy of the non-linear response of the bulk would be attained. Among other coupling criteria, (energetic) variational approaches could be explored as an elegant resource to seek models with optimal failure mechanisms. Some aspects of this type of energetic constraints have been discussed along the simulation of similar numerical tests to study compatibility in Azua-Gonzalez et al. (2019, 2020, 2021).

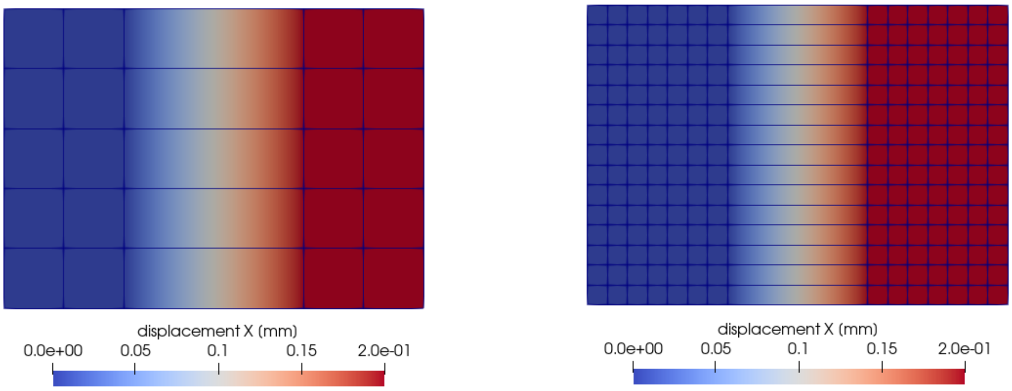

(a) EFEM, 25 Elements: deformed shape (b) EFEM, 225 Elements: deformed shape

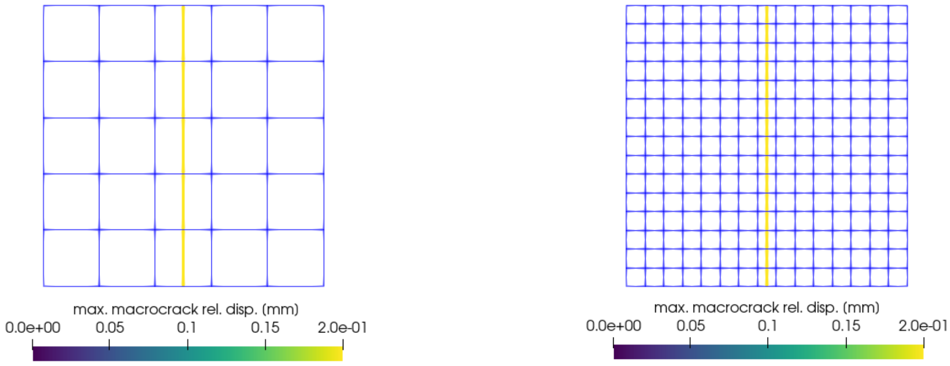

(c) EFEM, 25 Elements: crack opening (d) EFEM, 225 Elements: crack opening

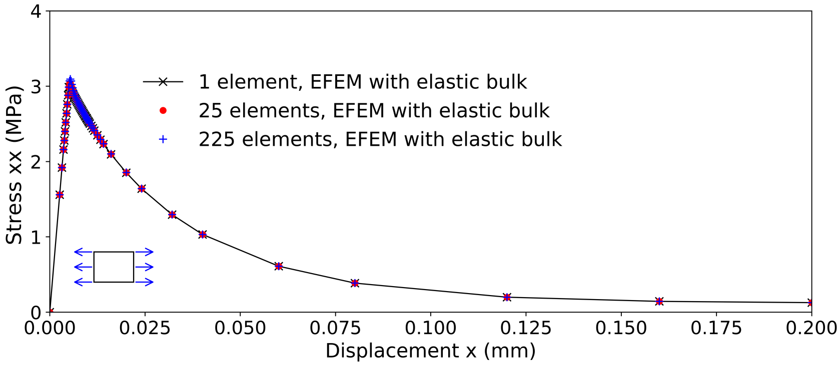

(e) Uniaxial extension: load-displacement response for EFEM approach

Figure 3.16: Uniaxial extension test on $\boldsymbol{\Omega}^{\mathrm{M}}(50mm\times50mm\times50mm)$, using EFEM approach for quasi-brittle solids with elastic bulk, where weakened material is used in central elements. Ultimate deformation and macrocrack opening contours are shown.

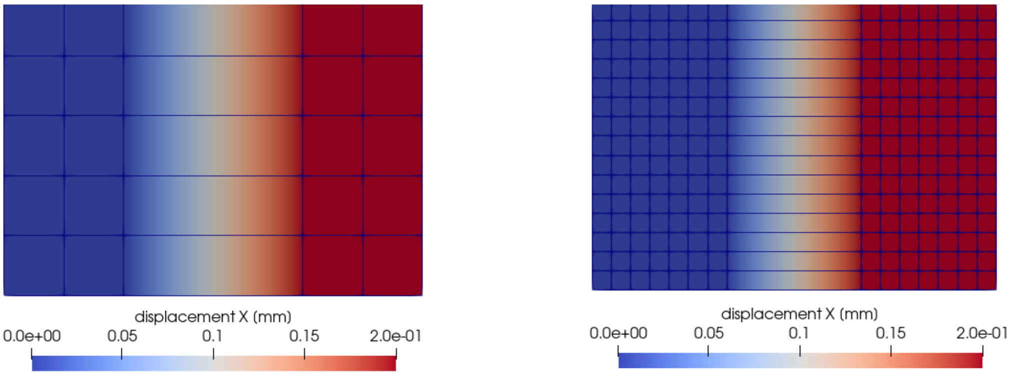

(a) Micromechanics, 25 Elements: deformed (b) Micromechanics, 225 Elements: deformed

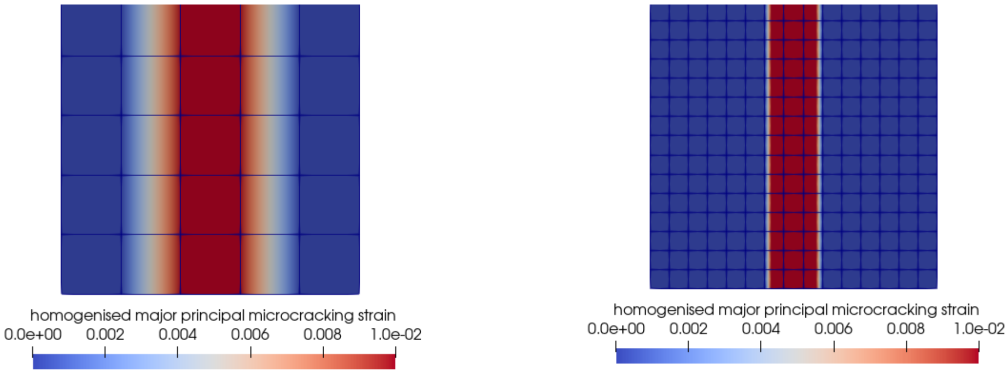

(c) Homogenised strain: 25 Elements (d) Homogenised strain: 225 Elements

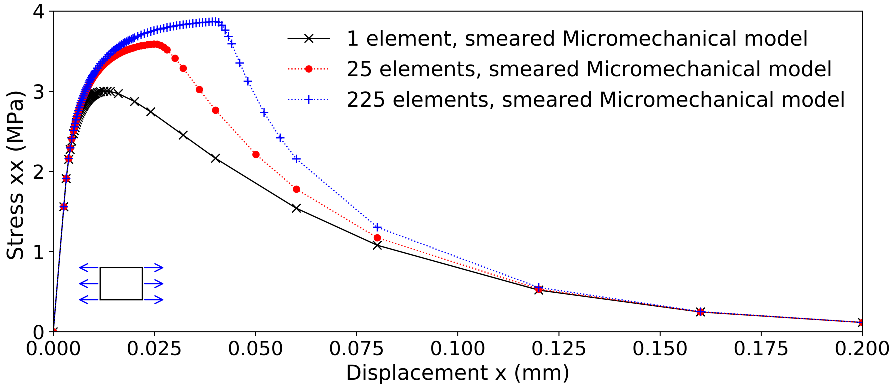

(e) Uniaxial extension: load-displacement response for regularised micromechanical model

Figure 3.17: Simulation of uniaxial extension test on $\mathbf{\Omega}^{\mathrm{M}}(50mm{\times}50mm{\times}50mm)$, using smeared crack approach for quasi-brittle micromechanical solids. Model adjusted from Jefferson and Bennett (2007). Various grids used with slightly weakened material in central line of elements. Nodal deformation and homogenised micromechanics-induced strain (major principal component) contours shown for end stage.

3.5 Summarised formulations for micro and macro fracture modelling in quasi-brittle materials

The main features of the Micromechanical model at the bulk domain (see Section 3.2) as used in a standard Finite Element program are summarised in Box 3.1, and the basic element formulation for an EFEM approach is described in Box 3.2.

Box 3.1 Summary of Micromechanical material model for cementitious materials with directional microcracking, adapted from Jefferson and Bennett (2007)

Constitutive equation [§3.2.5]: $\bar{\boldsymbol{\sigma}} = \bar{\mathbf{D}}_e \cdot (\bar{\boldsymbol{\varepsilon}} - \bar{\boldsymbol{\varepsilon}}^{add})$ or $\bar{\boldsymbol{\sigma}} = \bar{\mathbf{D}}_{sec} \cdot \bar{\boldsymbol{\varepsilon}}$

where $\bar{\mathbf{D}}_{sec} = \left[\mathbf{I} + \bar{\mathbf{D}}_e \cdot \left(\sum_{i=1}^{n_{int}^{m}} \frac{\omega_\alpha^{\mathrm{m}}}{1-\omega_\alpha^{\mathrm{m}}} \mathbf{N}_\sigma^{\mathrm{T}} \mathbf{C}_L \mathbf{N}_\sigma w_\alpha^{\mathrm{num}}\right)\right]^{-1} \cdot \bar{\mathbf{D}}_e$

Consistently-linearised constitutive tangent operator [§3.2.8]:

$$\bar{\mathbf{D}}_{tan} = \bar{\mathbf{D}}_{sec} \cdot \left[\mathbf{I} - \sum_{i=1}^{n_{int}^{m} | \dot{\zeta}_\alpha^{\mathrm{m}} > 0} \frac{1}{(1-\omega_\alpha^{\mathrm{m}})^2} \frac{d\omega_\alpha^{\mathrm{m}}}{d\zeta_\alpha^{\mathrm{m}}} \frac{d\zeta_\alpha^{\mathrm{m}}}{d\zeta_{\alpha,\mathrm{eff}}^{\mathrm{m}}} \mathbf{N}_\sigma^{\mathrm{T}} \mathbf{C}_L \mathbf{N}_\sigma \bar{\boldsymbol{\sigma}} \left\{\frac{\partial \zeta_{\alpha,\mathrm{eff}}^{\mathrm{m}}}{\partial \bar{\boldsymbol{\varepsilon}}_L}\right\}^{\mathrm{T}} \mathbf{N}_\varepsilon w_{int}^{\mathrm{num}}\right]$$

where $\mathbf{C}_L = \frac{1}{\bar{E}_{am}} \begin{bmatrix} 1 & 0 \\ 0 & \frac{2}{2-\bar{\upsilon}_{am}} \end{bmatrix}$ is simplified to account for plane-stress conditions ;

In every microcracking direction ($\alpha = 1 \ldots n_{int}^{m}$), as used for numerical integration:

Directional microcracking variable [§3.2.6]: $\omega_\alpha^{\mathrm{m}}(\zeta_\alpha^{\mathrm{m}}) = 1 - \frac{\zeta_0^{\mathrm{m}}}{\zeta_\alpha^{\mathrm{m}}} \exp\left\{- c_s \frac{\zeta_\alpha^{\mathrm{m}} - \zeta_0^{\mathrm{m}}}{u_{\max}/h_{el} - \zeta_0^{\mathrm{m}}}\right\}$

Microcracking surface [§3.2.7]: $\Theta_\alpha^{\mathrm{m}}(\zeta_{\alpha,\mathrm{eff}}^{\mathrm{m}}, \zeta_\alpha^{\mathrm{m}}) \equiv \zeta_{\alpha,\mathrm{eff}}^{\mathrm{m}} - \zeta_\alpha^{\mathrm{m}} \leq 0$

Microcracking strain [§3.2.7]: $\zeta_{\alpha,\mathrm{eff}}^{\mathrm{m}}(\bar{\boldsymbol{\varepsilon}}_L) = \frac{\bar{\varepsilon}_{rr}}{2}\left[1 + \left(\frac{\mu_\varepsilon}{r_\varepsilon}\right)^2\right] + \frac{1}{2r_\varepsilon^2}\sqrt{\left(r_\varepsilon^2 - \mu_\varepsilon^2\right)^2 \bar{\varepsilon}_{rr}^2 + 4 r_\varepsilon^2 \bar{\gamma}_L^2}$

Initialial effective microcracking strain [§3.2.7]: $\zeta_{\alpha,\mathrm{eff}}^{\mathrm{m}} \geq \zeta_0^{\mathrm{m}}$; $\zeta_0^{\mathrm{m}} \equiv \varepsilon_t^{\mathrm{m}} = \frac{{f_t}^{\mathrm{m}}}{\bar{E}_{am}}$

Microcracking growth irreversibility [§3.2.7]: $\dot{\zeta}_\alpha \geq 0$; $\Theta_\alpha^{\mathrm{m}} \leq 0$; $\Theta_\alpha^{\mathrm{m}} \cdot \dot{\zeta}_\alpha^{\mathrm{m}} = 0$

Caveat on Micromechanical model: Hereby, the basic components adopted at quadrature-level neglect the dilative response upon shearing on re-closed directional microcracks and the plastic irreversible deformation components upon full unloading. Although including such mechanical components may help in having more accurate predictive response of cementitious composites, e.g. in biaxial response (Jefferson and Bennett, 2010), the focus of this PhD was on tailoring the coupling strategies between the underlying micromechanical consitutive strategy and an EFEM appoach.

Box 3.2 Summary of EFEM model for embedded fracture propagation in quasi-brittle solids with elastic bulk, adapted from Alnaas (2016); Freeman et al. (2020).

Mechanical Balance (m.b.) equations [§3.3.11]:

m.b.1. Equilibrium: $\phi^{\text{el}}_{F,ck}(\mathbf{u}^{\text{el}}) \equiv \mathbf{F}^{\text{el}}_{\text{ext}} - \int_{\Omega\setminus\Gamma} \mathbf{B}^{\text{T}} \cdot \boldsymbol{\sigma} d\Omega = \mathbf{0} \quad ; \quad \boldsymbol{\sigma} = \mathbf{D}_e \cdot \left[\mathbf{B}\mathbf{u}^{\text{el}} - \mathbf{M}\hat{\mathbf{I}}\mathbf{W}\right]$

$$\therefore \left\{ \begin{array}{l} \textbf{Consistent tangent: } \left\{\mathbf{K}^{\text{el}}_{\text{EFEM}}\right\}_{ij} = \left\{\mathbf{K}^{\text{el}}_{\text{EFEM,sec}}\right\}_{ij} + \left(\dfrac{\partial\left\{\mathbf{K}^{\text{el}}_{\text{EFEM,sec}}\right\}_{ir}}{\partial \mathbf{u}^{\text{el}}_j}\right)\mathbf{u}^{\text{el}}_r \text{ (Eq. 3.74)} \\ \mathbf{K}^{\text{el}}_{\text{EFEM,sec}} = \int_{\Omega\setminus\Gamma} \left\{\mathbf{B} - \mathbf{M}\cdot\hat{\mathbf{I}}\cdot\mathbf{C}_\Gamma\right\}^{\text{T}} \cdot \mathbf{D}_e \cdot \left\{\mathbf{B} - \mathbf{M}\cdot\hat{\mathbf{I}}\cdot\mathbf{C}_\Gamma\right\} d\Omega + (\mathbf{C}_\Gamma)^{\text{T}} \cdot \hat{\mathbf{I}} \cdot \mathbf{K}_\Gamma \cdot \mathbf{C}_\Gamma \end{array} \right.$$

m.b.2. Quasi-static condensation: $\phi^{\text{el}}_w\left(\mathbf{u}^{\text{el}}\right) \equiv \mathbf{W}(\mathbf{u}^{\text{el}}) - \mathbf{C}_\Gamma \cdot \mathbf{u}^{\text{el}} = \mathbf{0}$ (Eq.3.67)

$$\text{where,} \quad \left. \begin{array}{l} \mathbf{C}_\Gamma\left(\mathbf{W}(\mathbf{u}^{\text{el}}), \mathbf{u}^{\text{el}}\right) = \left(\mathbf{B}_\Gamma\right)^{-1} \cdot \mathbf{A}_\Gamma \\ \mathbf{B}_\Gamma = \left(\int_{\Omega\setminus\Gamma} \mathbf{M}^{\text{T}} \cdot \mathbf{D}_e \cdot \mathbf{M} d\Omega\right) \cdot \hat{\mathbf{I}} + \mathbf{K}_\Gamma \\ \mathbf{A}_\Gamma = \int_{\Omega\setminus\Gamma} \mathbf{M}^{\text{T}} \cdot \mathbf{D}_e \cdot \mathbf{B} d\Omega \end{array} \right\} \iff \overset{*}{\frac{\partial \Pi_{int}}{\partial \mathbf{W}}} = \mathbf{0} \quad \text{(Energy minimisation)}$$

Kinematic-enhancement (k.e.) with embedded band [§3.3.5]:

k.e.1. Enriched nodal displacement: $\mathbf{u}_{c,inode} = \mathbf{u}_{inode} - H_\Omega(\mathbf{x}_{inode}) \otimes [|\mathbf{u}|]_{inode}\left(\mathbf{x}_{inode}\right)$

$$\text{where } \mathbf{u}^{\text{el}}_c = \left\{ \begin{array}{c} \mathbf{u}_{c,\text{node1}} \\ \hdashline \mathbf{u}_{c,\text{node2}} \\ \hdashline \vdots \\ \hdashline \mathbf{u}_{c,\text{nnode}} \end{array} \right\} = \left\{ \begin{array}{c} \mathbf{u}_{\text{node1}} \\ \hdashline \mathbf{u}_{\text{node2}} \\ \hdashline \vdots \\ \hdashline \mathbf{u}_{\text{nnode}} \end{array} \right\} - \left\{ \begin{array}{c} H_\Omega(\mathbf{x}_{\text{node1}}) \otimes \mathbf{T}_w(\mathbf{x}_{\text{node1}}) \\ \hdashline H_\Omega(\mathbf{x}_{\text{node2}}) \otimes \mathbf{T}_w(\mathbf{x}_{\text{node2}}) \\ \hdashline \vdots \\ \hdashline H_\Omega(\mathbf{x}_{\text{nnode}}) \otimes \mathbf{T}_w(\mathbf{x}_{\text{nnode}}) \end{array} \right\} \cdot \hat{\mathbf{I}} \cdot \mathbf{W}$$

k.e.2. Strain: $\boldsymbol{\varepsilon} = \mathbf{B}\mathbf{u}^{\text{el}}_c = \mathbf{B}\mathbf{u}^{\text{el}} - \underbrace{\left(\sum^{nnode} \mathbf{B}_{inode} H_\Omega(\mathbf{x}_{inode}) \otimes \mathbf{T}_w(\mathbf{x}_{inode})\right)}_{\mathbf{M}} \hat{\mathbf{I}}\mathbf{W}$ (Eq.3.36)

$$\text{where } \mathbf{B}_{inode} = \begin{bmatrix} \partial_x N_{inode} & 0 \\ 0 & \partial_y N_{inode} \\ \partial_y N_{inode} & \partial_x N_{inode} \end{bmatrix}, \text{ and } H_\Omega(\mathbf{x} \in \boldsymbol{\Omega}^+) = 1 \text{ while } H_\Omega(\mathbf{x} \in \boldsymbol{\Omega}^-) = 0$$

Embedded localisation band (e.mc.) [§3.3.6]:

e.mc.1. Equivalent crack force: $\mathbf{F}_{\text{ck}} = \mathbf{K}^e_\Gamma \cdot \mathbf{W}^e = \mathbf{K}_\Gamma \cdot \mathbf{W}$ (Eq. 3.40)

$$\text{where, } \mathbf{K}_\Gamma = \frac{E \cdot t_g}{h_{ca}} \begin{bmatrix} \int_{\partial\Gamma}(1-\omega)dl & 0 & \int_{\partial\Gamma}(1-\omega)l dl \\ & \int_{\partial\Gamma} \frac{1-\omega}{2(1+\upsilon)} dl & 0 \\ \text{symm} & & \int_{\partial\Gamma}(1-\omega)l^2 dl \end{bmatrix}$$

$$\text{and } \mathbf{K}^e_\Gamma = \frac{E \cdot t_g}{h_{ca}} \begin{bmatrix} \int_{\partial\Gamma} dl & 0 & \int_{\partial\Gamma} l dl \\ & \int_{\partial\Gamma} \frac{1}{2(1+\upsilon)} dl & 0 \\ \text{symm} & & \int_{\partial\Gamma} l^2 dl \end{bmatrix}, \text{ while } \omega \in [0,1]$$

e.mc.2 Inelastic relative displacement: $\widehat{\mathbf{W}} = \left(\mathbf{I} - (\mathbf{K}^e_\Gamma)^{-1} \cdot \mathbf{K}_\Gamma\right) \cdot \mathbf{W} = \hat{\mathbf{I}} \cdot \mathbf{W}$

with ω as Smooth Unloading-Reloading (SUR) law [§3.3.7]

3.6 Concluding remarks

In this chapter, an introductory theory for macroscopic damage and micromechanical degradation based on the use of mechanical defects was described. This covered more precisely stress and strain fields in a continuum with embedded stress-free ellipsoids, which represent (a series of diffuse aligned) microcracks.

Then, the research gap identified in the previous chapter was addressed by the investigation of a Micromechanics model and an element with embedded strong discontinuities. These methods are described thoroughly before coupling details and implementation guidelines are presented in the next chapter.

The micromechanical homogenisation scheme belongs to the series of models developed by Jefferson and Bennett (2010, 2007); Mihai and Jefferson (2011), whereas the embedded strong discontinuity method has been recently under development in-house at Cardiff University (Freeman et al., 2020; Jefferson and Freeman, 2022), and in this study the variational nature of this specialised EFEM model has been exploited.

From the analysis of compatibility some hypotheses have been drawn. In such a novel coupled methodology, the underlying micromechanics is envisaged to evolve independently of deformation localisation at macroscale. Therefore, avoiding "ad-hoc" phenomenological criteria for constraining directionality of microscale degradation is desirable in these new type of scale-bridging strategies.

N.B.: The author has implemented the micro and macro-based models for quasi-brittle fracture modelling, which are described in detail and tested numerically in this Chapter, in such a way that the models could be used separately. This eased the study of compatibility of both models from a numerical and implementation standpoint, and helped in tailoring initial ideas to develop a robust coupling strategy, which is described in detail in the next Chapter.

Chapter 4

Variationally-consistent coupling of Micromechanics & EFEM

> *"All the effects of Nature are only the mathematical consequences of a small number of immutable laws."*
>
> **Pierre Simon Laplace** 1749 - 1827
>
> French Mathematician and pioneer of the Mathematical Principles of Mechanics

4.1 Seamless micro-macro fracture mechanics model

This chapter focuses on developing a Micromechanics-enriched variationally-consistent framework, which enables a diffuse-to-localised representation of fracture propagation in quasi-brittle solids, with emphasis on cementitious composites and structures. This naturally follows the analysis of micro and macro model components in Section 3.2 and Section 3.3 in the previous Chapter. Localised fracture is addressed using an element-based strong discontinuity approach (EFEM) (Armero and Linder, 2009; Freeman et al., 2020; Oliver et al., 2003; Simo et al., 1993). This is considered more convenient than the X-FEM method (Belytschko and Black, 1999; Moës et al., 1999; Oliver et al., 2006) because the number of degrees of freedom in the assembled global matrix system do not change throughout the analysis and no remeshing is required. The key contribution is the seamless coupling of these two computational components, enabling simultaneous updates of micro- and macromechanical states:

- **Micromechanical continua**: An enriched continua is employed for the bulk, hereafter referred as a Micromechanical continua, which combines Eshelby's theory for micromechanical inclusions (Eshelby, 1957; Mura, 1987) and computational homogenisation schemes (Jefferson and Bennett, 2010, 2007). The Micromechanical framework enables diffuse directional microcracking evolution along with macroscopic crack propagation. Conveniently, the use of this Micromechanical framework circumvents the need for a multigrid approach.

- **Embedded (macro) strong discontinuities**: Deformation localisation, manifesting as nucleating cracks, is simulated using embedded strong discontinuities in a variational setting at the global scale (Armero and Linder, 2009; Freeman et al., 2020; Oliver et al., 2003; Simo et al., 1993). The variational principle exploited here assumes a minimum energetic state of the micro and macro components simultaneously. Energy minimisation serves as a means to condense additional degrees of freedom at the element level.

4.2 Variational micro-to-macro coupling in EFEM

At first the BVP of a micromechanical solid with embedded strong discontinuities is described. Such a problem represents an extension to that in Section 3.3.1 by adding a Micromechanics constitutive model at the bulk domain as described in Section 3.2.5. Then, emphasis is placed in describing modifications to both components. In this regard, it is often shown that some changes to the departing framework components are small, although these are needed to account for multiscale concepts.

Later, a variational principle is exploited in Section 4.2.7 as a means to update macrocrack degrees of freedom through quasi-static condensation. This energy minimisation procedure ensures that micro and macro mechanical state variables are updated simultaneously at the element-level. An artifice is used in representing homogenised stresses $\bar{\boldsymbol{\sigma}}$ in the bulk in such a way that the new derivation follows closely the steps as that shown in Section 3.3.10.

In addition, Section 4.3 describes algorithms that govern the mechanical components of the new formulation including the global incremental iterative solution of the coupled system, the iterative solution of the element-based quasi-static condensation procedure and other associated operations such as the computations of stresses and the equivalent force of an embedded macrocrack, as well as other relevant computational procedures such as macrocrack tracking and techniques for robust implementation.

4.2.1 Governing equation of BVP for Micromechanical solid with embedded discontinuities

Let the body $\boldsymbol{\Omega}^{\mathrm{M}}$ in Figure 4.1 be constituted by a solid with micromechanical constituents that can evolve along with an embedded macrocrack. Reference Volume subdomains $\boldsymbol{\Omega}^{\mathrm{m}}$ (RVEs) depict a representative portion of the body that can capture the macroscopic response sufficiently accurately. The BVP is solved for the displacement field $\mathbf{u} : \boldsymbol{\Omega}^{\mathrm{M}} \times (0, T] \rightarrow \mathrm{I\!R}^2$, where $t \in (0, T]$. Considering macroscopic response to be quasi-static, while body forces are sufficiently small compared with externally-induced forces, equilibrium gives the conditions stated in Equation 4.1.

$$\left.\begin{array}{lcr}
\text{1 Momentum balance:} & \mathbf{Div}[\bar{\boldsymbol{\sigma}}] = \mathbf{0} & \text{in } \boldsymbol{\Omega}^{\mathrm{M}} \\
\text{2 Constitutive relation:} & \bar{\boldsymbol{\sigma}} = \bar{\boldsymbol{D}}_{sec} : \bar{\boldsymbol{\varepsilon}} & \text{in } \boldsymbol{\Omega}^{\mathrm{M}} \backslash \boldsymbol{\Gamma}^{\mathrm{M}} \\
\text{3 Kinematic relation:} & \bar{\boldsymbol{\varepsilon}} = \nabla^s \mathbf{u} = \nabla^s (\mathbf{u}_c + H_{\Omega} \otimes [|\mathbf{u}|]) & \text{in } \boldsymbol{\Omega}^{\mathrm{M}} \ \backslash \boldsymbol{\Gamma}^{\mathrm{M}} \\
\text{4 Traction continuity:} & \bar{\boldsymbol{\sigma}}_{\Omega^+} \cdot \mathbf{n}^+_{\Gamma^{\mathrm{M}}} + \bar{\boldsymbol{\sigma}}_{\Omega^-} \cdot \mathbf{n}^-_{\Gamma^{\mathrm{M}}} = \mathbf{0} & \text{on } \partial \boldsymbol{\Gamma}^{\mathrm{M}} \\
\text{5 Traction equilibrium:} & \bar{\boldsymbol{\sigma}}_{\Omega^+} \cdot \mathbf{n}^+_{\Gamma^{\mathrm{M}}} + \mathbf{t}_{\Gamma^{M+}} = \mathbf{0} & \text{on } \partial \boldsymbol{\Gamma}^{\mathrm{M}} \\
\text{6 Natural boundary condition:} & \bar{\boldsymbol{\sigma}} \cdot \mathbf{n}_{\partial \Omega^{\mathrm{M}}_{\sigma}} - \check{\mathbf{t}} = \mathbf{0} & \text{on } \partial \boldsymbol{\Omega}^{\mathrm{M}}_{\sigma} \\
\text{7 Essential boundary condition:} & \mathbf{u} = \check{\mathbf{u}} & \text{on } \partial \boldsymbol{\Omega}^{\mathrm{M}}_{u}
\end{array}\right\} \tag{4.1}$$

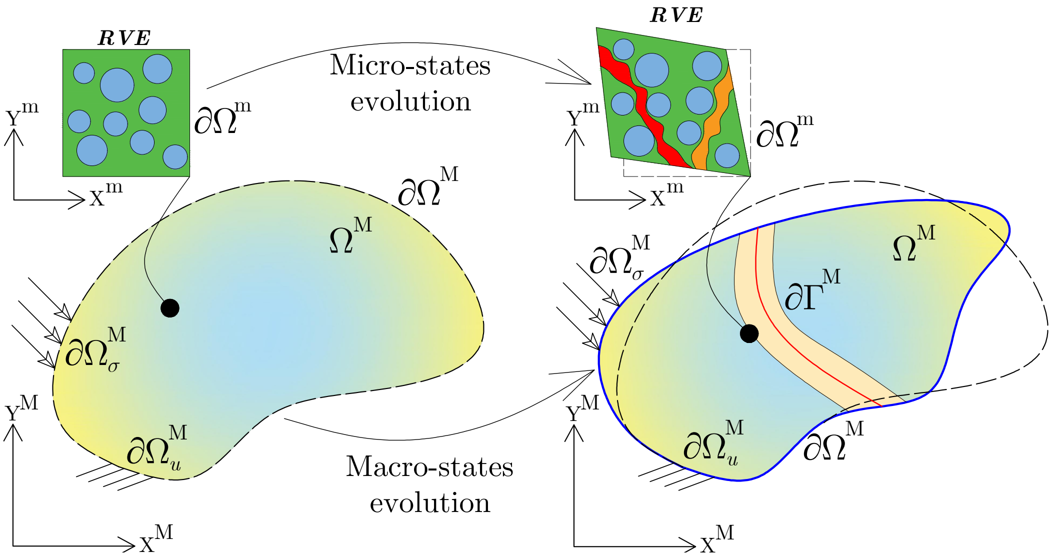

Figure 4.1: Fracture in quasi-brittle solids across two interacting length-scales.

where clear distinction between the Equations 4.1 and 3.22 exists by adopting a homogenised constitutive response as described in Equation 3.13 into Equation 4.1-2.

In this regard, the elastic constants are defined as $\bar{E}_{am}$ and $\bar{\upsilon}_{am}$ for the homogenised aggregate-matrix response, and these govern the response of the homogenised Continuum in intact state as well as that of the undamaged embedded macrocrack band. More details on how the homogenised strains are downscaled due to the embedded strong discontinuity kinematics (Freeman et al., 2020) are described in Section 4.2.4.

4.2.2 Computational homogenisation in a micromechanical continua within a multiscale EFEM framework

The homogenised constitutive equation remains in its mathematical form with all its constituents in tensor as well as matrix notation, as defined previously in Section 3.2.5. Nonetheless, a minor change has been made to provide a consistent homogenised response which is mesh insensitive within pre-peak regime, opposed to a mesh sensitive response around peak response when the micromechanical model uses a simple crack band approach as shown in Section 3.4.3.2. In this regard, the rate of evolution of microcracking has been made independent of the element size as highlighted in Section 4.2.2.1. This minor change has modified only one equation from the homogenisation scheme, and has little implications in stress recovery as well as in the computations of tangents of uncracked elements as described in Section 4.2.2.2. The computational aspects of stress recovery in the micromechanical bulk are explained in Section 4.3.3.

4.2.2.1 Directional microcracking growth at the bulk domain in multiscale EFEM

The micromechanical model in the present work is based on the microcracking growth law in Equation 3.17 which was first given in Jefferson and Bennett (2010, 2007); Mihai and Jefferson (2011); however, a few modifications are described here that ensure the consistency between macro and micro cracking models.

A key improvement to the model, as presented in this thesis, lies in the adjustment of the relationship for directional microcrack density $\mathscr{F}_{\alpha}(\omega_{\alpha}^{\mathrm{m}}(\bar{\boldsymbol{\varepsilon}}))$ to render softening objectively at the structural-level, as a consequence of combined action of directional microcracking and macroscopic fracture as illustrated in Figure 4.2.

In this regard, the growth of microcracks is slowed or fully arrested by the occurrence of macroscopic cracks, which is underpinned on the philosophy of macrocracks interacting with sub-parallel coalescing microcracks (Ortiz, 1988), compared to the case of microcracking-only driven degradation.

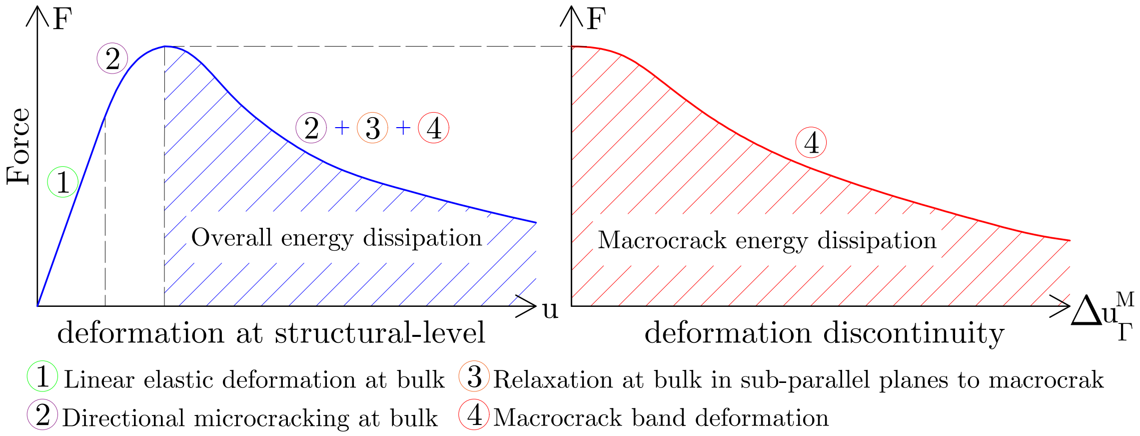

Figure 4.2: Softening response and energy dissipation in a micromechanical solid under quasi-brittle fracture. Energy dissipation is underpinned on directional microcracking, macro-to-microcrack shielding and unloading, and macrocrack evolution.

Hence, the characteristic length parameter at micro-scale h_{fa} is introduced in the evolution law of directional microcracking scalar variables $\omega_\alpha^{\mathrm{m}}(\bar{\boldsymbol{\varepsilon}})$ in Equation 4.2, which supersedes that in Equation 3.17:

$$\omega_\alpha^{\mathrm{m}}(\zeta_\alpha^{\mathrm{m}}(\bar{\boldsymbol{\varepsilon}})) = 1 - \frac{\varepsilon_t^{\mathrm{m}}}{\zeta_\alpha^{\mathrm{m}}} \exp\left[-c_s \frac{\zeta_\alpha^{\mathrm{m}} - \varepsilon_t^{\mathrm{m}}}{u_{max}/h_{fa} - \varepsilon_t^{\mathrm{m}}}\right], \quad \zeta_\alpha^{\mathrm{m}} \geq \varepsilon_t^{\mathrm{m}} \tag{4.2}$$

where u_{max} is still treated as the maximum displacement discontinuity that can be observed due to fracture at the macroscopic level before collapse, and a (constant) characteristic length-scale parameter at micro-scale is defined as h_{fa}. This new type of normalisation of u_{max} into an ultimate strain within the micromechanical degradation evolution law $\omega_\alpha^{\mathrm{m}}(\bar{\boldsymbol{\varepsilon}})$ is made to ensure a slower microcracking growth specially during post-peak response, as compared to original models (Jefferson and Bennett, 2010, 2007). The characteristic length-scale parameter at micro-scale h_{fa} is set in the range of a few times the size of the finer aggregate, although it is used more precisely as a numerical parameter in this thesis. In practice, this new characteristic length can be set to a fraction of the macrocrack band width, so that deformation localisation occurs at the macro-scale with $h_{fa} \approx (1/5) \cdot h_{ca}$ being a good first estimate.

N.B.: Since the microcracking growth rate is dominating within the pre-peak structural response and this evolution has been made independent of the element size, fracture energy is expected to be preserved, with the embedded macrocrack now dominating the structural peak as well the post-peak response (opposed to undesirable dependency of peak states in crack band approaches in Section 3.4.3.2).

4.2.2.2 Material tangent stiffness in the Micromechanical bulk in uncracked elements in multiscale EFEM

The aforementioned modification of the microcracking growth law $\omega_\alpha^{\mathrm{m}}(\zeta_\alpha^{\mathrm{m}}(\bar{\boldsymbol{\varepsilon}}))$ implies that the partial derivative $\frac{\partial \omega_\alpha^{\mathrm{m}}}{\partial \zeta_\alpha^{\mathrm{m}}}$ in the material tangent $\bar{\mathbf{D}}_{tan}$ at the bulk domain from Equation 3.20 changes to the following expression:

$$\frac{\partial \omega_\alpha^{\mathrm{m}}}{\partial \zeta_\alpha^{\mathrm{m}}} = \left(1 - \omega_\alpha^{\mathrm{m}}\right)\left[\frac{1}{\zeta_\alpha^{\mathrm{m}}} + \frac{c_s}{u_{max}/h_{fa} - \varepsilon_t^{\mathrm{m}}}\right] \tag{4.3}$$

Note that the mathematical definition of the tangent $\bar{\mathbf{D}}_{tan}$, including all other variables and derivatives in Equation 3.20 remain unchanged in uncracked elements in the new multiscale EFEM. In this case, the consistent tangent $\bar{\mathbf{D}}_{tan}$ is only used when micro and macro variables across the Fracture Process Zone (FPZ) are on its way to get settled (see comment box below).

N.B.: A secant stiffness $\bar{\mathbf{D}}_{sec}$ from Equation 3.13 replaces the micromechanics-derived consistent tangent $\bar{\mathbf{D}}_{tan}$, for the first **itfix** global iterations. The consistent tangent in uncracked and cracked elements is simultaneoulsy as described in Section 4.3.5.2.

4.2.3 Degrees of Freedom associated with an embedded localisation band in multiscale EFEM

The dofs $\mathbf{W} = [u_{rc}, u_{sc}, \alpha_c]^{\mathrm{T}}$ as described in Section 3.3.2 are applied to impose a fracture-induced rigid body motion to the positive part of the domain $\boldsymbol{\Omega}^{+}$ as shown in Figure 4.3.

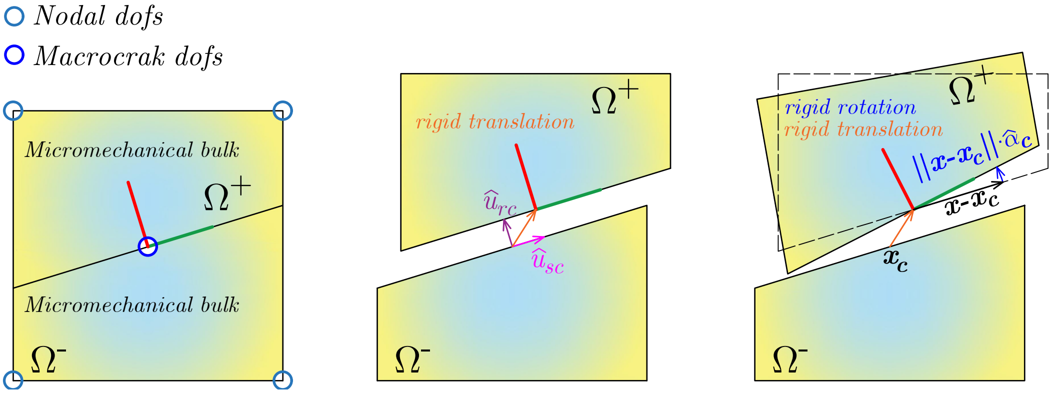

Figure 4.3: Superposition of rigid body motion of $\boldsymbol{\Omega}^{+}$ induced by small deformation at the macrocrack level in multiscale EFEM. The superposition of macrocrack induced deformation $H_{\Omega} \otimes [|\mathbf{u}|](\mathbf{x})$ is superposed onto the continuous deformation field $\mathbf{u}_c(\mathbf{x})$: original configuration (left), fracture-induced rigid translation (centre), and fracture-induced translation and rotation (right)

This fracture-induced displacement $H_{\Omega} \otimes [|\mathbf{u}|](\mathbf{x})$ is superposed on the continuous displacement field $\mathbf{u}_c$ due to (nonlinear) deformation of the homogenised Continuum. Therefore, Equations 3.23 to 3.25 remain applicable to the coupled multiscale EFEM model.

4.2.4 On embedded strong discontinuity kinematics for multiscale crack propagation

The continuum strain $\bar{\boldsymbol{\varepsilon}}$ is taken as that one considering the rigid body motion of the positive part of the domain $\boldsymbol{\Omega}$, and therefore, it considers there is a relaxation of the continuum due to the embedded strong discontinuity, as opposed to standard strain computations. This is equivalent to the mathematical operation presented in Equation 3.26, with the only difference that the strain $\bar{\boldsymbol{\varepsilon}}$ is now considered to be the volume-average at any material point within the micromechanical Continuum. For consistency in notation of superscripts M denoting a 'macro' term, the strain reads as follows:

$$\bar{\boldsymbol{\varepsilon}} = \nabla^s \mathbf{u} = \underbrace{\nabla^s \mathbf{u}_c}_{\text{regular}} + \underbrace{\left([|\mathbf{u}|] \otimes (\delta_{\Gamma^{\mathrm{M}}} \otimes \mathbf{n}_{\Gamma^{\mathrm{M}}})\right)^s}_{= \mathbf{0} \text{ , only unbounded in } \Gamma^{\mathrm{M}}}, \quad \text{in } (\boldsymbol{\Omega}^+ \cup \boldsymbol{\Omega}^-) \backslash \boldsymbol{\Gamma}^{\mathrm{M}} \tag{4.4}$$

Similarly, the interpolation of the continuous displacement field and its gradient fields using FE approximations from Sections 3.3.4 and 3.3.5 are admissible for the multiscale formulation. Therefore, the continuum strain $\bar{\boldsymbol{\varepsilon}}$ at Gauss Points within the micromechanical bulk is equivalent to that of Equation 3.36, and reads as follows:

$$\bar{\boldsymbol{\varepsilon}} = \mathbf{B} \cdot \mathbf{u}^{\mathrm{el}} - \widehat{\mathbf{M}} \cdot \mathbf{W}, \quad \text{in } (\boldsymbol{\Omega}^+ \cup \boldsymbol{\Omega}^-) \backslash \boldsymbol{\Gamma}^{\mathrm{M}} \tag{4.5}$$

where $\widehat{\mathbf{M}}(\mathbf{M}, \widehat{\mathbf{I}}(\mathbf{K}_{\Gamma}^{e}, \mathbf{K}_{\Gamma}))$ from Equation 3.34 and $\widehat{\mathbf{I}}$ from Equation 3.23 are now computed using the matrices defined in Equations 4.9 and 4.10.

4.2.5 Local tractions in embedded strong discontinuities and the equivalent crack force in multiscale EFEM

In the multiscale approach the phenomenological damage-informed response $\mathbf{t}'_{\Gamma^{\mathrm{M}+}}$ from Section 3.3.6, the adoption of an SUR method from Section 3.3.7 for the evolution of damage $\omega^{\mathrm{M}}(\zeta^{\mathrm{M}}, \zeta^{\mathrm{M}}_{eff})$ at the embedded localisation band, as well as the computation of the equivalent macrocrack relative displacement terms ζ^{M} and ζ^{M}_{eff}

from Section 3.3.8 remains as for the standard finite element with embedded discontinuities, i.e. Equations 3.37 to 3.51 are admissible.

The only minor changes in the new formulation correspond to the nomenclature of the macroscopic scalar damage variable ω^{M}, the equivalent macrocracking relative displacement ζ^{M} and ζ^{M}_{eff}, which are now defined with a superscript M to clarify that the embedded macrocrack acts at the macroscale, i.e. within the element-level. Note that the intact homogenised continuum and its projected response within the undamaged macrocrack band is characterised within an elastic response dominated by the material constants for the mixture $\bar{E}_{am}$ and $\bar{\upsilon}_{am}$.

Following this explanation on the nomenclature for evolution terms within the macrocrack, the traction separation law for the embedded macrocrack band is equivalent to that in Equation 3.37, and now reads as follows :

$$\mathbf{t}'_{\Gamma^{\mathrm{M}+}}(x') = \frac{1-\omega^{\mathrm{M}}(x')}{h_{ca}} \begin{bmatrix} \bar{E}_{am} & 0 \\ 0 & \bar{E}_{am}/(2(1+\bar{\upsilon}_{am})) \end{bmatrix} \Delta\mathbf{u}_{\Gamma^{\mathrm{M}}}(x'), \quad \forall x' \in \partial\Gamma^{\mathrm{M}} \tag{4.6}$$

$$\left.\begin{aligned} \Delta\mathbf{u}_{\Gamma^{\mathrm{M}}}(x') &= \mathbf{\Lambda}\cdot\mathbf{W}, \quad \forall x' \in \partial\Gamma^{\mathrm{M}} \\ \mathbf{\Lambda} &= \begin{bmatrix} 1 & 0 & l(x' \text{ on } \partial\Gamma^{\mathrm{M}}) \\ 0 & 1 & 0 \end{bmatrix} \end{aligned}\right\} \tag{4.7}$$

Therefore, following the integration of tractions, as done to obtain Equation 3.40, the equivalent macrocrack force $\mathbf{F}_{ck}$ is now computed with the new matrices $\mathbf{K}_{\Gamma}$ and $\mathbf{K}^{e}_{\Gamma}$ as shown below:

$$\mathbf{F}_{\mathrm{ck}} = \left[F_{rc}, F_{sc}, M_{c}\right]^{\mathrm{T}} = \mathbf{K}_{\Gamma}\mathbf{W} = \mathbf{K}^{e}_{\Gamma}\{\mathbf{W} - \widehat{\mathbf{W}}\}, \quad \text{at the centre of } \partial\Gamma^{\mathrm{M}} \tag{4.8}$$

$$\mathbf{K}_{\Gamma} = \frac{\bar{E}_{am}\cdot t_{g}}{h_{ca}} \left[\begin{array}{c:c:c} \int_{\partial\Gamma^{\mathrm{M}}}(1-\omega^{\mathrm{M}})dl & 0 & \int_{\partial\Gamma^{\mathrm{M}}}(1-\omega^{\mathrm{M}})l dl \\ \hdashline & \int_{\partial\Gamma^{\mathrm{M}}} \frac{1-\omega^{\mathrm{M}}}{2(1+\bar{\upsilon}_{am})}dl & 0 \\ \hdashline \text{symm} & & \int_{\partial\Gamma^{\mathrm{M}}}(1-\omega^{\mathrm{M}})l^{2}dl \end{array}\right] \tag{4.9}$$

$$\mathbf{K}^{e}_{\Gamma} = \frac{\bar{E}_{am}\cdot t_{g}}{h_{ca}} \left[\begin{array}{c:c:c} \int_{\partial\Gamma^{\mathrm{M}}} dl & 0 & \int_{\partial\Gamma^{\mathrm{M}}} l dl \\ \hdashline & \int_{\partial\Gamma^{\mathrm{M}}} \frac{1}{2(1+\bar{\upsilon}_{am})}dl & 0 \\ \hdashline \text{symm} & & \int_{\partial\Gamma^{\mathrm{M}}} l^{2}dl \end{array}\right] \tag{4.10}$$

where the computational aspects of the updates of scalar macrocracking variables $\omega^{\mathrm{M}}(\zeta^{\mathrm{M}}, \zeta^{\mathrm{M}}_{eff})$ are explained in Section 4.3.4.1, while the updates of the equivalent macrocracking relative displacement terms ζ^{M} and ζ^{M}_{eff} are described in Section 4.3.4.2.

4.2.6 Weak form of BVP for micromechanical solid with embedded strong discontinuities: a variational approach

The energy based functional for a solid with embedded strong discontinuities in Equation 3.55 as derived in Section 3.3.9 is recalled, for the general case of a micromechanical bulk domain $\boldsymbol{\Omega}^{+} \cup \boldsymbol{\Omega}^{-}$:

$$\delta\Psi_{\Omega\backslash\Gamma} = \underbrace{\int_{\Omega\backslash\Gamma} \underbrace{\nabla^{s}(\delta\mathbf{u}_{c})}_{\bar{\boldsymbol{\varepsilon}}} : \bar{\boldsymbol{\sigma}} d\Omega + \int_{\partial\Gamma^{+}} \delta[|\mathbf{u}|] \cdot \mathbf{t}_{\Gamma^{+}} d\Gamma}_{\overset{*}{\delta\Pi}_{int}} \underbrace{- \int_{\Omega} \delta\mathbf{u} \cdot \boldsymbol{b} d\Omega - \int_{\partial\Omega_{\sigma}} \delta\mathbf{u} \cdot \mathbf{t}_{\partial\Omega} dS}_{-\delta\Pi_{ext}} = 0 \tag{4.11}$$

where the minimisation of the functional in Equation 4.11 leads to the required minimum energy solution:

$$\underset{in\ \boldsymbol{\Omega}\backslash\boldsymbol{\Gamma}}{\mathbf{minimise}} \left\{ \int_{\Omega\backslash\Gamma} \nabla^{s}(\delta\mathbf{u}_{c}) : \bar{\boldsymbol{\sigma}} d\Omega + \int_{\partial\Gamma^{+}} \delta[|\mathbf{u}|] \cdot \mathbf{t}_{\Gamma^{+}} d\Gamma - \int_{\Omega} \delta\mathbf{u} \cdot \boldsymbol{b} d\Omega - \int_{\partial\Omega_{\sigma}} \delta\mathbf{u} \cdot \mathbf{t}_{\partial\Omega} dS \right\} \tag{4.12}$$

Therefore, the functional for the internal energy which satisfies this variational statement reads as follows:

$$\boxed{\delta\Pi_{int} := \underset{in\ \boldsymbol{\Omega}\backslash\boldsymbol{\Gamma}}{\mathbf{inf}} \left\{ \overset{*}{\delta\Pi}_{int} \right\} = \underset{in\ \boldsymbol{\Omega}\backslash\boldsymbol{\Gamma}}{\mathbf{inf}} \left\{ \underbrace{\int_{(\Omega^{+}\cup\Omega^{-})\backslash\Gamma} \nabla^{s}(\delta\mathbf{u}_{c}) : \bar{\boldsymbol{\sigma}} d\Omega}_{\text{homogenised strain energy}} + \underbrace{\int_{\partial\Gamma^{+}} \delta[|\mathbf{u}|] \cdot \mathbf{t}_{\Gamma^{+}} d\Gamma}_{\text{macro-fracture energy}} \right\}} \tag{4.13}$$

where this functional possesses a homogenised strain energy component, exerted by the micromechanical continua, and a macro-fracture energy component, induced by the embedded strong discontinuity at the element-level.

4.2.7 Variational Finite Element setting of micromechanical solids with embedded strong discontinuities

In the following derivations, the homogenised stress $\bar{\boldsymbol{\sigma}} = \bar{\mathbf{D}}_{\mathrm{sec}} \cdot \bar{\boldsymbol{\varepsilon}}$ in vector form is conveniently used in combination with a homogenised secant stiffness matrix from

Section 4.2.2. Although other ways could be used to recover stresses for a micromechanical solid, such an artifice allows a derivation of the minimum-energy variational solution of the PDEs by following closely the steps shown in Section 3.3.10. Therefore, by using Equation 4.13, the following expression is obtained:

$$\overset{*}{\delta\Pi}_{int}(\mathbf{u}^{\mathrm{el}},\mathbf{W}) = \int_{\Omega\backslash\Gamma}\left(\delta\bar{\boldsymbol{\varepsilon}}^{\mathrm{T}}\bar{\mathbf{D}}_{\mathrm{sec}}\bar{\boldsymbol{\varepsilon}}\right)d\Omega + \delta\widehat{\mathbf{W}}^{\mathrm{T}}\mathbf{F}_{\mathrm{ck}} \tag{4.14}$$

Also the full variational statement in Equation 4.11 in combination with the mechanical equilibrium condition in Equation 4.12 give:

$$\left.\begin{aligned} \delta\Psi_{\Omega\backslash\Gamma} &= \delta\Pi_{ext} - \delta\Pi_{int} = 0 \\ \delta\Pi_{ext} &= \{\delta\mathbf{u}^{\mathrm{el}}\}^{\mathrm{T}}\mathbf{F}^{\mathrm{el}}_{\mathrm{ext}} \\ \delta\Pi_{int} &= \underset{in\ \Omega\backslash\Gamma}{\mathbf{inf}}\left\{\overset{*}{\delta\Pi}_{int}\right\} \end{aligned}\right\} \tag{4.15}$$

Combining the expansion of the strain vector considering strong-discontinuity kinematic enhancement $\bar{\boldsymbol{\varepsilon}} = \mathbf{B}\mathbf{u}^{\mathrm{el}} - \mathbf{M}\widehat{\mathbf{W}}$ from Equation 4.5 and the equivalence $\boldsymbol{\delta}\widehat{\mathbf{W}} = \hat{\mathbf{I}}\cdot\boldsymbol{\delta}\mathbf{W}$ from Equation 3.23 into Equation 4.14 gives:

$$\overset{*}{\delta\Pi}_{int}(\mathbf{u}^{\mathrm{el}},\mathbf{W}) = \{\delta\mathbf{u}^{\mathrm{el}}\}^{\mathrm{T}}\underbrace{\left\{\int_{\Omega\backslash\Gamma}\mathbf{B}^{\mathrm{T}}\bar{\mathbf{D}}_{\mathrm{sec}}\bar{\boldsymbol{\varepsilon}}d\Omega\right\}}_{\partial\overset{*}{\Pi}_{int}/\partial\mathbf{u}^{\mathrm{el}}} + \{\delta\mathbf{W}\}^{\mathrm{T}}\cdot\underbrace{\hat{\mathbf{I}}\cdot\left\{\mathbf{F}_{\mathrm{ck}} - \int_{\Omega\backslash\Gamma}\mathbf{M}^{\mathrm{T}}\bar{\mathbf{D}}_{\mathrm{sec}}\bar{\boldsymbol{\varepsilon}}d\Omega\right\}}_{\partial\overset{*}{\Pi}_{int}/\partial\mathbf{W}=\mathbf{0}} \tag{4.16}$$

where a local minimum of $\overset{*}{\delta\Pi}_{int}$ is obtained from fixing displacement field $\mathbf{u}^{\mathrm{el}}$ by using $\delta\mathbf{u}^{\mathrm{el}} = \mathbf{0}$ in Equation 4.16, while enforcing the constraint $\overset{*}{\delta\Pi}_{int} = 0$, and this gives an expression for quasi-static condensation of $\mathbf{W}$:

$$\left.\begin{aligned} \boldsymbol{\phi}^{\mathrm{el}}_{w}(\mathbf{W}) &:= \mathbf{W} - \mathbf{C}_{\Gamma}(\mathbf{W},\mathbf{u}^{\mathrm{el}})\mathbf{u}^{\mathrm{el}} = \mathbf{0} \\ \mathbf{C}_{\Gamma}(\mathbf{W},\mathbf{u}^{\mathrm{el}}) &= \left\{\mathbf{K}_{\Gamma} + \underbrace{\left\{\int_{\Omega\backslash\Gamma}\mathbf{M}^{\mathrm{T}}\bar{\mathbf{D}}_{\mathrm{sec}}\mathbf{M}d\Omega\right\}}_{\mathbf{B}^{*}_{\Gamma}}\cdot\hat{\mathbf{I}}\right\}^{-1}\underbrace{\left\{\int_{\Omega\backslash\Gamma}\mathbf{M}^{\mathrm{T}}\bar{\mathbf{D}}_{\mathrm{sec}}\mathbf{B}d\Omega\right\}}_{\mathbf{A}_{\Gamma}} \end{aligned}\right\} \tag{4.17}$$

Combining Equations 4.15 to 4.17, a variational multiscale equilibrium equation for fracture propagation is derived:

$$\left.\begin{aligned} \boldsymbol{\phi}^{\mathrm{el}}_{F}(\mathbf{u}^{\mathrm{el}}) &:= \mathbf{F}^{\mathrm{el}}_{\mathrm{ext}} - \mathbf{F}^{\mathrm{el}}_{\mathrm{int}}(\mathbf{u}^{\mathrm{el}}) = \mathbf{0} \\ \mathbf{F}^{\mathrm{el}}_{\mathrm{int}}(\mathbf{u}^{\mathrm{el}}) &:= \int_{\Omega}\mathbf{B}^{\mathrm{T}}\bar{\mathbf{D}}_{\mathrm{sec}}\left\{\mathbf{B}\mathbf{u}^{\mathrm{el}} - \widehat{\mathrm{M}}\mathbf{W}\right\}d\Omega\ , \quad \mathbf{W} = \mathbf{C}_{\Gamma}(\mathbf{W},\mathbf{u}^{\mathrm{el}})\cdot\mathbf{u}^{\mathrm{el}} \end{aligned}\right\} \tag{4.18}$$

Similarly as for standard method with embedded strong discontinuities in Equation 3.68, when no macrocracks have formed, the system in Equation 4.18 degenerates into standard (non-linear global-local) FEM.

4.2.8 Numerical tangent stiffness for macrocracked elements

Following the procedure shown in Section 3.3.11 and using the new equations derived in Section 4.2.7, the element-wise secant stiffness operator for an element with micromechanical continua and embedded strong discontinuities is derived below:

$$\begin{aligned} \delta\Pi_{int}(\mathbf{u}^{\mathrm{el}}) \;=\; & \int_{\Omega\backslash\Gamma} \left\{\mathbf{B}\delta\mathbf{u}^{\mathrm{el}} - \mathbf{M}\hat{\mathbf{I}}\{\mathbf{C}_\Gamma\delta\mathbf{u}^{\mathrm{el}}\}\right\}^{\mathrm{T}} \bar{\mathbf{D}}_{\mathrm{sec}} \left\{\mathbf{B}\mathbf{u}^{\mathrm{el}} - \mathbf{M}\hat{\mathbf{I}}\{\mathbf{C}_\Gamma\mathbf{u}^{\mathrm{el}}\}\right\} d\Omega \\ & + \left\{\hat{\mathbf{I}}\{\mathbf{C}_\Gamma\delta\mathbf{u}^{\mathrm{el}}\}\right\}^{\mathrm{T}} \mathbf{K}_\Gamma \left\{\mathbf{C}_\Gamma\mathbf{u}^{\mathrm{el}}\right\} \end{aligned} \tag{4.19}$$

where further re-arrangement in Equation 4.19 and by combining with Equation 4.15, to conveniently use the FE setting of the variational principle gives:

$$\left\{\delta\mathbf{u}^{\mathrm{el}}\right\}^{\mathrm{T}} \left\{ \int_{\Omega\backslash\Gamma} \left\{\mathbf{B} - \widehat{\mathbf{M}}\mathbf{C}_\Gamma\right\}^{\mathrm{T}} \bar{\mathbf{D}}_{\mathrm{sec}} \left\{\mathbf{B} - \widehat{\mathbf{M}}\mathbf{C}_\Gamma\right\} d\Omega + \mathbf{C}_\Gamma^{\mathrm{T}}\widehat{\mathbf{K}}_\Gamma\mathbf{C}_\Gamma \right\} \left\{\mathbf{u}^{\mathrm{el}}\right\} = \left\{\delta\mathbf{u}^{\mathrm{el}}\right\}^{\mathrm{T}} \mathbf{F}^{\mathrm{el}}_{\mathrm{ext}} \tag{4.20}$$

Therefore, the secant stiffness at the element level $\mathbf{K}^{\mathrm{el}}_{coupled,sec}$ is obtained after cancelling $\delta\mathbf{u}^{\mathrm{el}} \neq \mathbf{0}$ from both sides of Equation 4.20, and reads as follows:

$$\mathbf{K}^{\mathrm{el}}_{coupled,sec} = \int_{\Omega\backslash\Gamma} \left\{\mathbf{B} - \widehat{\mathbf{M}}\mathbf{C}_\Gamma\right\}^{\mathrm{T}} \bar{\mathbf{D}}_{\mathrm{sec}} \left\{\mathbf{B} - \widehat{\mathbf{M}}\mathbf{C}_\Gamma\right\} d\Omega + \mathbf{C}_\Gamma^{\mathrm{T}}\widehat{\mathbf{K}}_\Gamma\mathbf{C}_\Gamma \tag{4.21}$$

By differentiating each side of Equation 4.20 a consistent tangent $\mathbf{K}^{\mathrm{el}}_{coupled}$ for a macrocracked element is derived:

$$\left\{K^{\mathrm{el}}_{coupled}\right\}_{ij} = \left\{K^{\mathrm{el}}_{coupled,sec}\right\}_{ij} + \underbrace{\left(\frac{\partial\left\{K^{\mathrm{el}}_{coupled,sec}\right\}_{ir}}{\partial u^{\mathrm{el}}_j}\right)}_{\text{by central differences}} u^{\mathrm{el}}_r, \quad i,j,r = 1 \ldots \underbrace{\mathrm{ndofn} \cdot \mathrm{nnode}}_{\mathrm{ndofe}} \tag{4.22}$$

$$\frac{\partial\left\{K^{\mathrm{el}}_{coupled,sec}\right\}_{ir}}{\partial u^{\mathrm{el}}_j} \approx \frac{\left\{K^{\mathrm{el}}_{coupled,sec}(\mathbf{u}^{\mathrm{el}+})\right\}_{ir} - \left\{K^{\mathrm{el}}_{coupled,sec}(\mathbf{u}^{\mathrm{el}-})\right\}_{ir}}{2|\Delta_{\mathrm{FD}} u^{\mathrm{el}}_j|}, \quad i,j,r = 1 \ldots \mathrm{ndofe} \tag{4.23}$$

N.B.: Secant operators are used until the macrocracking direction is settled, and this is generally known '*a posteriori*' of updating macrocracking dofs using quasi-static element-based condensation. Therefore, consistent tangent operators for macrocracked elements are only activated for global iterations $iiter > itfix + 1$, i.e. after macrocracking directions are settled.

4.2.9 Summary of multiscale EFEM for modelling micro-macro quasi-brittle fracture

The main features of the micromechanical model at the bulk domain from Section 3.2.5 as used in the multiscale EFEM program are summarised in Box 4.1.

Box 4.1 Summary of micromechanical material model for cementitious materials with directional microcracking, adapted from Jefferson and Bennett (2010, 2007)

Constitutive equation [§3.2.5]: $\bar{\boldsymbol{\sigma}} = \bar{\mathbf{D}}_e \cdot (\bar{\boldsymbol{\varepsilon}} - \bar{\boldsymbol{\varepsilon}}^{add})$ or $\bar{\boldsymbol{\sigma}} = \bar{\mathbf{D}}_{sec} \cdot \bar{\boldsymbol{\varepsilon}}$

where $\bar{\mathbf{D}}_{sec} = \left[\mathbf{I} + \bar{\mathbf{D}}_e \cdot \left(\sum_{i=1}^{n^m_{int}} \frac{\omega^{\mathrm{m}}_\alpha}{1-\omega^{\mathrm{m}}_\alpha} \mathbf{N}^{\mathrm{T}}_\sigma \mathbf{C}_L \mathbf{N}_\sigma w^{\mathrm{num}}_\alpha \right)\right]^{-1} \cdot \bar{\mathbf{D}}_e$

Consistently-linearised constitutive tangent operator [§3.2.8]:

$\bar{\mathbf{D}}_{tan} = \bar{\mathbf{D}}_{sec} \cdot \left[\mathbf{I} - \sum_{i=1}^{n^m_{int} | \dot{\zeta}^{\mathrm{m}}_\alpha > 0} \frac{1}{(1-\omega^{\mathrm{m}}_\alpha)^2} \frac{d\omega^{\mathrm{m}}_\alpha}{d\zeta^{\mathrm{m}}_\alpha} \frac{d\zeta^{\mathrm{m}}_\alpha}{d\zeta^{\mathrm{m}}_{\alpha,\mathrm{eff}}} \mathbf{N}^{\mathrm{T}}_\sigma \mathbf{C}_L \mathbf{N}_\sigma \bar{\boldsymbol{\sigma}} \left\{ \frac{\partial \zeta^{\mathrm{m}}_{\alpha,\mathrm{eff}}}{\partial \bar{\boldsymbol{\varepsilon}}_L} \right\}^{\mathrm{T}} \mathbf{N}_\varepsilon w^{\mathrm{num}}_{int} \right]$

where $\mathbf{C}_L = \frac{1}{\bar{E}_{am}} \begin{bmatrix} 1 & 0 \\ 0 & \frac{2}{2-\bar{\upsilon}_{am}} \end{bmatrix}$ is simplified to account for plane-stress conditions ;

Note that the derivative $\frac{d\omega^{\mathrm{m}}_\alpha}{d\zeta^{\mathrm{m}}_\alpha}$ is computed using Eq. 4.3

In every microcracking direction ($\alpha = 1 \ldots n^m_{int}$), as used for numerical integration:

Directional microcracking variable [§3.2.6]: $\omega^{\mathrm{m}}_\alpha(\zeta^{\mathrm{m}}_\alpha) = 1 - \frac{\zeta^{\mathrm{m}}_0}{\zeta^{\mathrm{m}}_\alpha} \exp\left\{ - c_s \frac{\zeta^{\mathrm{m}}_\alpha - \zeta^{\mathrm{m}}_0}{u_{\max}/h_{fa} - \zeta^{\mathrm{m}}_0} \right\}$

Note that the microcracking growth evolution is now computed by Eq. 4.2

Microcracking surface [§3.2.7]: $\Theta^{\mathrm{m}}_\alpha(\zeta^{\mathrm{m}}_{\alpha,\mathrm{eff}}, \zeta^{\mathrm{m}}_\alpha) \equiv \zeta^{\mathrm{m}}_{\alpha,\mathrm{eff}} - \zeta^{\mathrm{m}}_\alpha \leq 0$

Microcracking strain [§3.2.7]: $\zeta^{\mathrm{m}}_{\alpha,\mathrm{eff}}(\bar{\boldsymbol{\varepsilon}}_L) = \frac{\bar{\varepsilon}_{rr}}{2}\left[1 + \left(\frac{\mu_\varepsilon}{r_\varepsilon}\right)^2\right] + \frac{1}{2r^2_\varepsilon}\sqrt{\left(r^2_\varepsilon - \mu^2_\varepsilon\right)^2 \bar{\varepsilon}^2_{rr} + 4r^2_\varepsilon \bar{\gamma}^2_L}$

Initial effective microcracking strain [§3.2.7]: $\zeta^{\mathrm{m}}_{\alpha,\mathrm{eff}} \geq \zeta^{\mathrm{m}}_0$; $\zeta^{\mathrm{m}}_0 \equiv \varepsilon^{\mathrm{m}}_t = \frac{f_t^{\mathrm{m}}}{\bar{E}_{am}}$

Microcracking growth irreversibility [§3.2.7]: $\dot{\zeta}_\alpha \geq 0$; $\Theta^{\mathrm{m}}_\alpha \leq 0$; $\Theta^{\mathrm{m}}_\alpha \cdot \dot{\zeta}^{\mathrm{m}}_\alpha = 0$

In addition, the other relevant mechanical components of the new multiscale EFEM model are presented in the Box 4.2.

Box 4.2 Summary of multiscale EFEM model for embedded fracture propagation in quasi-brittle solids, adapted from Freeman et al. (2020).

Mechanical Balance (m.b.) equations [§4.2.7]:

m.b.1. Equilibrium: $\phi^{\mathrm{el}}_{F,ck}(\mathbf{u}^{\mathrm{el}}) \equiv \mathbf{F}^{\mathrm{el}}_{\mathrm{ext}} - \int_{\Omega\setminus\Gamma} \mathbf{B}^{\mathrm{T}} \cdot \bar{\boldsymbol{\sigma}} d\Omega = \mathbf{0} \quad ; \quad \bar{\boldsymbol{\sigma}} = \bar{\mathbf{D}}_{\mathrm{sec}} \cdot \left[\mathbf{B}\mathbf{u}^{\mathrm{el}} - \mathbf{M}\hat{\mathbf{I}}\mathbf{W}\right]$

$$\therefore \begin{cases} \textbf{Consistent tangent: } \left\{K^{\mathrm{el}}_{\mathrm{EFEM}}\right\}_{ij} = \left\{K^{\mathrm{el}}_{\mathrm{EFEM,sec}}\right\}_{ij} + \left(\dfrac{\partial\left\{K^{\mathrm{el}}_{\mathrm{EFEM,sec}}\right\}_{ir}}{\partial u^{\mathrm{el}}_{j}}\right) u^{\mathrm{el}}_{r} \text{ (Eq. 4.22)} \\ \mathbf{K}^{\mathrm{el}}_{\mathrm{EFEM,sec}} = \int_{\Omega\setminus\Gamma} \left\{\mathbf{B} - \mathbf{M} \cdot \hat{\mathbf{I}} \cdot \mathbf{C}_{\Gamma}\right\}^{\mathrm{T}} \cdot \bar{\mathbf{D}}_{\mathrm{sec}} \cdot \left\{\mathbf{B} - \mathbf{M} \cdot \hat{\mathbf{I}} \cdot \mathbf{C}_{\Gamma}\right\} d\Omega + (\mathbf{C}_{\Gamma})^{\mathrm{T}} \cdot \hat{\mathbf{I}} \cdot \mathbf{K}_{\Gamma} \cdot \mathbf{C}_{\Gamma} \end{cases}$$

m.b.2. Quasi-static condensation: $\phi^{\mathrm{el}}_{w}(\mathbf{u}^{\mathrm{el}}) \equiv \mathbf{W}(\mathbf{u}^{\mathrm{el}}) - \mathbf{C}_{\Gamma} \cdot \mathbf{u}^{\mathrm{el}} = \mathbf{0}$ (Eq.4.17)

$$\text{where,} \quad \left.\begin{array}{l} \mathbf{C}_{\Gamma}\left(\mathbf{W}(\mathbf{u}^{\mathrm{el}}), \mathbf{u}^{\mathrm{el}}\right) = \left(\mathbf{B}_{\Gamma}\right)^{-1} \cdot \mathbf{A}_{\Gamma} \\ \mathbf{B}_{\Gamma} = \left(\int_{\Omega\setminus\Gamma} \mathbf{M}^{\mathrm{T}} \cdot \bar{\mathbf{D}}_{\mathrm{sec}} \cdot \mathbf{M} d\Omega\right) \cdot \hat{\mathbf{I}} + \mathbf{K}_{\Gamma} \\ \mathbf{A}_{\Gamma} = \int_{\Omega\setminus\Gamma} \mathbf{M}^{\mathrm{T}} \cdot \bar{\mathbf{D}}_{\mathrm{sec}} \cdot \mathbf{B} d\Omega \end{array}\right\} \iff \frac{\partial \Pi_{int}}{\partial \mathbf{W}} \overset{*}{=} \mathbf{0} \quad \text{(Energy minimisation)}$$

Kinematic-enhancement (k.e.) with embedded band [§4.2.4]:

k.e.1. Enriched nodal displacement: $\mathbf{u}_{c,inode} = \mathbf{u}_{inode} - H_{\Omega}(\mathbf{x}_{inode}) \otimes [|\mathbf{u}|]_{inode}(\mathbf{x}_{inode})$

$$\text{where } \mathbf{u}^{\mathrm{el}}_{c} = \left\{\begin{array}{c} \mathbf{u}_{c,\mathrm{node1}} \\ \hdashline \mathbf{u}_{c,\mathrm{node2}} \\ \hdashline \vdots \\ \hdashline \mathbf{u}_{c,\mathrm{nnode}} \end{array}\right\} = \left\{\begin{array}{c} \mathbf{u}_{\mathrm{node1}} \\ \hdashline \mathbf{u}_{\mathrm{node2}} \\ \hdashline \vdots \\ \hdashline \mathbf{u}_{\mathrm{nnode}} \end{array}\right\} - \left\{\begin{array}{c} H_{\Omega}(\mathbf{x}_{\mathrm{node1}}) \otimes \mathbf{T}_{w}(\mathbf{x}_{\mathrm{node1}}) \\ \hdashline H_{\Omega}(\mathbf{x}_{\mathrm{node2}}) \otimes \mathbf{T}_{w}(\mathbf{x}_{\mathrm{node2}}) \\ \hdashline \vdots \\ \hdashline H_{\Omega}(\mathbf{x}_{\mathrm{nnode}}) \otimes \mathbf{T}_{w}(\mathbf{x}_{\mathrm{nnode}}) \end{array}\right\} \cdot \hat{\mathbf{I}} \cdot \mathbf{W}$$

k.e.2. Strain: $\boldsymbol{\varepsilon} = \mathbf{B}\mathbf{u}^{\mathrm{el}}_{c} = \mathbf{B}\mathbf{u}^{\mathrm{el}} - \underbrace{\left(\sum^{nnode} \mathbf{B}_{inode} H_{\Omega}(\mathbf{x}_{inode}) \otimes \mathbf{T}_{w}(\mathbf{x}_{inode})\right)}_{\mathbf{M}} \hat{\mathbf{I}}\mathbf{W}$ (Eq.4.5)

$$\text{where } \mathbf{B}_{inode} = \begin{bmatrix} \partial_x N_{inode} & 0 \\ 0 & \partial_y N_{inode} \\ \partial_y N_{inode} & \partial_x N_{inode} \end{bmatrix}, \text{ and } H_{\Omega}(\mathbf{x} \in \boldsymbol{\Omega}^{+}) = 1 \text{ while } H_{\Omega}(\mathbf{x} \in \boldsymbol{\Omega}^{-}) = 0$$

Embedded localisation band (e.mc.) [§4.2.5]:

e.mc.1. Equivalent crack force: $\mathbf{F}_{\mathrm{ck}} = \mathbf{K}^{e}_{\Gamma} \cdot \mathbf{W}^{e} = \mathbf{K}_{\Gamma} \cdot \mathbf{W}$ (Eq. 4.8)

$$\text{where, } \mathbf{K}_{\Gamma} = \frac{\bar{E}_{am} \cdot t_g}{h_{ca}} \begin{bmatrix} \int_{\partial\Gamma^{\mathrm{M}}} (1-\omega^{\mathrm{M}}) dl & 0 & \int_{\partial\Gamma^{\mathrm{M}}} (1-\omega^{\mathrm{M}}) l dl \\ & \int_{\partial\Gamma^{\mathrm{M}}} \frac{1-\omega^{\mathrm{M}}}{2(1+\bar{\upsilon}_{am})} dl & 0 \\ \text{symm} & & \int_{\partial\Gamma^{\mathrm{M}}} (1-\omega^{\mathrm{M}}) l^2 dl \end{bmatrix}$$

$$\text{and } \mathbf{K}^{e}_{\Gamma} = \frac{\bar{E}_{am} \cdot t_g}{h_{ca}} \begin{bmatrix} \int_{\partial\Gamma^{\mathrm{M}}} dl & 0 & \int_{\partial\Gamma^{\mathrm{M}}} l dl \\ & \int_{\partial\Gamma^{\mathrm{M}}} \frac{1}{2(1+\bar{\upsilon})} dl & 0 \\ \text{symm} & & \int_{\partial\Gamma^{\mathrm{M}}} l^2 dl \end{bmatrix}, \text{ while } \omega^{\mathrm{M}} \in [0,1]$$

e.mc.2 Inelastic relative displacement: $\widehat{\mathbf{W}} = \left(\mathbf{I} - (\mathbf{K}^{e}_{\Gamma})^{-1} \cdot \mathbf{K}_{\Gamma}\right) \cdot \mathbf{W} = \hat{\mathbf{I}} \cdot \mathbf{W}$

with ω as Smooth Unloading-Reloading (SUR) law [§3.3.7 and Algorithm 6 in §4.3.4.1]

4.3 Algorithms of the new multiscale EFEM model

4.3.1 On displacement-driven iterative incremental procedure

In this variationally consistent method, as for other methods that employ *embedded* strong discontinuities (Armero and Linder, 2009; Freeman et al., 2020; Jirásek, 2000; Oliver et al., 2003; Simo et al., 1993), displacement degrees of freedom $\mathbf{u}$ are the only field required to be updated at the global level. Although other more complex approaches have been explored in the literature, e.g. by employing the Hu-Washizu variational statement based on the interpolations of a discontinuous displacement field, and the complementary stress and strain fields (Lotfi and Shing, 1995), the proposition in this PhD research is to keep the element formulation simple for implementation with a unique solvable field.

Consequentially, macrocrack degrees of freedom $\mathbf{W}$ are condensed quasi-statically at the element-level for every global update. The global tangent stiffness of the system $\mathbf{K}_g$ is assembled as for a standard FEM method, typically with continuous primary field which is unique at nodal locations. Therefore, nodal connectivity guides the distribution of local stiffness terms into global positions during FEM assemblage:

$$\dot{\mathbf{F}}_{\text{int}} = \mathbf{K}_g \dot{\mathbf{u}} = \left(\mathop{\mathbf{A}}_{ielem=1}^{nelem} \mathbf{K}^{\text{el}}_{ielem} \right) \dot{\mathbf{u}} = \left(\mathop{\mathbf{A}}_{ielem=1}^{nelem} \frac{\partial \mathbf{F}^{\text{el}}_{\text{int}}}{\partial \mathbf{u}^{\text{el}}} \right) \dot{\mathbf{u}} \tag{4.24}$$

$$\mathbf{K}^{\text{el}}_{ielem} = \begin{cases} \int_\Omega \mathbf{B}^{\text{T}} \bar{\mathbf{D}}_{tan} \mathbf{B} d\Omega, & \text{if no macrocracks in } \mathbf{\Omega}_{ielem} \\ \mathbf{K}^{\text{el}}_{coupled} \text{ (numerical approximation)}, & \text{if macrocrack no.} \geq 1 \text{ in } \mathbf{\Omega}_{ielem} \end{cases} \tag{4.25}$$

where $\mathbf{K}^{\text{el}}_{ielem}$ is the element tangent stiffness for the element domain $\mathbf{\Omega}_{ielem}$. Newton's method is applied until a specified tolerance is achieved to preserve momentum balance after an out-of-balance force is prescribed at each incremental step. Note that for an incremental iterative solution with an updated total loading step $\mathbf{F}^{iincr}_{\text{ext}} = \mathbf{F}^{iincr-1}_{\text{ext}} + \Delta\lambda \mathbf{F}^{\text{input}}_{\text{ext}}$, where $\Delta\lambda$ defines the loading step size or increment, the mechanical equilibrium condition in Equation 4.18 takes the form:

$$\boldsymbol{\phi}_F(\mathbf{u}) := \mathbf{F}^{iincr}_{\text{ext}} - \mathbf{F}_{\text{int}}(\mathbf{u}) = \mathbf{0} \tag{4.26}$$

Linearisation of the global equilibrium condition yields Equation 4.27, which is presented as a Newton's representation to solve for $\mathbf{u}$.

$$\mathbf{\Phi}^i_F(\mathbf{u}_g) := \mathbf{F}^{iincr}_{\text{ext}} - \mathbf{F}^{i-1}_{\text{int}} - \left(\mathop{\mathbf{A}}_{ielem=1}^{nelem} \frac{\partial \mathbf{F}^{\text{el}}_{\text{int}}}{\partial \mathbf{u}^{\text{el}}} \right)^{i-1} d\mathbf{u}^i = \mathbf{0} \tag{4.27}$$

where $d\mathbf{u}^i$ is the iterative change of the global displacement field, and tangent operators at the element-level $\frac{\partial \mathbf{F}_{\text{int}}^{\text{el}}}{\partial \mathbf{u}^{\text{el}}}$ are computed as consistent tangents (Simo and Taylor, 1985) to achieve numerical efficiency. In case of mixed boundary conditions, i.e. tractions or displacement nodal components are known across the domain, reactions are taken into account into the iterative procedure. An illustrative sketch of the global incremental iterative solution is depicted in Figure 4.4.

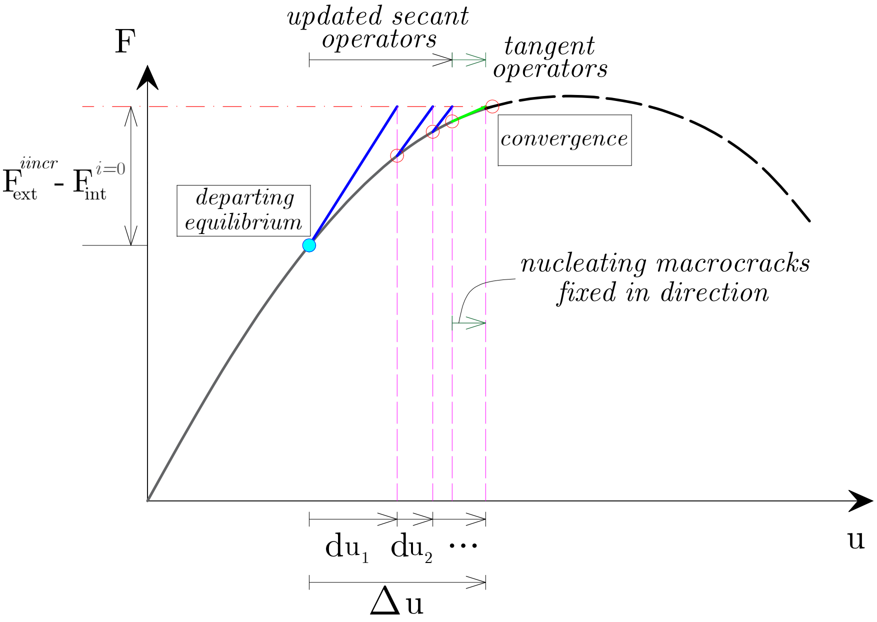

Figure 4.4: Nonlinear incremental iterative solution of variational multiscale EFEM methodology with propagating embedded macrocracks at the element level.

A closed-form material tangent $\bar{\mathbf{D}}_{tan}$ for a micromechanical continua from Sections 3.2.8 and 4.2.2.2 is cast in standard form into the element tangent $\int_\Omega \mathbf{B}^{\mathrm{T}} \bar{\mathbf{D}}_{tan} \mathbf{B} d\Omega$ for uncracked elements; whereas a numerically-derived consistent element tangent $\mathbf{K}_{coupled}^{\text{el}}$ from Section 4.2.8 is used for elements with a nucleated embedded macrocrack. Since deriving analytical tangents becomes more elaborate in macrocracked elements, numerical tangents are computed using central difference approximations.

N.B.: Tangent operators are used only after new macrocracks are fixed in geometry within a new increment, i.e. considered as fully nucleated macrocracks due to microcracking coalescence. Before defining a definitive macrocrack orientation, secant stiffness operators are used instead. Upon fixing nucleating macrocrack orientation, maximum experienced macro-state variables ζ^{M} are fixed to obtain positive tangents from a fixed Smooth-Unloading-Reloading (SUR) branch.

Some algorithmic aspects of the variational micromechanics-enriched embedded strong discontinuity Finite Element method are summarised in Algorithm 1.

Algorithm 1: Non-linear incremental global-local iterative analysis for a micromechanical solid with propagating embedded strong discontinuities

```
input : Starting from equilibrium $||\boldsymbol{\phi}_F||/||\mathbf{F}^{\text{max}}_{\text{ext}}|| < \text{tol}$, $\boldsymbol{\phi}_F = \mathbf{F}_{\text{ext}} - \mathbf{F}_{\text{int}}$, given:
        a. Micro/macro states: $\{\zeta\}^{\text{m}}$(GP in bulk), $\{\zeta\}^{\text{M}}$(macrocrack number)
        b. Primary/secondary macro-fields: $\mathbf{u}$, $\{\mathbf{W}\}$(macrocrack number)
        c. Force increment (incl. prescribed displacement): $\Delta\mathbf{F}_{\text{ext}} \leftarrow \Delta\lambda\mathbf{F}^{\text{input}}_{\text{ext}}$
output: New states $\{\zeta\}^{\text{m}}, \{\zeta\}^{\text{M}}$ and updated macro-fields $\mathbf{u}$, $\{\mathbf{W}\}$ in equilibrium
Update external force vector for the new increment: $\mathbf{F}_{\text{ext}} \leftarrow \mathbf{F}_{\text{ext}} + \Delta\mathbf{F}_{\text{ext}}$ ;
Update out-of-balance force vector: $\boldsymbol{\phi}_F \leftarrow \mathbf{F}_{\text{ext}} - \text{F}_{\text{int}}$ , $f_{\text{check}} \leftarrow 1$;
Initialise iteration number: iiter $\leftarrow 0$, miter $\leftarrow$ maximum iteration number;
//Start iterative procedure until momentum balance is re-gained, i.e. $f_{\text{check}} \leftarrow 0$;
while $iiter < miter$ and $f_{check} \neq 0$ do
    Iterations number updated: iiter $\leftarrow$ iiter $+ 1$ ;
    Compute element tangents $\mathbf{K}^{\text{el}}_{ielem} \,|\Omega_{ielem} \in \Omega^{\text{M}} \rightarrow$ Assemble tangent $\mathbf{K}_g$;
    Modify tangent $\mathbf{K}_g$ and out-of-balance vector $\boldsymbol{\phi}_F$ for prescribed displacement;
    Update displacement: $\mathbf{u} \leftarrow \mathbf{u} + d\mathbf{u}$ , for new iterative array $d\mathbf{u} = \mathbf{K}_g^{-1}\boldsymbol{\phi}_F$;
    // Element-wise treatment of micro-macro fracture;
    for $ielem = 1 \dots nelem$ do
        // Detect macrocracks: use flow chart in Figure 4.10;
        Detect new macrocrack nucleation, then proceed to force recovery;
        // Force recovery at element level;
        if (no macrocracks in $\Omega_{ielem}$) then
            Standard FEM update: micro states at GPs $\{\zeta\}^m$ [Alg. 4];
            Update strain/stiffness at GPs: $\bar{\boldsymbol{\varepsilon}} \leftarrow \mathbf{B}\mathbf{u}^{\text{el}}$, $\bar{\mathbf{D}}_{\text{sec}}(\bar{\boldsymbol{\varepsilon}})$ [Alg. 3];
            Recover stresses: $\bar{\boldsymbol{\sigma}} \leftarrow \bar{\mathbf{D}}_{\text{sec}}\mathbf{B}\mathbf{u}^{\text{el}}$ [Eq. 3.13 in §3.2.5 & §4.2.2.1];
            Recover force $\mathbf{F}^{\text{el}}_{\text{int}}$: $\mathbf{F}^{\text{el}}_{\text{int}} \leftarrow \int \mathbf{B}^{\text{T}}\bar{\boldsymbol{\sigma}}d\Omega$ ;
        else
            Variational energetic scheme: $\mathbf{W} \leftarrow \mathbf{C}_{\Gamma}\mathbf{u}^{\text{el}}$ [Eq. 4.17 in §4.2.7, Alg. 2];
            Update micro/macro states: $\{\zeta\}^{\text{m}}$ and $\{\zeta\}^{\text{M}}$ in $\Omega_{ielem}$ [Alg. 4 & 7];
            Update strain/stiffness at GPs: $\bar{\boldsymbol{\varepsilon}} \leftarrow \mathbf{B}\mathbf{u}^{\text{el}} - \widehat{\mathbf{M}}\mathbf{W}$, $\bar{\mathbf{D}}_{\text{sec}}(\bar{\boldsymbol{\varepsilon}})$ [Alg. 5 & 3] ;
            Recover stresses: $\bar{\boldsymbol{\sigma}} \leftarrow \bar{\mathbf{D}}_{\text{sec}}\{\mathbf{B}\mathbf{u}^{\text{el}} - \widehat{\mathbf{M}}\mathbf{W}\}$ [Eq. 3.13 in §3.2.5 & §4.2.2.1];
            Recover force $\mathbf{F}^{\text{el}}_{\text{int}}$: $\mathbf{F}^{\text{el}}_{\text{int}} \leftarrow \int \mathbf{B}^{\text{T}}\bar{\boldsymbol{\sigma}}d\Omega$;
        end
        Assemble element internal force $\mathbf{F}^{\text{el}}_{\text{int}} = \int \mathbf{B}^{\text{T}}\bar{\boldsymbol{\sigma}}d\Omega$ into global array $\mathbf{F}_{\text{int}}$;
    end
    Compute new out-of-balance vector including reactions: $\boldsymbol{\phi}_F \leftarrow \mathbf{F}^{\text{r}}_{\text{ext}} - \mathbf{F}_{\text{int}}$;
    if ($||\boldsymbol{\phi}_F||/||\mathbf{F}^{\text{r,max}}_{\text{ext}}|| < \text{tol}$[a]) then $f_{\text{check}} \leftarrow 0$;
end
```

---

[a] Tolerance is set to 10^{-4} for force residuals, unless otherwise stated in simulations in this PhD.

4.3.2 Numerical solution of quasi-static condensation scheme in a finite element with embedded macrocracks and micromechanical bulk

The set of PDEs in Equation 4.17 are solved for $\mathbf{W}$ using Newton's method consecutively, until the residual reduces to a specified tolerance. Linearisation of Equation 4.17 leads to a Newton's type representation of the energetic minimisation procedure as follows:

$$\left.\begin{array}{c} \{\boldsymbol{\Phi}_w^{\mathrm{el}}(\mathbf{W})\}^{\mathrm{j}} := \mathbf{W}^{\mathrm{j}-1} - \{\mathbf{C}_\Gamma(\mathbf{W},\mathbf{u}^{\mathrm{el}})\}^{\mathrm{j}-1}\cdot\mathbf{u}^{\mathrm{el}} + (\partial\boldsymbol{\phi}_w^{\mathrm{el}}/\partial\mathbf{W})^{\mathrm{j}-1}\cdot d\mathbf{W}^{\mathrm{j}} = \mathbf{0} \\ \partial\boldsymbol{\phi}_w^{\mathrm{el}}/\partial\mathbf{W} := \mathbf{I} - \partial\{\mathbf{C}_\Gamma\mathbf{u}^{\mathrm{el}}\}/\partial\mathbf{W} \end{array}\right\} \tag{4.28}$$

where the tangent $\partial\{\mathbf{C}_\Gamma\mathbf{u}^{\mathrm{el}}\}/\partial\mathbf{W}$ is conveniently approximated by central differences, for use in the element-wise energetic optimisation:

$$\frac{\partial\left\{\{C_\Gamma\}_{ik}u_k^{\mathrm{el}}\right\}}{\partial W_j} \approx \frac{\left\{\{C_\Gamma(\mathbf{W}^+,\mathbf{u}^{\mathrm{el}})\}_{ik} - \{C_\Gamma(\mathbf{W}^-,\mathbf{u}^{\mathrm{el}})\}_{ik}\right\}u_k^{\mathrm{el}}}{2|\Delta_{\mathrm{FD}}W_j|} \tag{4.29}$$

where standard index notation is used for matrix operations.

The steps for the numerical solution of Equation 4.28 are summarised in Algorithm 2. Also, a geometric interpretation of the variational updates of the macrocrack relative displacement array $\mathbf{W}$ is illustrated in Figure 4.5, where an initial trial solution $\mathbf{W}_o$ is driven towards the minimum-energy solution:

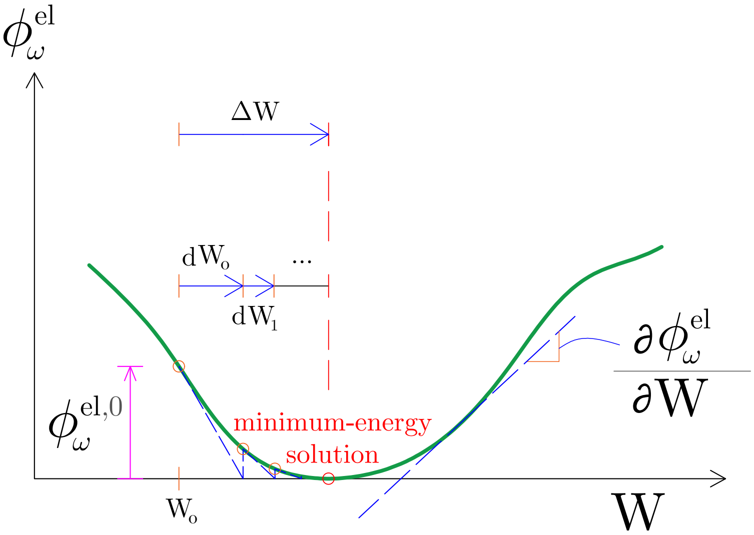

Figure 4.5: Geometric interpretation of variational iterative updates of macrocrack dofs $\mathbf{W}$, upon an update of the element-based nodal displacement vector $\mathbf{u}^{\mathrm{el}}$.

Algorithm 2: Element-wise variational update of macrocraking dofs $\mathbf{W}$ for a Micromechanical solid with propagating embedded macrocracks in §4.2.7

```
input : After global-iterative displacement $\mathbf{u}^{\text{el}} \leftarrow \mathbf{u}^{\text{el}} + d\mathbf{u}^{\text{el}}$ in $\boldsymbol{\Omega}_{ielem}$, given:
        a. Last-converged states: $\{\zeta\}^{\text{m}}$(GP in bulk), $\{\zeta\}^{\text{M}}$(macrocrack number)
        b. Last global iteration macrocrack dofs: $\mathbf{W}^{\text{iiter-1}}$(macrocrack number)
        c. Macrocrack geometry: centre $\mathbf{x}_{\text{ck}}$, length $l_{\text{ck}}$ , plane-normal $\mathbf{r}_\Gamma$
output: Current global-iterative states $\{\zeta\}^{\text{m,iiter}}, \{\zeta\}^{\text{M,itter}}$ and updated
        macrocrack dofs $\mathbf{W}^{\text{iiter}}$, preserving minimum energy at element-level
Store previous global-iterative macrocrack dofs: $\mathbf{W} \leftarrow \mathbf{W}^{\text{iiter-1}}$ ;
Activate flag for element-level iterations, to seek energetic minimum: $f^{\text{el}}_{\text{check}} \leftarrow 1$;
Initialise element-level iterations: $\text{iiter}^{\text{el}} \leftarrow 0$, $\text{miter}^{\text{el}} \leftarrow$ maximum iteration;
//Start iterative procedure until energetic minimum is obtained, i.e. $f^{\text{el}}_{\text{check}} \leftarrow 0$;
while $iiter^{el} < miter^{el}$ and $f^{el}_{check} \neq 0$ do
    Iteration number updated: $\text{iiter}^{\text{el}} \leftarrow \text{iiter}^{\text{el}} + 1$ ;
    if $iiter^{el} > 1$ then
        Evaluate the numerical tangent $\partial\boldsymbol{\phi}^{\text{el}}_w/\partial\mathbf{W} \leftarrow \mathbf{I} - \partial(\mathbf{C}_\Gamma \cdot \mathbf{u}^{\text{el}})/\partial\mathbf{W}$ ;
        Update macrocrack dofs: $\mathbf{W} \leftarrow \mathbf{W} + d\mathbf{W}$ , for $d\mathbf{W} = -(\partial\boldsymbol{\phi}^{\text{el}}_w/\partial\mathbf{W})^{-1}\boldsymbol{\phi}^{\text{el}}_w$;
    end
    // Update macro-states from last-converged;
    Update macro-states along macrocrack: $\{\zeta\}^{\text{M}}$ and $\{\zeta_{\text{eff}}\}^{\text{M}}$ [Alg. 7];
    Compute macrocrack stiffness $\mathbf{K}_\Gamma$, $\mathbf{K}^e_\Gamma$ , then update $\widehat{\mathbf{I}}$ [Alg. 6, Eq. 4.9 & 4.10];
    //Proceed to compute iterative update of condensation matrix $\mathbf{C}_\Gamma$;
    Initialise matrices for integration: $\mathbf{B}^*_\Gamma \leftarrow \mathbf{0}$, $\mathbf{A}_\Gamma \leftarrow \mathbf{0}$;
    // Loop over RVEs: update micro-states from last-converged;
    for $igp = 1 \dots ngp$ do
        Evaluate and store GP-level enhanced-strain $\bar{\boldsymbol{\varepsilon}} \leftarrow \mathbf{B}\mathbf{u}^{\text{el}} - \widehat{\mathbf{M}}\mathbf{W}$ [Alg. 5];
        Update micro-states $\{\zeta_{\text{eff}}\}^{\text{m}}$, $\{\zeta\}^{\text{m}}$ and $\{\omega\}^{\text{m}}$ at GP [Alg. 4];
        Update and store secant stiffness operator: $\bar{\mathbf{D}}_{\text{sec}}$ [Alg. 3];
        Compute matrices: $\mathbf{B}^*_{\Gamma,\text{igp}} \leftarrow \mathbf{M}^{\text{T}}\bar{\mathbf{D}}_{\text{sec}}\mathbf{M}w^{\text{num}}_{\text{igp}}$ , $\mathbf{A}_{\Gamma,\text{igp}} \leftarrow \mathbf{M}^{\text{T}}\bar{\mathbf{D}}_{\text{sec}}\mathbf{B}w^{\text{num}}_{\text{igp}}$ ;
        Accumulate matrix terms: $\mathbf{B}^*_\Gamma \leftarrow \mathbf{B}^*_\Gamma + \mathbf{B}^*_{\Gamma,\text{igp}}$ , $\mathbf{A}_\Gamma \leftarrow \mathbf{A}_\Gamma + \mathbf{A}_{\Gamma,\text{igp}}$ ;
    end
    Compute condensation matrix: $\mathbf{C}_\Gamma \leftarrow (\mathbf{K}_\Gamma + \mathbf{B}^*_\Gamma \cdot \hat{\mathbf{I}})^{-1} \cdot \mathbf{A}_\Gamma$ [Eq. 4.17];
    Compute residual: $\boldsymbol{\phi}^{\text{el}}_w \leftarrow \mathbf{W} - \mathbf{C}_\Gamma \cdot \mathbf{u}^{\text{el}}$, $\boldsymbol{\phi}^{\text{el},*}_w \leftarrow \mathbf{diag}\{1, 1, \sqrt{A_{ielem}}\} \cdot \boldsymbol{\phi}^{\text{el},}_w$;
    if $(||\boldsymbol{\phi}^{\text{el},*}_w||/u_{max} < \text{tol})$ then $f^{\text{el}}_{\text{check}} \leftarrow 0$;
end
```

Note that the tolerance for quasi-static condensation in Algorithm 2 is set to 10^{-6}, which becomes 10^{-10} after the first (**itfix**) global iterations. This is done to reduce the number of local iterations at the element level when macrocracks are still evolving in nucleation direction.

4.3.3 Computations of stresses in the Micromechanical bulk

Stress recovery is done using the secant material stiffness $\bar{\boldsymbol{\sigma}} = \bar{\mathbf{D}}_{\text{sec}} \cdot \bar{\boldsymbol{\varepsilon}}$ as detailed in Sections 3.2.5 and 4.2.2.1. Note that storage of the updated microcracking variables, the secant operator and the homogenised stress at Gauss Points in the bulk is done through iterations until a macrocracked element is first in a minimum energy state. To reach that state, which is not the same as the element being in internal mechanical equilibrium with respect to external forces, multiple strain computations are carried for each Gauss Point in the bulk as described in Section 4.3.3.3, to include the effect of an evolving strong discontinuity over a trial step.

4.3.3.1 Computation of the homogenised secant stiffness matrix $\bar{\mathbf{D}}_{\text{sec}}$

The numerical integration of the homogenised secant stiffness operator $\bar{\mathbf{D}}_{\text{sec}}$ is done upon updates of the directional scalar variables ω_α^{m} from Section 4.3.3.2. These steps are presented in Algorithm 3.

Algorithm 3: Update scheme for homogenised secant stiffness $\bar{\mathbf{D}}_{\text{sec}}$

```
input  : Given new RVE directional microcracking scalar variables ${\omega}^{\text{m}}_{RVE}$
output: Updated homogenised secant stiffness operator $\bar{\mathbf{D}}_{\text{sec}}$
Initialise homogenised additional compliance: $\bar{\mathbf{C}}^{\Gamma_m} \leftarrow \mathbf{0}$;
// Use numerical integration over the perimeter of a semi-circle to compute $\bar{\mathbf{C}}^{\Gamma_m}$;
for $\alpha = 1 \ldots n^m_{int}$ do
    Compute local unit vectors $\boldsymbol{r}_\alpha$, $\boldsymbol{s}_\alpha$, $\boldsymbol{t}_\alpha$ and transformation operators $\mathbf{N}_\sigma$, $\mathbf{N}_\sigma^{\text{T}}$;
    Compute new additional compliance component:
    $\bar{\mathbf{C}}^{\Gamma_m}_\alpha \leftarrow \frac{\omega^{\text{m}}_\alpha}{1-\omega^{\text{m}}_\alpha}\mathbf{N}_\sigma^{\text{T}}\mathbf{C}_L\mathbf{N}_\sigma w^{\text{num}}_\alpha$,   $w^{\text{num}}_\alpha :=$ weighting coefficient;
    Accumulate additional compliance components:  $\bar{\mathbf{C}}^{\Gamma_m} \leftarrow \bar{\mathbf{C}}^{\Gamma_m} + \bar{\mathbf{C}}^{\Gamma_m}_\alpha$ ;
end
Update homogenised secant stiffness in matrix form: $\bar{\mathbf{D}}_{\text{sec}} \leftarrow (\mathbf{I} + \bar{\mathbf{D}}_e\bar{\mathbf{C}}^{\Gamma_m})^{-1}\bar{\mathbf{D}}_e$;
```

4.3.3.2 Computation of scalar microcracking variables $\omega_\alpha^{\text{m}}(\zeta_\alpha^{\text{m}})$

The computations of directional microcracking state variables ζ_α^{m}, microcracking scalar variables ω_α^{m}, and the material secant operator $\bar{\mathbf{D}}_{\text{sec}}$ remains as first presented by Jefferson and Bennett (2010, 2007), although variations in the evolution law for the directional microcracking scalar variables $\omega_\alpha^{\text{m}}(\zeta_\alpha^{\text{m}}(\bar{\boldsymbol{\varepsilon}}))$ from Section 4.2.2.1 need to be considered. These steps are summarised in Algorithm 4.

```
Algorithm 4: Update scheme for RVE micro-states $\zeta^{\mathrm{m}}_{\alpha} (\alpha \in \{1, .., \mathrm{n}^{\mathrm{m}}_{int}\})$
input  : Given an updated homogenised strain $\bar{\boldsymbol{\varepsilon}} = \{\nabla^{s}\mathbf{u}_c\}_{\mathrm{vec}}$
output: New RVE micro-states $\{\zeta\}^{\mathrm{m}}_{RVE}$ and directional scalar variables $\{\omega\}^{\mathrm{m}}_{RVE}$
        for the updated homogenised strain $\bar{\boldsymbol{\varepsilon}}$
// Loop over degradation directions used for numerical integration;
for $\alpha = 1 \dots n^{m}_{int}$ do
    Compute local unit vectors $\boldsymbol{r}_{\alpha}$, $\boldsymbol{s}_{\alpha}$, $\boldsymbol{t}_{\alpha}$ and the transformation operator $\mathbf{N}_{\varepsilon}$;
    Compute resolved strain: $\bar{\boldsymbol{\varepsilon}}_{L} \leftarrow \mathbf{N}_{\varepsilon}\bar{\boldsymbol{\varepsilon}}$ ;
    Compute effective directional micro-state:
    $\zeta^{\mathrm{m}}_{\alpha,\mathrm{eff}} \leftarrow \frac{1}{2}\bar{\varepsilon}_{rr}\left[1+\left(\frac{\mu_{\varepsilon}}{r_{\varepsilon}}\right)^{2}\right] + \frac{1}{2r_{\varepsilon}^{2}}\sqrt{\left(r_{\varepsilon}^{2}-\mu_{\varepsilon}^{2}\right)^{2}\bar{\varepsilon}_{rr}^{2} + 4r_{\varepsilon}^{2}\left(\bar{\gamma}_{rs}^{2}+\bar{\gamma}_{rt}^{2}\right)}$ ;
    if $\zeta^{m}_{\alpha,eff} > \zeta^{m}_{\alpha}$ then
        Update maximum experienced directional micro-state: $\zeta^{\mathrm{m}}_{\alpha} \leftarrow \zeta^{\mathrm{m}}_{\alpha,\mathrm{eff}}$;
        Update directional microcracking scalar variable:
        $\omega^{\mathrm{m}}_{\alpha} \leftarrow 1 - (\varepsilon^{\mathrm{m}}_{t}/\zeta^{\mathrm{m}}_{\alpha})\exp\left[-c_{s}\cdot(\zeta^{\mathrm{m}}_{\alpha}-\varepsilon^{\mathrm{m}}_{t})/(u_{max}/h_{fa}-\varepsilon^{\mathrm{m}}_{t})\right]$ ;
    end
end
```

4.3.3.3 Computation of the strains $\bar{\boldsymbol{\varepsilon}}$ in the micromechanical bulk due to embedded strong discontinuities

Note that due to the complex nature of the quasi-static condensation of the multiscale EFEM model proposed, strain calculations $\bar{\boldsymbol{\varepsilon}}$ in the bulk from Equation 4.5 are performed for every update of $\mathbf{W}$ as illustrated in Figure 4.6, to seek a minimum energy solution within a single trial step with updated $\mathbf{u}^{\mathrm{el}}$ as described in Equation 4.17. These steps are described in Algorithm 5.

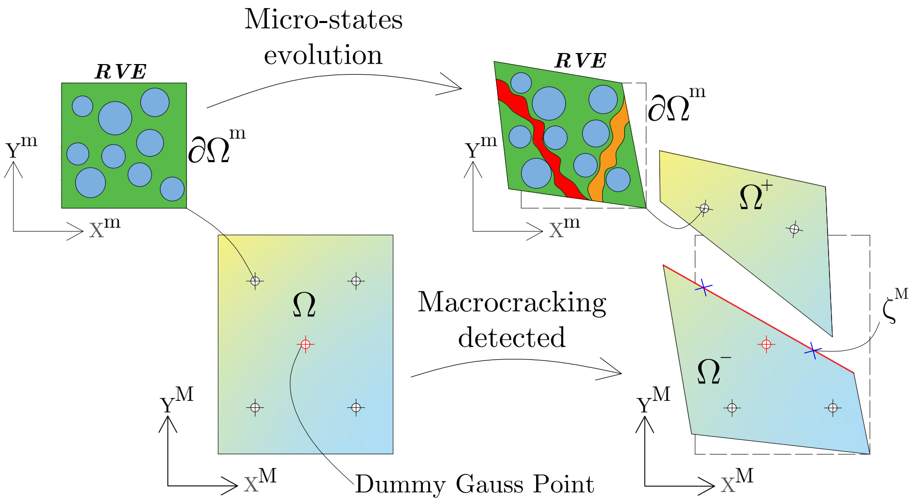

Figure 4.6: Intermediate micromechanical strains $\bar{\boldsymbol{\varepsilon}}$ are taken upon the activation of the embedded strong discontinuity for a fixed updated nodal displacement $\mathbf{u}^{\mathrm{el}}$.

Algorithm 5: Updating trial strains $\bar{\boldsymbol{\varepsilon}}(\mathbf{x}_{igp})$ at a specific Gauss Point in a macrocracked element.

```
input  : Trial variation of macrocrack degrees of freedom $d\mathbf{W}$ and nodal
         displacement $\mathbf{u}^{\mathrm{el}}$ at the element.
output: Trial strains $\bar{\boldsymbol{\varepsilon}}$ at a specified GP, for a given nodal displacement $\mathbf{u}^{\mathrm{el}}$,
         and trial $d\mathbf{W}$
Compute newly updated macrocrack dofs: $\mathbf{W} \leftarrow \mathbf{W} + d\mathbf{W}$ ;
// Note that the new effective macrocrack variables $\zeta^{\mathrm{M}}_{eff}$, may not push further
// the maximum experienced macrocrack variables $\zeta^{\mathrm{M}}$ if $iiter > itfix$
Compute new macrocrack based stiffness matrices: $\mathbf{K}^{e}_{\Gamma}$ and $\mathbf{K}_{\Gamma}$ ;
Compute inelastic component of macrocrack degress of freedom :
First compute $\hat{\mathbf{I}} \leftarrow \mathbf{I} - (\mathbf{K}^{e}_{\Gamma})^{-1} \cdot \mathbf{K}_{\Gamma}$ , then store $\hat{\mathbf{I}}$ or compute $\widehat{\mathbf{W}} \leftarrow \hat{\mathbf{I}} \cdot \mathbf{W}$ ;
At this stage, igp is specified ;
Compute strain-displacement matrix $\mathbf{B}$ and store it for further manipulation ;
// Initialise strain-macrocrrack displacement matrix
$\mathbf{M} \leftarrow \mathbf{0}$ ;
// Loop over nodes to compute strain-macrocrrack displacement matrix
for $inode = 1 \ldots nnode$ do
    Extract $\mathbf{B}_{inode}$ from strain-displacement matrix $\mathbf{B}$;
    Compute $H_{\Omega}(\mathbf{x}_{inode}) \leftarrow \begin{cases} 1 & \text{, if } \mathbf{x}_{inode} \in \Omega^{+} \\ 0 & \text{, if } \mathbf{x}_{inode} \in \Omega^{-} \end{cases}$ ;
    // Note the macrocrack normal $n_{\Gamma}$ and centre $\mathbf{x}_{ck}$ should be known 'a priori'
    Compute $\mathbf{T}_{w}(\mathbf{x}_{inode})$;
    Update strain-macrocrack displacement matrix:
    $\mathbf{M} \leftarrow \mathbf{M} + \mathbf{B}_{inode} H_{\Omega} \otimes \mathbf{T}_{w}(x_{inode})$
end
Compute $\widehat{\mathbf{M}}$ by matrix multiplication: $\widehat{\mathbf{M}} \leftarrow \mathbf{M} \cdot \hat{\mathbf{I}}$, if $\widehat{\mathbf{W}}$ is not stored ;
Compute the product $\widehat{\mathbf{M}} \cdot \mathbf{W}$, equivalent to $\mathbf{M} \cdot \widehat{\mathbf{W}}$ in case $\widehat{\mathbf{W}}$ was stored ;
Compute trial strain $\bar{\boldsymbol{\varepsilon}}(\mathbf{x}_{igp}) \leftarrow \mathbf{B} \cdot \mathbf{u}^{\mathrm{el}} - \widehat{\mathbf{M}} \cdot \mathbf{W}$ [Eq. 4.5] ;
```

4.3.4 Computation of the equivalent force $\mathbf{F}_{\mathbf{ck}}$ in embedded localisation bands

The computation of the equivalent force $\mathbf{F}_{\mathrm{ck}}$ from Equation 4.8, which acts on the embedded strong discontinuity, is done upon the updates of the scalar macrocracking variables $\omega^{\mathrm{M}}(\zeta^{\mathrm{M}}, \zeta^{\mathrm{M}}_{eff})$, which are described in Section 4.3.4.1.

4.3.4.1 Computation of SUR scalar macrocracking variables $\omega^{\mathrm{M}}(\zeta^{\mathrm{M}}, \zeta^{\mathrm{M}}_{eff})$

The Smooth-Unloading-Reloading (SUR) method that uses branch and target softening functions to deal with the response of Gauss Points along embedded strong discontinuities is used to compute the scalar macrocracking variables $\omega^{\mathrm{M}}(\zeta^{\mathrm{M}}, \zeta^{\mathrm{M}}_{eff})$ from Section 3.3.7. This is summarised in Algorithm 6 and shown in Figure 4.7.

Algorithm 6: Compute SUR tractions $\mathrm{t}^n_{\Gamma,ur}$ and macrocracking scalar variables ω^{M}, upon updates of effective ζ^{M}_{eff} and maximum experienced equivalent relative displacement ζ^{M} at macrocrack's Gauss Point.

```
input  : Trial updates of macrocrack effective and maximum experienced
         relative displacement $\zeta^{\mathrm{M}}_{eff}$ and $\zeta^{\mathrm{M}}$, along macrocrak Gauss Points.
output: SUR tractions $\mathrm{t}^n_{\Gamma,ur}$ and macrocracking scalar variables $\omega^{\mathrm{M}}$
// Loop over Gauss Points along macrocrack; $n^{GP}_{ck}$ being total number of GPs
for $igp_{ck} = 1 \dots n^{GP}_{ck}$ do
    Compute traction from target function, for given maximum experienced $\zeta^{\mathrm{M}}$:
    $\mathrm{t}^n_{\Gamma,t}(\zeta^{\mathrm{M}}) \leftarrow f_t^{\mathrm{M}}\left[r_s^{\mathrm{M}} + (1-r_s^{\mathrm{M}})\exp\left\{-c_s \frac{\zeta^{\mathrm{M}} - a_{k,ur}\cdot h_{ca}\cdot f_t{}^{\mathrm{M}}/\bar{E}_{am}}{u_{max} - a_{k,ur}\cdot h_{ca}\cdot f_t{}^{\mathrm{M}}/\bar{E}_{am}}\right\}\right], \zeta^{\mathrm{M}} \geq a_{k,ur}\cdot\zeta_t^{\mathrm{M}}$ ;
    Compute asymptotic SUR traction $\mathrm{t}^n_{\Gamma,k}(\zeta^{\mathrm{M}})$ associated with target function:
    $\mathrm{t}^n_{\Gamma,k}(\zeta^{\mathrm{M}}) \leftarrow \mathrm{t}^n_{\Gamma,t}(\zeta^{\mathrm{M}}) \cdot \nu_{ur} \cdot a_{k,ur}$, in $\zeta^{\mathrm{M}} \geq a_{k,ur}\cdot\zeta_t^{\mathrm{M}}$ ;
    Compute macrocracking auxiliar displacement for detecting SUR transition:
    $\zeta^{\mathrm{M}}_{eff,aux}(\zeta^{\mathrm{M}}, \zeta^{\mathrm{M}}_{eff}) \leftarrow \begin{cases} a_{p,ur}\cdot\zeta^{\mathrm{M}} & \text{if } \zeta^{\mathrm{M}}_{eff} \leq a_{p,ur}\cdot\zeta^{\mathrm{M}} \\ \zeta^{\mathrm{M}}_{eff} & \text{if } \zeta^{\mathrm{M}}_{eff} > a_{p,ur}\cdot\zeta^{\mathrm{M}} \end{cases}$ ;
    Compute SUR traction at the macrocracking auxiliar displacement $\zeta^{\mathrm{M}}_{eff,aux}$:
    $\mathrm{t}^n_{\Gamma,ur}(\zeta^{\mathrm{M}}, \zeta^{\mathrm{M}}_{eff,aux}) \leftarrow \mathrm{t}^n_{\Gamma,k}(\zeta^{\mathrm{M}}) \cdot \left[1 - \left(1 - \frac{a_{p,ur}}{\nu_{ur}}\right)\exp\left\{-\frac{\zeta^{\mathrm{M}}_{eff,aux} - a_{p,ur}\zeta^{\mathrm{M}}}{(\nu_{ur} - a_{p,ur})\zeta^{\mathrm{M}}}\right\}\right]$ ;
    Compute SUR-derived scalar macrocracking variable:
    $\omega^{\mathrm{M}} \leftarrow 1 - \frac{\mathrm{t}^n_{\Gamma,ur}(\zeta^{\mathrm{M}}, \zeta^{\mathrm{M}}_{eff,aux})}{\bar{E}_{am}\cdot[\zeta^{\mathrm{M}}_{eff,aux}/h_{ca}]}$;
end
```

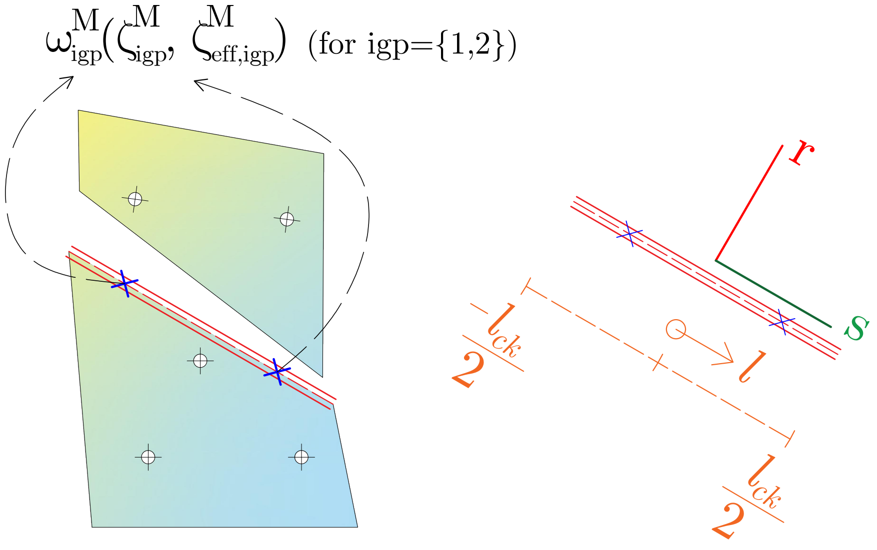

Figure 4.7: Sketch that illustrates the update of scalar macrocracking variables $\omega^{\mathrm{M}}(\zeta^{\mathrm{M}}, \zeta^{\mathrm{M}}_{eff})$ at Gauss Points along embedded strong discontinuity $\partial\Gamma^{\mathrm{M}}$.

4.3.4.2 Computation of the equivalent macrocracking relative displacement terms ζ^{M} and ζ^{M}_{eff}

The updates of the macrocracking equivalent displacement terms ζ^{M}, ζ^{M}_{eff} are tracked at macrocrack Gauss Points, using local relative displacements for subsequent update of scalar macrocracking variables $\omega^{\mathrm{M}}(\zeta^{\mathrm{M}}, \zeta^{\mathrm{M}}_{eff})$ and integration of the equivalent macrocrack force $\mathbf{F}_{\mathrm{ck}}$ as described in Algorithm 7.

Algorithm 7: Update scheme for macro-states $\{\zeta\}^{\mathrm{M}}$, $\{\zeta_{\mathrm{eff}}\}^{\mathrm{M}}$ for an embedded macrocrack Γ^{M}

```
input  : Given an updated macrocrack relative displacement $\mathbf{W} = [u_{rc}, u_{sc}, \alpha_c]^{\mathrm{T}}$
output: New macro-states $\{\zeta\}^{\mathrm{M}}$, $\{\zeta_{\mathrm{eff}}\}^{\mathrm{M}}$ and scalar variables $\{\omega\}^{\mathrm{M}}$
// Loop over Gauss Points along macrocrack for numerical integration, $\mathrm{n}^{\mathrm{GP}}_{\mathrm{ck}} := 2$;
for $igp_{ck} = 1 \ldots n^{GP}_{ck}$ do
    Compute local position along macrocrack: $l_{\mathrm{igp}} \leftarrow \{\mathbf{N}(\xi_{\mathrm{igp,ck}})\}^{\mathrm{T}}\mathbf{x}_{\mathrm{ck,edge}}$;
    Compute separation array $\Delta\mathbf{u}_{\Gamma^{\mathrm{M}}} \leftarrow [\Delta \mathrm{u}^{\mathrm{n}}_{\Gamma^{\mathrm{M}}}, \Delta \mathrm{u}^{\mathrm{t}}_{\Gamma^{\mathrm{M}}}]^{\mathrm{T}}$ for normal and tangential separation components: $\Delta \mathrm{u}^{\mathrm{n}}_{\Gamma^{\mathrm{M}}} \leftarrow u_{rc} + l_{\mathrm{igp}} \cdot \alpha_c$, and $\Delta \mathrm{u}^{\mathrm{t}}_{\Gamma^{\mathrm{M}}} \leftarrow u_{sc}$ ;
    Compute effective macro-state:
    $\zeta^{\mathrm{M}}_{eff,\mathrm{igp}} \leftarrow \frac{1}{2}\Delta \mathrm{u}^{\mathrm{n}}_{\Gamma^{\mathrm{M}}}\left[1+\left(\frac{\mu_\varepsilon}{r_\varepsilon}\right)^2\right] + \frac{1}{2r_\varepsilon^2}\sqrt{\left(r_\varepsilon^2-\mu_\varepsilon^2\right)^2(\Delta \mathrm{u}^{\mathrm{n}}_{\Gamma^{\mathrm{M}}})^2 + 4r_\varepsilon^2(\Delta \mathrm{u}^{\mathrm{t}}_{\Gamma^{\mathrm{M}}})^2}$ ;
    if $(\zeta^{M}_{eff,igp} > \zeta^{M}_{igp})$ & $(iiter \leq itfix)$ then
        Update maximum experienced macro-state: $\zeta^{\mathrm{M}}_{\mathrm{igp}} \leftarrow \zeta^{\mathrm{M}}_{eff,\mathrm{igp}}$;
    end
end
```

4.3.5 Algorithms for macrocrack continuity and diffuse-to-localised transition strategies

In this section, algorithms for macrocrack continuous propagation and detection are described. At first, criteria for continuity of macrocrack paths is elucidated. Secondly, the mechanical criteria behind macrocrack detection and directionality of macrocrack nucleation is discussed.

4.3.5.1 On geometric continuity of macrocracking trajectories

The implementation incorporates the philosophy of geometric path continuity for embedded macrocracks. In this context, in case no elements are being macroscopically cracked in the vicinity of the current element $\mathbf{\Omega}_{ielem}$, the macrocrack is sensibly assumed to form crossing the element centroid; whereas, when macrocracks are detected in the surroundings, the path of the continuous macrocrack is tracked using the method in Alfaiate et al. (2003, 2002); Freeman et al. (2020) as in Algorithm 8.

Algorithm 8: Sequential tracking criteria for embedded macrocracks in a multiscale EFEM framework with arbitrary fracture propagation direction, at every global iteration with iiter ≤ itfix.

```
input  : Global macroscale displacement at nodes $\mathbf{u}_g$.
output: New macrocrack geometry at fracturing elements.
// Loop over all elements in a sequential fashion
for ielem = 1 ... nelem do
    if macrocracking detected (§4.3.5.2) then
        Detect advancing macrocrack tips at boundaries;
        if number of macrocracks at boundaries ≥ 2 then
            Use two existing macrocrack tips to form macrocrack geometry
        else
            Extract element-based macroscale displacement at nodes $\mathbf{u}^{\mathrm{el}}$;
            Compute predictor strains at tracking positions $\bar{\boldsymbol{\varepsilon}} = \mathbf{B} \cdot \mathbf{u}^{\mathrm{el}}$;
            // Major principal homogenised strain direction defines $\mathbf{n}_{\Gamma^{\mathrm{M}}}$
            if number of macrocracks at boundaries ≥ 1 then
                Existing macrocrack tip serves as starting point for nucleation
            else
                Macrocrack is nucleated through the centre of gravity of the element
            end
        end
    end
end
```

Two cases occur as continuity is enforced, which depend upon the number of macrocrack tips detected in the element boundaries as shown in Figure 4.8 and described below:

- One macrocrack tip detected: the macrocrack is nucleated to depart from the existing macrocrack tip at the element boundary and the micromechanics-informed major principal strain direction defines the macrocrack normal;
- Two macrocrack tips detected: the macrocrack nucleation direction is not governed any more by mechanics only, and rather the two advancing macrocrack tips are used to form a newly nucleated macrocrack with the aim of providing continuity of the macrocracking trajectories

Note that special cases for more than two macrocracks being driven towards one element may occur, and the current macrocrack tracking algorithm would only join two of these incident macrocracks, without considering a more mechanically-meaningful criteria for macrocrack nucleation in such particular cases.

The following section provides details on the role of (i) Micromechanics and that of (ii) the iterative effective macrocracking relative displacement ζ^{M}_{eff} within macrocrack detection.

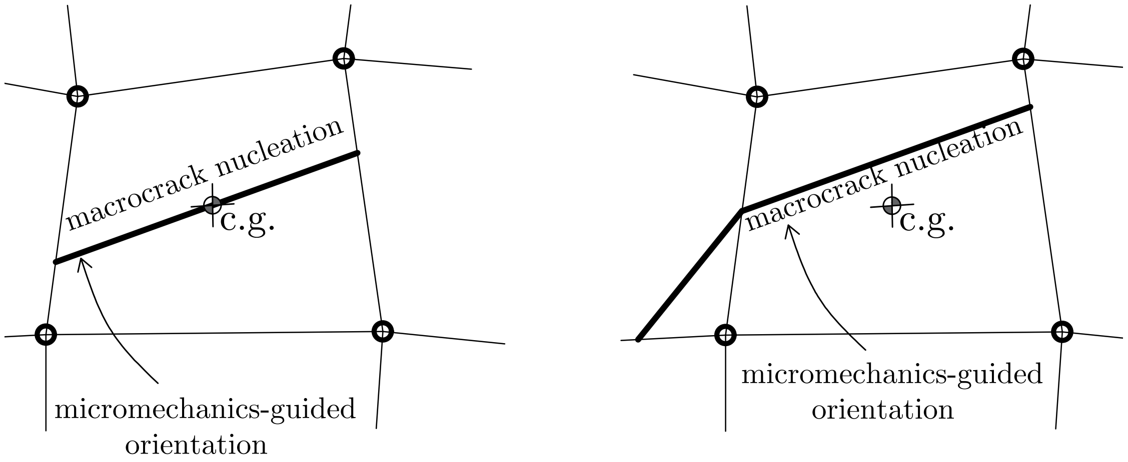

(a) Micromechanics-guided macrocracking in multiscale EFEM: nucleation through centre of gravity (left), and micromechanically-guided macrocrack through existing tip (right)

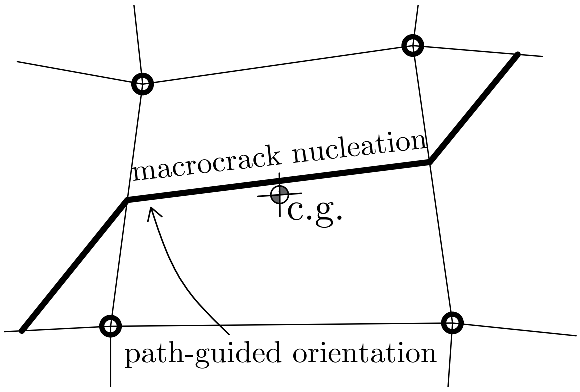

(b) Macrocrack-path continuity enforcement in multiscale EFEM: micromechanics-informed nucleation orientation superseded by full enforcement of geometric continuity.

Figure 4.8: Illustration of sequential embedded macrocrack tracking cases, to enforce geometric continuity of macrocracking trajectory, in combination with micromechanically-guided criteria for defining macrocrack nucleation orientation.

4.3.5.2 On theoretical and computational aspects of micro- to macrocracking transition

Macrocracking detection is treated as an element-wise procedure in $\boldsymbol{\Omega}_{ielem} \subset \boldsymbol{\Omega}^{\mathrm{M}}$. Two criteria are used, to identify the appropriate instant, at which embedded macrocracks can enable displacement jumps $\boldsymbol{\Delta}\widehat{\mathbf{u}}_{\Gamma^{\mathrm{M}}}(x' \in \partial\Gamma_{\mathrm{M}}) = \boldsymbol{\Lambda} \cdot \widehat{\mathbf{W}}$ along the embedded strong discontinuity as described in Equation 3.39.

The first macrocrack detection criterion postulates the major principal homogenised stress $\bar{\sigma}_1$ at the tracking GP (or average from two GPs) shall comply with the following criteria to enable element-wise macrocracking:

$$\bar{\sigma}_1 \geq \bar{\sigma}_{crit}, \quad \bar{\sigma}_{crit} := [a_{p,ur}a_{k,ur} + (1 - a_{p,ur}a_{k,ur})k_{mM}]f_t^{\mathrm{M}} \tag{4.30}$$

where tracking of the major principal homogenised stress $\bar{\sigma}_1$ is carried out, at a chosen Gauss Point (GP) (or average from two GPs) at the Micromechanical continua in $\boldsymbol{\Omega}_{ielem} = \boldsymbol{\Omega}^+_{ielem} \cup \boldsymbol{\Omega}^-_{ielem}$; $a_{p,ur}$, $a_{k,ur}$ are parameters that control the Smooth-Unloading/Reloading (SUR) character of the traction-separation law of the embedded macrocrack band from Section 3.3.7 ; f_t^{M} is the macroscopic tensile peak-stress that can be observed at the onset of failure; and $k_{mM} \in [0, 1]$ is a micro-to-macro transition parameter that controls the delay of macrocrack occurrence. Conveniently, k_{mM} has been incorporated as a user-defined transition parameter, which allows the analyst to control to some extent the nucleation of macrocracks. It has been found that for practical use $k_{mM} \approx 1$, renders an adequate micro- to macrocracking transition.

A few observations are made regarding the selection of the GP for macrocrack detection based on Equation 4.30:

- Tracking of the major principal homogenised stress $\bar{\sigma}_1$ at the dummy (central) GP is used for macrocrack detection in most situations, although not adequate for cases of complicated fracture patterns. Tracking at the central GP is also used when no adjacent elements are fractured.

- Tracking of the average major principal homogenised stress $\frac{1}{2}(\bar{\sigma}_{1,\mathrm{GP}_1} + \bar{\sigma}_{1,\mathrm{GP}_2})$, at the two closest GPs to the advancing macrocrack tip, is used in cases of more complex fracture patterns.

The second macrocrack detection criterion states the average effective macrocracking relative displacement $\zeta^{\mathrm{M}}_{eff,avg} = \frac{1}{2}(\zeta^{\mathrm{M}}_{eff,1} + \zeta^{\mathrm{M}}_{eff,2})$, upon a variationally-consistent force recovery described in Equation 4.17, must exceed a minimum threshold defined below:

$$\zeta^{\mathrm{M}}_{eff,avg} \geq \zeta^{\mathrm{M}}_{crit}, \quad \zeta^{\mathrm{M}}_{crit} := a_{k,ur} h_{ca} \frac{f_t^{\mathrm{M}}}{\bar{E}_{am}} \tag{4.31}$$

It is also convenient to track the evolution of inelastic deformation beyond the threshold in Equation 4.31, along nucleated macrocracks in an objective way using a normalised inelastic macrocrack relative displacement $\zeta^{\mathrm{M}}_{in,norm}$:

$$\zeta^{\mathrm{M}}_{in,norm} := \frac{\zeta^{\mathrm{M}}_{eff,avg} - \zeta^{\mathrm{M}}_{crit}}{(1 - a_{p,ur})\zeta^{\mathrm{M}}_{crit}} \tag{4.32}$$

After a macrocrack has been detected, geometric features are derived ensuring the macrocrack propagation direction is perpendicular to the major principal direction of the homogenised strain $\bar{\boldsymbol{\varepsilon}}$, obtained at the chosen GP for tracking in the Micromechanical continua (or an average direction, derived from two GPs consistently with stress-based tracking, can be used). Such detection and propagation direction criteria are combined with geometric path continuity philosophies as explained in the Section 4.3.5.1. An illustration of the procedure of macrocrack detection, combined with a sequential macrocrack tracking algorithm is shown in Figure 4.9.

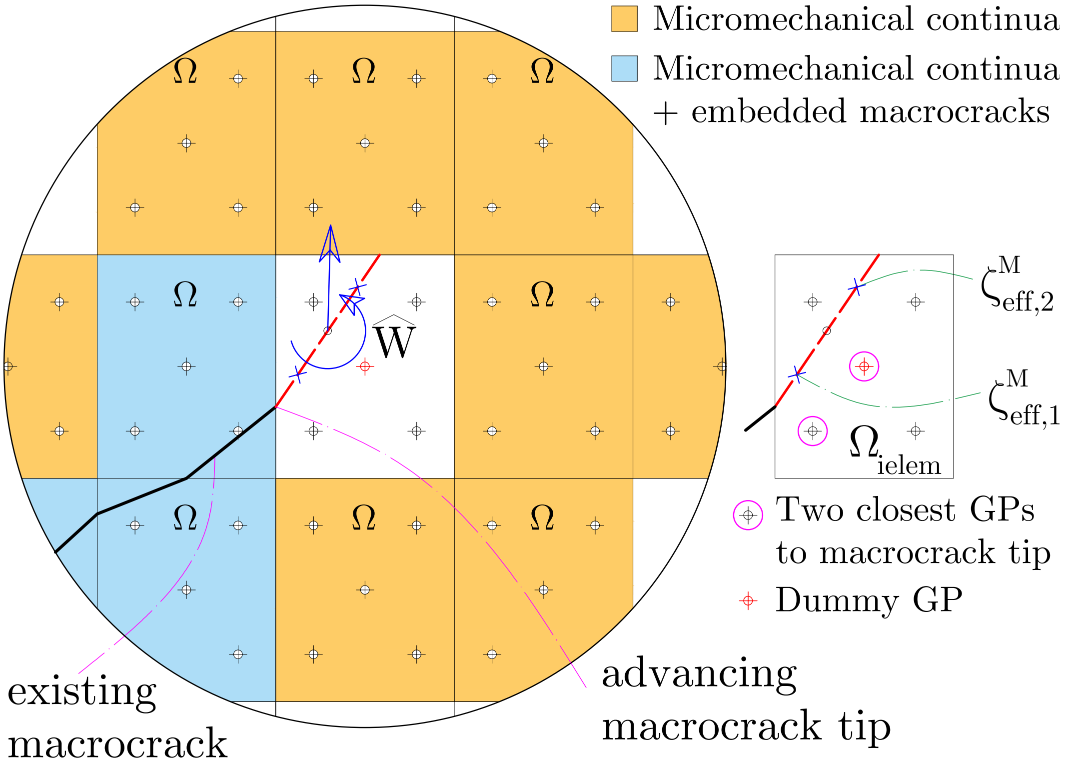

Figure 4.9: Macrocrack detection in a Micromechanical continua, combined with geometric continuity features of macrocracking trajectories.

N.B.: Newly nucleated macrocracks that comply with both macrocracking criteria in Equations 4.30 and 4.31, are allowed to rotate and be updated in geometry in the current global iteration (within a single incremental step). Geometric updates are allowed for the first **itfix** global iteration (**itfix** = 3).

Figure 4.10 shows a flow chart incorporating steps for macrocrack detection, and for combining this with macrocrack tracking.

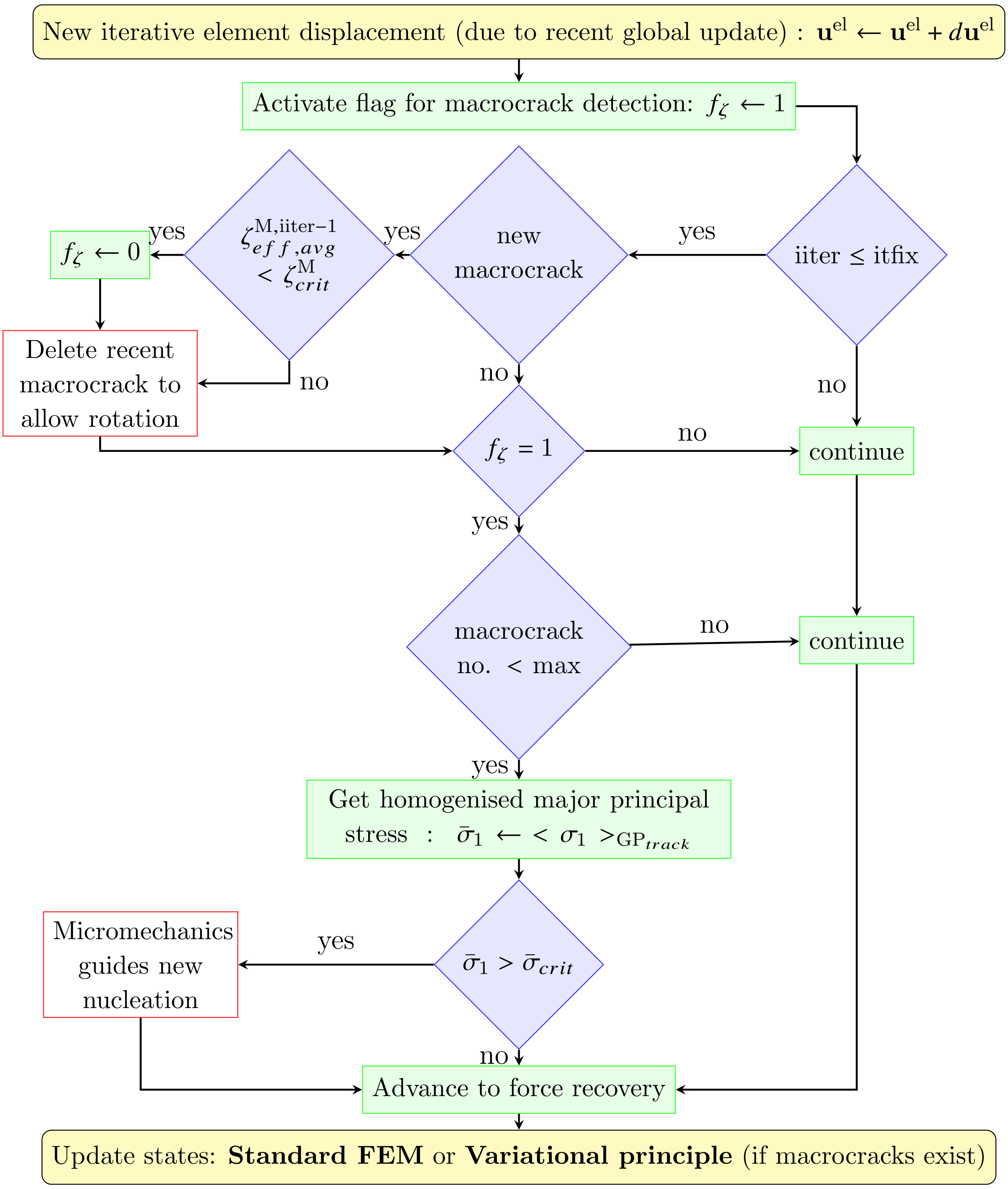

Figure 4.10: Flow chart for macrocrack nucleation criteria in a Micromechanical solid, and subsequent choice of update schemes for micro/macro state variables.

The implementation of both, macrocrack detection and geometric continuity enforcement algorithms, have the slight limitation of being sequential. The improvement of the proposed method, via a global macrocrak detection and tracking algorithm, is a subject for future research.

4.4 On techniques for robust implementation

In some cases, the standard Newton's scheme for the solution of equations associated with the minimum energy quasi-static condensation procedure from Section 4.3.2 has been found to be insufficient, since the very first trial solution must be close enough to the actual solution of the system of PDEs, otherwise the numerically updated solution may bounce within the proximity of the solution or break-down the iterative solution with increasingly diverging error norms, where typical values of tolerances are reported in Algorithm 2.

In this regard, two different techniques have been tailored for improving the robustness of the proposed multiscale EFEM methodology.

- 4.4.1 Line search algorithm at the element level: this numerical strategy helps the trial solution to get closer to the element-based minimum energy solution upon numerical bouncing, which is typical failure of a Newton's iterative solver if the first trial solution is far away from the expected solution.
- 4.4.2 Arc-length control scheme for crack analysis: this has not been fully completed due to the time limits of the PhD. The main idea is to allow snapping-back response to be simulated with the new multiscale fracture method by restricting an equivalent arc-length in force-displacement space.

4.4.1 Line search for improving element-based iterative quasi-static condensation scheme

To stabilise the convergence of macrocracking dofs $\mathbf{W}$ at the element-level, a simple 'one-dimensional' search is done in the space $\bar{\psi}_\phi$ vs ζ_ϕ, to find an abscissa $\zeta_\phi = ||\mathbf{W}_{trial} - \mathbf{W}_{prev}||/||\Delta\mathbf{W}||$ associated with an approximate minimum residual norm as expressed in Equation 4.33.

$$
\left.
\begin{aligned}
&\bar{\psi}_\phi(\zeta_\phi) = \frac{\sqrt{\left(\boldsymbol{\psi}_\phi\left(\mathbf{W}_{trial(\zeta_\phi)}\right)\right)^{\mathrm{T}} \cdot \left(\boldsymbol{\psi}_\phi\left(\mathbf{W}_{trial(\zeta_\phi)}\right)\right)}}{u_{max}} \\
&\boldsymbol{\psi}_\phi\left(\mathbf{W}_{trial}(\zeta_\phi)\right) = \begin{bmatrix} 1 & 0 & 0 \\ 0 & 1 & 0 \\ 0 & 0 & \sqrt{A_{ielem}} \end{bmatrix} \cdot \boldsymbol{\phi}_w^{\mathrm{el}}\left(\mathbf{W}_{trial}(\zeta_\phi)\right) \\
&\boldsymbol{\phi}_w^{\mathrm{el}}\left(\mathbf{W}_{trial}(\zeta_\phi)\right) = \mathbf{W}_{trial}(\zeta_\phi) - \mathbf{C}_\Gamma\left(\mathbf{W}_{trial}(\zeta_\phi), \mathbf{u}^{\mathrm{el}}\right) \cdot \mathbf{u}^{\mathrm{el}} \\
&\mathbf{W}_{trial}(\zeta_\phi) = \mathbf{W}_{prev} + \zeta_\phi \cdot \Delta\mathbf{W}
\end{aligned}
\right\} \tag{4.33}
$$

where the residual norms are interpolated for macrocracking dofs $\mathbf{W}$ within the range $\mathbf{W} \in \left[\mathbf{W}_{prev}, \mathbf{W}_{prev} + \Delta\mathbf{W}\right]$. In the literature (see e.g. Press et al. (1988)), recommendations for cubic or higher order interpolations are reported. Hence, a cubic polynomial is used as the basis for finding a local minimum as illustrated in Figure 4.11:

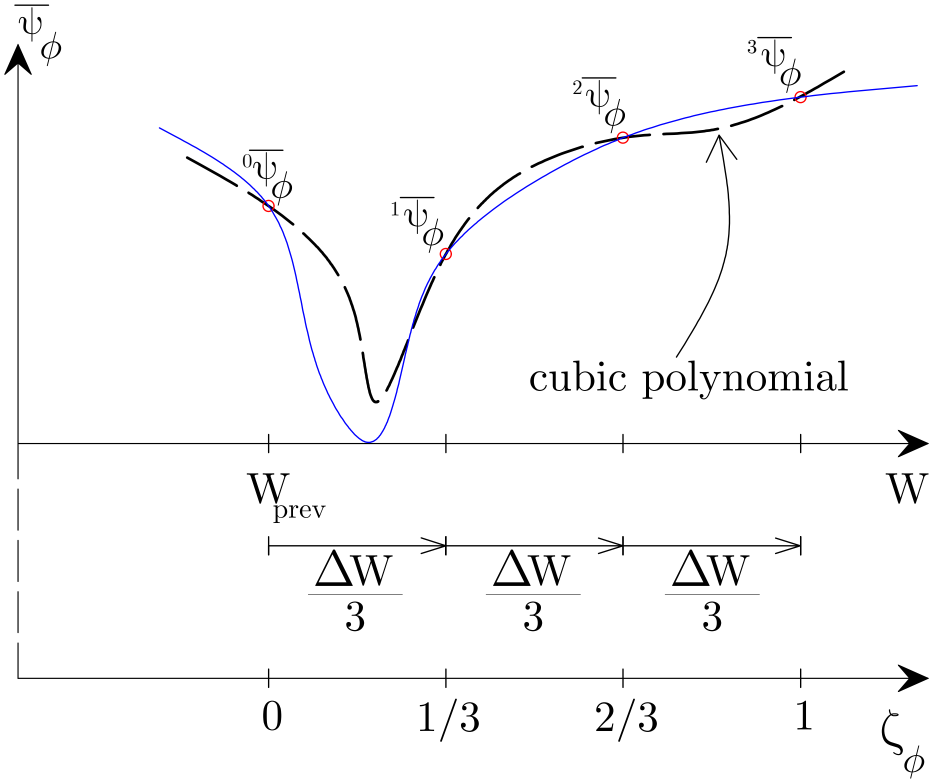

Figure 4.11: Interpolation of residual norms as a function of a normalised variation of macrocracking dofs $\zeta_\phi = ||\mathbf{W}_{trial} - \mathbf{W}_{prev}||/||\Delta\mathbf{W}||$, within the domain $\mathbf{W} \in [\mathbf{W}_{prev}, \mathbf{W}_{prev} + \Delta\mathbf{W}]$.

Note that two additional intermediate ζ_ϕ-points, aside from the extremes of the domain $\zeta_\phi = 0.0$ and $\zeta_\phi = 1.0$, are used to collect at least four data points for cubic interpolation, e.g. evaluation of the residual norm is done over $\boldsymbol{\zeta}_\phi = [0.0, 1/3, 2/3, 1.0]^{\mathrm{T}}$. Therefore, the computing overhead for the cubic interpolation is in the order of repeating the evaluation of the quasi-static condensation equation a few times. The interpolated polynomial for residual norms takes the form:

$$\bar{\psi}_\phi\left(\zeta_\phi\right) = a_{\phi,3} \cdot \zeta_\phi^3 + a_{\phi,2} \cdot \zeta_\phi^2 + a_{\phi,1} \cdot \zeta_\phi + a_{\phi,0} \tag{4.34}$$

where the coefficient, which is not associated with powers of ζ_ϕ, is defined as $a_{\phi,0} =^0 \bar{\psi}_\phi = \bar{\psi}_\phi(\zeta_\phi = 0.0)$. Hence, by re-arranging the cubic polynomial for residuals:

$$\bar{\psi}_\phi\left(\zeta_\phi\right) -^0 \bar{\psi}_\phi = \left[\begin{array}{ccc} \zeta_\phi & \zeta_\phi^2 & \zeta_\phi^3 \end{array}\right] \cdot \left\{\begin{array}{c} a_{\phi,1} \\ a_{\phi,2} \\ a_{\phi,3} \end{array}\right\} \tag{4.35}$$

By evaluating the polynomial over the remaining three data points ${}^1\zeta_\phi = 1/3$, ${}^2\zeta_\phi = 2/3$ and ${}^3\zeta_\phi = 1.0$, the coefficients of the cubic polynomial can be recovered:

$$\mathbf{a}_\phi = \mathbf{M}_\phi^{-1} \cdot \bar{\boldsymbol{\psi}}_{\phi,m} \tag{4.36}$$

where $\bar{\boldsymbol{\psi}}_{\phi,m} = [\bar{\psi}_\phi({}^1\zeta_\phi) -^0 \bar{\psi}_\phi, \bar{\psi}_\phi({}^2\zeta_\phi) -^0 \bar{\psi}_\phi, \bar{\psi}_\phi({}^3\zeta_\phi) -^0 \bar{\psi}_\phi]^{\mathrm{T}}$, the array of coefficients is defined as $\mathbf{a}_\phi = [a_{\phi,1}, a_{\phi,2}, a_{\phi,3}]^{\mathrm{T}}$, and the interpolation matrix $\mathbf{M}_\phi$ is a constant [1], hence, it can be initialised once and re-utilised every time the line search procedure is re-called:

$$\mathbf{M}_\phi = \left[\begin{array}{ccc} {}^1\zeta_\phi & \left({}^1\zeta_\phi\right)^2 & \left({}^1\zeta_\phi\right)^3 \\ {}^2\zeta_\phi & \left({}^2\zeta_\phi\right)^2 & \left({}^2\zeta_\phi\right)^3 \\ {}^3\zeta_\phi & \left({}^3\zeta_\phi\right)^2 & \left({}^3\zeta_\phi\right)^3 \end{array}\right] \tag{4.37}$$

Upon computation of the coefficients of the interpolating cubic polynomial of residuals, an approximate ζ_ϕ-point for a local minima can be obtained equating the first derivative $\partial\bar{\psi}_\phi/\partial\zeta_\phi$ to zero, and checking that the second derivative $\partial^2\bar{\psi}_\phi/\partial\zeta_\phi^2$ is larger than zero. Elaborating on these premises, by using a quadratic form solution, leads to the following roots and local minima criteria:

$$\left.\begin{array}{lcl} \partial\bar{\psi}_\phi/\partial\zeta_\phi = 0 & \rightarrow & \zeta_{\phi,min} = \frac{-2\cdot a_{\phi,2} \pm \sqrt{4\cdot a_{\phi,2}^2 - 12\cdot a_{\phi,3}\cdot a_{\phi,1}}}{6\cdot a_{\phi,3}} \\ \partial^2\bar{\psi}_\phi/\partial\zeta_\phi^2 > 0 & \rightarrow & \text{check that} \quad 2\cdot a_{\phi,2} + 6\cdot a_{\phi,3}\cdot\zeta_{\phi,min} > 0 \end{array}\right\} \tag{4.38}$$

where only one of the roots, if it exists in the real domain, will comply with the second derivative criteria. Such local minima would serve to trace back the Newton's scheme to a closer trial solution $\mathbf{W}_{trial,min} = \mathbf{W}_{prev} + \zeta_{\phi,min} \cdot \Delta\mathbf{W}$, which can be used as a departing numerical solution towards finding the true solution for a stringent tolerance using Newton's iterations in the usual way.

---

[1] Numerical evaluation leads to $\mathbf{M}_\phi = \left[\begin{array}{ccc} \frac{1}{3} & \left(\frac{1}{3}\right)^2 & \left(\frac{1}{3}\right)^3 \\ \frac{2}{3} & \left(\frac{2}{3}\right)^2 & \left(\frac{2}{3}\right)^3 \\ 1 & (1)^2 & (1)^3 \end{array}\right]$, and $\mathbf{M}_\phi^{-1} = \left[\begin{array}{ccc} 9 & -\frac{9}{2} & 1 \\ -\frac{45}{2} & 18 & -\frac{9}{2} \\ \frac{27}{2} & -\frac{27}{2} & \frac{9}{2} \end{array}\right]$

4.4.2 On arc-length control for global iterative procedure to circumvent snapping-back

A scalar-valued constraint equation is proposed to be coupled to the global equilibrium equation, which possesses a total number of degrees of freedom ntdof = npoin · ndofn, to form an ntdof + 1 space of unknowns and ntdof + 1 equations (De Borst et al., 2012; Pretti et al., 2022; Riks, 1979). The ntdof + 1 system of PDEs is solved for the iterative unknowns $\{\delta\lambda, \boldsymbol{\delta}\mathbf{u}_g\}$ using a Newton's type split scheme:

$$\left.\begin{aligned} \boldsymbol{\Phi}_F^* = \mathbf{F}_{\text{ext}}^0 + \mathbf{r}_{\text{react}}^0 + \Delta\lambda(\mathbf{F}_{\text{ext}} + \mathbf{r}_{\text{react}}) - \mathbf{F}_{\text{int}} + \delta\lambda(\mathbf{F}_{\text{ext}} + \mathbf{r}_{\text{react}}) - \mathbf{K}_g\boldsymbol{\delta}\mathbf{u}_g = \mathbf{0} \\ g_{ac} = \boldsymbol{\Delta}\mathbf{L}_{ac}^{\text{T}} \cdot \Delta\mathbf{L}_{ac} - (\Delta l)^2 = \{\mathbf{A}_{ac} \cdot \Delta\mathbf{u}_g\}^{\text{T}} \cdot \{\mathbf{A}_{ac} \cdot \Delta\mathbf{u}_g\} - (\Delta l)^2 = 0 \end{aligned}\right\} \tag{4.39}$$

where $\boldsymbol{\Delta}\mathbf{L}_{ac} = \mathbf{A}_{ac}\Delta\mathbf{u}_g$ contains the vectorial expression for the difference in position between two chosen nodal locations. Some rearrangement of Equation 4.39 leads to the following system to be solved sequentially, in such a manner that prescribed zero nodal displacements can be included in the iterative procedure:

$$\left.\begin{aligned} \boldsymbol{\delta}\mathbf{u}_g^{\text{II}} &= \mathbf{K}_g^{-1} \cdot \phi_F \\ \boldsymbol{\delta}\mathbf{u}_g^{\text{I}} &= \mathbf{K}_g^{-1} \cdot (\mathbf{F}_{\text{ext}} + \mathbf{r}_{\text{react}}) \\ a_{\lambda,2} \cdot \delta\lambda^2 + a_{\lambda,1} \cdot \delta\lambda + a_{\lambda,0} &= 0 \\ \boldsymbol{\delta}\mathbf{u}_g &= \boldsymbol{\delta}\mathbf{u}_g^{\text{II}} + \delta\lambda\boldsymbol{\delta}\mathbf{u}_g^{\text{I}} \end{aligned}\right\} \tag{4.40}$$

where the constants for the quadratic form of the arc-length equation, to solve for a physically meaningful iterative load-amplification factor $\delta\lambda$, are as follows:

$$\left.\begin{aligned} a_{\lambda,2} &= \{\mathbf{A}_{ac}\boldsymbol{\delta}\mathbf{u}_g^{\text{I}}\}^{\text{T}} \cdot \mathbf{A}_{ac} \cdot \boldsymbol{\delta}\mathbf{u}_g^{\text{I}} \\ a_{\lambda,1} &= 2\{\mathbf{A}_{ac} \cdot (\Delta\mathbf{u}_g^{j-1} + \boldsymbol{\delta}\mathbf{u}_g^{\text{II}})\}^{\text{T}} \cdot \mathbf{A}_{ac} \cdot \boldsymbol{\delta}\mathbf{u}_g^{\text{I}} \\ a_{\lambda,0} &= \{\mathbf{A}_{ac} \cdot (\Delta\mathbf{u}_g^{j-1} + \boldsymbol{\delta}\mathbf{u}_g^{\text{II}})\}^{\text{T}} \cdot \mathbf{A}_{ac} \cdot (\Delta\mathbf{u}_g^{j-1} + \boldsymbol{\delta}\mathbf{u}_g^{\text{II}}) - (\Delta l)^2 \end{aligned}\right\} \tag{4.41}$$

After each new update of $\Delta\lambda$ and $\Delta\mathbf{u}_g$ equilibrium is checked by subtracting the newly recovered internal force vector $\mathbf{F}_{\text{int}}$ from the updated external forces. This envisaged strategy for coupling a scalar-valued constraint equation to the global incremental iterative solution of the proposed multiscale EFEM framework, has yet to be completed. This is subject for future research.

4.5 Concluding remarks

In this chapter, algorithmic and numerical details of the proposed variationally-consistent multiscale EFEM framework have been given, as summarised below:

- Numerical aspects have been presented for the computational solution of the new multiscale EFEM model, by presenting a force recovery algorithm. In addition, for robustness and numerical efficiency, the computation of consistently-linearised element stiffness tangents has been described, for the case that elements are undergoing micro and/or macrocracking. In this regard, the need to adopt a central difference approximation in element stiffness tangents when macrocraking occurs is also explained.
- Algorithmic aspects of the global incremental iterative procedure have been clarified for a robust and efficient implementation, by taking advantage of positive tangents used in the SUR solution scheme. The added stability of the SUR method has been tested with representative numerical examples in the following chapter.
- The numerical schemes used for detecting and tracking marocracks have been described. These have been tailored to allow macrocracks to be continuous, while macrocracks are activated at an adequate instant of deformation localisation. Two criteria are proposed for detection, which are associated with the micromechanics-enriched strain field and with the evolution of the equivalent macrocrack relative displacement upon force recovery before nucleating macrocracks are fixed.
- Some numerical methods have been described for improving the robustness of the multiscale EFEM method, tackling both the element-based quasi-static iterative procedure and global incremental iterative solution. The first one mentioned has been implemented, whereas the second one requires attention in further research.

Chapter 5

Numerical examples of multiscale quasi-brittle fracture

"Essentially, all models are wrong, but some are useful."
George E. P. Box 1919 - 2013
British Mathematician of the 20th century

5.1 Representative numerical examples

A series of problem examples are presented to analyse computational features, including robustness and efficiency, grid-insensitivity of structural response and applicability of the method to simulate cementitious composites, focusing on directional micromechanical degradation and macro-fracture propagation. The list of problems analysed is as follows:

5.1.3 Ex.1-Theoretical analyses on a single element.

5.1.4 Ex.2-Failure test on concrete L-panel by Winkler et al. (2001).

5.1.5 Ex.3-Uniaxial tensile test on bone-shaped concrete member by Petersson (1981).

5.1.6 Ex.4-Four-point bending test on plain concrete with no initial notch.

5.1.7 Ex.5-Failure test on hexagonal concrete member by Bennett and Jefferson (2007).

5.1.1 Explanation of features tested on numerical examples

The examples in 5.1.3-Ex.1 are theoretical problems in a single element to test the ability of directional microcracking to evolve along with evolution of macrocracking. All of the other examples use multi-element meshes . In addition, mesh sensitivity analyses are shown respectively in 5.1.4-Ex.2 and 5.1.6-Ex.4, for a single macrocrack propagating in a curved path, and for multiple macrocracks propagating almost parallel to each other so that some macrocracks shut while others become dominant.

A study of convergence of residuals is provided for 5.1.4-Ex.2. This presents sequential embedded macrocrack nucleation of a single propagating fracture until a stage of large post-peak deformation, which is hereby referred as an ultimate incremental step in the numerical model. Therefore, such an example tests the performance of the framework with sequential and crack tracking in a critical situation, opposed to less computationally demanding single element tests in 5.1.3-Ex.1. Such simpler element tests are expected to preserve a generic quadratic convergence of the equilibrium equations without much interference of computational choices for macrocrack propagation, after the only macrocrack expected settles, i.e. computational expense of deleting and nucleating more embedded macrocracks is avoided.

In addition, 5.1.5-Ex.3 elucidates the macrocrack tracking algorithm works for two or more incident macrocracks connecting in a macrocracking element, where macrocracks cut the Finite Element mesh all across the computing domain.

Finally, 5.1.7-Ex.5 tests the sequential macrocrack tracking and multiscale components, stringently, for an atypical concrete specimen, with hexagonal shape based on in-house experimental data (Bennett and Jefferson, 2007).

5.1.2 Multiscale fracture model calibration

5.1.2.1 On the Smooth-Unloading-Reloading numerical constants

Numerical constants that characterise the SUR macrocrack response were fixed as $\nu_{ur} = 0.85$ and $a_{p,ur} = 0.65$ for all numerical examples. Note that these values are different from the recommended values $\nu_{ur} = 0.75$ and $a_{p,ur} = 0.60$, which are reported in the literature for models using the SUR algorithm at the Gauss Point level only (Alnaas and Jefferson, 2016). It was found that the gradient of the SUR branch due to the chosen set of SUR parameters at the macrocrack level, eases the convergence of the new multiscale fracture method when compared to standard parameters.

5.1.2.2 On the number of integration directions for homogenisation

The number of degradation directions over half a circle has been fixed to $\mathrm{n}_{int}^{\mathrm{m}} = 21$ for numerical integration of the homogenised response at the RVE-level. This number of integration directions is fixed at all Gauss Points within the micromechanical bulk, including the dummy Gauss Point at the element centre. The preferred number of integration directions is an odd number to trace adequately symmetric microcracking evolution, and 9 directions or above tend to give good details of evolution. Nonetheless, having more than 21 integration directions in each Gauss Point can be challenging for data storage management without much gain in accuracy of microcracking evolution.

5.1.2.3 Guidance on calibration of mechanistic parameters

The remaining parameters are more physically-based opposed to more numerically oriented ones in Section 5.1.2.1 and 5.1.2.2. A first guide on calibration of such parameters has been presented before on Chapter 3 shown in Table 3.2.

Upon the coupling of both micro and macro components the cohesive-frictional constants r_σ and μ_σ, and the softening parameters u_{max} and c_s are assumed to be the same for both micro and macro-scales, which aims to reduce the number of input parameters.

Note that the macrocrack band virtual thickness h_{ca} can be based to a few times the coarse aggregate size in structural members of lab-scale. In addition, it is expected that the value of h_{ca} be larger in large-scale structural members, since the macrocrack band would represent the fracture process zone at a much coarser scale than one which only involves few aggregate grains.

Further guidance on mechanistic model parameters is summarised in Table 5.1.

Table 5.1: Guidance on model calibration for modelling quasi-brittle response of cementitious composites using a variational micromechanics-enriched EFEM.

Parameter	Comments on calibration
	Aggregate-matrix mixture elasticity constants
E, υ	Comments in Table 3.2 apply.
	Micro and macro strength parameters
f_t^{M}, f_t^{m}	Comments in Table 3.2 apply.
	Micro and macro length parameters
h_{ca}	This is set to a few times a characteristic component at the macroscale, e.g. coarse grain size in lab-scale structural members, or thick enough to represent the fracture process zone in larger structural members.
h_{fa}	The is set to a fraction of h_{ca}. In practice, $h_{fa} \approx (1/5) \cdot h_{ca}$ is a good starting point for calibration.
	Cohesive-frictional parameters
r_σ, μ_σ	Comments in Table 3.2 apply. These are set as equal for both micro and macroscales.
	Softening parameters
u_{max}, c_s	Comments in Table 3.2 apply. These are set as equal for both micro and macroscales.
r_s^{M}	Comments in Table 3.2 apply.

5.1.2.4 Sets of model parameters

A summary of model parameters used for the series of problems in this Chapter are summarised in Table 5.2, which were calibrated using guidelines in Table 5.1.

Table 5.2: Summary of model parameters for BVPs, including theoretical problems in a single element (examples analysed with set no. 1), as well as, numerical examples which have been validated using experimental data, or analytical means.

Parameter	Unit	5.1.3-Ex.1	5.1.4-Ex.2	5.1.5-Ex.3	5.1.6-Ex.4	5.1.7-Ex.5
		Aggregate-matrix mixture elasticity constants				
$\bar{E}_{am}$	N/mm^2	30000	20000	38000	30000	30000
$\bar{\upsilon}_{am}$	–	0.2	0.2	0.2	0.2	0.35
		Micro and macro strength parameters				
f_t^{m}	N/mm^2	1.70	2.00	1.80	1.30	4.00
f_t^{M}	N/mm^2	3.00	2.70	3.25	2.28	8.90
		Micro and macro length parameters				
h_{fa}	mm	0.50	0.30	0.03	0.15	0.03
h_{ca}	mm	2.00	2.00	0.15	0.75	0.15
		Cohesive-frictional parameters: identical for micro and macro-scale				
r_σ	–	1.50	1.20	1.50	1.31	1.50
μ_σ	–	1.00	1.30	1.00	1.20	0.50
		Softening parameters: u_{max} and c_s are set identical for micro and macro-scale				
u_{max}	mm	0.20	0.40	0.20	0.20	0.35
c_s	–	7.00	7.00	7.00	7.00	7.00
r_s^{M}	–	0.04	0.04	0.05	0.05	0.05

5.1.3 Theoretical analyses on a single element

At first, theoretical analyses are considered on a single element departing from an intact state, through micro and macrocracking until a large post-peak deformation. Two types of boundary conditions are used, namely, a) uniaxial tensile deformation applied along horizontal axis, and b) uniaxial tensile deformation along the horizontal axis until macrocracking occurrence, followed by tensile deformation combined with a tangential force applied incrementally.

The first boundary condition type is used to study (i) the effect of the user-defined transition parameter k_{mM} on macrocrack nucleation, (ii) the evolution of microcracking after the activation of a macrocrack, and (iii) the effect of the macrocrack virtual thickness h_{ca} on the overall response.

The second boundary condition is used to illustrate, the capacity of directional microcracking to evolve, upon the occurrence of macrocraking, in other directions not dominated by the nucleated macrocrack. In turn, an element $\mathbf{\Omega} \equiv \mathrm{b} \times \mathrm{d} \times t_g$ (b = d = 50 *mm* and out-of-page thickness t_g = 50 *mm*) is considered under plane stress settings, with boundary conditions as illustrated in Figure 5.1.

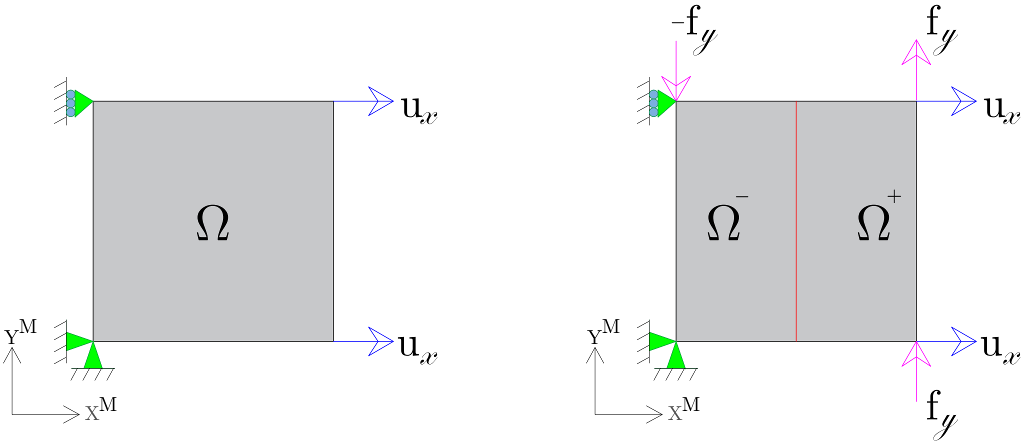

(a) (b)

Figure 5.1: Boundary conditions for macro-fracture propagation analyses on a cementitious solid, using a single element $\mathbf{\Omega}$: (a) uniaxial tension, (b) uniaxial tension and incremental tangential force applied upon macrocracking.

5.1.3.1 Single element under pure tensile deformation

The BVP in Figure 5.1a has been solved using 50 incremental steps until the horizontally prescribed deformation reaches u_x = 0.20 *mm*, considering smaller step size within the pre-peak and early post-peak structural response to capture non-linearities adequately with results shown in Figure 5.2a.

Remark 5.1.: Polar plots in Figures 5.2b and 5.2c present the magnitude of the directional microcracking scalar variable $\omega^{\mathrm{m}}_{\alpha}$ ($\alpha = 1 \ldots \mathrm{n}^{\mathrm{m}}_{int}$) for each unit normals which are perpendicular to the microcracking propagation direction. Note that the maximum values within the polar plots would tend to reveal the direction perpendicular to the nucleating macrocracks, which is similar to that obtained by tracing the eigen-vectors of the strain tensor. Other studies in the literature use an acoustic tensor (Zhao et al., 2018), or configurational crack measures (Bird et al., 2022) to trace such direction of accumulated damage.

Remark 5.2.: Note that the symmetry of loading and geometry, for a single square element under uniaxial tension, leads to equal directional microcracking evolution at any of the Gauss Points in the bulk. Hence, a single polar plot, which applies to any of the Gauss Points in the micromechanical bulk, is sufficient to study directional microcracking evolution before and after macrocraking in this uniaxial case.

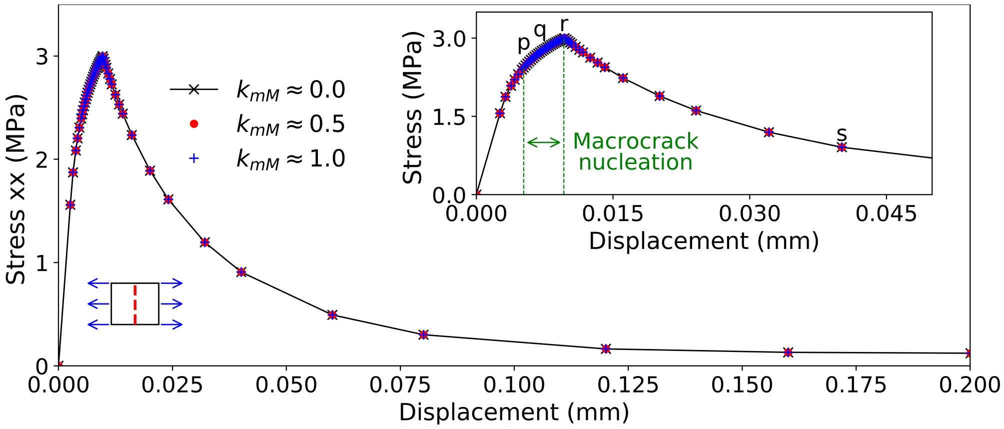

(a) Uniaxial tension: average stress vs displacement, $k_{mM} \in [0, 1]$

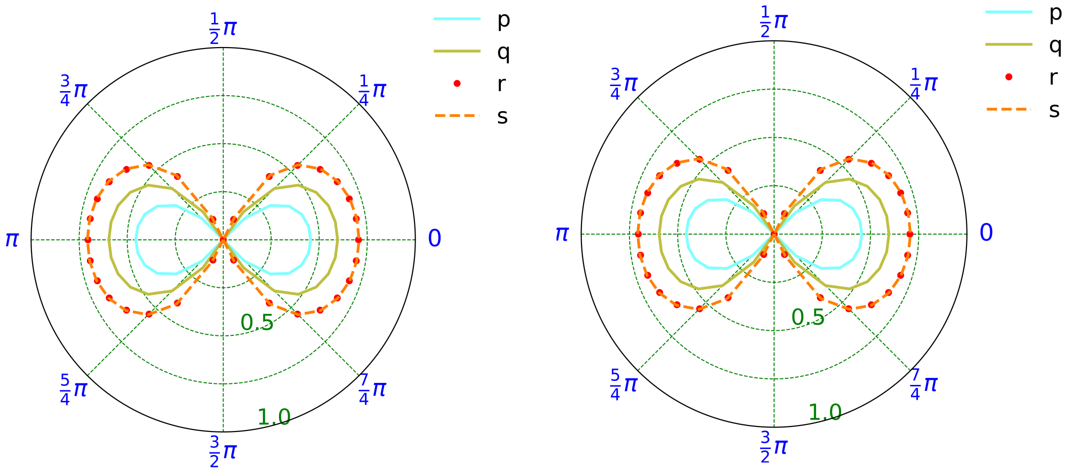

(b) Microcracking variables $\omega_\alpha^{\mathrm{m}}$: $k_{mM} = 0$ (c) Microcracking variables $\omega_\alpha^{\mathrm{m}}$: $k_{mM} = 1$

Figure 5.2: Uniaxial response of a cementitious solid: (a) stress-displacement curve, (b-c) bulk directional microcracking evolution.

In all cases presented for this BVP, global iterations did not exceed a maximum of three iterations for updates of the displacement field at the macroscale, i.e. it reached quadratic convergence. In these illustrative analyses, only the first macrocracking criteria in Equation 4.30 has been used. It is highlighted that, for practical use of this variational multiscale EFEM framework in other numerical examples, both macrocracking criteria described in Section 4.3.5.2 are used simultaneously, with $k_{mM} = 1.0$.

Regarding sensitivity of the structural-level response with respect to the micro-to-macrocracking transition parameter $k_{mM} \in [0, 1]$, under uniaxial tension, the start of macrocracking has been delayed as k_{mM} increases. For values $k_{mM} = 0.0$, $k_{mM} = 0.5$ and $k_{mM} = 1.0$, the start of macrocracking is points p, q and r as seen in Figure 5.2a.

The variational update of micro and macro states upon macrocrack activation at p (with $k_{mM} = 0.0$), q (with $k_{mM} = 0.5$) and r (with $k_{mM} = 1.0$) has been observed to produce in all cases a smooth transition from micro to macrocracking dominated phenomena in the load-displacement space as depicted in Figure 5.2a. This highlights that the parameter has little effect on the structural response for simple boundary conditions. For more complex problems, delaying macrocrack nucleation by setting $k_{mM} = 1$ seems appealing to allow well developed eigenvector fields in the microcracking bulk to track macrocracking directions.

Note that for either of the transition parameter limits $k_{mM} = 0.0$ and $k_{mM} = 1.0$ the microcracking directions are able to evolve until the structural peak r, since the variational updates sorts out the amount of deformation absorbed by the Continuum and the strong discontinuity as shown in Figures 5.2b and 5.2c. The structural-level bifurcation state r entails relaxation of the micromechanical continua as tensile deformation progresses at the macroscale (deformation is then absorbed by the nucleated macrocrack at the central axis of the element). Such relaxation is linked to the halt of the evolution of directional microcracking variables immediately after the peak structural stress, as illustrated by comparison of the microcracking states evolution $\omega_\alpha^{\mathrm{m}}$ from stage r and s at any of the Gauss Points in the bulk.

In addition, the value of the macro length parameter h_{ca} has been observed to cause negligible effects in the load-displacement curve for $h_{ca} \leq 0.30 \cdot h_{el}$, where h_{el} stands for the element length as illustrated in Figure 5.3.

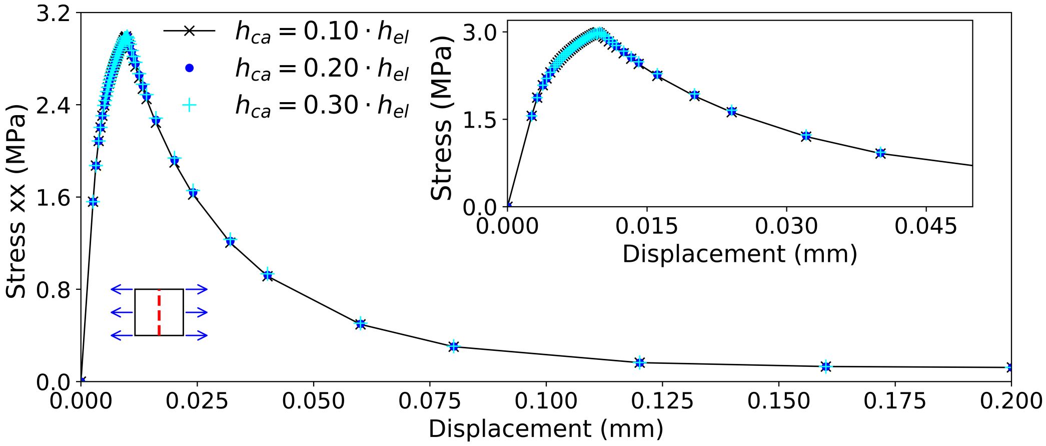

Figure 5.3: Uniaxial response of a cementitious solid in stress-displacement space: $h_{ca} \in [0.1 \cdot h_{el}, 0.3 \cdot h_{el}]$, $k_{mM} = 1$

Remark 5.3.: Calibration of the virtual thickness of macrocrack bands has been carried carefully to avoid imposing large ratios h_{ca}/h_{el}, which may have physically meaningful implications, such as an embedded macrocrack virtual thickness occupying a large proportion of the element although zero thickness is assigned at the Finite

Element spatial discretisation. Similarly, small values of the ratio $h_{ca}/h_{el} << 5\%$ have been refrained from use, to alleviate any undesired overflow challenges since the thickness of the virtual band is used as a denominator in the computation of the equivalent macrocrack force in Equation 4.8.

5.1.3.2 Single element under combined tensile and tangential action

The BVP in Figure 5.1b has been solved for various incremental nodal tangential forces actived only at the end of the step where the macrocrack is nucleated, whereas tensile deformation is imposed before and after macrocracking occurs, until the instant at which the average stress normal to the macrocrack vanishes. Mechanical splitting action before and after macrocracking is imposed in the horizontal direction. The post peak response was studied for four different levels of the (nodal) total tangential force; $f_y = 1500\ N$, $f_y = 1200\ N$, $f_y = 720\ N$, $f_y = 0\ N$. It is highlighted that the nodal total force f_y has been applied progressively only after macrocracking has been detected, to test the capability of the multiscale framework to capture combined tangential and normal mechanical actions upon macrocrack nucleation. The average stress-displacement curve, with components in the direction perpendicular to the macrocrack plane is shown in Figure 5.4a.

The stages stages t, w and z have been marked in Figure 5.4a, in addition to stages p, q, r and s that were previously studied under pure tensile deformation. These stages have been employed to study microcraking evolution under combined loading upon macrocracking occurrence. In addition, the problem example with $f_y = 0\ N$ degrades down as an equivalent response to the BVP in Figure 5.1a. It is remarked that only the Gauss Point closest to the node under full displacement constraint is used for this theoretical analysis, since the objective is to show the capacity of microcracking evolution, upon macrocracking, in various microcracking directions.

Note that for microcracking normals $\pi/4 \leq \theta^{\mathrm{m}} \leq \pi/2$ and $5\pi/4 \leq \theta^{\mathrm{m}} \leq 3\pi/2$, microcracking is enabled to evolve with respect to stage r, when macrocracking is detected and a macrocrack is nucleated with unit normal pointing into $\theta^{\mathrm{M}} = 0$ (or $\theta^{\mathrm{M}} = \pi$ interchangeably). Such microcracking evolution is more easily visualised in the polar plot corresponding to Figure 5.4b, for $f_y = 1500\ N$, while further microcracking is less perceptible for $f_y \leq 1200\ N$ in Figure 5.4c. In fact, as f_y decreases the response tends to resemble that under pure tensile deformation as observed in Figures 5.4d and 5.4e, for $f_y = 720\ N$ and $f_y = 0\ N$. Therefore, as f_y decreases principal directions within the micromechanical bulk tend to remain while deformation is absorbed by the embedded macrocrack.

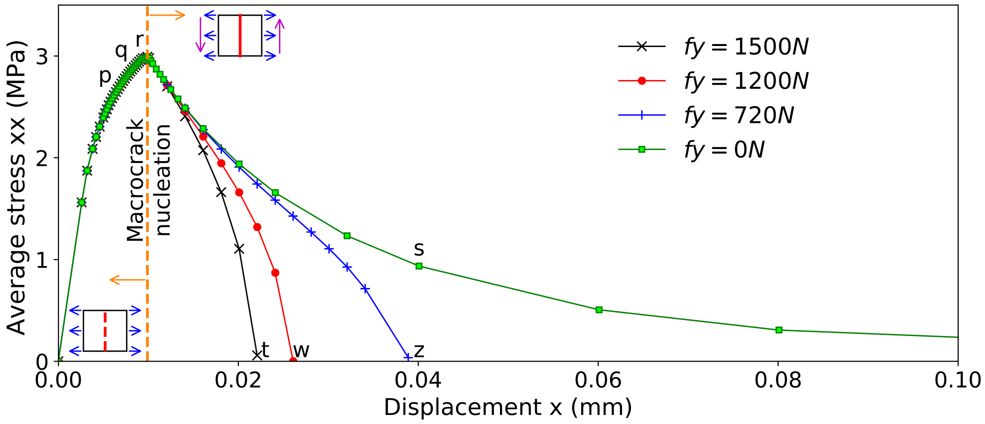

(a) Stress - displacement curve: f_y = 1500 N, f_y = 1200 N, f_y = 720 N, f_y = 0 N

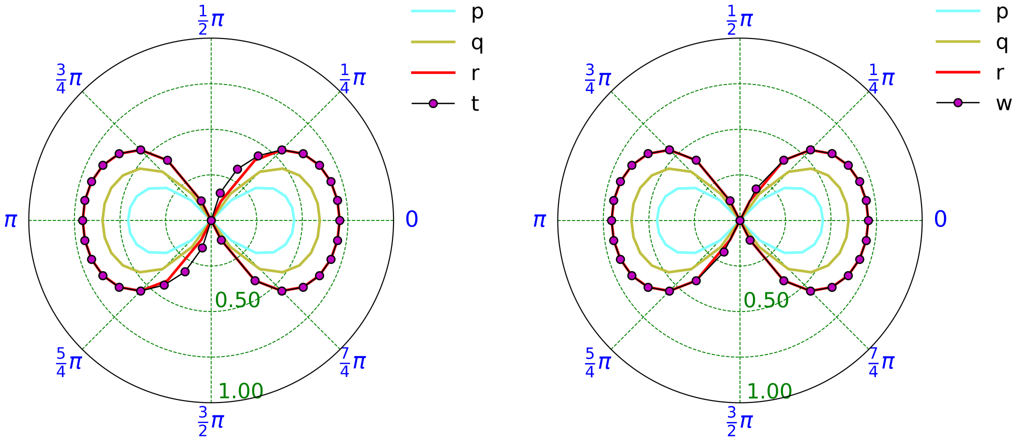

(b) Microcracking $\omega_\alpha^{\mathrm{m}}$: f_y = 1500 N (c) Microcracking $\omega_\alpha^{\mathrm{m}}$: f_y = 1200 N

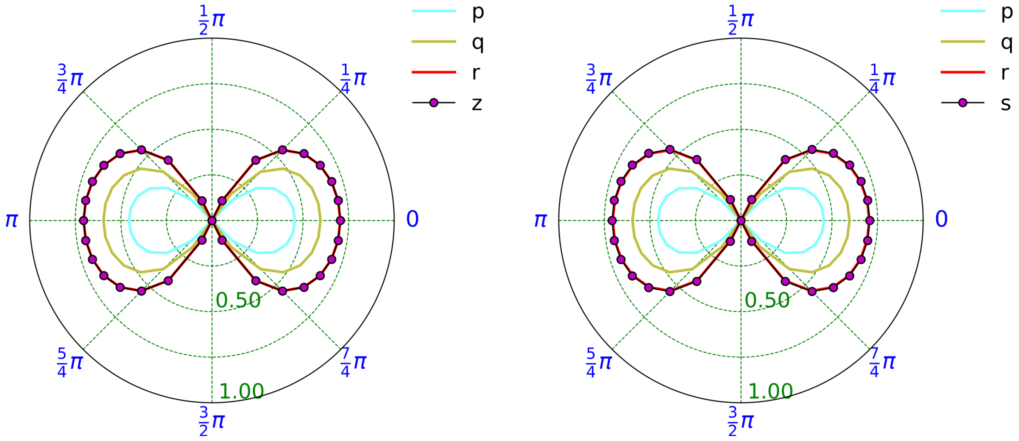

(d) Microcracking $\omega_\alpha^{\mathrm{m}}$: f_y = 720 N (e) Microcracking $\omega_\alpha^{\mathrm{m}}$: f_y = 0 N

Figure 5.4: Response of a cementitious solid. A single element $\mathbf{\Omega}$ is first subjected to pure tensile deformation until macrocracking occurrence, then subjected to combined incremental normal deformation and incremental tangential force.

Remark 5.4.: It is highlighted that the variational update of micro and macrocracking states dictates which microcracking directions remain active without any additional criteria to halt microcracking directions. This ensures that the overall micro-macro response corresponds to the minimum energy failure mechanism.

5.1.4 Failure test on concrete L-panel by Winkler et al. (2001)

5.1.4.1 Problem description

Winkler et al. (2001) tested a concrete L-panel, with the geometry shown in Figure 5.5a. The bottom of the specimen is restrained in horizontal and vertical direction. In the experiment, deformation was prescribed at a point located 30 *mm* away horizontally from the bottom corner of the hanging leg. Such conditions let to a single macrocrack be developed from the inner corner of the L-panel towards the right edge of the vertical leg. A representative fracture pattern, as recorded in experiments, and approximate boundary conditions to represent the setup in a numerical model are shown in Figure 5.5b

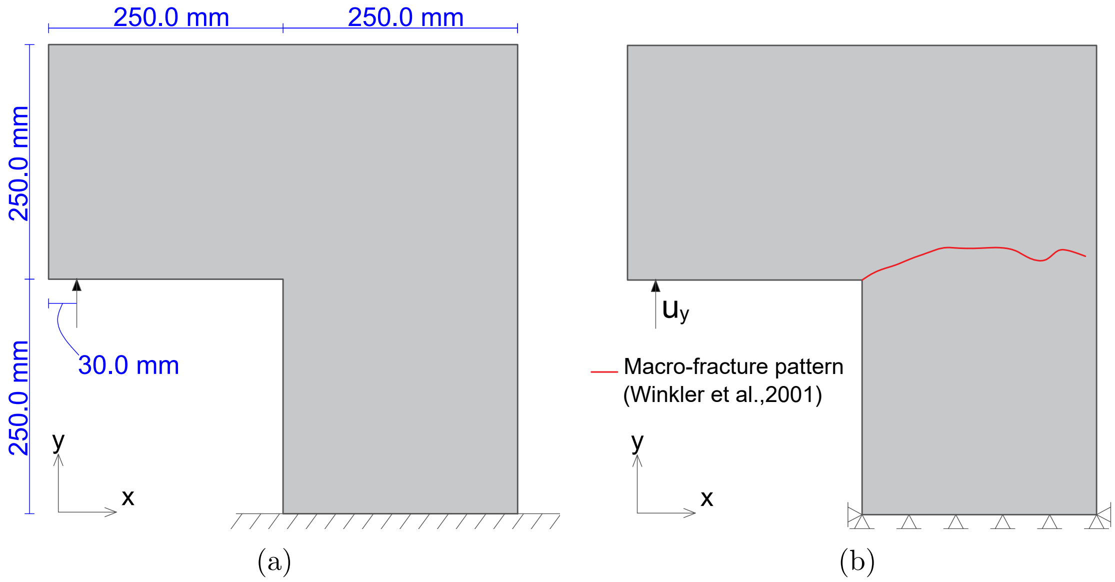

Figure 5.5: Sketch of L-panel, tested by Winkler et al. (2001): (a) geometric features (thickness = 100.0 *mm*), (b) boundary conditions, and representative macroscopic fracture pattern as recorded experimentally.

5.1.4.2 Numerical simulation

The domain is discretised with various meshes, opposed to the simpler single element domain in previous examples. The application of the newly presented formulation for coupled micro-macro quasi-brittle fracture is studied, to model the single macrocrack recorded in experiments. In addition, the reaction force that induces this macrocrack propagation is also predicted and compared with the experimentally-recorded reaction.

The self-weight of the specimen is neglected in all incremental stages, and the geometry presented in Figure 5.5 is adopted as the undeformed configuration. For the sake of simplicity, no contact considerations have been included between the loading device and the specimen at the point of uplift. In this regard, incremental stages of deformation were applied at the loading point.

In this problem example, 90 increments have been employed with an ultimate prescribed vertical displacement of 0.88 mm at the control point. Two meshes have been used to simulate adequately the L-panel test by Winkler et al. (2001), namely, Mesh 1 and Mesh 2, as illustrated in Figure 5.6. Note that unstructured meshes can be used with this new multiscale fracture modelling technique although the illustrative meshes are structured, as used to study objectivity with mesh refinement.

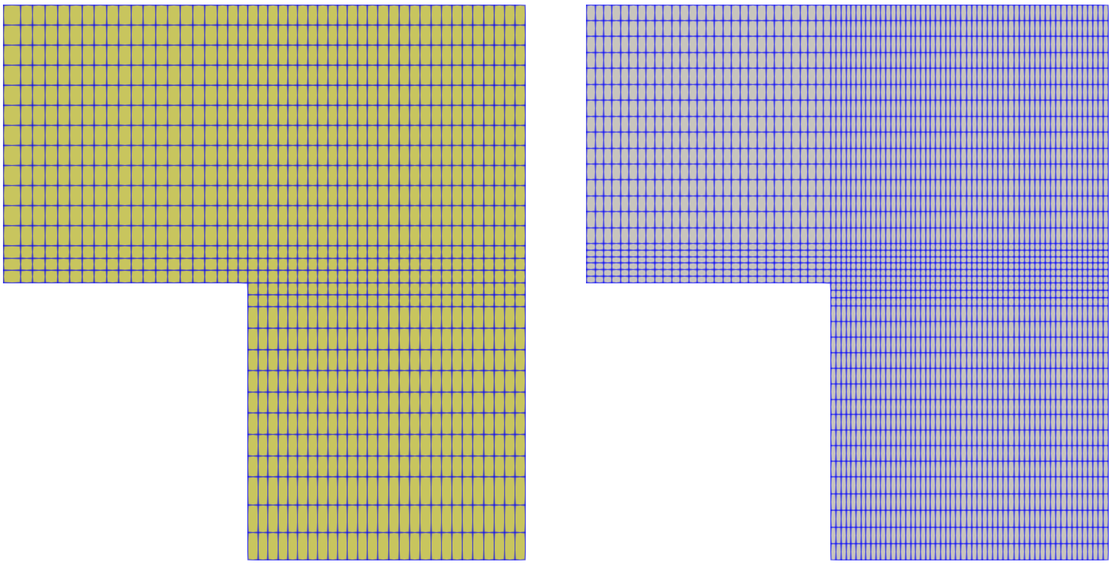

(a) Mesh 1: 1086 elements, 1164 nodes (b) Mesh 2: 2853 elements, 2981 nodes

Figure 5.6: Mesh settings for the simulation of the L-panel test by Winkler et al. (2001).

5.1.4.3 Analysis of numerical predictions

The load-displacement prediction for the reaction and deformation prescribed in the loading point of the hanging leg is presented in Figure 5.7.

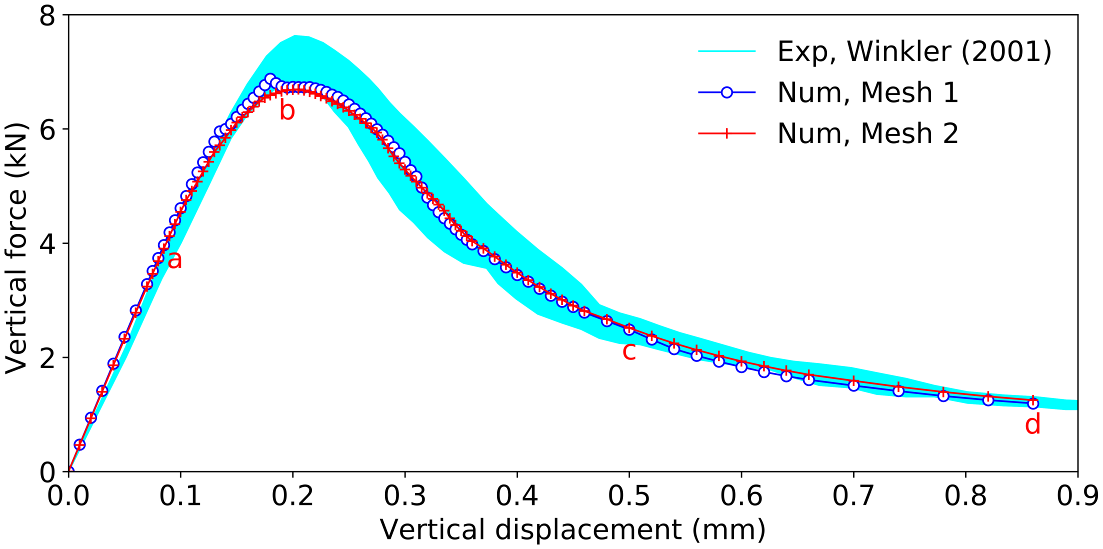

Figure 5.7: Load-displacement response of L-panel test: experimental data by Winkler et al. (2001) is presented on background. Key stages are marked as points a-b-c-d with associated snapshots of fracture evolution presented in Figure 5.8.

Remarkably, the parameter set in Table 5.2 upon calibration captures very well the load-displacement response. Nonetheless, note that small force jumps have been observed in the load-displacement space for Mesh 1, more noticeably at the transition from pre- to post-peak regime, given the mesh was not sufficiently dense to detect macrocracking adequately. It is highlighted that after macrocracking has advanced considerably into a peak response in Mesh 1, the converging path returns to the true equilibrium path occurring when macrocrack detection is adequate as for Mesh 2. Such a return to the actual response is believed to be possible due to a redistribution of stresses following converged steps, that satisfies a least energetic solution. In this regard, the load-displacement response is smoothed at the pre-to-post peak transition by reducing the element size in the micro and macrocracking-dominated zone, as it is the case for the mesh 2 analysis.

Note that a few stages have been marked in the load-displacement curve (**a-d**) for illustration of fracture pattern evolution, from incipient macroscopic fracture combined with surrounding microcracking to the experimental failure as shown in Figure 5.8.

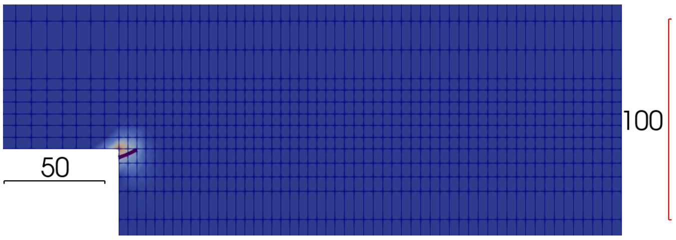

(a) Mesh 2: step 12, $u_y = 0.095$ mm.

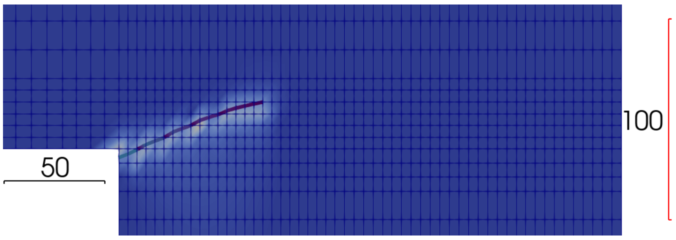

(b) Mesh 2: step 32, $u_y = 0.195$ mm.

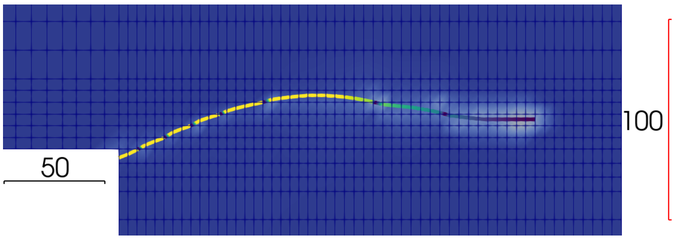

(c) Mesh 2: step 77, $u_y = 0.500$ mm.

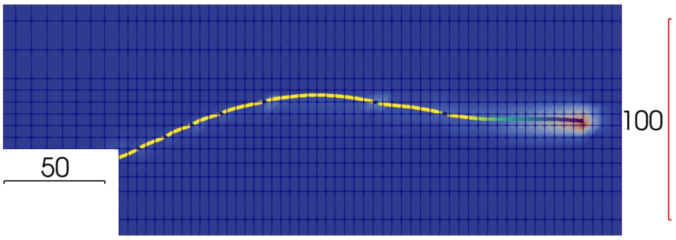

(d) Mesh 2: step 90, $u_y = 0.860$ mm.

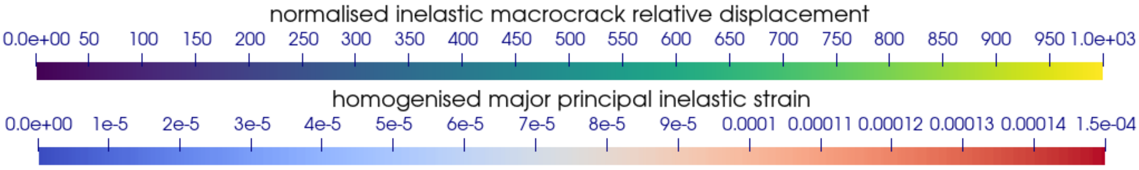

Figure 5.8: Evolution of contour plots in L-panel test: homogenised major principal inelastic strain (continuum level), and normalised measure of the inelastic macrocrack relative displacement (discrete crack level). Reference scales(x-y): 50 mm-100 mm

The point of experimental failure was captured closely by the ultimate numerical stage in the load-displacement curve, which was achieved after a large post-peak deformation being prescribed in stage **d** as shown in Figure 5.8d.

In the snapshots in Figure 5.8, contour plots are shown for the homogenised inelastic strain (major principal component) and a normalised inelastic macrocrack relative displacement. The normalisation for the inelastic macrocrack relative displacement is adopted as defined previously in Equation 4.32.

Note that additional information on microcracking across the Fracture Process Zone (FPZ) is visualised over a narrowly defined zone surrounding the advancing macrocrack, as observed from the snapshots in Figure 5.8. Such additional information is not readily available in standard EFEM formulations were the bulk domain is elastic.

In addition, a comparison of multiscale fracture zones at the final stage **d** for the meshes used are presented in Figure 5.9.

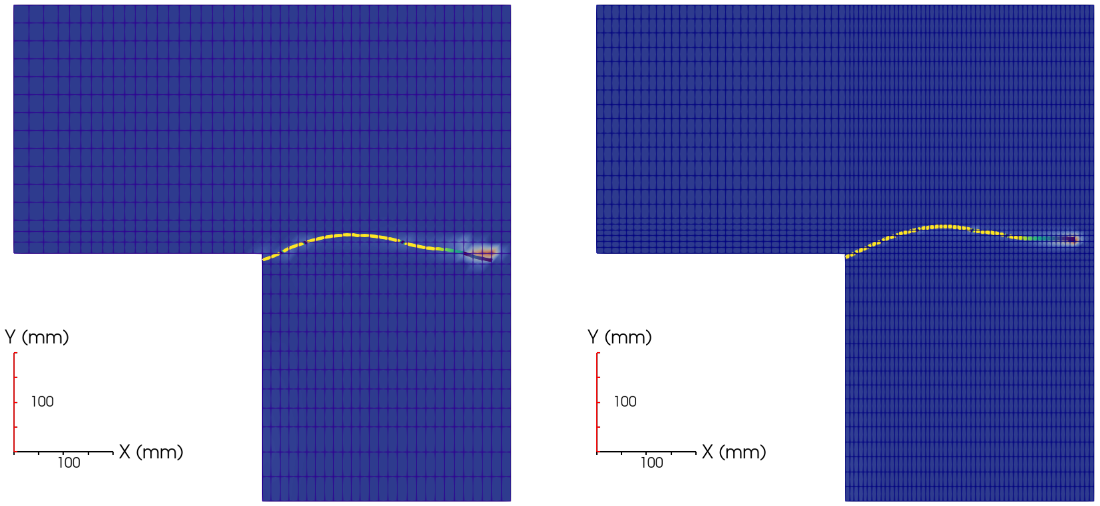

(a) Mesh 1: 1086 elements, 1164 nodes

(b) Mesh 2: 2853 elements, 2981 nodes

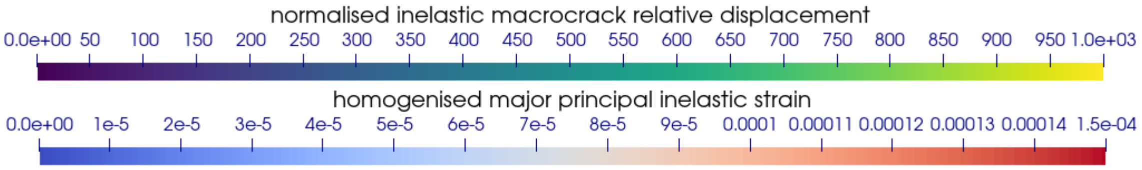

Figure 5.9: Contour plots in L-panel test at final step: homogenised major principal inelastic strain (micromechanical Continuum level), and normalised measure of the inelastic macrocrack relative displacement (discrete macrocrack level).

Note that some differences are observed in the micro and macrocacking fields at the ultimate simulation stage, and this can be attributed to a need of further mesh refinement around the Fracture Process Zone (FPZ) in the case of Mesh 1, as opposed to Mesh 2 which seems adequate to capture a closer fracture pattern as observed experimentally. In this regard, a comparison of predicted macrocracking patterns at the final stage **d** with the experimental crack is shown in Figure 5.10. These are sufficiently close to validate this aspect of the model.

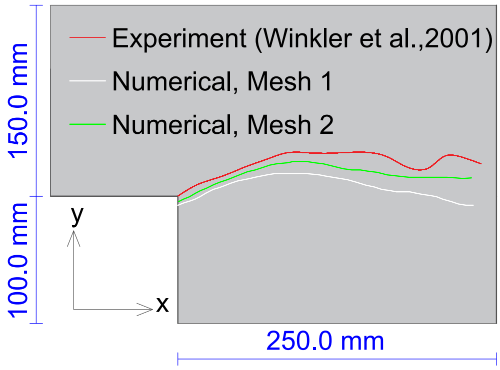

Figure 5.10: Comparison of numerically predicted macrocrack patterns in L-panel test, at final step, against representative experimental pattern by Winkler et al. (2001).

Remark 5.5.: The new multiscale EFEM framework has successfully passed a stringent test for objectivity with respect to mesh grading at the post-peak regime upon macrocracking in the L-panel test by Winkler et al. (2001), where macrocrack propagation follows a curved trajectory. In addition, this new proposed multiscale method provides an objective pre- and pre-to-post-peak transition response, when the FPZ is discretised adequately.

5.1.4.4 Analysis of incremental step size and macrocrack tracking

The sizes of the incremental steps have been chosen to avoid more than two elements being macrocracked over an incremental stage. This type of step size was found sufficient to obtain an adequate fracture pattern, although in this numerical example principal stress and strain directions in the micromechanical Continuum tend to rotate considerably in the first global iterations for each incremental step. This observation becomes more problematic as incremental steps get closer to the ultimate stage.

Note that heavily rotating macrocracks induce deletion and re-nucleation steps, which slow down the theoretical quadratic convergence rate in a global iterative procedure of Newton's type. An alternative to that practical rule of limiting the number of macrocracked elements, lies in providing a larger threshold for the number of iterations **itfix** where deletion, re-nucleation and rotation of newly nucleated macrocracks is allowed.

Remark 5.6.: In order to track macrocrack growth adequately through the mesh in numerical examples with heavily rotating macrocracks within each incremental stage, macrocrack nucleation at the element level is more conveniently detected based on an average for the major principal homogenised stress, computed from the two closest quadrature points to the advancing macrocrack tip.

5.1.4.5 Analysis of convergence of residuals and global iteration number

The history of global iteration number per incremental step is shown in Figure 5.11a, for the two meshes, in order to study robustness and convergence characteristics in this example. It is highlighted embedded macrocracks were nucleated across the computing domain until the ultimate stage, and this makes this problem more challenging to achieve the theoretical quadratic convergence of Newton's type of iterative method.

The post-peak regime at the structural level (step no. ≥ 32) remains numerically stable, with global iteration numbers mostly below from that of a critical step, e.g. the incremental step 24 for the mesh 2 which reached 20 global iterations.

Note that a stringent tolerance tol = 10^{-4} has been set for the normalised residual force norm ψ_F^{iiter}, evaluated at the end of the current iterative update **iiter** within the current incremental step **iincr** as in Algorithm 1. The expression for the force residual is shown in Equation 5.1.

$$\left.\begin{array}{lcl} \psi_F^{\mathrm{iiter}} & = & ||\boldsymbol{\phi}_F^{\mathrm{iiter}}||/||\mathbf{F}_{\mathrm{ext}}^{\mathrm{r,max}}|| \\ \boldsymbol{\phi}_F^{\mathrm{iiter}} & = & \mathbf{F}_{\mathrm{ext}}^{\mathrm{r,iincr}} - \mathbf{F}_{\mathrm{int}}^{\mathrm{iiter}} \\ ||\mathbf{F}_{\mathrm{ext}}^{\mathrm{r,max}}|| & = & \max\{||\mathbf{F}_{\mathrm{ext}}^{\mathrm{r,1}}||, ||\mathbf{F}_{\mathrm{ext}}^{\mathrm{r,2}}|| \ldots ||\mathbf{F}_{\mathrm{ext}}^{\mathrm{r,iincr}}||\} \end{array}\right\} \tag{5.1}$$

where $\mathbf{F}_{\mathrm{ext}}^{\mathrm{r,iincr}}$ includes iterative reactions due to nodal prescribed displacements.

In addition, for illustration of convergence evolution over a global incremental step, the history for the normalised residual force norm has been reported for the incremental step 24 in Figure 5.11b.

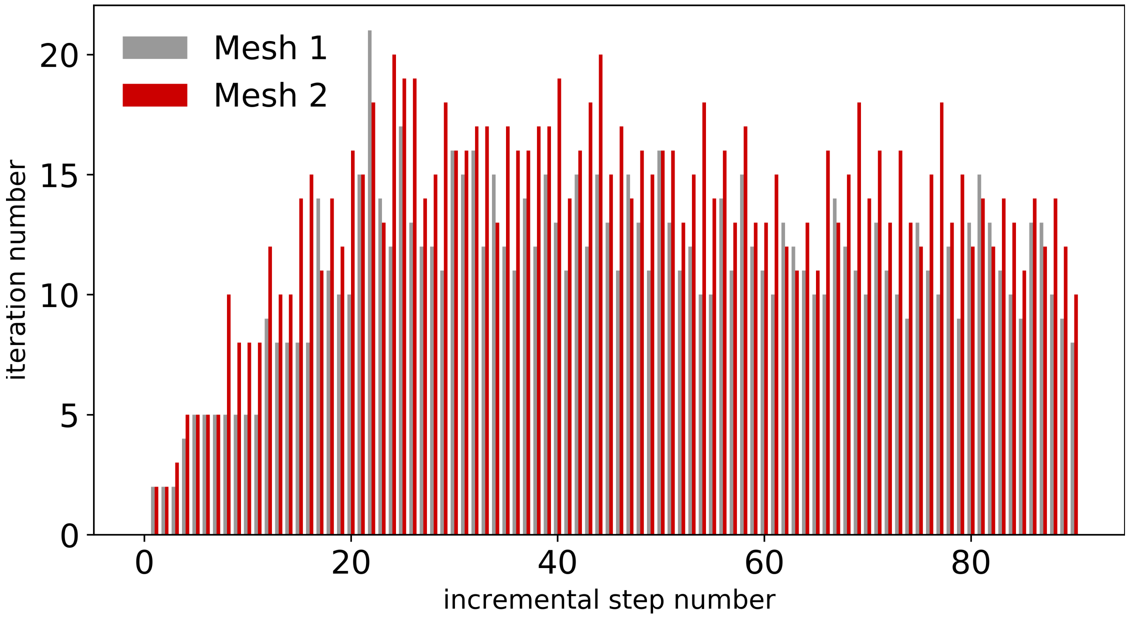

(a) Global iteration number per incremental step: Mesh 1 and Mesh 2

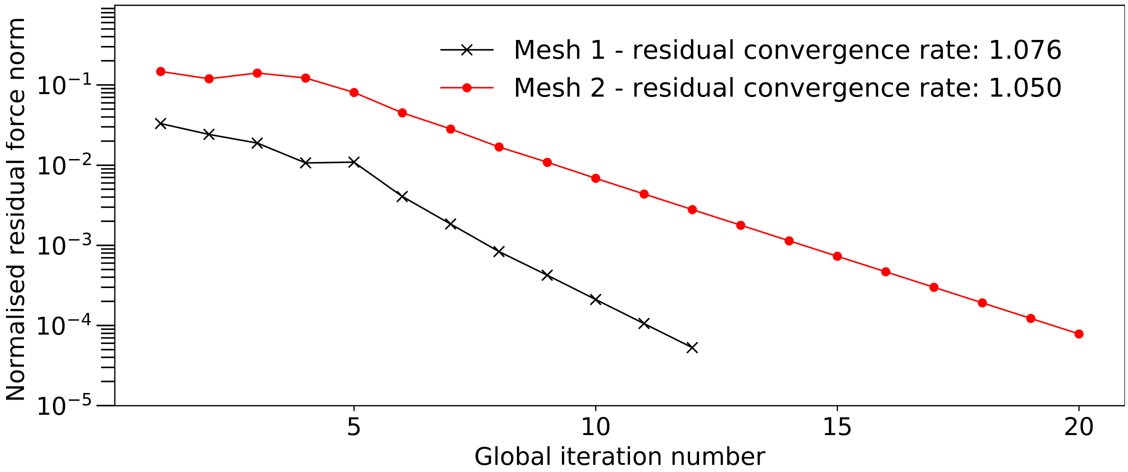

(b) Residual force norm vs global iteration in step 24: Mesh 1 and Mesh 2

Figure 5.11: Study of convergence features in L-panel test: (a) global iteration number per incremental step, (b) evolution of residual force norm $||\mathbf{F}_{\text{ext}}^{\text{r,iincr}} - \mathbf{F}_{\text{int}}^{\text{iiter}}||/||\mathbf{F}_{\text{ext}}^{\text{r,max}}||$ for incremental step 24.

The convergence rate[1] at which the residuals decrease is at least linear but less than quadratic as observed from studying the most difficult step in convergence for both meshes as shown in Figure 5.11b. The unavailability of quadratic convergence of the modified Newton's iterative scheme is expected due to the deletion and re-

---

[1] The convergence rate $n_{r,F}$ for force residual comes from $\psi_F^{\text{iiter}} = k \cdot \{\psi_F^{\text{iiter}-1}\}^{n_{r,F}}$ where the residual ψ_F^{iiter} is computed as in Eq. 5.1

nucleation steps as the macrocrack propagates and rotates within a single global incremental iterative procedure. Note that in simpler cases as it is the situation of the uniaxial deformation simulation in Section 5.1.3.1, a quadratic convergence rate has been generally obtained after the only-ocurring macrocrack is nucleated, opposed to what was observed for the L-panel where macrocrack nucleation steps occur till the very last stage of the simulation.

Note that although the last iterations tend to provide convergence rate better than linear, the very first steps for both meshes tend to be slower for convergence. This can be explained by the fact that the first **itfix** global iterations cracks are deleted and allowed to rotate, as well as due to numerical difficulties during the enforcement of fixed displacements in the iterative procedure.

It has been observed that $\approx 77\%$ of the incremental steps required more global iterations for the denser mesh as in is the case of Mesh 2 in Figure 5.11a, possibly due to the larger number of elements being macrocracked, for which only a numerical approximation of the element-level consistent tangent is computed employing central differences for gradients in the developed chain rule. A better degree of approximation, and therefore improved convergence, is expected if the number of significant figures were increased for computing central difference based gradients, as opposed to the double precision format used currently.

5.1.4.6 A brief comparison of the new multiscale fracture method with other approaches

Various other methodologies have been used in the aim to replicate different aspects of the L-panel test on plain concrete, among these are smeared plasticity models (Winkler et al., 2001), and new phase-field approaches to model fracture in (quasi) brittle materials, which can be categorised as variational (Miehe et al., 2010b,c) or non-variational (Ambati et al., 2015). These phase-field approaches have gained popularity within the Computational Mechanics community. It is now common knowledge of the research community that these phase-field schemes for fracture propagation often require very fine meshes for an adequate performance, which is detrimental to the computational cost of the methodology.

In order to illustrate the computational consumption of the new variational multiscale method for fracture propagation against other approaches, a brief comparison is presented in Table 5.3, considering the meshes used for simulation of the L-panel test as found in the literature.

Table 5.3: Comparison of mesh requirements to simulate plain concrete L-panel test.

Method	Variational	Element type	Elements	Reference
Anisotropic phase-field	Yes	4-noded quadrilateral	9650	Miehe et al. (2010b)
Hybrid phase-field	No	4-noded quadrilateral	9650	Ambati et al. (2015)
Smeared plasticity	No	3-noded triangular	9600	Winkler et al. (2001)
micro-macro EFEM	Yes	4-noded quadrilateral	2853	Azua-Gonzalez et al. (2020, 2021)

Note that from the comparison of various methodologies it was found that the variational micromechanics-enriched EFEM method is able to simulate adequately the L-panel test with considerably less number of elements when compared to a popular variational phase-field model (Miehe et al., 2010b) (in the order of 30% the number of elements needed for the phase field model). This is highlighted in the global concluding remarks in Section 6.1 in the following Chapter.

5.1.5 Uniaxial tensile test on bone-shaped concrete member by Petersson (1981)

5.1.5.1 Problem description

Petersson (1981) tested a concrete specimen of dog-bone shape under uniaxial deformation under. The specimen's bottom face is fully fixed and the top face is subjected to the action of progressive deformation. Particularly, the failed specimen was reported to present a wide presence of diffuse microcracking at the moment of failure. Macroscopic failure is predominantly triggered by direct macrocrack opening, although curved macrocracks were reported which branched and encountered in an intricate pattern. This type of asymmetric failure was expected due to the difficulties of providing a homogeneous mixture considering the small size of the specimen. The specimen geometry is shown in Figure 5.12a. Boundary conditions are described in a simplified form for numerical simulation, as well as a representative recorded failure pattern for comparison with numerical predictions (Petersson, 1981) as in Figure 5.12b.

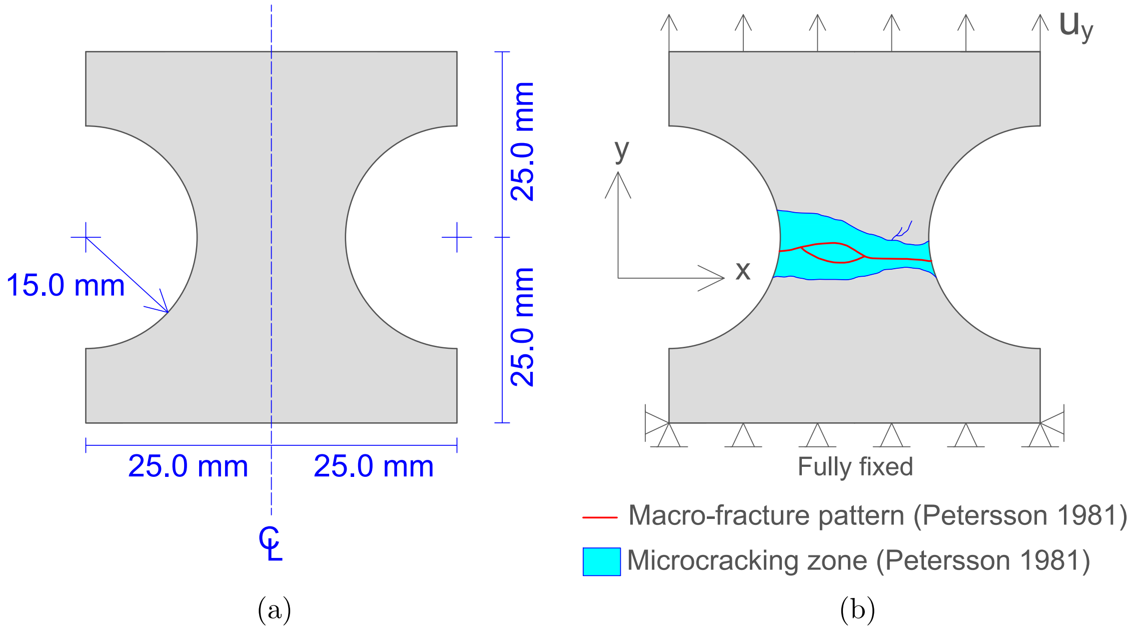

(a) (b)

Figure 5.12: Sketch of bone-shaped specimen, test by Petersson (1981): (a) geometric features (thickness = 30.0 *mm*), (b) boundary conditions, and representative experimental macro-fracture pattern and microcracking-dominated failure zone.

5.1.5.2 Numerical simulation

In this numerical example the bone-shaped cementitious composite specimen is discretised by a regular mesh. The employed Finite Element mesh, which has been obtained after a mesh convergence study, is shown in Figure 5.13. Note that the neck of the bone-shaped specimen has progressively smaller elements in the neck to allow better prediction of fracture patterns. The representative mesh used for this simulation is composed by 952 elements and 1042 nodes.

The specimen's bottom face is fully fixed and the top face is subjected to prescribed incremental displacements. The resultant displacement vector $\mathbf{u}_y = [0, u_y]^{\mathrm{T}}$ is applied at the nodes within the top face progressively through 40 incremental steps. Such selection of top surface boundary condition, with restricted lateral move of the top face, was chosen for the sake of representing adequately experimental setup conditions, where some friction-associated lateral restriction is deduced by the experimental constraints associated with the size of the experiment. In all incremental stages, body forces due to self-weight are neglected.

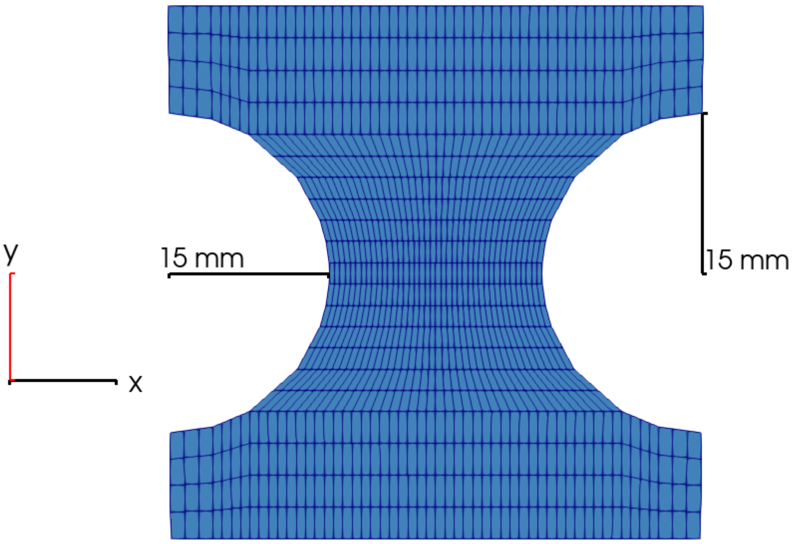

Figure 5.13: Mesh used for the analysis of the tensile test on bone-shaped concrete specimen (Petersson, 1981): 952 elements, 1042 nodes.

5.1.5.3 Analysis of numerical predictions

The prediction of the load-displacement curve is shown in Figure 5.14. In this figure, a representative experimental curve was used as a guidance to calibrate parameter set in Table 5.2.

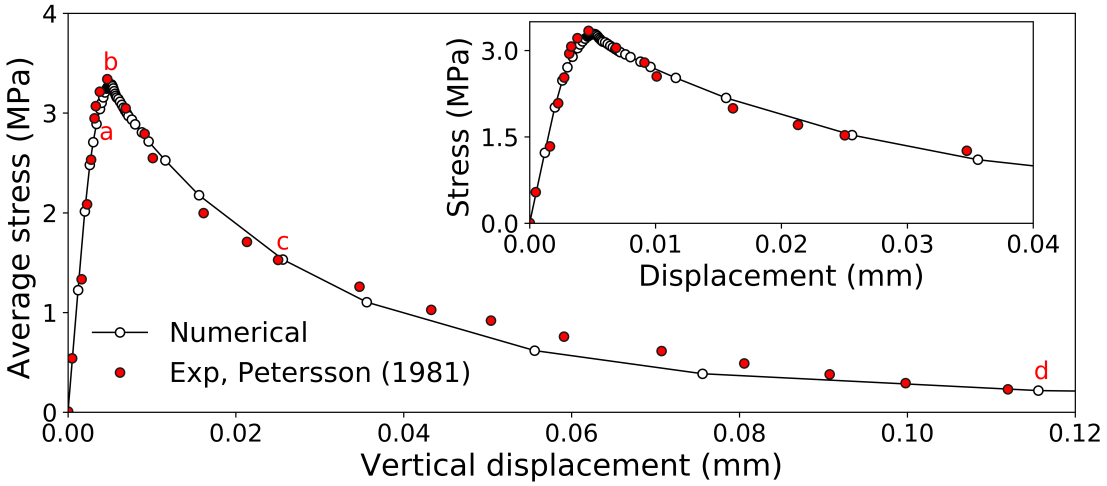

Figure 5.14: Stress-displacement response for uniaxial tensile test on bone-shaped concrete : average vertical stress is considered at bone neck. Key stages are marked as a-b-c-d with associated snapshots of fracture evolution presented in Figure 5.15.

Note that the calibrated model reproduced very well the non-linearities observed in the pre-peak response, and all along the post-peak response during fracture until a large post-peak deformation in stage **d**. A small magnifying window is presented in Figure 5.14 to exaggerate the non-linearities in the pre-peak and early post-peak regime to confirm the previous statement.

The evolution of diffuse-micro and localised-macro cracking is shown in Figure 5.15. Upon analysis using the newly proposed multiscale method, the numerically predicted distribution of diffuse microcracking through associated strains is noticeable in the surroundings of the narrowing area of the dog-bone neck, as depicted for stages a - b in Figure 5.15.

In these snapshots, a well defined microcracking zone within the Micromechanical continua is observed to be advancing ahead of macrocracks being nucleated, departing from the external curved faces within the neck of the bone-shaped specimen. Multiple macrocracks, including a few following a curved trajectory, get nucleated until the peak state occurring at stage **b**. At this peak-strength stage, macrocracks advancing from both sides of the neck get connected and form continuous paths of macrocracks. The connection of macrocracks in an element was enabled by the adapted macrocrack continuity algorithm implemented within this method (Alfaiate et al., 2003, 2002; Freeman et al., 2020).

In addition, the interaction of micro and macrocracking in this example is complex although the overall boundary conditions are simple. In this regard, along the overall softening of the specimen, some macrocracks which never get to localise fully tend to shut while the micromechanical continuum gets relaxed (homogenised inelastic strains tend to decrease), whereas localisation takes place in the macrocrak along the horizontal axis of symmetry with straight trajectory. This observation continues progressively until the main macrocrack has fully localised, i.e. large deformation accumulates within this main macrocrack while the reaction force applied onto the specimen keeps decreasing.

Remark 5.7.: It is emphasised that when Micromechanics-derived inelastic strains drop within the micromechanical continuum, the maximum experienced material deterioration remains, i.e. microcracks do not disappear as dictated by the loading/unloading conditions for microcrack growth set by Equation 3.19. This is possible since microcracking variables memorise the cracking density at degradation directions at microscale in a damage-informed relationship.

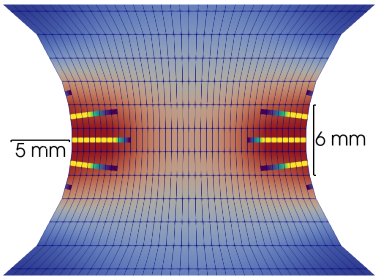

(a) Step 10, $u_y = 0.0046\ mm$

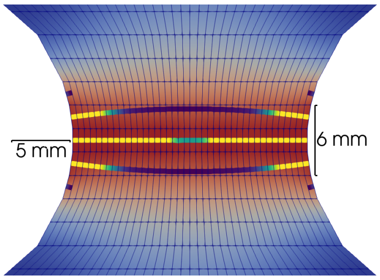

(b) Step 15, $u_y = 0.0051\ mm$

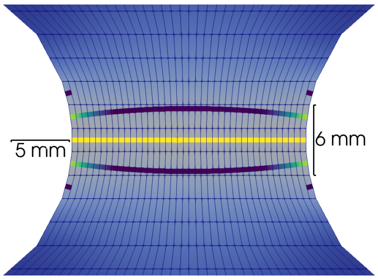

(c) Step 36, $u_y = 0.0256\ mm$

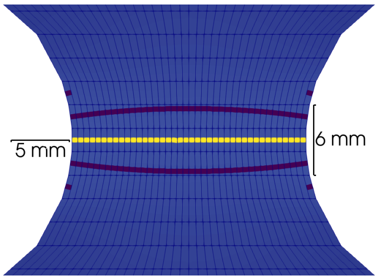

(d) Step 40, $u_y = 0.1160\ mm$

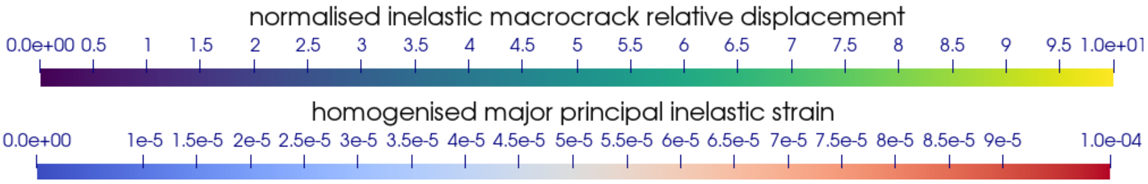

Figure 5.15: Evolution of contour plots in bone-shaped concrete test: homogenised major principal inelastic strain and inelastic macrocrack relative displacement.

For illustration purposes of microcracking irreversibility, microcracking scalar variables related to the major principal direction have been extrapolated onto nodal locations to form a Micromechanical field as shown in Figure 5.16.

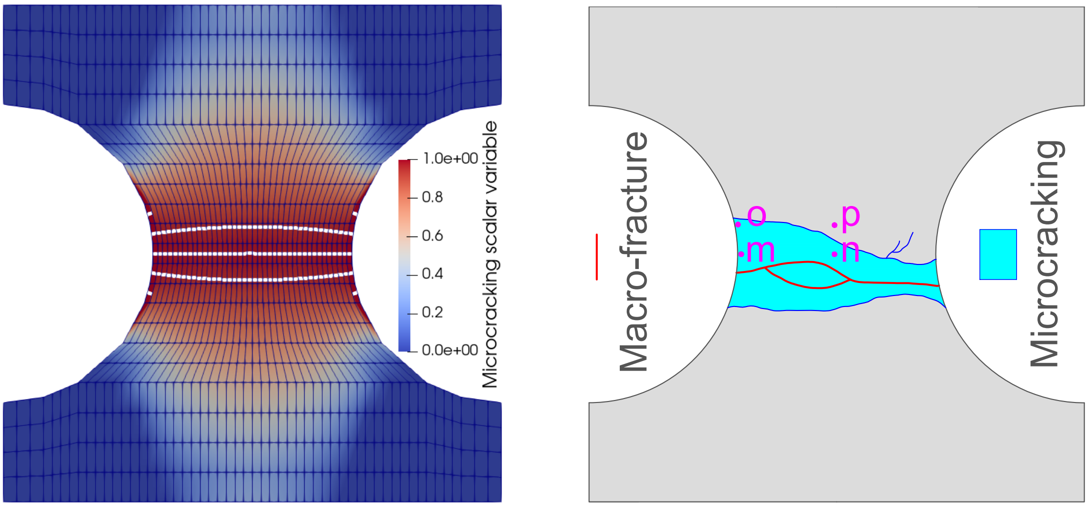

Figure 5.16: Failure patterns: microcracking scalar variable at major principal direction is extrapolated to nodal positions with macrocracks in solid white (left), and experimental patterns (Petersson, 1981) with approximate locations for sample Gauss Points in bulk (right). Notice o-p points are 3 mm away vertically from m-n.

To this point, the numerical prediction in Figure 5.16 shows a widely distributed microcracking zone, although larger than that identified experimentally (Petersson, 1981). In addition, it is stated that the symmetric distribution of microcracking is attributed to the homogeneous setting of model parameters, whereas in the experimental setup by Petersson (1981) the asymmetric failure can be attributed among other aspects to the heterogeneity of the specimen mixture around the neck of the bone-shaped specimen.

Additionally, to gain insights on directional material degradation, sample Gauss Points **m**, **n**, **o** and **p** have been located next to the specimen's outer surface and along the vertical symmetry axis, as observed in Figure 5.16 (right). The line formed by the segment o - p is located at 3 mm above the horizontal symmetry line. Stages a-b-c-d, as marked in Figure 5.14, are used to showcase directional scalar variable arrays $\omega_{\alpha}^{\mathrm{m}}(\alpha = 1 \dots \mathrm{n}_{int}^{\mathrm{m}})$ for each stage in Figure 5.17.

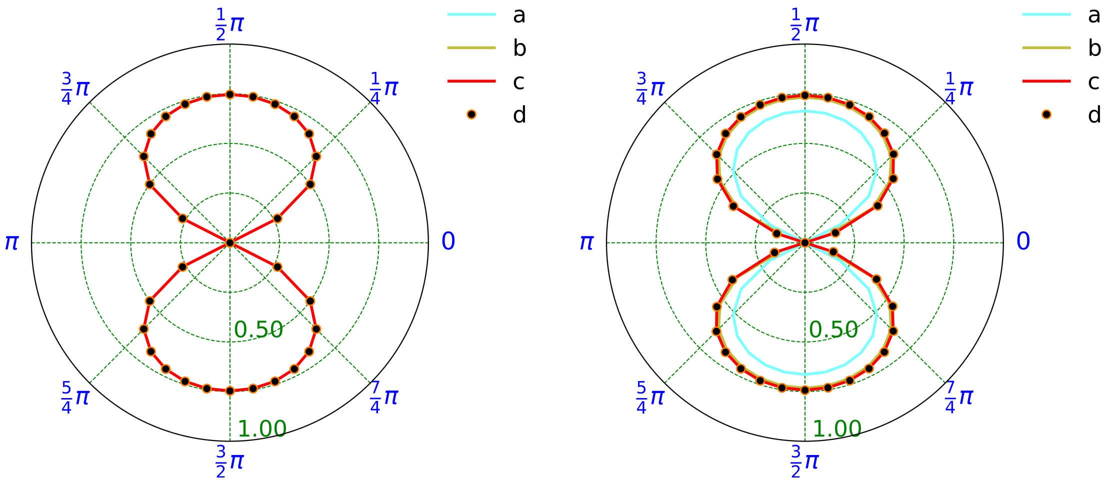

(a) Microcracking $\omega^{\mathrm{m}}_{\alpha}$: point m

(b) Microcracking $\omega^{\mathrm{m}}_{\alpha}$: point n

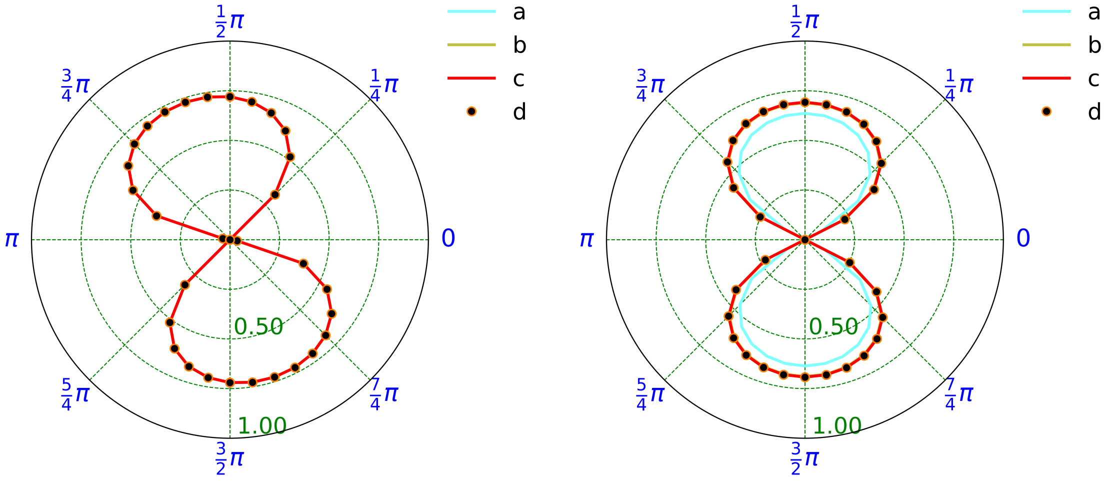

(c) Microcracking $\omega^{\mathrm{m}}_{\alpha}$: point o

(d) Microcracking $\omega^{\mathrm{m}}_{\alpha}$: point p

Figure 5.17: Polar plots for directional microcracking evolution $\omega^{\mathrm{m}}_{\alpha}$ ($\alpha = 1 \ldots \mathrm{n}^{\mathrm{m}}_{int}$) within the bone-shaped specimen test by Petersson (1981). Various sample Gauss Points in the micromechanical continua are selected, as shown in Figure 5.16, at stages a, b, c and d marked in the stress-displacement curve in Figure 5.14.

It is observed that points **m** and **o** have undergone already large microcracking at step 10 (stage a), whereas microcracking keeps progressing after this stage in points n and p. Note that the distribution of microcracking scalar variables for point **o** is symmetric towards a rotated horizontal axis and hence a macrocrack nucleates in the surroundings with an inclined propagation direction. Such propagation direction is consistently orthogonal to the major principal direction of the homogenised strain in the Micromechanical continua. Therefore, the homogenised variables are demonstrated to reveal the connection between the micromechanical degradation and macroscopic fractures, which is consistent with experimental observations in terms of slightly curved fracture trajectories. It is clarified that no effects due to randomness of fracture resistance of the material has been taken into account, and such effects could help to improve our current understanding of micromechanics-based detection and tracking algorithms for macrocracks.

5.1.5.4 Analysis of step size and macrocrack tracking

In this example, the step size was set to adequately capture non-linearities in the stress-displacement curve in Figure 5.14, specially within the pre-peak state and the very first post peak structural response. Additionally, it is reported that tracking of macrocrack detection at the central Gauss Point was sufficient to capture the complex micro- and macrocracking interaction while slightly curved macrocrack paths were also present. The number of elements that are permitted to develop a macrocrack within an incremental step does not dictate the step size as opposed to previous numerical example for the L-panel, since principal directions for the homogenised stress and strain in the Micromechanical continua are well settled within the first iterations along the relatively simple macroscopic splitting conditions imposed. It is remarked that macrocrack propagation detection and propagation direction are underpinned by such principal stresses and strains, and therefore a good approximation during the non-linear iterative procedure is pivotal.

The incremental step size by stage **c** in Figure 5.14 has been set to an order of magnitude higher than that for the preceding steps in the pre-peak regime and the multiscale framework is still able to converge. An explanation of this is that the computational iterative procedure becomes more manageable if the macrocrack propagation direction is fixed adequately, and therefore, the step size can be increased considerably without much consequences when nucleation of additional embedded macrocracks is no longer necessary. By the mentioned stage **c**, all macrocracks had already cut across the neck of the bone-shaped concrete member, and no more substantial nucleation occurred, which eased the step size requirements. Note that although no more nucleation occurred during this stage, macrocracks kept interacting with the surrounding micromechanical continuum.

5.1.6 Four-point bending test on plain concrete with no initial notch

5.1.6.1 Problem description: a theoretical benchmark test

This numerical example addresses a typical characterisation test in concrete, where no notch is present, as opposed to other characterisation tests for cementitious composites in the literature, where macrocracks are typically driven by an initial notch or an artificial imperfection.

It is hereby highlighted that the purpose of this theoretical simulation is to test the interaction of multiple macrocracks and considerable microcracking in a large zone (note that the whole segment between loads in the mid-span of a four point bending test is subjected to critical bending). In this regard, the use of notches was discarded. Indeed, when fracture-driving notches are present, e.g. specimens under complex tension and shear conditions by Nooru-Mohamed et al. (1993), three-point bending with driving-notch for flexural fracture analysis (Xu and Zhu, 2009), double-edge-notched beam shear test by Schlangen (1993), among others, the fracture process zone has been reported as narrow, and therefore, the interaction of micro and macrocracks is limited.

In this theoretical setting, a concrete beam of square section is subjected to point loads located at $L/3$ and $(2/3) \cdot L$, with L being the length of the main span and with supports at the extremes of the main span. The longitudinal dimension of the mid-span is $L = 400\ mm$. The arrangement is shown in Figure 5.18.

Note that analytical formulas for benchmark comparison are given in Section 5.1.6.6.

5.1.6.2 Numerical simulation

In this situation, the effects of contact at supports and loading devices have been simplified by adding thin layers of elastic material. Such elastic layers serve as stress distributors into the concrete beam, and avoid singularities which may drive unrealistic stresses and potential cracking around contact points. These artificial elastic layers are modelled as continuum elements.

Note that the parameter set was chosen by trial and error until a complex micro-macro fracture interaction was induced, while keeping parameters in a sensible range for standard concrete applications.

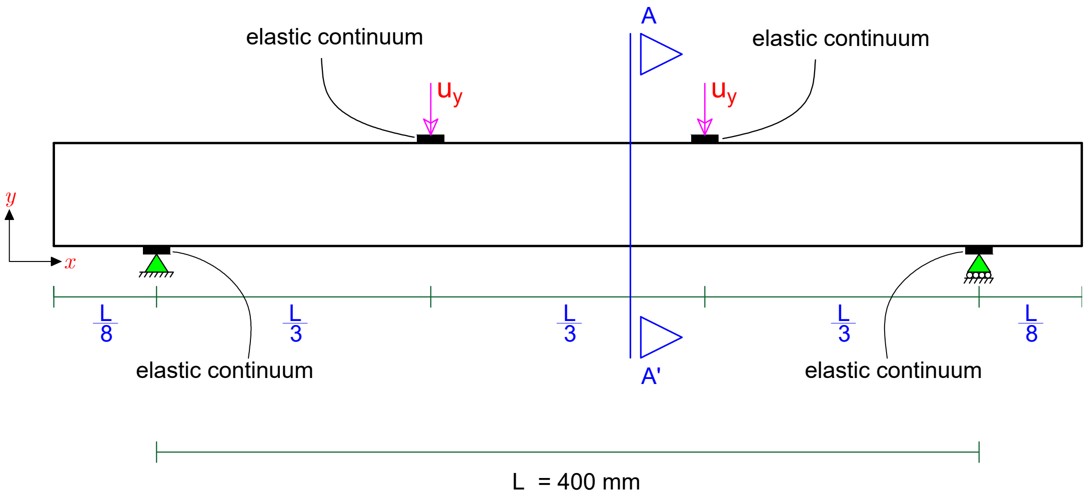

(a) Longitudinal view of the concrete beam under four-point bending.

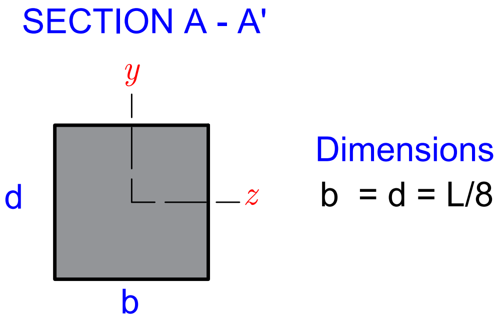

(b) Typical cross section of the concrete beam.

Figure 5.18: Four-point bending test in concrete: a) geometry and boundary conditions are detailed in a longitudinal view, and b) a typical cross section is provided. Note that the cross section is not drawn to the same scale as the longitudinal view.

Prescribed displacements and fixities are applied at the outer mid-point of those elastic layers, as observed in Figure 5.18. Note that body forces have been neglected for this small specimen.

Three mesh configurations have been used for simulations, mesh 1, 2 and 3 as observed in Figure 5.19. The step sizes have been considered to minimise the chance of deformation localisation becoming dominant at one side of the beam at least until the very last loading stages. In the very last stage one last row of elements remain in compression at the top surface of the beam upon macrocrack propagation from the bottom of the beam in tension. Results for mesh 2 are considered as mesh converged.

Figure 5.19 shows macrocracking patterns on top of the mesh at the ultimate loading stage.

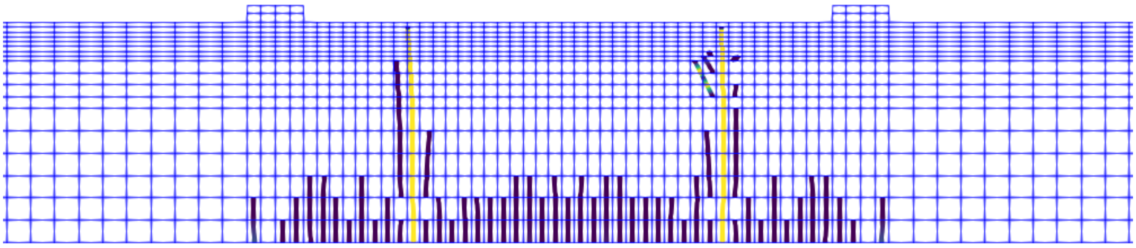

(a) Mesh 1: 2244 nodes, 2102 elements. Macrocrack pattern at final stage.

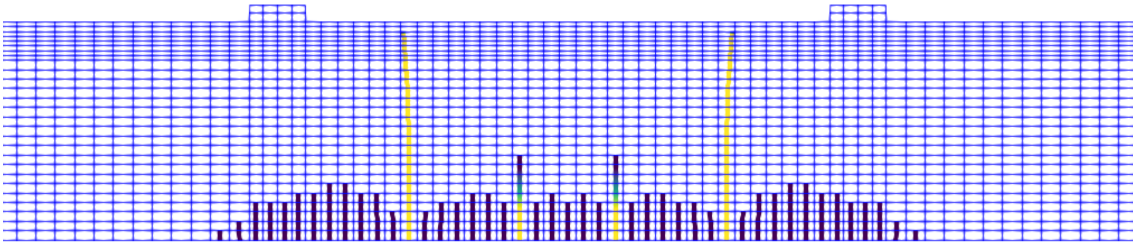

(b) Mesh 2: 3456 nodes, 3299 elements. Macrocrack pattern at final stage.

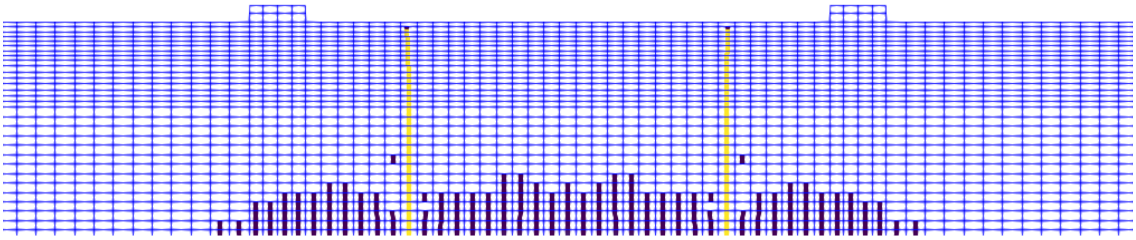

(c) Mesh 3: 3822 nodes, 3662 elements. Macrocrack pattern at final stage.

Figure 5.19: Four-point bending test in concrete with no initial notch: mesh configurations at macroscale are shown, with normalised inelastic relative displacement at macrocracks, at ultimate stage with deflection $u_y = 0.7\ mm$ at loading points.

It has been found that the smaller the element in the last row next to the top surface of the beam, the simulation converges adequately for bigger deflection at the loading points. In addition, the closer an incremental step is to failure the lesser resolution of the principal strain direction fields to track macrocrack adequately in the proximity of the top surface of the beam. Therefore, mesh refinement has been concentrated on the top surface of the beam.

5.1.6.3 Analysis of numerical predictions: load-deflection

The load-deflection prediction of the four-point bending benchmark test on concrete is shown in Figure 5.20 for the set of parameters chosen to induce complex cracking deliberately, which are shown in Table 5.2.

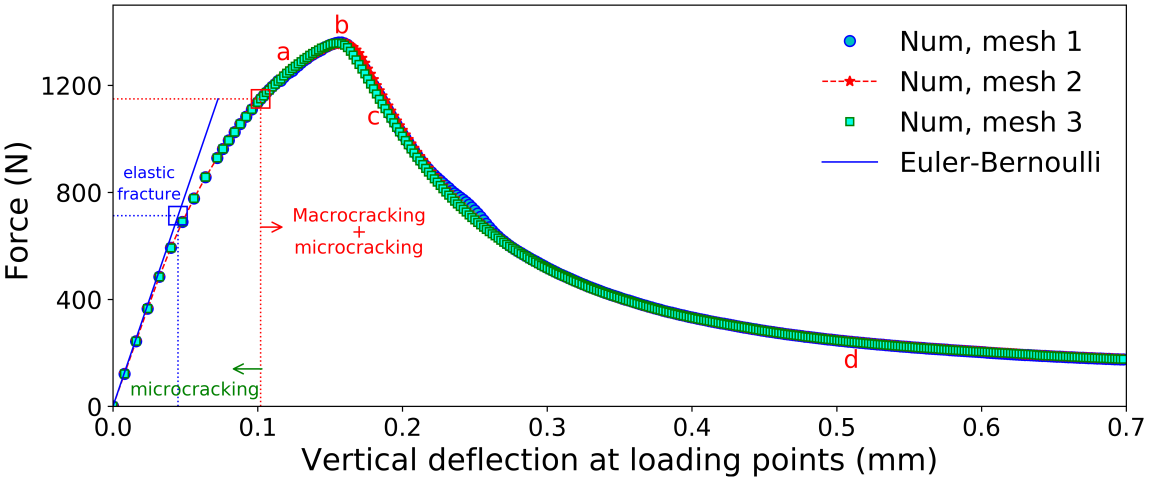

Figure 5.20: Curve of total load ($F_T = F_T^{(1)} + F_T^{(2)}$) vs deflection ($u_y$) at contact points in plates u_y, where $F_T^{(1)}$ and $F_T^{(2)}$ stand for the loads at each plate. Key stages are marked as a-b-c-d and are visualised as snapshots of evolution in Figure 5.21.

Note that the loads at each plate, $F_T^{(1)}$ and $F_T^{(2)}$, start to differ from each other at a stage of substantial macrocracking, i.e. $F_T^{(1)} \approx F_T^{(2)} \neq \frac{1}{2}F_T$ due to numerical rounding-off despite the fact that no imperfections in material properties nor geometric weakening notches have been considered. In such a situation, it has been found that deformation localisation may become dominant at one loading plate or the other. For an objective comparison of predictions corresponding to various meshes, both contributions have been accumulated to obtain the overall load $F_T = F_T^{(1)} + F_T^{(2)}$ of the beam.

The instant of theoretical macrocracking from Section 5.1.6.6 is highlighted with a blue square in Figure 5.20. However, it is highlighted that this prediction is restricted to the hypothesis that the beam is completely elastic until the extreme concrete ligament in tension reaches the maximum macroscopic tensile strength. In the hypothetical case the experiment is performed, there would be non-linear behaviour of the concrete beam and moment redistribution due to the directional microcracking which would allow deformation localisation to be dominant in certain locations.

The instant of macrocracking predicted by the model is highlighted with a red square in the load-deflection curve. The instant of fracture predicted by the multiscale EFEM model in the load-deflection curve differs from the theoretical one based on elasticity, due to the absence of micromechanical non-linearities in the analytical elastic solution as presented in Section 5.1.6.6.

It is noted that the three meshes provided an objective response in the load-deflection predictions with respect to mesh refinement, within the pre- and post-peak regime. However, a small overshooting of the SUR response, in the analysis using mesh 1, made the post-peak response move slightly away from the theoretical convex post-peak load-displacement response. This has been reported in the literature for SUR methods (Alnaas and Jefferson, 2016; Jefferson and Mihai, 2015), and a simple solution is to set a tolerance to avoid these small deviations, and re-peform additional updates of the chosen SUR branch. This type of challenge was not found for the refined meshes 1 and 2.

5.1.6.4 Analysis of fracture patterns and micromechanical evolution

Micro and macrocraking evolution is illustrated in Figure 5.21, for the stages marked previously in the load-displacement curve.

Note that there is considerable microcracking experienced at all times in stages **a-b-c-d** ahead of macrocrack growth. As deflection progresses at loading points, the homogenised microcracking-induced inelastic strains become more visible in narrower areas which surround the advancing tip of the two dominant macrocracks.

It is remarked that between stages **c** and **d** the two dominant macrocracks closer to the axis of symmetry tend to shut, whereas the two outer macrocracks become the ultimately dominant ones. Such situation is true for mesh 2, and similar variants of macrocracking patterns occur for the other meshes such as mesh 3. Nonetheless, if the mesh is too coarse the pattern of micro and macrocracking begins to evolve asymmetrically at some instant during the simulation.

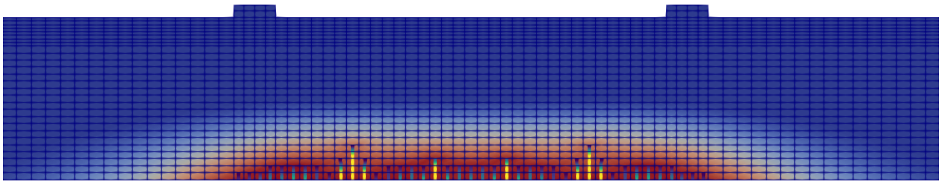

(a) Mesh 2: Step 25, $u_y = 0.118\ mm$

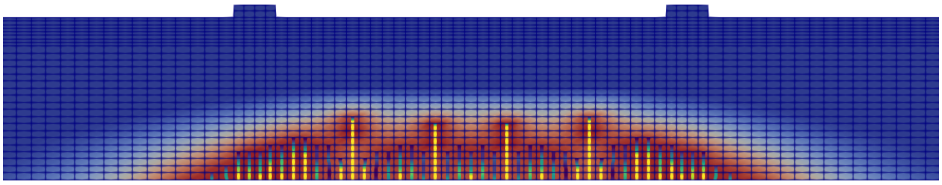

(b) Mesh 2: Step 45, $u_y = 0.158\ mm$

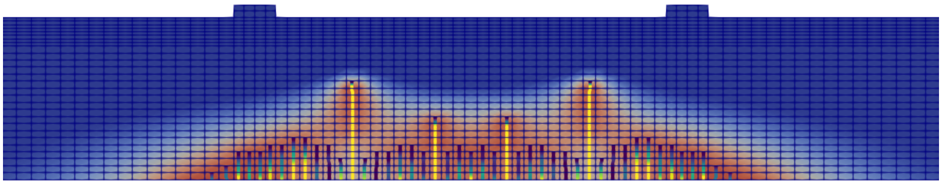

(c) Mesh 2: Step 56, $u_y = 0.180\ mm$

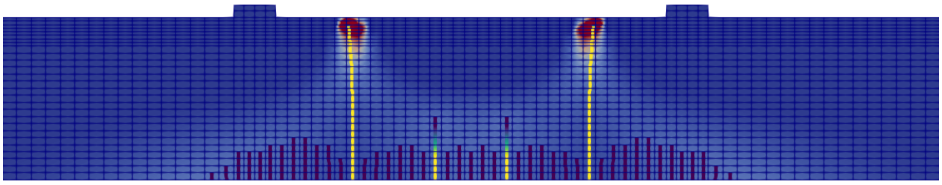

(d) Mesh 2: Step 221, $u_y = 0.510\ mm$

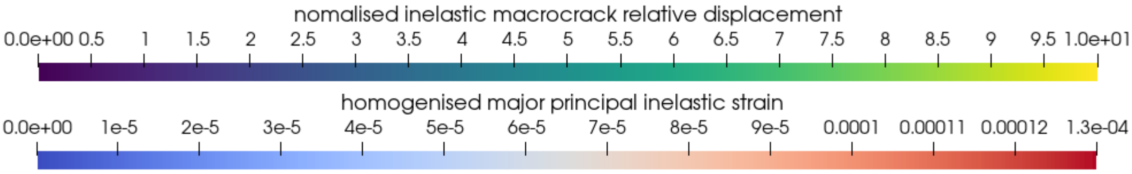

Figure 5.21: Contour plots in four-point bending test in concrete: homogenised major principal inelastic strain, and normalised inelastic macrocrack relative displacement. Evolution stages a-b-c-d are associated to the marks in the load-displacement curve in Figure 5.20.

A contour plot is shown in Figure 5.22 for the microcracking scalar variable at the ultimate incremental step, where the major principal values are extrapolated at nodal locations. The central part of the beam is magnified to illustrate better the FPZ in this region, where two dominating macrocracks cut the computing domain. All macrocracks are shown with solid white lines on top of the contour plot.

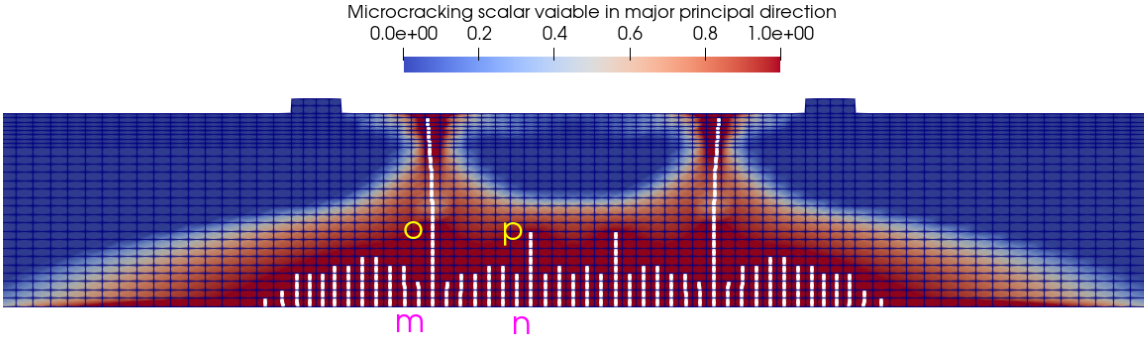

Figure 5.22: Contour plot of microcracking scalar variables corresponding to major principal direction at the Micromechanical bulk, at final loading stage for a deflection $u_y = 0.7\ mm$ at loading points. Macrocracking pattern is shown with white solid lines.

This figure elucidates the regional advancement of maximum experienced microcracking at ultimate stage **d**. In addition, the associated macrocraking pattern is also showcased in solid white lines. Points **o** and **p** are 18.5 mm above the bottom surface of the beam, and **m** and **n** are at the level of the bottom surface. Gauss Points **m** and **o** are cut by the dominant macrocrack, whereas **n** and **p** are cut by the second largest macrocrack.

In addition, the evolution of microcracking is tracked at selected Gauss points in the polar plots in Figure 5.23. The chosen Gauss Points are marked in their locations as **m**, **n**, **o** and **p** in the Figure 5.22.

Note that by stage **a**, microcracking has already experienced its maximum growth in Gauss Points **m** and **n** in Figures 5.23a and 5.23b, whereas Gauss Points **o** and **p** in Figures 5.23c and 5.23d experience continuing microcracking as macrocracks advance through the Gauss points in a direction towards the top surface in further stages **b**-**c**.

Furthermore, it has been found that by stage **d**, microcracking growth has reached its maximum values in all these selected Gauss Points, which is explained by the fact that macrocrack tips are advancing further away from this region.

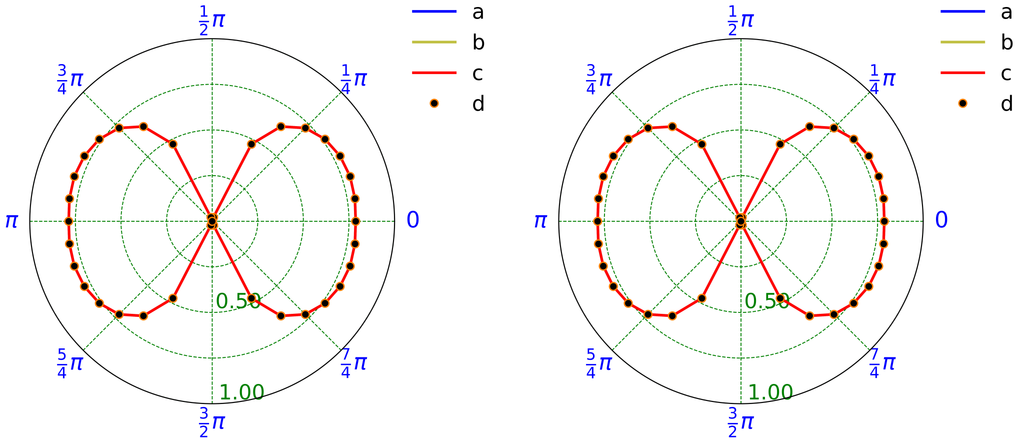

(a) Microcracking $\omega^{\mathrm{m}}_{\alpha}$: point m (b) Microcracking $\omega^{\mathrm{m}}_{\alpha}$: point n

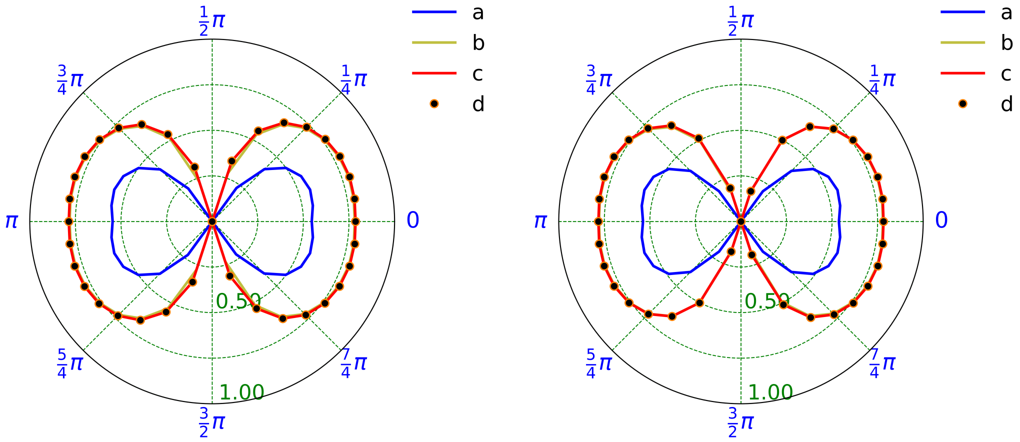

(c) Microcracking $\omega^{\mathrm{m}}_{\alpha}$: point o (d) Microcracking $\omega^{\mathrm{m}}_{\alpha}$: point p

Figure 5.23: Polar plots for directional microcracking evolution $\omega^{\mathrm{m}}_{\alpha}$ ($\alpha = 1 \ldots \mathrm{n}^{\mathrm{m}}_{int}$) within sampling Gauss Points in the Micromechanical continua, as shown in Figure 5.22, at stages a, b, c and d marked in the load-deflection curve in Figure 5.20.

5.1.6.5 Analysis of step size and macrocrack tracking

In this numerical example, the incremental step size in the post peak regime was chosen to obtain a good strain eigenvector field capable of leading the macrocrack tacking adequately. In such challenging example, at least one or more incremental steps have been allowed between the nucleation of new macrocracks specially for the last steps where macrocracks were approaching to the top surface of the beam.

In all cases, to track geometrically-continuous embedded macrocracks, macrocracking detection at central Gauss Point was found sufficient. In addition, as an artifice to allow a good tracking of continuous macrocracks the global numbering of elements was arranged so that element number increases from bottom to top surface, to make adequate use of the implemented sequential macrocrack tracking algorithms.

5.1.6.6 Elastic prediction of macrocrack occurrence

Euler-Bernoulli's theory of elasticity is used to compute the response in the elastic range. In this regard, the load $F_{ck}^{M,e}$ at the onset of macrocracking is computed by equating the macroscopic tensile strength f_t^M to the maximum tensile stress produced by loading, under the assumption that the full cross section remains behaving elastically:

$$f_t^M = -\frac{M_{ck}^{M,e} \cdot \delta y_{et}}{I_z} = \frac{M_{ck}^{M,e} \cdot \left(\frac{d}{2}\right)}{\frac{1}{12} b \cdot d^3} = \frac{F_{ck}^{M,e} \cdot L}{b \cdot d^2} \quad \rightarrow \quad F_{ck}^{M,e} = \frac{1}{512} \cdot L^2 \cdot f_t^M \tag{5.2}$$

where $M_{ck}^{M,e} = \frac{F_{ck}^{M,e} \cdot L}{6}$ is the critical flexural moment, in the mid-region between the loading points, which causes the onset of macrocracking, $\delta y_{et} = -d/2$ is the distance from the neutral axis of the beam to the extreme ligament in tension, and $b = d = L/8$ are the dimensions of the square cross section. A sketch of internal shear and moment is shown in Figure 5.24, where self-weight of the beam is neglected.

In addition, the elasticity-based relation between the instantaneous radius of curvature of the beam $1/R_{beam}(x) \approx d^2\{u_y^e(x)\}/dx^2 = M(x)/[\bar{E}_{am} \cdot I_z]$ and the ratio of the flexural moment to its rigidity $M(x)/[\bar{E}_{am} \cdot I_z]$ is used to compute the corresponding elastic deflection at $x = L/3$, at the instant of macrocracking in Equation 5.3.

$$u_y^e\left(x=\frac{L}{3}\right)=-\frac{5}{324}\cdot\frac{F_{ck}^{M,e}\cdot L^3}{\bar{E}_{am}\cdot I_z}\rightarrow\quad u_y^e\left(x=\frac{L}{3}\right)=-\frac{40}{27}\cdot\frac{f_t^M}{\bar{E}_{am}}\cdot L \tag{5.3}$$

In this regard, the elastic predictors for macrofracture, in terms of deflection and mobilised total force have been computed as $\{u_y^e(x=L/3), F_{ck}^{M,e}\}=[-0.045mm, 712.5N]$ and this pair is depicted in the load-deflection curve in Figure 5.20, for validation of the multiscale EFEM predictions.

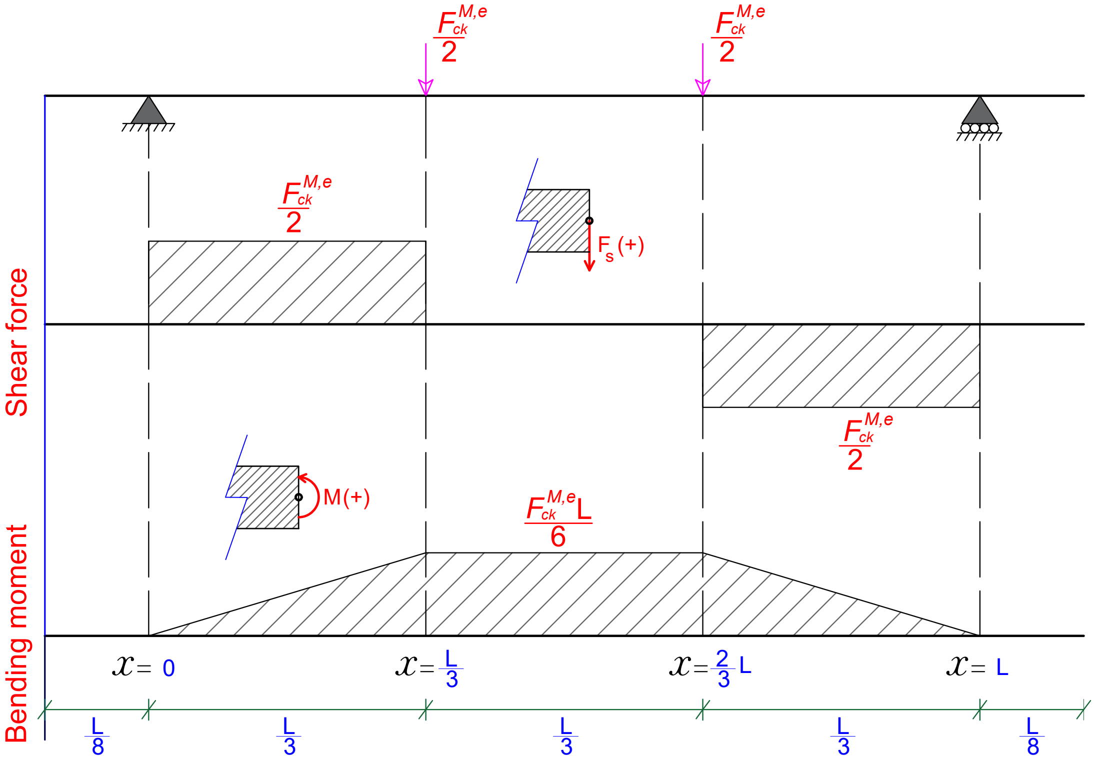

Figure 5.24: Internal shear force and bending moments along the concrete beam under four-point bending, at the instant of first macrocracking, for elastic predictions. For consistency with computational modelling, self-weight of the beam is neglected.

5.1.7 Failure test on hexagonal concrete member by Bennett and Jefferson (2007)

5.1.7.1 Problem description

Bennett and Jefferson (2007) tested hexagonal concrete specimens in two opposite sides, aside from other similar tests with variable axis of loading. It is clarified that only the monotonic uniaxial compression test on the hexagonal concrete specimens are considered in this PhD thesis.

In these tests, the relative linear displacement was monitored between two points located 10 *mm* away from the associated concrete face using LVDTs. In this regard, a diagonal LVDT was used to control the stroke during the test, whereas another LVDT gauged the verticaL relative displacement as shown in Figure 5.25a. In addition, some layers of soft material were placed between the loading plates and the specimen to allow a better distribution of loading. Particularly, some of the recorded experiments presented the tendency for a snap-back response as measured by the LVDTs and load cells.

Although reproducibility of the tests was proved in Bennett and Jefferson (2007) by presenting various load-displacement curves for each of the LVDTs, only one representative fracture pattern was recorded per type of experiment. In these pictures reported in the publication, the devices were interfering with the visibility of the fracture pattern. Therefore, the reconsturction of such pattern presented in this PhD may vary slightly with the actual fracture pattern in the experiment.

The geometry of the specimen, simplified boundary conditions for use in a numerical model and a (re-constructed) representative fracture pattern at failure stage are illustrated in Figure 5.25b.

The response of such a complicated test in terms of load-displacement curves has been reproduced by a non-linear model (Bennett and Jefferson, 2007; Jefferson, 2003a,b) that possesses components for crack-closure and aggregate interlock, which are absent in the formulations presented in this PhD. Therefore, it was expected that deviations would occur between the predicted structural response and that of monitored experiments. In this regard, the focus of simulating this complex test was on investigating if the model in the current state of development could reproduce to some extent fracture patterns.

The next section clarifies some of the assumptions used for simulation, some challenges and potential measures to overcome any limitations. Also some directions which may be subject for future research are discussed.

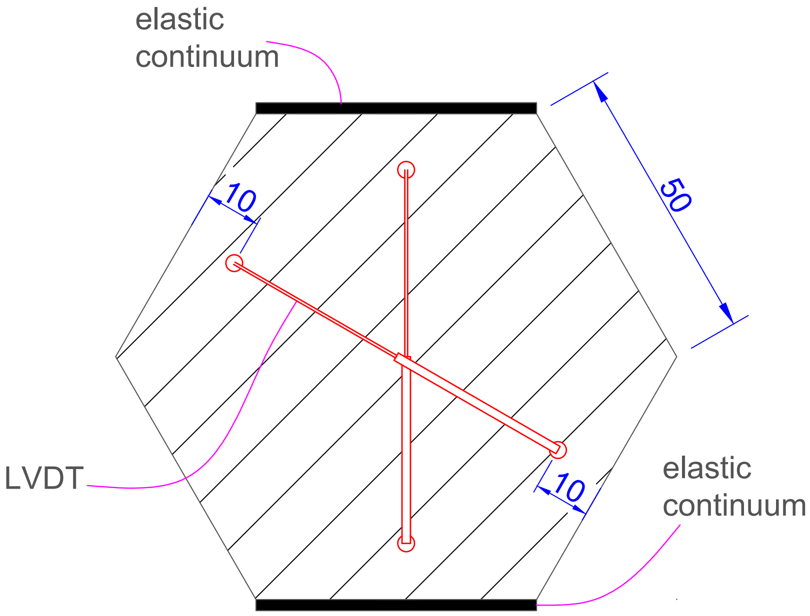

(a) Geometry of hexagonal concrete specimen, thickness = 60 *mm*

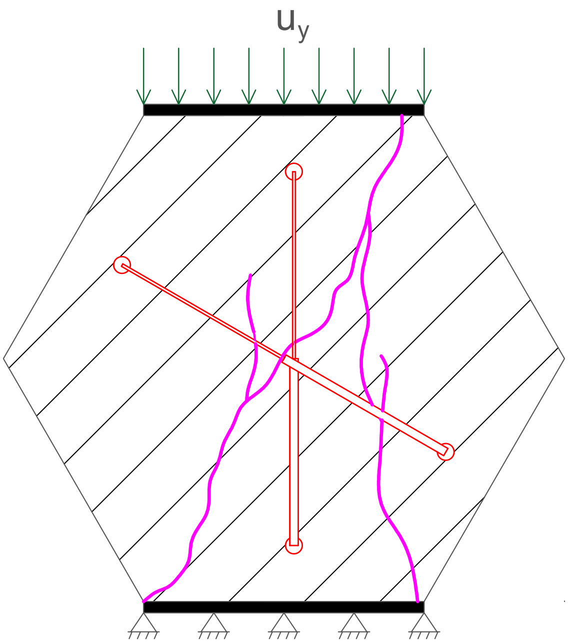

(b) Boundary conditions and representative experimental fracture pattern

Figure 5.25: Hexagonal concrete specimen under compression in two opposite sides, as tested by Bennett and Jefferson (2007): a) geometry, b) boundary conditions and representative fracture pattern. Units shown in sketch are all in *mm*.

5.1.7.2 Numerical simulation

The following prediction has used a regular mesh with 6630 nodes and 6468 elements as shown in Figure 5.26. Calibration of parameters as shown in Table 5.2 allowed to capture some the geometric features of the reconstructed experimental macrocrack pattern.

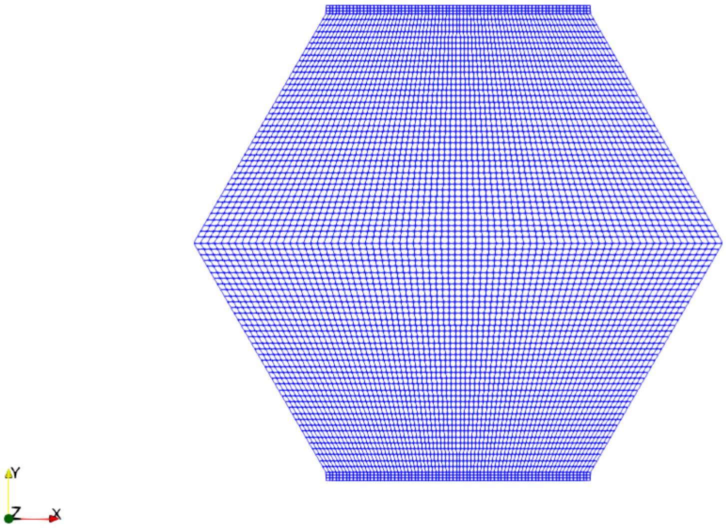

Figure 5.26: Mesh for simulating the hexagonal concrete test by Bennett and Jefferson (2007), including elastic continuum layers to simulate soft material layers from experiments. Mesh is comprised of 6630 nodes and 6468 elements.

The bottom and top faces of the specimen were restrained respectively under fully fixed and prescribed displacement in the vertical direction, while both bottom and top surfaces were restrained laterally. Although another possibility was to simulate this problem with a coupled constraint equation from the arc-length type (De Borst et al., 2012), which was under development in Section 4.4.2, this could not be included in the PhD thesis within the limits of the degree.

In contrast to other simulations in this chapter, the tolerance for force residuals was relaxed from 10^{-4} to 10^{-3} during calibration when convergence became a challenge. The simulation results in Section 5.1.7.3 were obtained from a simulation that was enabled to converge by relaxing the tolerance in the last 5 increments.

5.1.7.3 Analysis of numerical predictions

A curve of the load-displacement response is presented in Figure 5.27, where the associated fracture pattern is presented as well. Note that this simulation reached a large number of global iterations (40 iterations) at a stage for which the specimen is close to reach its peak. It is believed that challenges of arriving to a minimum energy solution is due to a large number of rotating macrocracks present. Such situation might make it very difficult for the modified Newton's scheme to converge with strict tolerances. Further discussion is presented in the following paragraphs.

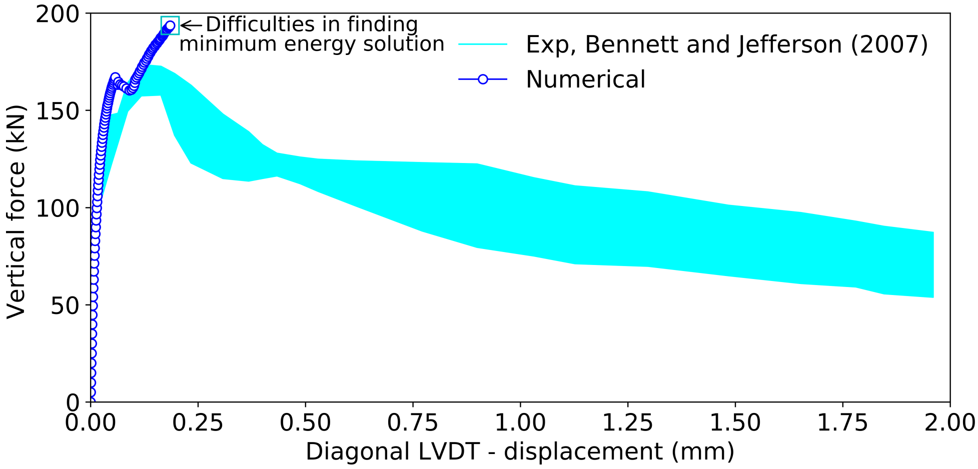

(a) Load-displacement curve for hexagonal concrete test: diagonal LVDT

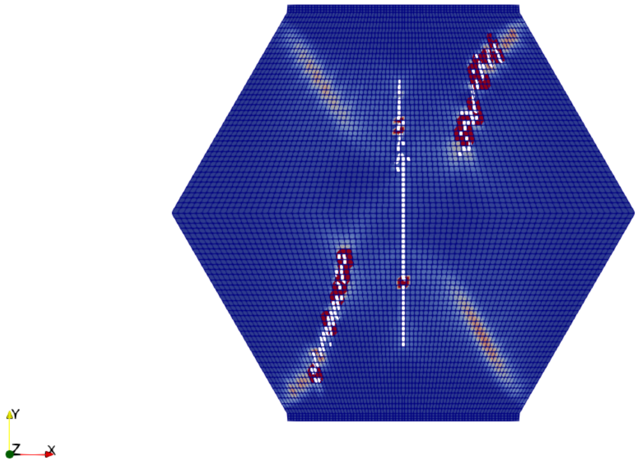

(b) Fracture pattern before difficulties arrive in finding a minimum energy solution.

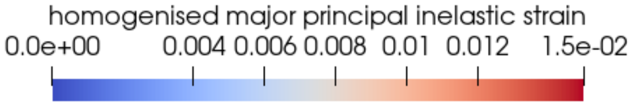

Figure 5.27: Numerical prediction of load-displacement and fracture pattern in hexagonal concrete specimen under compression in two opposite sides, as tested by Bennett and Jefferson (2007).

It is reported that the numerical prediction of the load-displacement response captures moderately well the very first stage of the pre-peak regime, although difficulties arrived in finding a minimum energy solution towards the structural peak response.

To alleviate such challenges a regional or global tracking algorithm may be required to produce a more continuous cracking trajectory, which would reduce the number of cracks activated to a minimum. In this regard, the global incremental iterative solution could be free of additional challenging iterations and micromechanical eigenvector fields could settle early on.

Regarding the fracture pattern predicted, it is encouraging that the current multiscale EFEM model can capture some of the geometric features of failure as recorded experimentally in such complicated test. Although, it is reminded that the model may still need some additional mechanical components to capture well the salient behaviour of cementitious composites.

5.1.7.4 The effect of the iteration number itfix for fixing macrocracks

Some challenges have been experienced, which build on top of the problem of finding a minimum energy solution, and that are related to the value of the parameter **itfix**. For such a complicated BVP, even after a sensible calibration of parameter sets is provided, the value of **itfix**=3 caused problems in the nucleating directions of macrocracks. It was observed that an apparent small numerical rounding off, during the intricate variational minimisation and global N-R procedure to find mechanical equilibrium, triggered small fluctuations in the solution of the PDEs, which in turn caused the strain eigenvector fields to fluctuate enough to be counterproductive for use in criteria for macrocrack nucleation as proposed in Section 4.3.5. Such an example of problematic fracture pattern is shown in Figure 5.28. A few options are described that could be used as a remedy for this in the future. At first, using higher values of **itfix** could be used as a simple solution for such complicated variational and global updates, although at the expense of having a larger number of iterations. A second option is a considerable reduction of step sizes during complicated response. Thirdly, an arc-length strategy would be suitable to constrain the solution into in an appropriate converging branch due to a reduced arc-length, particularly if the step size chosen causes large a jump between equilibrium states due to associated snapping-back.

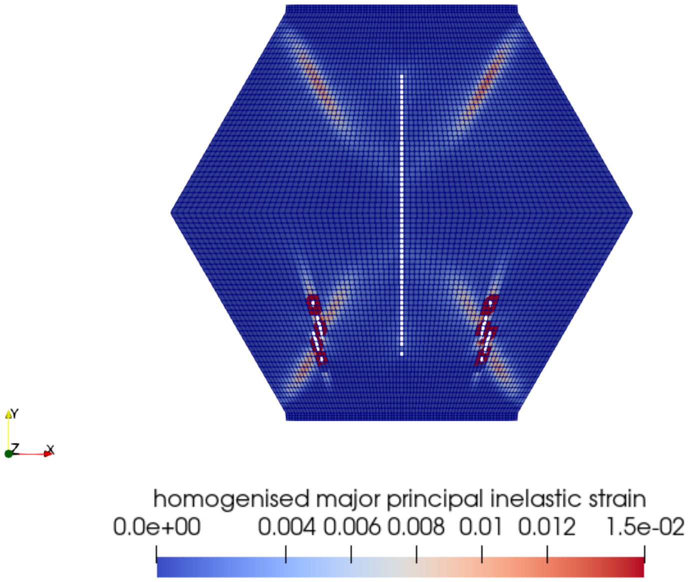

Figure 5.28: Numerical prediction of fracture pattern in hexagonal concrete specimen by Bennett and Jefferson (2007): elucidation of challenges of low values of **itfix** as a cause of obtaining unrealistic macrocrack patterns.

5.2 Disclosure on limitations of numerical components for capturing non-linear material behaviour

It is remarked that some numerical features of the behaviour of cementitious composites, such as frictional contact and dilatational response upon micro- and macrocrack opening and re-closure, as well as the ability to memorise permanent inelastic deformations upon unloading have been neglected in the current implementations. Such constitutive aspect of behaviour may not be fully separated from the computational aspects, which enable fracture propagation objectively across scales. The improvement of these numerical and computational components for material behaviour would be a substantial task in itself, which was not possible in this PhD since the main objective was targeted on coupling for the first time micromechanics-enriched continuum models and element-wise EFEM components.

5.2.1 Concluding remarks

In this chapter, several numerical examples have been presented to illustrate the capabilities of the proposed variational multiscale EFEM framework. The following conclusions may be drawn:

- Single element tests under uniaxial tension and combined tension-shear paths, which involve micromechanical damage and embedded macrocrack occurrence, have shown that directional microcracking and localised macrocracking can be modelled seamlessly, aided by energetic constraints and without the need of '*ad-hoc*' criteria for dictating the evolution of directional microcracks.

- Several comprehensive numerical examples involving macrocrack propagation with curved trajectories, which have been compared with experimental observations, have shown that the new multiscale EFEM model can exploit macrocrack tracking strategies available in the literature, see e.g. implementations by Freeman et al. (2020), to predict macroscopic failure mechanisms adequately while additional information on directional microcracking can be recovered.

- In general, it has been found that the method allows the load-displacement responses and failure mechanisms, observed in relatively complex experiments on cementitious composites, to be simulated adequately. Some numerical features of behaviour such as frictional contact and dilatational response in rough micro- and macro-cracks would require some additional constitutive as well as computational development.

- Good convergence characteristics have been identified in examples of moderate macrocracking complexity. Convergence features are expected to be fairly affected by choices of macrocrack tracking and the complexity of macrocrack patterns. It is envisaged that in some cases (such as failure tests on specimens of complex shapes, e.g. hexagonal concrete test), a global or regionally-improved tracking algorithm may give better predictions of failure patterns as well as reduced convergence challenges.

Chapter 6

Conclusions & future directions

"Further, the dignity of the science itself seems to require that every possible means be explored for the solution of a problem so elegant and so celebrated."
Carl Friedrich Gauss 1777 - 1855
German Physicist and pioneer of the Theory of Potentials in Mathematical Physics

6.1 Concluding remarks

A series of findings have been reported throughout this thesis. A summary of relevant conclusions is presented below:

- A new variational framework has been presented, which couples seamlessly, for the first time, a directional Micromechanics constitutive model and Finite Elements with embedded strong discontinuities at the macroscale. This framework contributes to the emerging literature on multiscale methods for modelling quasi-static deformation localisation across scales in quasi-brittle materials.
- The algorithms developed for the implementation of the coupled micro-macro crack model exhibited good convergence characteristics; e.g. they had a convergence rate between linear and quadratic for BVPs with a single macrocrack propagating across the mesh. Macrocrack tracking can adversely affect the convergence characteristics, particularly when complex multiple crack patterns develop.
- The framework has been found to capture adequately overall load-deformation responses, which are objective with respect to mesh refinement. In addition, due to the embedded strong discontinuity nature of the method, mesh refinement

needed for adequate prediction of the evolution of the fracture process zone is not excessive as opposed to other common variational methods such as phase-field models.

- The field derived from the strain tensor eigenvectors provides an effective basis for defining macrocrack propagation directions. It has been found that macrocrack normals are adequately defined by the major principal strain within the micromechanical bulk. It has also been found that delaying the activation of a strong discontinuity within an element and allowing the micromechanical strain field to further develop, can produce more realistic crack patterns.
- The proposed micro-macro scheme is more computationally efficient than multi-scale schemes that use discretisations at two scales e.g. FE2 methods. The proposed framework exploits algorithmic advantages of reduced-complexity homogenisation schemes in the bulk, and quasi-static condensation of macrocrack dofs at the element level. The latter is preserved as in classical formulations of embedded strong discontinuity Finite Element methods.

6.2 Future directions

Although substantial progress has been made on the development of micromechanical directional homogenisation schemes that are fully compatible, in a seamless fashion, with embedded strong discontinuity methods at the element-level, various aspects have been considered as secondary and further extensions of the framework are envisaged in the near future. Some proposed areas of future research include:

- Micro- and macrocracking frictional contact, and dilatational response at discontinuities upon re-closure, if included in a new extension of the model, would allow the model to better capture the response of concrete materials and structures under complex situations, e.g. to reproduce failure of hexagonal concrete characterisation tests by Bennett and Jefferson (2007).
- Other micromechanical components for a rigorous homogenisation analysis of concrete materials could be considered, such as two-phase Mori-Tanaka homogenisation (to explicitly consider micromechanical evolution at the aggregate phase and cement paste) in conventional concrete, and other components for unconventional concrete, e.g. reinforcing fibres.

- The model for the embedded macrocrack band could be extended to include a homogenised response in which the properties of the Micromechanical bulk could be projected in a similar way to its continuum counterpart. Then, energy dissipation across scales would be based on a reduced number of phenomological assumptions, while the variational basis of the method remains.

- Micromechanical fields could be further exploited to enhance sequential algorithms for geometric continuity of embedded macrocracks. Micromechanical fields could also serve as a basis for extending macrocrack tracking into parallelisable algorithms that consider both local and global domains.

- An adequate reproduction of snap-back response during macroscale fracture propagation could be ensured by extending the method with arc-length constraint equations. Implementation challenges may arrive over bouncing equilibrium states, which would push the limits of element-wise quasi-static condensation procedures, if large trial element distortions occurred.

- The current formulation does not consider continuity of displacement jumps. The method could be extended to consider a continuous field of displacement jumps. Whether full-continuity of displacement jumps or higher order schemes are beneficial for robustness is an open question.

- The methodology has been derived as a general framework which can be implemented in a 3D model, hence implementing the model in a 3D version is a subject for future research. In this case, the homogenised continuum would require three translation dofs, and the embedded macrocracks would be based on a quasi-static condensation scheme for three translational and three rotational dofs.

References

Agathos, K., Chatzi, E., and Bordas, S. P. (2016). Stable 3D extended finite elements with higher order enrichment for accurate non planar fracture. *Computer Methods in Applied Mechanics and Engineering*, 306:19–46.

Alfaiate, J., Simone, A., and Sluys, L. (2003). Non-homogeneous displacement jumps in strong embedded discontinuities. *International Journal of Solids and Structures*, 40(21):5799–5817.

Alfaiate, J., Wells, G., and Sluys, L. (2002). On the use of embedded discontinuity elements with crack path continuity for mode-I and mixed-mode fracture. *Engineering Fracture Mechanics*, 69(6):661–686.

Alnaas, W. F. (2016). *Nonlinear finite element analysis of quasi-brittle materials*. PhD thesis, Cardiff University.

Alnaas, W. F. and Jefferson, A. D. (2016). A smooth unloading-reloading approach for the nonlinear finite element analysis of quasi-brittle materials. *Engineering Fracture Mechanics*, 152:105–125.

Ambati, M., Gerasimov, T., and De Lorenzis, L. (2015). A review on phase-field models of brittle fracture and a new fast hybrid formulation. *Computational Mechanics*, 55(2):383–405.

Andrade, J. E. and Tu, X. (2009). Multiscale framework for behavior prediction in granular media. *Mechanics of Materials*, 41(6):652–669.

Andrieux, S., Bamberger, Y., and Marigo, J.-J. (1986). Model of Microcracked Material for Concrete and Rocks. *Journal de mecanique theorique et appliquee*, 5(3):471–513.

Armero, F. (2012). Strong discontinuities in antiplane/torsional problems of computational failure mechanics. *International Journal of Fracture*, 178(1-2):3–32.

Armero, F. and Linder, C. (2009). Numerical simulation of dynamic fracture using finite elements with embedded discontinuities. *International Journal of Fracture*, 160(2):119–141.

Azua-Gonzalez, C., Mihai, I., and Jefferson, A. (2019). A combined Micromechanics Strong-Discontinuity approach for Modelling Distributed and Localised Fracture in Cementitious Materials. In *UKACM 19 conference*, London.

Azua-Gonzalez, C., Mihai, I., and Jefferson, A. (2020). Micromechanics-driven variational method for diffuse-to-localised fracture in quasi-brittle solids. In Chinesta, F., Abgrall, R., Allix, O., and Kaliske, M., editors, *14th World Congress on Computational Mechanics (WCCM)-ECCOMAS Congress*.

Azua-Gonzalez, C., Mihai, I., and Jefferson, A. D. (2021). Coupled Micromechanics - embedded strong discontinuity model for quasi-brittle fracture: a variational appraisal. In *UKACM 21 conference*.

Bažant, Z. P. (1976). Instability, Ductility, and Size Effect in Strain-Softening Concrete. *Journal of the Engineering Mechanics Division*, 102(2):331–344.

Bažant, Z. P. (1984). Microplane model for strain-controlled inelastic behavior. In Desai, C. S. and Gallagher, R. H., editors, *Mechanics of engineering materials,*, pages 45–59, N.Y. John Wiley and Sons, Inc.

Bažant, Z. P., Belytschko, T. B., and Chang, T. (1984). Continuum Theory for Strain-Softening. *Journal of Engineering Mechanics*, 110(12):1666–1692.

Bazant, Z. P., Nguyen, H. T., and Dönmez, A. A. (2022). Critical Comparison of Phase-Field, Peridynamics and Crack Band Model M7 in Light of Gap Test and Classical Fracture Tests. *Journal of Applied Mechanics*, pages 1–79.

Bažant, Z. P. and Oh, B. H. (1983). Crack band theory for fracture of concrete. *Matériaux et Constructions*, 16(3):155–177.

Bažant, Z. P. and Pijaudier-Cabot, G. (1988). Nonlocal Continuum Damage, Localization Instability and Convergence. *Journal of Applied Mechanics*, 55(2):287.

Bažant, Z. P. and Prat, P. C. (1988a). Microplane Model for Brittle-Plastic Material: I. Theory. *Journal of Engineering Mechanics*, 114(10):1672–1688.

Bažant, Z. P. and Prat, P. C. (1988b). Microplane Model for Brittle-Plastic Material: II. Verification. *Journal of Engineering Mechanics*, 114(10):1689–1702.

Beese, S., Loehnert, S., and Wriggers, P. (2018). 3D ductile crack propagation within a polycrystalline microstructure using XFEM. *Computational Mechanics*, 61(1-2):71–88.

Belytschko, T. and Black, T. (1999). Elastic crack growth in finite elements with minimal remeshing. *International Journal for Numerical Methods in Engineering*, 45(5):601–620.

Belytschko, T., Fish, J., and Engelmann, B. E. (1988). A finite element with embedded localization zones. *Computer Methods in Applied Mechanics and Engineering*, 70(1):59–89.

Belytschko, T., Lu, Y., Gu, L., and Tabbara, M. (1995). Element-free galerkin methods for static and dynamic fracture. *International Journal of Solids and Structures*, 32(17-18):2547–2570.

Belytschko, T., Lu, Y. Y., and Gu, L. (1994). Element-free Galerkin methods. *International Journal for Numerical Methods in Engineering*, 37(2):229–256.

Bennett, T. and Jefferson, A. D. (2007). Experimental tests and numerical modelling of hexagonal concrete specimens. *Materials and Structures/Materiaux et Constructions*, 40(5):491–505.

Bird, R., Coombs, W. M., and Giani, S. (2022). Adaptive configurational force-based propagation for brittle and fatigue crack analysis. *International Journal for Numerical Methods in Engineering*, 123(7):1673–1709.

Bird, R. E., Coombs, W. M., and Giani, S. (2019). A posteriori discontinuous Galerkin error estimator for linear elasticity. *Applied Mathematics and Computation*, 344-345:78–96.

Bolander, J. and Saito, S. (1998). Fracture analyses using spring networks with random geometry. *Engineering Fracture Mechanics*, 61(5-6):569–591.

Bolander, J. E. and Sukumar, N. (2005). Irregular lattice model for quasistatic crack propagation. *Physical Review B*, 71(9):094106.

Bordas, S., Nguyen, P. V., Dunant, C., Guidoum, A., and Nguyen-Dang, H. (2007). An extended finite element library. *International Journal for Numerical Methods in Engineering*, 71(6):703–732.

Borja, R. I. (2002). Bifurcation of elastoplastic solids to shear band mode at finite strain. *Computer Methods in Applied Mechanics and Engineering*, 191(46):5287–5314.

Borja, R. I. (2008). Assumed enhanced strain and the extended finite element methods: A unification of concepts. *Computer Methods in Applied Mechanics and Engineering*, 197(33-40):2789–2803.

Borja, R. I. and Aydin, A. (2004). Computational modeling of deformation bands in granular media. I. Geological and mathematical framework. *Computer Methods in Applied Mechanics and Engineering*, 193(27-29):2667–2698.

Borja, R. I. and Wren, J. R. (1995). Micromechanics of granular media Part I: Generation of overall constitutive equation for assemblies of circular disks. *Computer Methods in Applied Mechanics and Engineering*, 127(1-4):13–36.

Bresler, B. and Bertero, V. V. (1979). Influence of high strain rate and cyclic loading on behaviour of unconfined and confined concrete in compression. Report No. EERC 75-16. Technical report, Dept. of Civil Engineering, University of California, Berkeley.

Budiansky, B. and O'Connell, R. J. (1976). Elastic moduli of a cracked solid. *International Journal of Solids and Structures*, 12(2):81–97.

Cedolin, L. and Bažant, Z. P. (1980). Effect of finite element choice in blunt crack band analysis. *Computer Methods in Applied Mechanics and Engineering*, 24(3):305–316.

Charlez, P. (1993). Internal Report. Technical report, Total Company.

Chen, Q., Andrade, J. E., and Samaniego, E. (2011). AES for multiscale localization modeling in granular media. *Computer Methods in Applied Mechanics and Engineering*.

Coenen, E., Kouznetsova, V., and Geers, M. (2012). Novel boundary conditions for strain localization analyses in microstructural volume elements. *International Journal for Numerical Methods in Engineering*, 90(1):1–21.

Cosserat, E. and Cosserat, F. (1909). Théorie des Corps déformables. *Nature*, 81(2072):67–67.

Crisfield, M. (1982). Local instabilities in the non-linear analysis of reinforced concrete beams and slabs. *Proceedings of the Institution of Civil Engineers*, 73(1):135–145.

Cundall, P. (1988). Formulation of a three-dimensional distinct element model-Part I. A scheme to detect and represent contacts in a system composed of many polyhedral blocks. *International Journal of Rock Mechanics and Mining Sciences & Geomechanics Abstracts*, 25(3):107–116.

Cundall, P. A. and Strack, O. D. L. (1979). A discrete numerical model for granular assemblies. *Géotechnique*, 29(1):47–65.

Cusatis, G., Pelessone, D., and Mencarelli, A. (2011). Lattice Discrete Particle Model (LDPM) for failure behavior of concrete. I: Theory. *Cement and Concrete Composites*, 33(9):881–890.

De Borst, R. (1987). Computation of post-bifurcation and post-failure behavior of strain-softening solids. *Computers & Structures*, 25(2):211–224.

De Borst, R. (1991). Simulation of strain localization: a reappraisal of the Cosserat Continuum. *Engineering Computations*, 8(4):317–332.

De Borst, R. (2018). Fracture Modeling Using Isogeometric Analysis. In *Computational Methods for Fracture in Porous Media*, pages 109–154. Elsevier.

De Borst, R., Crisfield, M. A., Remmers, J. J. C., and Verhoosel, C. V. (2012). *Nonlinear Finite Element Analysis of Solids and Structures.* Wiley.

De Borst, R. and Mühlhaus, H. B. (1992). Gradient-dependent plasticity: Formulation and algorithmic aspects. *International Journal for Numerical Methods in Engineering*, 35(3):521–539.

De Borst, R. and Verhoosel, C. V. (2016). Gradient damage vs phase-field approaches for fracture: Similarities and differences. *Computer Methods in Applied Mechanics and Engineering*, 312:78–94.

De Freitas, J. (1998). Formulation of elastostatic hybrid-Trefftz stress elements. *Computer Methods in Applied Mechanics and Engineering*, 153(1-2):127–151.

Desrues, J., Argilaga, A., Caillerie, D., Combe, G., Nguyen, T. K., Richefeu, V., and Dal Pont, S. (2019). From discrete to continuum modelling of boundary value problems in geomechanics: An integrated FEM/DEM approach. *International Journal for Numerical and Analytical Methods in Geomechanics*, 43(5):919–955.

Di Luzio, G. and Cusatis, G. (2013). Solidification–microprestress–microplane (SMM) theory for concrete at early age: Theory, validation and application. *International Journal of Solids and Structures*, 50(6):957–975.

Duda, F. P., Ciarbonetti, A., Sánchez, P. J., and Huespe, A. E. (2015). A phase-field/gradient damage model for brittle fracture in elastic–plastic solids. *International Journal of Plasticity*, 65:269–296.

Eshelby, J. D. (1957). The determination of the elastic field of an ellipsoidal inclusion, and related problems. *Proceedings of the Royal Society of London. Series A. Mathematical and Physical Sciences*, 241(1226):376–396.

Eshelby, J. D. (1959). The elastic field outside an ellipsoidal inclusion. *Proceedings of the Royal Society of London. Series A. Mathematical and Physical Sciences*, 252(1271):561–569.

Feyel, F. and Chaboche, J. (2000). FE2 multiscale approach for modelling the elasto-viscoplastic behaviour of long fibre SiC/Ti composite materials. *Computer Methods in Applied Mechanics and Engineering*, 183(3-4):309–330.

Fonseka, G. U. and Krajcinovic, D. (1981). The Continuous Damage Theory of Brittle Materials, Part 2: Uniaxial and Plane Response Modes. *Journal of Applied Mechanics*, 48(4):816.

Foster, C. D., Borja, R. I., and Regueiro, R. A. (2007). Embedded strong discontinuity finite elements for fractured geomaterials with variable friction. *International Journal for Numerical Methods in Engineering*, 72(5):549–581.

Freeman, B. L., Bonilla-Villalba, P., Mihai, I. C., Alnaas, W. F., and Jefferson, A. D. (2020). A specialised finite element for simulating self-healing quasi-brittle materials. *Advanced Modeling and Simulation in Engineering Sciences*, 7(1):32.

Garboczi, E. and Day, A. (1995). An algorithm for computing the effective linear elastic properties of heterogeneous materials: Three-dimensional results for composites with equal phase poisson ratios. *Journal of the Mechanics and Physics of Solids*, 43(9):1349–1362.

Geers, M. G. D., Kouznetsova, V., Matouš, K., and Yvonnet, J. (2017). Homogenization Methods and Multiscale Modeling: Nonlinear Problems. In Stein, E., de Borst, R., and R., H. T. J., editors, *Encyclopedia of Computational Mechanics Second Edition. Volume 2: Solids and Structures*. John Wiley and Sons Ltd.

Giambanco, G. and La Malfa Ribolla, E. (2019). A phase-field model for strain localization analysis in softening elastoplastic materials. *International Journal of Solids and Structures*, 172-173:84–96.

Griffith, A. A. (1921). The Phenomena of Rupture and Flow in Solids. *Philosophical Transactions of the Royal Society A: Mathematical, Physical and Engineering Sciences*, 221(582-593):163–198.

Gurtin, M. E. and Podio-Guidugli, P. (1996). Configurational forces and the basic laws for crack propagation. *Journal of the Mechanics and Physics of Solids*, 44(6):905–927.

Haghighat, E. and Pietruszczak, S. (2016). On modeling of fractured media using an enhanced embedded discontinuity approach. *Extreme Mechanics Letters*, 6:10–22.

Hashim, N. A., Coombs, W., Augarde, C., and Hattori, G. (2020). An implicit non-ordinary state-based peridynamics with stabilised correspondence material model for finite deformation analysis. *Computer Methods in Applied Mechanics and Engineering*, 371:113304.

Hashin, Z. and Shtrikman, S. (1961). Note on a variational approach to the theory of composite elastic materials. *Journal of the Franklin Institute*, 271(4):336–341.

Hentz, S., Daudeville, L., and Donzé, F. V. (2004). Identification and Validation of a Discrete Element Model for Concrete. *Journal of Engineering Mechanics*, 130(6):709–719.

Hill, R. (1963). Elastic properties of reinforced solids: Some theoretical principles. *Journal of the Mechanics and Physics of Solids*, 11(5):357–372.

Hinton, E. and Owen, D. R. J. (1979). *An introduction to finite element computations*. Pineridge Press, Swansea.

Hognestad, E., Hanson, N. W., and McHenry, D. (1955). Concrete stress distribution in ultimate strength design. *Journal of the American Concrete Institute*, 4(5):455–477.

Holl, M., Rogge, T., Loehnert, S., Wriggers, P., and Rolfes, R. (2014). 3D multiscale crack propagation using the XFEM applied to a gas turbine blade. *Computational Mechanics*, 53(1):173–188.

Hughes, T., Cottrell, J., and Bazilevs, Y. (2005). Isogeometric analysis: CAD, finite elements, NURBS, exact geometry and mesh refinement. *Computer Methods in Applied Mechanics and Engineering*, 194(39-41):4135–4195.

Jefferson, A. (2003a). Craft—a plastic-damage-contact model for concrete. I. Model theory and thermodynamic considerations. *International Journal of Solids and Structures*, 40(22):5973–5999.

Jefferson, A. (2003b). Craft—a plastic-damage-contact model for concrete. II. Model implementation with implicit return-mapping algorithm and consistent tangent matrix. *International Journal of Solids and Structures*, 40(22):6001–6022.

Jefferson, A. and Bennett, T. (2010). A model for cementitious composite materials based on micro-mechanical solutions and damage-contact theory. *Computers & Structures*, 88(23-24):1361–1366.

Jefferson, A. and Freeman, B. (2022). A crack-opening-dependent numerical model for self-healing cementitious materials. *International Journal of Solids and Structures*, 244-245:111601.

Jefferson, A. D. and Bennett, T. (2007). Micro-mechanical damage and rough crack closure in cementitious composite materials. *International Journal for Numerical and Analytical Methods in Geomechanics*, 31(2):133–146.

Jefferson, A. D. and Mihai, I. C. (2015). The simulation of crack opening-closing and aggregate interlock behaviour in finite element concrete models. *International Journal for Numerical Methods in Engineering*, 104(1):48–78.

Jirásek, M. (2000). Comparative study on finite elements with embedded discontinuities. *Computer Methods in Applied Mechanics and Engineering*, 188(1-3):307–330.

Jirousek, J. and Zielinski, A. P. (1993). Dual hybrid-Trefftz element formulation based on independent boundary traction frame. *International Journal for Numerical Methods in Engineering*, 36(17):2955–2980.

Kaczmarczyk, Ł. and Pearce, C. J. (2009). A corotational hybrid-Trefftz stress formulation for modelling cohesive cracks. *Computer Methods in Applied Mechanics and Engineering*, 198(15-16):1298–1310.

Kaczmarczyk, Ł., Ullah, Z., and Pearce, C. J. (2017). Energy consistent framework for continuously evolving 3D crack propagation. *Computer Methods in Applied Mechanics and Engineering*, 324:54–73.

Karamnejad, A., Ahmed, A., and Sluys, L. J. (2017). A Numerical Homogenization Scheme for Glass Particle-Toughened Polymers Under Dynamic Loading. *Journal of Multiscale Modelling*, 08(01):1750001.

Karamnejad, A. and Sluys, L. J. (2014). A dispersive multi-scale crack model for quasi-brittle heterogeneous materials under impact loading. *Computer Methods in Applied Mechanics and Engineering*, 278:423–444.

Klisinski, M., Runesson, K., and Sture, S. (1991). Finite Element with Inner Softening Band. *Journal of Engineering Mechanics*, 117(3):575–587.

Koiter, W. T. (1953). Stress-strain relations, uniqueness and variational theorems for elastic-plastic materials with a singular yield surface. *Quarterly of Applied Mathematics*, 11(3):350–354.

Kouznetsova, V., Geers, M. G. D., and Brekelmans, W. A. M. (2002). Multi-scale constitutive modelling of heterogeneous materials with a gradient-enhanced computational homogenization scheme. *International Journal for Numerical Methods in Engineering*, 54(8):1235–1260.

Krajcinovic, D. and Fonseka, G. U. (1981). The Continuous Damage Theory of Brittle Materials, Part 1: General Theory. *Journal of Applied Mechanics*, 48(4):809.

Kupfer, H., Hilsdorf, H. K., and Rusch, H. (1969). behaviour of concrete under biaxial stresses. *Am Concrete Inst Journal & Proceedings*, 66(8):656–666.

Lale, E. and Cusatis, G. (2021). Symmetric high order microplane model for damage localization and size effect in quasi-brittle materials. *International Journal for Numerical and Analytical Methods in Geomechanics*, 45(10):1458–1476.

Lemaitre, J. and Chaboche, J.-L. (1990). *Mechanics of solid materials*. Cambridge University Press.

Linder, C. and Armero, F. (2007). Finite elements with embedded strong discontinuities for the modeling of failure in solids. *International Journal for Numerical Methods in Engineering*, 72(12):1391–1433.

Linder, C. and Raina, A. (2013). A strong discontinuity approach on multiple levels to model solids at failure. *Computer Methods in Applied Mechanics and Engineering*, 253:558–583.

Liu, P. (2015). Extended finite element method for strong discontinuity analysis of strain localization of non-associative plasticity materials. *International Journal of Solids and Structures*, 72:174–189.

Loehnert, S. and Belytschko, T. (2007). A multiscale projection method for macro/microcrack simulations. *International Journal for Numerical Methods in Engineering*, 71(12):1466–1482.

Lotfi, H. R. and Shing, P. B. (1995). Embedded representation of fracture in concrete with mixed finite elements. *International Journal for Numerical Methods in Engineering*, 38(8):1307–1325.

Lu, M., Zhang, H., Zheng, Y., and Zhang, L. (2016). A multiscale finite element method with embedded strong discontinuity model for the simulation of cohesive cracks in solids. *Computer Methods in Applied Mechanics and Engineering*, 311:576–598.

Lu, M., Zhang, H., Zheng, Y., and Zhang, L. (2017). A multiscale finite element method for the localization analysis of homogeneous and heterogeneous saturated porous media with embedded strong discontinuity model. *International Journal for Numerical Methods in Engineering*, 112(10):1439–1472.

Martin, C. D. (1997). Seventeenth Canadian Geotechnical Colloquium: The effect of cohesion loss and stress path on brittle rock strength. *Canadian Geotechnical Journal*, 34(5):698–725.

Mazars, J. (1986). A description of micro- and macroscale damage of concrete structures. *Engineering Fracture Mechanics*, 25(5-6):729–737.

McLaughlin, R. (1977). A study of the differential scheme for composite materials. *International Journal of Engineering Science*, 15(4):237–244.

Miehe, C., Dettmar, J., and Zäh, D. (2010a). Homogenization and two-scale simulations of granular materials for different microstructural constraints. *International Journal for Numerical Methods in Engineering*, 83(8-9):1206–1236.

Miehe, C., Gürses, E., and Birkle, M. (2007). A computational framework of configurational-force-driven brittle fracture based on incremental energy minimization. *International Journal of Fracture*, 145(4):245–259.

Miehe, C., Hofacker, M., and Welschinger, F. (2010b). A phase field model for rate-independent crack propagation: Robust algorithmic implementation based on operator splits. *Computer Methods in Applied Mechanics and Engineering*, 199(45-48):2765–2778.

Miehe, C., Welschinger, F., and Hofacker, M. (2010c). Thermodynamically consistent phase-field models of fracture: Variational principles and multi-field FE implementations. *International Journal for Numerical Methods in Engineering*, 83(10):1273–1311.

Mihai, I. and Jefferson, A. (2011). A material model for cementitious composite materials with an exterior point Eshelby microcrack initiation criterion. *International Journal of Solids and Structures*, 48(24):3312–3325.

Moallemi, S. and Pietruszczak, S. (2017). Analysis of localized fracture in 3D reinforced concrete structures using volume averaging technique. *Finite Elements in Analysis and Design*, 125:41–52.

Moës, N., Dolbow, J., and Belytschko, T. (1999). A finite element method for crack growth without remeshing. *International Journal for Numerical Methods in Engineering*, 46(1):131–150.

Mori, T. and Tanaka, K. (1973). Average stress in matrix and average elastic energy of materials with misfitting inclusions. *Acta Metallurgica*, 21(5):571–574.

Mosby, M. and Matouš, K. (2016). Computational homogenization at extreme scales. *Extreme Mechanics Letters*, 6:68–74.

Mühlhaus, H. and Vardoulakis, I. (1987). The thickness of shear bands in granular materials. *Géotechnique*, 37(3):271–283.

Mura, T. (1987). *Micromechanics of Defects in Solids*. Springer Netherlands.

Nejati, M., Paluszny, A., and Zimmerman, R. W. (2016). A finite element framework for modeling internal frictional contact in three-dimensional fractured media using unstructured tetrahedral meshes. *Computer Methods in Applied Mechanics and Engineering*, 306:123–150.

Nemat-Nasser, S., Lori, M., and Datta, S. K. (1996). Micromechanics: Overall Properties of Heterogeneous Materials. *Journal of Applied Mechanics*, 63(2):561–561.

Neuner, M., Gamnitzer, P., and Hofstetter, G. (2020). A 3D gradient-enhanced micropolar damage-plasticity approach for modeling quasi-brittle failure of cohesive-frictional materials. *Computers & Structures*, 239:106332.

Nguyen, G. D., Einav, I., and Korsunsky, A. M. (2012). How to connect two scales of behaviour in constitutive modelling of geomaterials. *Géotechnique Letters*, 2(3):129–134.

Nguyen, G. D., Korsunsky, A. M., and Einav, I. (2014). A constitutive modelling framework featuring two scales of behaviour: Fundamentals and applications to quasi-brittle failure. *Engineering Fracture Mechanics*.

Nguyen, K. D., E.Augarde, C., Coombs, W. M., Nguyen-Xuan, H., and Abdel-Wahab, M. (2020). Non-conforming multipatches for NURBS-based finite element analysis of higher-order phase-field models for brittle fracture. *Engineering Fracture Mechanics*, 235:107133.

Nguyen, V. P., Lloberas-Valls, O., Stroeven, M., and Sluys, L. J. (2011). Homogenization-based multiscale crack modelling: From micro-diffusive damage to macro-cracks. *Computer Methods in Applied Mechanics and Engineering*, 200(9-12):1220–1236.

Nitka, M., Combe, G., Dascalu, C., and Desrues, J. (2011). Two-scale modeling of granular materials: a DEM-FEM approach. *Granular Matter*, 13(3):277–281.

Nooru-Mohamed, M., Schlangen, E., and van Mier, J. G. (1993). Experimental and numerical study on the behavior of concrete subjected to biaxial tension and shear. *Advanced Cement Based Materials*, 1(1):22–37.

Novák, J., Kaczmarczyk, Ł., Grassl, P., Zeman, J., and Pearce, C. J. (2012). A micromechanics-enhanced finite element formulation for modelling heterogeneous materials. *Computer Methods in Applied Mechanics and Engineering*, 201-204:53–64.

Oden, J. T. and Reddy, J. N. (2010). *An Introduction to the Mathematical Theory of Finite Elements*. Dover Publications Inc.

Oliver, J. (1995). Continuum modelling of strong discontinuities in solid mechanics using damage models. *Computational Mechanics*, 17(1-2):49–61.

Oliver, J. and Huespe, A. (2004). Theoretical and computational issues in modelling material failure in strong discontinuity scenarios. *Computer Methods in Applied Mechanics and Engineering*, 193(27-29):2987–3014.

Oliver, J., Huespe, A., and Sánchez, P. (2006). A comparative study on finite elements for capturing strong discontinuities: E-FEM vs X-FEM. *Computer Methods in Applied Mechanics and Engineering*, 195(37-40):4732–4752.

Oliver, J., Huespe, A. E., Pulido, M. D. G., and Samaniego, E. (2003). On the strong discontinuity approach in finite deformation settings. *International Journal for Numerical Methods in Engineering*, 56(7):1051–1082.

Ortiz, M. (1985). A constitutive theory for the inelastic behavior of concrete. *Mechanics of Materials*, 4(1):67–93.

Ortiz, M. (1988). Microcrack coalescence and macroscopic crack growth initiation in brittle solids. *International Journal of Solids and Structures*, 24(3):231–250.

Oskay, C., Su, Z., and Kapusuzoglu, B. (2020). Discrete eigenseparation-based reduced order homogenization method for failure modeling of composite materials. *Computer Methods in Applied Mechanics and Engineering*, 359:112656.

Ožbolt, J. and Bažant, Z. P. (1992). Microplane Model for Cyclic Triaxial Behavior of Concrete. *Journal of Engineering Mechanics*, 118(7):1365–1386.

Peerlings, R. H. J., De Borst, R., Brekelmans, W. A. M., and De Vree, J. H. P. (1996). Gradient enhanced damage for quasi-brittle materials. *International Journal for Numerical Methods in Engineering*, 39(19):3391–3403.

Pensée, V., Kondo, D., and Dormieux, L. (2002). Micromechanical Analysis of Anisotropic Damage in Brittle Materials. *Journal of Engineering Mechanics*, 128(8):889–897.

Petersson, P. (1981). *Crack growth and development of fracture zones in plain concrete and similar materials*. PhD thesis, Lund Institute of Technology.

Phillips, R., Rodney, D., Shenoy, V., Tadmor, E., and Ortiz, M. (1999). Hierarchical models of plasticity: dislocation nucleation and interaction. *Modelling and Simulation in Materials Science and Engineering*, 7(5):769–780.

Pietruszczak, S. and Mróz, Z. (1981). Finite element analysis of deformation of strain-softening materials. *International Journal for Numerical Methods in Engineering*, 17(3):327–334.

Pijaudier-Cabot, G. and Bažant, Z. P. (1987). Nonlocal Damage Theory. *Journal of Engineering Mechanics*, 113(10):1512–1533.

Prager, W. (1949). Recent Developments in the Mathematical Theory of Plasticity. *Journal of Applied Physics*, 20(3):235–241.

Press, W., Teukolsky, S., Vettering, W., and Flannery, B. (1988). *Numerical Recipes in C*. Cambridge University Press, Cambridge.

Pretti, G., Coombs, W. M., and Augarde, C. E. (2022). A displacement-controlled arc-length solution scheme. *Computers & Structures*, 258:106674.

Raina, A. and Linder, C. (2015). A micromechanical model with strong discontinuities for failure in nonwovens at finite deformations. *International Journal of Solids and Structures*, 75-76:247–259.

Regueiro, R. A. and Borja, R. I. (1999). A finite element model of localized deformation in frictional materials taking a strong discontinuity approach. *Finite Elements in Analysis and Design*, 33(4):283–315.

Riks, E. (1979). An incremental approach to the solution of snapping and buckling problems. *International Journal of Solids and Structures*, 15(7):529–551.

Rousseau, J., Frangin, E., Marin, P., and Daudeville, L. (2008). Damage prediction in the vicinity of an impact on a concrete structure: a combined FEM/DEM approach. *Computers and Concrete*, 5(4):343–358.

Saksala, T., Brancherie, D., Harari, I., and Ibrahimbegovic, A. (2015). Combined continuum damage-embedded discontinuity model for explicit dynamic fracture analyses of quasi-brittle materials. *International Journal for Numerical Methods in Engineering*, 101(3):230–250.

Saksala, T., Brancherie, D., and Ibrahimbegovic, A. (2016). Numerical modeling of dynamic rock fracture with a combined 3D continuum viscodamage-embedded discontinuity model. *International Journal for Numerical and Analytical Methods in Geomechanics*, 40(9):1339–1357.

Schlangen, E. (1993). *Experimental and numerical analysis of fracture processes in concrete*. PhD thesis, Delft University of Technology.

Schlangen, E. and Garboczi, E. (1996). New method for simulating fracture using an elastically uniform random geometry lattice. *International Journal of Engineering Science*, 34(10):1131–1144.

Schlangen, E. and Garboczi, E. (1997). Fracture simulations of concrete using lattice models: Computational aspects. *Engineering Fracture Mechanics*, 57(2-3):319–332.

Silling, S. and Askari, E. (2005). A meshfree method based on the peridynamic model of solid mechanics. *Computers & Structures*, 83(17-18):1526–1535.

Simo, J. and Taylor, R. (1985). Consistent tangent operators for rate-independent elastoplasticity. *Computer Methods in Applied Mechanics and Engineering*, 48(1):101–118.

Simo, J. C., Oliver, J., and Armero, F. (1993). An analysis of strong discontinuities induced by strain-softening in rate-independent inelastic solids. *Computational Mechanics*, 12(5):277–296.

Sluys, L., De Borst, R., and Mühlhaus, H. (1993). Wave propagation, localization and dispersion in a gradient-dependent medium. *International Journal of Solids and Structures*, 30(9):1153–1171.

Stroud, A. (1971). *Approximate Calculation of Multiple Integrals (A. H. Stroud)*. Englewood Cliffs.

Taylor, G. I. (1938). Plastic strain in metals. *Journal of the Institute of Metals*, 62:307–324.

Tenchev, R. and Purnell, P. (2005). An application of a damage constitutive model to concrete at high temperature and prediction of spalling. *International Journal of Solids and Structures*, 42(26):6550–6565.

Terada, K., Hori, M., Kyoya, T., and Kikuchi, N. (2000). Simulation of the multi-scale convergence in computational homogenization approaches. *International Journal of Solids and Structures*, 37(16):2285–2311.

Tijssens, M. (2001). *On the cohesive surface methodology for fracture of brittle heterogeneous solids - computational and material modeling*. PhD thesis, Delft University of Technology.

Tjioe, M. and Borja, R. I. (2015). On the pore-scale mechanisms leading to brittle and ductile deformation behavior of crystalline rocks. *International Journal for Numerical and Analytical Methods in Geomechanics*, 39(11):1165–1187.

Toro, S., Sánchez, P., Huespe, A., Giusti, S., Blanco, P., and Feijóo, R. (2014). A two-scale failure model for heterogeneous materials: numerical implementation based on the finite element method. *International Journal for Numerical Methods in Engineering*, 97(5):313–351.

Van Mier, J. (1984). *Strain-softening of concrete under multiaxial loading conditions*. PhD thesis, TU Eindhoven.

Verhoosel, C. V. and de Borst, R. (2013). A phase-field model for cohesive fracture. *International Journal for Numerical Methods in Engineering*, 96(1):43–62.

Wang, Y. and Waisman, H. (2016). From diffuse damage to sharp cohesive cracks: A coupled XFEM framework for failure analysis of quasi-brittle materials. *Computer Methods in Applied Mechanics and Engineering*, 299:57–89.

Winkler, B., Hofstetter, G., and Niederwanger, G. (2001). Experimental verification of a constitutive model for concrete cracking. *Proceedings of the Institution of Mechanical Engineers, Part L: Journal of Materials: Design and Applications*, 215(2):75–86.

Wren, J. R. and Borja, R. I. (1997). Micromechanics of granular media Part II: Overall tangential moduli and localization model for periodic assemblies of circular disks. *Computer Methods in Applied Mechanics and Engineering*, 141(3-4):221–246.

Xu, F., Hajibeygi, H., and Sluys, L. J. (2021). Multiscale extended finite element method for deformable fractured porous media. *Journal of Computational Physics*, 436:110287.

Xu, S. and Zhu, Y. (2009). Experimental determination of fracture parameters for crack propagation in hardening cement paste and mortar. *International Journal of Fracture*, 157(1-2):33–43.

Xu, X. P. and Needleman, A. (1994). Numerical simulations of fast crack growth in brittle solids. *Journal of the Mechanics and Physics of Solids*, 42(9):1397–1434.

Zhao, L. Y., Shao, J. F., and Zhu, Q. Z. (2018). Analysis of localized cracking in quasi-brittle materials with a micro-mechanics based friction-damage approach. *Journal of the Mechanics and Physics of Solids*, 119:163–187.

Zhao, L. Y., Zhu, Q. Z., Xu, W. Y., Dai, F., and Shao, J. F. (2016). A unified micromechanics-based damage model for instantaneous and time-dependent behaviors of brittle rocks. *International Journal of Rock Mechanics and Mining Sciences*, 84:187–196.

Zhu, Q., Kondo, D., and Shao, J. (2008a). Micromechanical analysis of coupling between anisotropic damage and friction in quasi brittle materials: Role of the homogenization scheme. *International Journal of Solids and Structures*, 45(5):1385–1405.

Zhu, Q., Kondo, D., Shao, J., and Pensee, V. (2008b). Micromechanical modelling of anisotropic damage in brittle rocks and application. *International Journal of Rock Mechanics and Mining Sciences*, 45(4):467–477.

Zhu, Q. Z., Shao, J. F., and Kondo, D. (2011). A micromechanics-based thermodynamic formulation of isotropic damage with unilateral and friction effects. *European Journal of Mechanics, A/Solids*.

Zhu, Y. (2017). A micromechanics-based damage constitutive model of porous rocks. *International Journal of Rock Mechanics and Mining Sciences*, 91:1–6.

Zimmerman, R. W. (1991). Elastic moduli of a solid containing spherical inclusions. *Mechanics of Materials*, 12(1):17–24.